Direct Simulation and Theoretical Study of Sub- and Supersonic Wakes

Simulation directe et étude théorique de sillages sous- et supersoniques

A Thesis Submitted

to the Division of Graduate Studies of the Royal Military College of Canada

by

Jean-Pierre Hickey

In Partial Fulfillment of the Requirements for the Degree of

Doctor of Philosophy

December 2012

ROYAL MILITARY COLLEGE OF CANADA
COLLÈGE MILITAIRE ROYAL DU CANADA

Division of Graduate Studies and Research
Division des études supérieures et de la recherche

This is to certify that the thesis prepared by / Ceci certifie que la thèse rédigée par

Jean-Pierre Hickey

entitled / intitulée

Direct Simulation and Theoretical Study of Sub- and Supersonic Wakes /
Simulation directe et étude théorique de sillages sous- et supersoniques

complies with the Royal Military College of Canada regulations and that it meets the accepted standards of the Graduate School with respect to quality, and, in the case of a doctoral thesis, originality, / satisfait aux règlements du Collège militaire royal du Canada et qu'elle respecte les normes acceptées par la Faculté des études supérieures quant à la qualité et, dans le cas d'une thèse de doctorat, l'originalité,

for the degree of / pour le diplôme de

Doctor of Philosophy / Doctorat en philosophie

Signed by the final examining committee: /
Signé par les membres du comité examinateur de la soutenance de thèse:

_____	Chair / Président Prof. Thomas Dececchi, Royal Military College
_____	External Examiner / Examinateur externe Prof. Johan Larsson, University of Maryland
_____	Main Supervisor / Directeur de thèse principal Prof. Xiaohua Wu, Royal Military College

Approved by the Head of Department : /
Approuvé par le directeur du département :_____ Date: _____

This thesis is not to be regarded as classified./Cette thèse n'est pas considérée comme à publication restreinte.

_____Main Supervisor / Directeur de thèse principal

Acknowledgments

I would like to thank Prof. Xiaohua Wu for his continued support and trust in my capabilities. He has relentlessly advocated for my success and has given me all the opportunities to succeed.

I am also deeply indebted to Prof. Fazle Hussain of the University of Houston for his mentorship. He has been the catalyst for many great ideas. Furthermore, he has spent time and energy to foster my creativity, curiosity and intellectual rigor while also instilling in me the importance of well-articulated and precise scientific prose.

I am very grateful for the friendship and intellectual stimulation of the immensely talented students, present and past, in the Piomelli group at Queen's University. I would also like to acknowledge the faculty, students, administrative assistants and colleagues in the Department of Mechanical and Aerospace Engineering at RMC who have helped forge a pleasant work atmosphere and an esprit de corps.

Andrea, thank you for your support, understanding and companionship.

Abstract

Hickey, Jean-Pierre, Ph.D., Department of Mechanical and Aerospace Engineering, Royal Military College of Canada, December 2012. Direct Simulation and Theoretical Study of Sub- and Supersonic Wakes. Supervised by Dr. Xiaohua Wu.

Wakes are constitutive components of engineering, aeronautical and geophysical flows. Despite their canonical nature, many fundamental questions surrounding wakes remain unanswered. The present work studies the nature of archetypal planar splitter-plate wakes in the sub- and supersonic regimes from a theoretical as well as a numerical perspective. A highly-parallelizable computational fluid dynamic solver was developed, from scratch, for the very-large scale direct numerical simulations of high-speed free shear flows.

Wakes maintain a near indelible memory of their origins; thus, changes to the state of the flow on the generating body lead to multiple self-similar states in the far wake. To understand the source of the lack of universality, three distinct wake evolution scenarios are investigated in the incompressible limit: the Kelvin-Helmholtz transition, the bypass transition in an asymmetric wake and the initially turbulent wake. The multiplicity of self-similar states is the result of a plurality of far wake structural organizations, which maintains the memory of the flow. The structural organization is predicated on the presence or absence of near wake anti-symmetric perturbations (as a result of shedding, instability modes and/or trailing edge receptivity). The plurality of large-scale structural organization contrasts with the commonality observed in the mid-sized structures, which are dominated by inclined vortical rods, and not, as previously assumed, by horseshoe structures.

The compressibility effects are a direct function of the maximal velocity defect in

the wake and are therefore only important in the transitional region - the far wake having an essentially incompressible character. The compressibility simultaneously modifies the growth rate and wavelength of the primary instability mode with a concomitant effect on the emerging transitional structures. As a direct result, the spanwise rollers have an increasing ellipticity and cross-wake domain of influence with the increasing Mach number of the wake. Consequently, structural pairing - a key feature of wake transition - is inhibited at a critical Mach number, which greatly modifies the transitional dynamics. In idealized wakes, the increased stability caused by the compressibility effects leads to a vortex breakdown of secondary structures prior to the full transition of the principal mode. These findings open the door to novel mixing enhancement and flow control possibilities in the high-speed wake transition.

Keywords: Fluid Dynamics, Direct Numerical Simulations, free shear flows, Turbulence, Numerical Methods

Résumé

Hickey, Jean-Pierre, Ph.D., Département de génie mécanique et aérospatial, Collège militaire royal du Canada, Décembre 2012. Simulation directe et théorique de sillages sous- et supersoniques. Thèse dirigée par M. Xiaohua Wu, Ph.D.

Le sillage est une composante constitutive de plusieurs types d'écoulements en ingénierie, en aéronautique et en géophysique. Malgré sa simplicité, de nombreuses questions sur la dynamique du sillage demeurent sans réponses. Une étude théorique et numérique est entreprise pour étudier la nature interne du sillage plan et canonique dans les régimes sous- et supersoniques. Un solveur pour des écoulements à grande vitesse a été développé, vérifié et validé pour effectuer des simulations numériques directes à très grande échelle.

Le sillage conserve une mémoire quasi indélébile de son origine, donc tout changement de l'état de l'écoulement du champ rapproché peut modifier les statistiques autosemblables du champ éloigné. Pour comprendre l'absence d'universalité qui caractérise le sillage, trois évolutions types sont étudiées: une transition de Kelvin-Helmholtz, une transition 'bypass' d'un sillage asymétrique et un sillage initialement turbulent. La multiplicité des statistiques autosemblables est le résultat d'une pluralité d'organisation structurelle du champ éloigné du sillage. Les structures à grandes échelles perpétuent la mémoire du sillage et s'organisent en fonction de la présence ou de l'absence de perturbations antisymétriques dans le champ rapproché (causé par le détachement, par des instabilités et/ou par la réceptivité du bord de fuite). La pluralité de l'organisation structurelle à grande échelle tranche avec l'uniformité des structures à moyenne échelle principalement en forme de bâtonnet de vorticité et non en forme de *fer à cheval*.

Les effets de compressibilité varient en fonction du déficit de vitesse du sillage. Par conséquent, la compressibilité joue un rôle important seulement dans le champ rapproché

ou lors de la transition du sillage, le champ éloigné ayant une dynamique essentiellement incompressible. La compressibilité allonge la longueur d'onde, diminue le taux de croissance de la perturbation principale et modifie les structures émergentes lors de la transition. Les structures deviennent ellipsoïdales avec un domaine d'influence principalement dans la direction transversale du sillage avec une croissance du nombre de Mach. Ces caractéristiques entravent le jumelage de structures, typique des écoulements à basse vitesse, et modifient les dynamiques internes de transition. On note un éclatement tourbillonnaire des structures secondaires qui précède la transition des structures principales. Cette observation offre de nouvelles possibilités pour le contrôle et une amélioration du mélange turbulent pour les écoulements à grande vitesse.

Mots-clés: Mécanique des fluides, simulation numérique directe, écoulements libres turbulents, écoulements supersoniques, méthodes numériques

Co-Authorship Statement

I hereby declare that this thesis incorporates three manuscripts resulting from the collaborative work with Prof. Xiaohua Wu from the Royal Military College of Canada and Prof. Fazle Hussain from the University of Houston. Chapter 4 is a manuscript that has been submitted to the **Journal of Fluid Mechanics** and is in the late stages of review. Chapter 5 is a manuscript on the transition of compressible planar wakes that will be submitted shortly to the **Journal of Fluid Mechanics**. Chapter 6, on the vortex breakdown mechanism in the high-speed wake, will also be submitted shortly to a leading journal of fluid mechanics.

In all works, the key ideas, primary contributions, numerical simulations, data analysis, interpretation and writing of the manuscripts were performed by the author. The contributions of co-authors were primarily through guidance, support, correction and review of the manuscripts.

I certify that all the manuscripts only contain work completed during my registration as a graduate student at the Royal Military College of Canada.

I certify the accuracy of the above statement,

Dr. Xiaohua Wu

Table of Contents

List of Tables

List of Figures

List of Symbols

Roman Symbols

$\mathbf{A}$	Coefficient matrix for the non-reflecting boundary conditions
A	Total area of the turbulent wake
b	Wake half-width
b_{ij}	Reynolds stress anisotropy tensor
c	Speed of sound
Coh	Spanwise coherence of the turbulent kinetic energy
E_t	Total energy (sum of internal and kinetic energy)
e	Internal energy per unit mass
h	Enthalpy
h	Distance to the turbulent/non-turbulent interface
h	Lateral separation of the rollers in the wake (chapter 6)
H	Normalized distance from to the turbulent/non-turbulent interface
H	Wake shape factor
L_i	Computational domain size in the i-direction
$\mathbf{L}$	Characteristic length scale
$\dot{m}$	Mass-flux defect
Ma	Mach number
Ma_c	Convective Mach number
Ma_r	Relative Mach number
Ma_t	Turbulent Mach number
Ma_∞	Freestream Mach number
p	Thermodynamic pressure
Pr	Prandtl number
Re	Reynolds number

Re_λ	Reynolds number based on the Taylor length scale
R	Dimensional gas constant
$R_{u_i u_i}$	Correlation coefficient (Chapter 4
R_{ij}	Integrated Favre averaged Reynolds stresses (Chapter 5
T	Temperature
$\mathbf{T}$	Characteristic time scale
$\mathbf{U}$	Characteristic velocity
$\mathbf{U}$	Matrix of the primary variables (Chapter 3)
U	Mean velocity
U_0	Centerline velocity defect
δU	Velocity defect
U_d	Initial centerline velocity defect
U_∞	Freestream velocity
U_c	Convection velocity
u, v, w or u_i	Instantaneous velocity in the i^{th}-direction
x, y, z or x_i	Spatial location in the i^{th}-direction
Δt	Time-step
Δx_i	Grid spacing in the i^{th} direction
$\langle \cdot \rangle$	Averaged quantity over the homogeneous directions

Greek Symbols

α, β, χ	Inclination of vorticity vector from the x, y and z-axes (chapter 4)
α	Streamwise wavenumber (chapter 5)
β	Spanwise wavenumber (chapter 5)
δ_{ij}	Kronecker Delta
η	Kolmogorov length scale
Γ	Circulation
γ	Heat capacity ratio
κ	Magnitude of the wavenumber vector; $\kappa^2 = \alpha^2 + \beta^2$
κ	Thermal conductivity (chapter 2)
λ	Taylor length scale (chapter 4)
λ	Wavelength (chapters 5 and 6)
λ_i	Eigenvalue for non-reflecting boundary conditions (chapter 3)
λ_2	Visualization technique developed by Jeong & Hussain (1995)
μ	Dynamic viscosity
ν	Kinematic viscosity
ω	Exponential growth rate (complex parameter)

ω_i	Vorticity in the i-direction
ϕ	Local scalar concentration
ρ	Fluid density
σ_{ij}	Shear stress tensor
θ	Momentum flux defect
θ	Inclination angle (chapter 5)
η, ξ, ζ	Local coordinate system (chapter 6)
$\phi_{spatial}^{temporal}$	Notation for the numerical scheme

Abbreviations

LLB	Initially laminar wake with a double Blasius boundary profile
LLG	Initially laminar wake with a Gaussian velocity profile
LL	Refers to the transitional wakes (LLB and LLG)
LT	Asymmetric wake with a laminar and turbulent velocity profile
TT	Wake formed from two fully turbulent boundary layers
$TNTI$	Turbulent/non-turbulent interface
PDF	Probability density function
$JPDF$	Joint probability density function
TKE	Turbulent kinetic energy
rms	Root mean square
$NRBC$	Non-reflecting boundary conditions
DNS	Direct numerical simulation
LES	Large-Eddy Simulation
$RANS$	Reynolds Averaged Navier-Stokes

Chapter 1

Introduction

Wakes are ubiquitous free shear flows occurring downstream of a body moving relative to a fluid. They are encountered in most engineering, aeronautical, geo-, astro- and bio-physical flows at all scales - from the nano (*e.g.*, Bingham, 2007) all the way up to the planetary scale (*e.g.,* Martin *et al.*, 2007). In all these cases, wakes are characterized by a momentum defect which can be related to the total drag of the generating body (see *e.g.,* Batchelor, 1967). Given their inflectional mean velocity profile, wakes are often encountered in the turbulent state. The turbulence amplifies the diffusion of vorticity imparted to the flow by the wake generating body, which results in a spreading and reduction of the velocity defect as the wake evolves. Despite the disarming simplicity of this canonical flow, the understanding of the turbulence and the organized structures is far from complete and many fundamental questions are left to be answered. The ever increasing possibilities of computational mechanics have allowed us to re-visit one of the simplest free shear flows in both the sub- and supersonic regimes. The contributions of the present work, listed in section 1.4, provide new insight into the physics and the underlying coherent structures of the planar wake. Aside from a better understanding of the intrinsic physics of this constitutive flow, the present work affords new possibilities to improve existing turbulence

models for free shear flows which in turn can indirectly improve the modelling of wakes in more complex engineering settings.

Wakes have long been a subject of scientific inquiry. Over five centuries ago, the renaissance thinker Leonardo da Vinci placed an obstacle in a stream and illustrated his understanding of turbulent wakes, see figure 1.1. The figure and insightful explanation written - as is the case for most of his personal notes - in mirror, provide a prophetic description of the coherent turbulent motion in the wake, understood as the organization of curls in a lock of hair (translation by Piomelli (2009)):

> Observe the motion of the water surface, which resembles that of hair, that has two motions: one due to the weight of the shaft, the other to the shape of the curls; thus, water has eddying motions, one part of which is due to the principal current, the other to the random and reverse motion.

The nature of da Vinci's description pre-dates the formal understanding of turbulence but foreshadows the development of the concept of coherent structures. As early as 1509, da Vinci recognized the importance of organized turbulent motion as a defining characteristic of the wake.

Interestingly, the depiction of a centerplane symmetric structural organization in da Vinci's renaissance work is formally incorrect. For a minimal (finite) Reynolds number, von Karman (1911) showed that a laminar wake sheds anti-symmetric, counter-rotating vortices. Using inviscid flow theory applied to an anti-symmetric configuration of idealized vortex filaments, von Karman elegantly showed the neutral stability of a wake vortex configuration, a flow feature that now bears his name: the Karman vortex street.

Much of our current understanding of wake turbulence is attributed to the studies by Townsend (1956) and Grant (1958). Using two-point velocity correlations, they inferred

Figure 1.1: Illustration by Leonardo da Vinci in 1509 of obstacle in a stream (The Royal Collection ©2012, Her Majesty Queen Elizabeth II)

the structural composition of the turbulent far wake. They identified two prototypical structures: the spanwise coherent *jets* and the inclined *double-roller eddy*. Although the existence of coherent structures had long been discussed, it was not until the classical mixing layer work by Brown & Roshko (1974) that the importance of the large-scale organized turbulence motion on the dynamics of the flow found recognition, see figure 1.2. This re-emphasis on coherent structures and vortex dynamics inspired an active decade of wake research in the 1980s (*e.g.,* Antonia & Browne, 1986; Antonia *et al.*, 1987; Bonnet & Chaput, 1986; Bonnet *et al.*, 1986; Meiburg & Lasheras, 1987; Cimbala *et al.*, 1988; Hussain & Hayakawa, 1987; Hayakawa & Hussain, 1989; Weygandt & Mehta, 1989). These important experimental works have helped forge much of our current state of knowledge on wakes. The increasing possibility afforded by computational fluid dynamics has done relatively little in furthering our understanding of this canonical flow, although we note the important

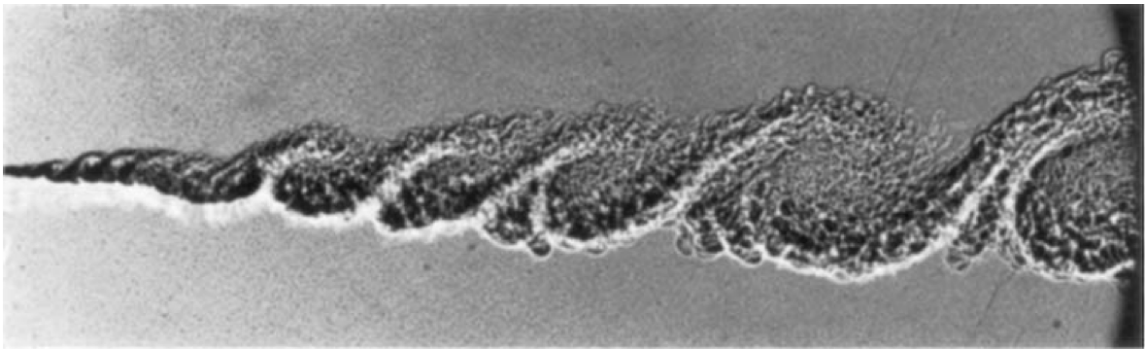

Figure 1.2: Visualisation of the large-scale coherent structures in the mixing layer using two different gases, from Brown & Roshko (1974).

numerical contributions by Meiburg & Lasheras (1987), Lasheras & Meiburg (1990) and Moser *et al.* (1998). Surprisingly, the canonical wake remains a topic of research in both sub- and supersonic regimes as many fundamental questions beg to be answered, as will be more thoroughly discussed at the beginning of chapters 4, 5 and 6. These important unanswered questions transcend the field of theoretical fluid mechanics, being central to many engineering relevant problems.

1.1 Motivation

The quest for a deeper understanding of the canonical wake remains pertinent. A multi-disciplinary survey is conducted to highlight the many current applications and issues regarding wake flow dynamics.

With the continual increase of air traffic, wake turbulence (primarily the influence of the counter-rotating wing-tip vortices) is the most important limiting factor in reducing the temporal and spatial distances between aircrafts. The current regulations (FAA, 2012), which are overly conservative, estimate the required spacing between aircrafts based on a

variety of environmental and physical parameters. In order to increase the capacity at existing airports, a better estimation of a safe minimal distance is required. To this effect, in 2008, the National Academy of Engineering in the United States put together a panel of experts to review the limitations to modern air traffic capacity (Broderick *et al.*, 2008). The first and most important conclusion of the panel was that : "Air transportation system capacity could be significantly enhanced by applying the results of robust and focused wake vortex research and development. These results will be required in order to use the system at its maximum efficiency."

In turbomachinery, the wake/boundary layer interaction provokes a bypass transition (Wu *et al.*, 1999; Hickey *et al.*, 2009, 2010), which is followed by a "becalmed region" of robust laminar flow. This re-laminarization under the vortical disturbance of the wake has been shown to reduce the periodically averaged drag in low-pressure turbines (Schulte & Hodson, 1998*a*,*b*), yet the exact mechanism of the interaction between the wake and the boundary layer remains unclear. A better understanding of the interaction of wake flow structures with transitioning boundary layers affords new possibilities in improving the efficiencies in modern turbomachinery.

In supersonic flows, the use of strut-type fuel injectors in supersonic combustion ramjet (scramjet) engines present many desirable attributes (*e.g.,* Curran & Murthy, 2000; Segal, 2009). The fuel is injected in the center of the domain, the increased wake turbulence provides large-scale mixing of the fuel and the reflected bow shock interaction enhances the small-scale mixing (Desikan & Kurian, 2006). The stabilizing effect and reduced turbulence production caused by the increased compressibility hinders a broader use of the strut injector in scramjet engines. In addition, the flow structures may be responsible for downstream combustion oscillations as noted by Choi *et al.* (2005). Understanding of the effects of compressibility on the canonical wake will provide invaluable paths for mixing

enhancement strategies with strut-type fuel injectors.

At a completely different scale, the turbulent wake of astrophysical bodies, in which mass loss occurs, can be used as a tracer to identify the history of a variable star. Mira, one of the first variable stars observed, has been traced 30,000 years back thanks to its wake (Martin *et al.*, 2007). In geophysical flows, wakes are observed far downstream of their origin, particularly when generated by high-altitude islands in a stratified atmosphere. These wakes modulate the interaction between the ocean and atmosphere and have been known to modify, albeit very slightly, the ocean surface temperature. For example, the influence of the wake is observed 3,000 kilometres westwards of the Hawaiian islands and is thought to explain the variation of plankton and fish concentration near the ocean surface (Xie *et al.*, 2001). The science behind both of these very large-scale wakes would benefit from an improved understanding of the underlying structural features and the possible memory effects which are associated with all free shear flows.

These examples along with many more in wind turbine placement (Whittlesey *et al.*, 2010), submarine detection (Bandyopadhyay, 2005) and biomimicry (Liao *et al.*, 2003) would benefit from a better understanding of the inherent physics of the turbulent wake.

1.2 Statement of the Problem

In many applied contexts, the multi-scale nature of the turbulent wake requires the use of turbulence closure models for the Reynolds Averaged Navier-Stokes (RANS) equations. By construction, the effects of the turbulence must be modelled using local mean flow properties. Although these closure models provide valuable flow information and are computationally tractable, they fall short in capturing some of the intrinsic physics, most importantly the *memory effects* of the wake.

Free shear flows have the unique property of maintaining a *memory* of their origin. Therefore, depending on the generating body, the state of the trailing edge boundary layer or even minor splitter-plate variations (*e.g.,* added roughness or serrated trailing edge) have been shown to modify drastically the evolution of the wake, see detailed discussion in chapter 4. It comes as no surprise that the initial condition dependance results in a disturbing scatter among many of the previous experimental and numerical wake investigations. Compared to wall bounded cases, the free shear flows show significant variations in integral and turbulence statistics during the entire wake evolution, even when properly normalized in the far wake. Most of the variability can be traced back to the origin of the wake. In typical closure models, the memory effects are not captured and therefore may grossly under- or over-predict important quantities such as wake spreading or turbulence intensity. In the first part of the work, we seek to clarify the connection between the memory effects and the structural organization in the incompressible wake.

In the second part of the work (chapters 5 and 6), we study the effects of compressibility on the transitional planar wake dynamics. Compressibility has a well-known stabilizing effect in most wall-bounded and free shear flows. Unlike the mixing layer, the compressibility effects decay with the centerline velocity of the wake (further details provided in chapter 5). The compressibility is only significant in the transitional or near wake region and, as the velocity defect tends toward zero, so does the relative Mach number of the wake. Even though the freestream may be supersonic (relative to the generating body), the far wake is fully incompressible if the velocity defect is small. This is not to say that compressibility does not play a role in the far wake. As previously stated, the influence of near wake compressibility is perpetuated into the far wake by the memory effects. As a result, even though the far wake compressibility effects are negligible, the turbulence statistics differ between low- and high-speed wakes (Bonnet *et al.*, 1991; Gatski & Bonnet, 2009). We seek

a clarification on the statistical differences in the far wake based on a better understanding of the effects of compressibility on the structures in the transition of planar wakes.

1.3 Methodology and Research

The present work studies the dynamics of the wake using theoretical tools and very-large-scale Direct Numerical Simulations (DNS). Using the governing equations of fluid flow, we numerically compute the three-dimensional Eulerian flow field across all scales. In turbulent flows such as the wake, the scale separation between the smallest viscous and the largest integral scale limits the investigation to computationally feasible Reynolds numbers.

The computational requirements to fully resolve all scales of turbulence for a canonical wake are significant - even at the modest Reynolds numbers we are considering. For the simulations in the present work, we need up to 700 million grid points which need to be computed over nearly 100,000 time steps. These computations take between 2-4 months to complete on up to 128 dedicated cores on the shared-memory computers at the High Performance Computational Virtual Library (HPCVL).

The sizeable computational needs of these simulations require a highly-optimized and parallelized computational tool. An important part of the present thesis is the development, verification and validation, from scratch, of a numerical code for the solution of the fully compressible Navier-Stokes equations. The detailed numerical methods and validation are discussed in chapter 3. The code includes the development of the grid generation, all post-processing and eduction software used in the present work. In addition to the computational fluid dynamic solver, a viscous, compressible linearized Navier-Stokes stability code was developed.

Complimentary to the high quality direct numerical simulations, a broad toolset within vortex dynamics, statistical turbulence theory and structural eduction techniques were used. The use of these techniques is discussed in the corresponding chapters of the thesis.

1.4 Contributions

The study of a canonical flow such as the planar wake can only be justified if one is able to extend the boundaries of knowledge. The novel contributions to the understanding of the planar wake in the sub- and supersonic regimes are summarized as follows:

1.4.1 Contribution to the incompressible planar wake

- **Description of the non-universality of far wake structures.** The structural non-universality of the far wake has been hypothesized (*e.g.,* Ewing *et al.*, 2007), but, until now, never clearly demonstrated. We showed that the structural organization of the planar wake is non-universal and strongly depends on the initial generating conditions of the wake. Two types of large-scale coherent structures were identified - a symmetric and anti-symmetric type. The differing structural organization elucidates a quarter-century old inconsistency in far wake turbulence statistics first identified by Bonnet *et al.* (1984) and Bonnet & Chaput (1986).

- **Connection between the coherent structures in the statistical multiplicity of the self-similar wake.** We established that wakes maintain a memory of their origin, which results in a multiplicity of self-similar states. The novelty of the contribution was to relate the self-similar multiplicity to the structural plurality identified in the far wake.

- **Identification of the universality of inclined mid-sized far wake structures:**

We proved that the mid-size turbulent structures are inclined rods at $30° - 35°$ to the streamwise direction. This finding contradicts the previously held belief concerning the predominance of horseshoe structures. We also show that these structures are independent of the generating conditions of the wake and have a shallower inclination than the vorticity vectors.

- **Quantification of the effects of the exit state boundary layer on the evolution of the planar wake.** We provide a comprehensive study of the effects of the exit boundary layer state on the wake evolution.

- **Proof of the connection between the spanwise vorticity flux across the centerplane and the spreading rate.** We theoretically showed that the self-similar spread of the wake is directly tied to the centerplane gradient of $\langle u_1 u_2 \rangle$. This Reynolds shear stress is influenced by the structural organization of the wake. Physically, the gradient of $\langle u_1 u_2 \rangle$ is related to the flux of spanwise vorticity across the centerplane of the wake.

- **Connection between the coherent structures and the entrainment in the far wake.** We clarified the influence of the structural wake organization on the entrainment of irrotational flow into the far wake. We showed that the spread rate and entrainment are not as strongly coupled as previously assumed. Instead the corrugations of the turbulent/non-turbulent interface (TNTI) - caused by the underlying coherent structures - drive the engulfment, and consequently, the entrainment in the far wake.

1.4.2 Contribution to the transition of high-speed wakes

- **Quantification of the effects of compressibility on the wavelength of most unstable linear mode.** Using linear stability theory, supported by our direct numerical simulations, we showed that the wavelength of the most unstable mode increases proportionally to the relative Mach number of the flow.

- **Proof of the increasing cross-wake communication with increasing Mach number.** Based on a geometric interpretation of the characteristic lines, we showed the increasing zones of silence in the up- and downstream regions of a perturbation in the wake with increasing Mach number. The reduction of streamwise communication occurs simultaneously to an increased cross-wake zone of influence with increasing Mach number.

- **Explanation of the effects of compressibility on the transition of the wake.** We observed that the increased instability wavelength results in rollers with increased streamwise separation and circulation while maintaining a constant cross-wake separation. In addition to the reduced streamwise communication, we inferred that the structural pairing is hindered in the high-speed wakes. These results are confirmed by our direct numerical simulations.

- **Identification and explanation of a new breakdown mechanism of the rib structures in high-speed wakes.** We showed that the increasing stability and cross-wake communication results in the formation of rod-like structures with different dynamical properties in the high-speed wake. The vortex breakdown of these structures precedes the transition to turbulence of the principal rollers. This result implies that a secondary instability transitions before the primary instability. The

breakdown mechanism is explained through the study of critical point theory.

- **Description of the formation of spanwise rollers.** Using an eduction algorithm, we demonstrate the increasing ellipticity of the rollers with increasing Mach number which is related to the increasing wavelength and reduced growth rate of the principal instability modes.

1.5 Organization of Thesis

The present doctoral thesis describes the computational and theoretical study of canonical wake flows in the subsonic and supersonic regimes; the work is compiled in an integrated article format. The thesis is composed of three manuscripts, which are supplemented with chapters on the theoretical (chapter 2) and numerical (chapter 3) frameworks. Chapter 4 describes a comprehensive study of the role of coherent structures in the multiplicity of self-similar states in the incompressible planar wake. This manuscript has been submitted to the **Journal of Fluid Mechanics** and is in the late review stages. Chapter 5 is a comprehensive study on the effects of compressibility in the transition of high-speed planar wakes. This manuscript will be submitted shortly to the **Journal of Fluid Mechanics**. Finally, chapter 6 is an investigation into the vortex breakdown of secondary rib structures in the high-speed wake. This last work will be submitted shortly to a leading journal of fluid mechanics. The discussion, conclusions and future works will be summarized in chapter 7.

Chapter 2

Theoretical Framework

This chapter details the main theoretical framework used in the following chapters, for the study of sub- and supersonic wakes. In section 2.1, we present the normalization of the governing equation set for compressible fluid flow. The mathematical concepts behind linear stability theory of high-speed free shear flows are detailed in section 2.2. The concept of self-similarity and its use in asymptotic free shear flows is explained in section 2.3. Finally, the conceptual understanding of coherent structures is explained in section 2.4.

2.1 Governing Equations

The Navier-Stokes equations are variations of the Newtonian conservation laws written in a Eulerian frame of reference. The detailed derivation of these conservation equations is found in most fluid mechanics books (*e.g.,* Pope, 2000; Kundu & Cohen, 2004) and not repeated here for brevity. To avoid any misunderstanding, we refer to the Navier-Stokes equations as the partial differential equation set containing the conservation of

mass, momentum and energy. Written in conservative form, the governing equations are:

$$\frac{\partial \tilde{\rho}}{\partial \tilde{t}} + \frac{\partial \left(\tilde{\rho}\tilde{u}_i\right)}{\partial \tilde{x}_i} = 0, \tag{2.1a}$$

$$\frac{\partial \left(\tilde{\rho}\tilde{u}_i\right)}{\partial \tilde{t}} + \frac{\partial \left(\tilde{\rho}\tilde{u}_i\tilde{u}_j\right)}{\partial \tilde{x}_j} + \frac{\partial \left(\tilde{p}\delta_{ij}\right)}{\partial \tilde{x}_j} = \frac{\partial \tilde{\sigma}_{ij}}{\partial \tilde{x}_j}, \tag{2.1b}$$

$$\frac{\partial \tilde{E}_t}{\partial \tilde{t}} + \frac{\partial \left(\tilde{E}_t\tilde{u}_i\right)}{\partial \tilde{x}_i} + \frac{\partial \tilde{p}\tilde{u}_i}{\partial \tilde{x}_i} = -\frac{\partial \tilde{Q}_i}{\partial \tilde{x}_i} + \frac{\partial \tilde{u}_j\tilde{\sigma}_{ij}}{\partial \tilde{x}_j}, \tag{2.1c}$$

where $\tilde{\rho}$ is the density, $\tilde{p}$ the pressure, $\tilde{t}$ the time, $\tilde{x}_i$ and $\tilde{u}_i$ are respectively the spatial and velocity components in the i^{th}-direction. Here, the tilde is used to denote dimensional parameters. As usual with Einstein notation, the repeated indices indicate a summation. The total energy, $\tilde{E}_t$, represents the sum of the internal and kinetic energies:

$$\tilde{E}_t = \tilde{\rho}\left(\tilde{e} + \tfrac{1}{2}\tilde{u}_i\tilde{u}_i\right), \tag{2.2}$$

where $\tilde{e}$ is the internal energy per unit mass.

In equations (2.1), the shear stress tensor is expanded as:

$$\tilde{\sigma}_{ij} = \tilde{\mu}\left(\frac{\partial \tilde{u}_i}{\partial \tilde{x}_j} + \frac{\partial \tilde{u}_j}{\partial \tilde{x}_i} - \tfrac{2}{3}\frac{\partial \tilde{u}_k}{\partial \tilde{x}_k}\delta_{ij}\right), \tag{2.3}$$

where $\tilde{\mu}$ is the dynamic viscosity of the fluid. The strain rate tensor (without the constant coefficient), ϵ_{ij}, can be seen in the first two terms in the parentheses; the last term is related to the shear stress caused by the dilatation of the flow.

Using the Fourier law for heat conduction, we relate:

$$\tilde{Q}_i = -\tilde{\kappa}\frac{\partial \tilde{T}}{\partial \tilde{x}_i}, \tag{2.4}$$

where $\tilde{\kappa}$ is the thermal conductivity and $\tilde{T}$ the thermodynamic temperature of the fluid.

To adequately close this set of differential equations, the ideal gas law is used to relate the pressure, temperature and density:

$$\tilde{p} = \tilde{\rho}\tilde{R}\tilde{T}, \tag{2.5}$$

where $\tilde{R}$ is the dimensional gas constant.

The equations are non-dimensionalized by defining a characteristic length, $\mathbf{L}$, and velocity scale, $\mathbf{U}$. The related time scale is then: $\mathbf{T} = \mathbf{L}/\mathbf{U}$. The length and velocity scale is problem dependant and differs slightly between the low-speed (chapter 4) and high-speed cases (chapters 5 and 6). The specific non-dimensionalization is discussed in each of these chapters.

We define a dimensional reference state for the density ρ_0 and for the speed of sound, assuming an isentropic propagation condition, $c_0 = \sqrt{\gamma \tilde{R} T_0}$, where γ the adiabatic gas constant is equal to 1.4. The reference states for the viscosity μ_0 and for the heat conductivity constant, κ_0 are defined. The variables are then correspondingly non-dimensionalized:

$$x = \frac{\tilde{x}}{\mathbf{L}}; \quad \rho = \frac{\tilde{\rho}}{\rho_0}; \quad u = \frac{\tilde{u}}{\mathbf{U}}; \quad p = \frac{\tilde{p}}{p_0} = \frac{\tilde{p}}{\rho_0 c_0^2/\gamma}; \quad E_t = \frac{\tilde{E}_t}{\rho_0 \mathbf{U}^2}; \quad \mu = \frac{\tilde{\mu}}{\mu_0}. \tag{2.6}$$

The governing equations (2.1) are non-dimensionalized using the same parameters:

$$\frac{\partial \rho}{\partial t} + \frac{\partial \left(\rho u_i\right)}{\partial x_i} = 0, \tag{2.7a}$$

$$\frac{\partial \left(\rho u_i\right)}{\partial t} + \frac{\partial \left(\rho u_i u_j + p/\left(\gamma M a^2\right)\delta_{ij}\right)}{\partial x_j} = \frac{1}{Re}\frac{\partial}{\partial x_j}\left[\mu\left(\frac{\partial u_i}{\partial x_j} + \frac{\partial u_j}{\partial x_i} - \tfrac{2}{3}\frac{\partial u_k}{\partial x_k}\delta_{ij}\right)\right], \tag{2.7b}$$

$$\frac{\partial E_t}{\partial t} + \frac{\partial \left[\left(E_t u_i + p/\left(\gamma M a^2\right)\right)\right]}{\partial x_i} = \frac{1}{Pr Re\left(\gamma - 1\right) M a^2}\frac{\partial}{\partial x_i}\left(\kappa \frac{\partial T}{\partial x_i}\right) + \frac{1}{Re}\frac{\partial}{\partial x_j}\left(u_j \mu\left(\frac{\partial u_i}{\partial x_j} + \frac{\partial u_j}{\partial x_i} - \tfrac{2}{3}\frac{\partial u_k}{\partial x_k}\delta_{ij}\right)\right). \tag{2.7c}$$

In the above equations, μ is the non-dimensional dynamic viscosity of the fluid which is related to the thermodynamic temperature ratio through a power law:

$$\left(\frac{\tilde{\mu}}{\mu_0}\right) = \left(\frac{\tilde{T}}{T_0}\right)^n, \tag{2.8}$$

where n is equal to 0.76 (White, 1999). The Reynolds, Mach and Prandtl numbers emerge in equation (2.7) from the non-dimensionalization of the Navier-Stokes equations. These

parameters are respectively defined as:

$$Re = \frac{\rho_0 U L}{\mu_0}, \tag{2.9a}$$

$$Ma = \frac{U}{c_0}, \tag{2.9b}$$

$$Pr = \frac{\mu_0 C_p}{\kappa_0}. \tag{2.9c}$$

Similarly, the non-dimensionalization of the equation of state yields:

$$p = \frac{p'}{\rho_0 c_0^2/\gamma} = \frac{\tilde{\rho}\tilde{R}\tilde{T}}{\rho_0 R T_0} = \rho T. \tag{2.10}$$

For numerical investigations, the conservative form of the Navier-Stokes equations, as shown above, is preferred as it represents the smooth as well as the discontinuous part of the solution. The non-conservative form shows considerable advantages for the analytical manipulations as the dissipative processes are explicit. But, the equation set must then be supplemented with the adequate jump conditions (Chapman, 2000). The numerical implementation of the above equations will be discussed in chapter 3. The expanded form of the above governing equations are detailed in the appendix A.

2.2 Linear Stability Theory of High-Speed Wake

Temporal linear stability analysis is used in chapter 5 to characterize the transition of the high-speed planar wake. The theoretical development rests on the work by Chen *et al.* (1990) and Watanabe & Maekawa (2004). The Navier-Stokes equations are linearized and an infinitesimal perturbation is added to the laminar base flow. If the infinitesimal perturbation grows in time (or in space, for a spatially evolving linear stability analysis), the flow is unstable to the defined perturbation. Here, we summarize the mathematical framework of linear stability theory.

The linearization of the non-conservative Navier-Stokes equations yields a sizeable equation set, written out in appendix B (equation (B.1)). The laminar base flow of a wake has an approximate Gaussian profile. The base flow for the linear stability calculations has the form: $\langle u \rangle = 1 - U_d \exp(-by^2)$, where U_0 and b are respectively the initial centerplane wake defect and wake half-width, see figure 2.1 for details. As the base flow of the planar wake is two-dimensional: $\langle v \rangle = \langle w \rangle = 0$. Given the temporal nature of the stability analysis, we must approximate the mean state as a parallel flow; an acceptable approximation given the slow lateral viscous spreading of the laminar base state. Assuming a constant pressure wake, the mean temperature profile is computed using the Crocco-Busemann relation (see, *e.g.,* Chen *et al.*, 1990): $T = 1 + 0.5Ma^2(\gamma - 1)\left(1 - u^2\right)$.

The infinitesimal perturbations are denoted with the prime $(\cdot)'$ in equations (B.1) in the appendix B. The infinitesimal disturbances are assumed sinusoidal and of the form:

$$\boldsymbol{\phi'} = \hat{\boldsymbol{\phi}} \exp^{i(\alpha x + \beta z - \omega t)}, \tag{2.11}$$

where $\boldsymbol{\phi'} = [\rho', u', v', w', T']^T$ is the vector of infinitesimal perturbations in physical space, while $\hat{\boldsymbol{\phi}}$ represents the Fourier coefficient of the variables. The terms α and β are the (real) wavenumbers respectively in the streamwise and spanwise directions. The term ω represents the complex frequency. It is clear from equation (2.11) that a perturbation is unstable if the imaginary part of ω is positive. By replacing the above ansatz (equation (2.11)) in the linearized equation set (B.1), it is possible to separate the spatial and temporal terms. The grouping of the spatial and temporal terms yields:

$$\mathcal{L}\hat{\boldsymbol{\phi}} = \omega\hat{\boldsymbol{\phi}}, \tag{2.12}$$

where $\mathcal{L}$ is $5N \times 5N$ coefficient matrix (see equation (B.2)) and N represents the number of discrete points used in the cross-wake direction (for the present computations, at least 150 points were used). The equation (2.12) represents an eigenvalue problem, where ω

represents the eigenvalue and $\hat{\phi}$, the corresponding eigenvector. In order to solve the problem numerically, we must map the infinite domain in the cross-wake direction onto a finite domain. To do so, we use a spectral mapping proposed by Cain *et al.* (1984) following the approach by Sandham (1989) and Chen *et al.* (1990). The above eigenvalue problem was implemented by the author in Python and solved using standard numerical eigenvalue techniques. Given an initial tuple of perturbation wavenumbers (α and β) and flow characteristics (Re and Ma), the perturbation is considered unstable if one of the eigenvalues, ω, has a positive complex part. In which case, the mode is exponentially growing in time and, hence, unstable. To find the fastest growing wavenumber tuple over all the domain of interest, we used a gradient-based Sequential Least Squares Programming (SLSQP) optimizer, which is implemented in the pyOpt package (Perez *et al.*, 2012). The implementation of the optimizer greatly reduced the computational requirements to find the most unstable mode.

2.3 Self-Similarity in Free Shear Flows

Self-similarity is a powerful concept for the analysis of free shear flows, which is extensively used in chapter 4. A self-similar state is reached when the flow variables, through proper scaling, become a function of a single independent parameter. In the wake, mixing layer and jet flows, a self-similar state is reached and maintained in the far field. As a result, the mean velocity and Reynolds stress profiles become independent of the evolution of the wake (independent of time for temporal simulations, or streamwise location for spatial simulations or experiments).

For simplicity and generality, we describe the self-similar evolution of a temporally evolving wake; the theoretical development for the spatially evolving case is fully analogous.

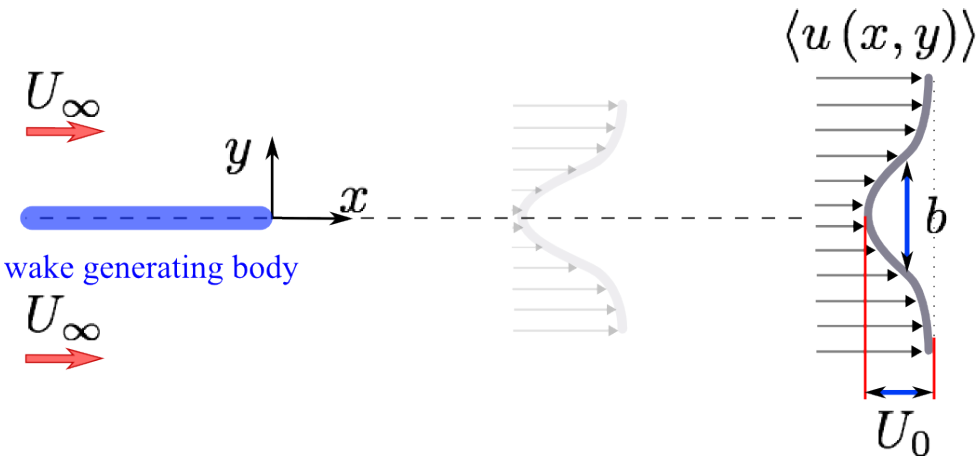

Figure 2.1: Principal parameters defining the planar wake

The wake velocity defect, δU, is defined as:

$$\delta U(y,t) = U_\infty - \langle U(y,t)\rangle \tag{2.13}$$

where the brackets $\langle\cdot\rangle$ denote the average over the homogeneous directions (x and z discussed in more detail in chapter 4) at a given time evolution. Naturally, the maximal centerline defect in a symmetric wake is: $U_0(t) = \max(\delta U(0,t)) = U_\infty - \langle U(0,t)\rangle$. The wake half-width, b, represents the total wake width at the location of half the centerline defect.

$$\langle U(b,t)\rangle = U_\infty - \frac{U_0(x,t)}{2} \tag{2.14}$$

In wakes, compressibility plays a marginal role in the self-similar evolution. As the velocity defect must be small for a self-similar evolution to occur (generally $|U_0/U_\infty| << 1$), the relative Mach number (which defines the large-scale compressibility effects, see details in chapter 5) is similarly very small. Therefore, the self-similar evolution in the wake may be studied using the incompressible governing equations. Assuming a two-dimensional

incompressible wake ($\langle V\rangle = \langle W\rangle = 0$), the mean momentum equation is:

$$\rho\frac{\partial \langle U(y,t)\rangle}{\partial t} + \rho\frac{\partial \langle uv\rangle}{\partial y} = \mu\frac{\partial^2 \langle U(y,t)\rangle}{\partial y^2}. \tag{2.15}$$

Using equation (2.13), we may rewrite equation (2.15) as:

$$\rho\frac{\partial \delta U}{\partial t} - \rho\frac{\partial \langle uv\rangle}{\partial y} = \mu\frac{\partial^2 \delta U}{\partial y^2}. \tag{2.16}$$

By integrating the equation (2.16) in the cross-wake direction from $-\infty$ to $+\infty$ (assuming $\langle uv\rangle \to 0$ as $y \to \pm\infty$), it is clear that the two last terms are either zero or constant. As a result, the mass-flux defect, $\dot{m}$, is independent of the time evolution.

$$\dot{m} = \int_{\infty}^{\infty} \rho U_\infty - \langle U\rangle \, dy = \int_{\infty}^{\infty} \rho\delta U \, dy = cst. \tag{2.17}$$

The mass-flux defect is a preserved quantity in temporally evolving wakes. The same approach can be used to show that in the spatially evolving case, the preserved quantity is the momentum flux defect:

$$\theta = \int_{\infty}^{\infty} \rho\langle U\rangle (U_\infty - \langle U\rangle) \, dy. \tag{2.18}$$

The conservation of momentum flux defect is of particular interest to experimentalists as it relates the wake profile to the total drag on a body (*e.g.,* Batchelor, 1967). Both the momentum and mass-flux defect are related in the far wake such that: $\dot{m} = U_\infty\theta$ (Moser *et al.*, 1998).

Similar to the approach by George (1989) and Moser *et al.* (1998), we assume a self-similar evolution in which the characteristic velocity is the centerline defect, U_0, and the characteristic length scale is the wake half-width, b. If the variables are self-similar, then :

$$\frac{\delta U}{U_0} = f(\eta), \tag{2.19a}$$

$$\frac{\langle uv\rangle}{U_0^2} = g(\eta), \tag{2.19b}$$

where the normalized spatial parameter is : $\eta = y/b(t)$ and functions $f(\eta)$ and $g(\eta)$ represent the self-similar profiles.

By replacing the self-similar variables (2.19) in the mass-flux defect equation (2.17) and by changing the integration parameter, we can show that:

$$\dot{m} = \underbrace{\rho U_\infty}_{A} - \underbrace{\rho b U_0}_{B} \underbrace{\int_\infty^\infty f(\eta)\, d\eta}_{C} = cst. \tag{2.20}$$

As we previously proved, the mass-flux defect is a preserved quantity (recall equation (2.17)) and since the terms (A) and (C) are invariant in time, it is trivial to show that $b{\cdot}U_0$ must also be constant. Replacing the variables (2.19a) and (2.19b) into the momentum equation (2.16) yields:

$$f(\eta)\frac{d\,U_0}{d\,t} - U_0\frac{\eta}{b}\frac{db}{dt}\frac{df}{d\eta} - \frac{U_0^2}{b}\frac{dg(\eta)}{d\eta} = \nu\frac{U_0}{b^2}\frac{d^2 f(\eta)}{d\eta^2}. \tag{2.21}$$

In the self-similar state, all time-dependant terms must be proportional to each other, otherwise, by definition, the flow would not be self-similar. Therefore, we can show that:

$$\frac{d\,U_0}{d\,t} \propto \frac{U_0}{b}\frac{d\,b}{d\,t}. \tag{2.22}$$

Along with the result from equation (2.20), it can be shown that the wake half-width and centerline defect evolve according to $t^{1/2}$ and $t^{-1/2}$, respectively. These results are confirmed by our direct numerical simulations in chapter 4.

2.4 Coherent Structures in Free Shear Flows

Coherent structures are a central concept in the present work. It is often said that the coherent structures, more specifically their underlying vortical motion, are the sinews and muscles of turbulent motion. Many definitions of coherent structures are found in the literature. For semantic clarity, we use the definition by Hussain & Clark (1981*a*) that states that a coherent structure is: "[...] a connected turbulent fluid mass with instantaneously

phase-correlated vorticity over its spatial extent". Therefore, a coherent structure must be reoccurring in time or space. It should be noted that the present definition of coherent structures does not *necessarily* include the instantaneous turbulent structures identified through visualization techniques such as minimal pressure iso-surfaces, Q-criteria or λ_2-criteria. For this reason, we resort to structural eduction techniques, which separate the coherent from the incoherent turbulence. The eduction algorithms developed in the present work are detailed in the corresponding chapters of the thesis.

Chapter 3

Development of a High-Speed Flow Solver

The development, from scratch, of a numerical solver for high-speed canonical free shear flows was undertaken as an integral part of the present doctoral thesis. The solver was developed for direct numerical simulations (DNS), therefore, all the scales of turbulence must be resolved without resorting to any turbulence models. The section 3.1 details the spatial and temporal scheme implemented in the solver; a comparative evaluation of the numerical characteristics of the scheme are presented in sub-section 3.1.1 and appendix C. Specific topics on the generation of the computational mesh (section 3.2) and boundary conditions (section 3.3) are detailed for completeness. Verification steps for the numerical solver are explained in section 3.4. The details of the validation are discussed in the corresponding chapters 4 and 5.

3.1 Definition of the Numerical Scheme

Prior to the development of the solver, a survey of existing computational methods for high-speed flows was undertaken. Although many recent works tend to favour compact

finite difference schemes with explicit time advancement, we opted for a modified high-order MacCormack scheme. This robust numerical method for hyperbolic equations had the distinct advantages of being numerically stable, having very low memory requirements, being computationally efficient and massively parallelizable. Although, for the same grid resolution, the MacCormack scheme under-performs compared to compact methods. It is significantly more dispersive and dissipative. To comprehend the shortfalls of the MacCormack scheme relative to other numerical methods, a study of numerical properties is conducted in sub-section 3.1.1.

The original MacCormack explicit scheme (MacCormack, 1969), a direct variant of the Lax-Wendroff scheme, consists of a predictor and a corrector stage in which the convective terms are computed with an alternatively biased finite difference stencil. The dissipative terms are computed with a centered stencil. The original scheme represents one of the classical numerical methods for hyperbolic partial differential equations, which, in the inviscid case (especially in the presence of high gradients), must be supplemented with artificial viscosity for numerical stability. Formally, it has a second-order accuracy in space and time. In the solver, we implemented a variable-order MaCormack scheme (Hixon, 1997), although for all of our simulations, a fourth-order spatial scheme is used with the usual second-order temporal advancement (Gottlieb & Turkel, 1976). As it is a predictor/corrector scheme, the explicit time advancement shares the same numerical properties as the second-order Runge-Kutta scheme.

To highlight the numerical scheme, we suppose a one-dimensional toy problem of the form:

$$\frac{\partial u}{\partial t} = -c\frac{\partial u}{\partial x} + \mu\frac{\partial^2 u}{\partial x^2}. \tag{3.1}$$

Using the MacCormack 24 scheme (preferred notation, implying a 2^{nd} and 4^{th}-order in

time and space respectively), the above equation is discretized as:

$$\begin{aligned} u_i^{n+\frac{1}{2}} &= u_i^n - \left(\frac{\Delta t}{6\Delta x}\right)\left(7\left(u_{i+1}^n - u_i^n\right) - \left(u_{i+2}^n - u_{i+1}^n\right)\right) \\ &\quad + \left(\frac{\Delta t \mu}{12\Delta x^2}\right)\left(-u_{i-2}^n + 16u_{i-1}^n - 30u_i^n + 16u_{i+1}^n - u_{i+2}^n\right), \end{aligned} \tag{3.2a}$$

$$\begin{aligned} \delta u_i^{n+\frac{1}{2}} &= -u_i^{n+\frac{1}{2}} \left(\frac{\Delta t}{6\Delta x}\right)\left(7\left(u_i^{n+1/2} - u_{i-1}^{n+1/2}\right) - \left(u_{i-1}^{n+1/2} - u_{i-2}^{n+1/2}\right)\right) \\ &\quad + \left(\frac{\Delta t \mu}{12\Delta x^2}\right)\left(-u_{i-2}^{n+1} + 16u_{i-1}^{n+1} - 30u_i^{n+1} + 16u_{i+1}^{n+1} - u_{i+2}^{n+1}\right), \end{aligned} \tag{3.2b}$$

$$u_i^{n+1} = \frac{1}{2}\left(u_i^n + u_i^{n+\frac{1}{2}} + \delta u_i^{n+\frac{1}{2}}\right), \tag{3.2c}$$

where the subscripts are the spatial and superscripts the temporal discretization of the variables. The superscript $n + \frac{1}{2}$ represents the value of the variables at the predictor stage. Obviously, Δt and Δx are respectively the temporal time-step and the homogeneous grid spacing. The MacCormack 24 scheme along with 22 and 46 were implemented in the solver for the solution of the normalized Navier-Stokes equations (2.7). In order to avoid biasing, the up-winding/down-winding of the predictor/corrector stages are alternated at every time-step in each spatial direction.

3.1.1 Numerical properties of the MacCormack scheme

An investigation was undertaken to understand the numerical properties of the MacCormack 24 scheme with respect to other classical finite difference schemes and compact methods. As the dispersive properties of the alternatively-biased MacCormack scheme are equivalent to the central difference stencil of the same order (Rona *et al.*, 2009), the effect of dispersion can be investigated with a modified wavenumber analysis (see *e.g.,* Moin, 2010, for details on modified wavenumber analysis), see figure 3.1. The MacCormack 24 shows a poorer high-frequency resolution compared equivalent order compact schemes. These deficiencies in the dispersion characteristics can be reduced by increasing the grid resolution

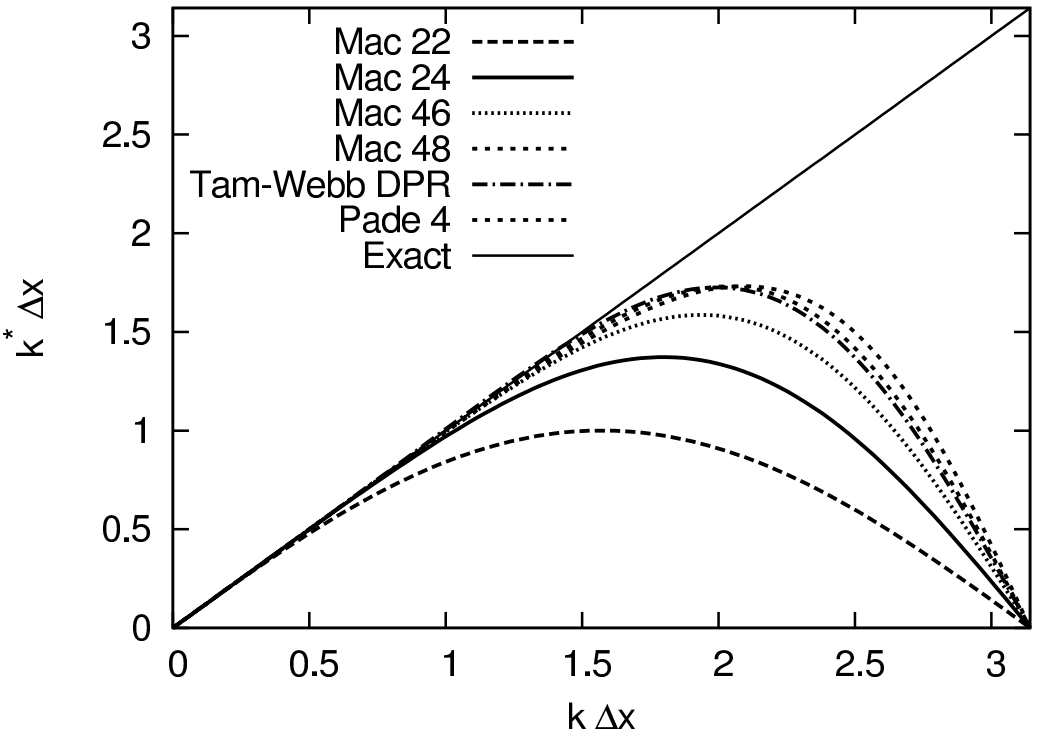

Figure 3.1: The modified wavenumber of various finite differencing schemes. The different orders of the MacCormack schemes (Mac) are compared to the fourth-order Padé and to the dispersion-relation-preserving scheme by Tam & Webb (1993).

but, as seen in figure 3.1, the increased resolution can be significant. Further detailed comparison of the numerical properties of the MacCormack schemes for typical high-speed toy problems (Burgers' equation, Sod problem, Shu-Usher problem and NACA 1135 problem) can be found in appendix C.

3.2 Computational Mesh

The region of interest in the wake is located within approximately one wake half-width on either side of the centerplane. As the flow is fully turbulent with high local velocity and

pressure gradients, the grid resolution must be fine enough to resolve all scales of interest. In the freestream, the grid requirement is significantly reduced as the flow is essentially irrotational. The computational domain must be finite in the cross-wake direction (details in section 3.3) and the artificial boundaries must be far enough from the region of interest to avoid any spurious interference. The contradicting requirement of a high grid resolution wake within a large computational domain with a low grid resolution makes a homogeneous grid distribution in the cross-wake direction far too prohibitive. But, the use of finite difference methods on an inhomogeneously distributed grid reduces the formal order of accuracy of the numerical scheme. To bypass this limitation, we construct a grid mapping from the inhomogeneous physical domain, with clustered centerplane resolution, onto a homogeneous computational grid before solving the governing equations. Through the use of well defined metrics, we simply convert the results back from the computational grid onto the initial inhomogeneous grid without adversely affecting the accuracy of the scheme. The present mapping technique follows Mahesh *et al.* (1996).

The cross-wake grid is mapped onto a computational domain s, such that: $y \rightarrow y(s)$. Therefore, the derivatives of the dependant variables are computed using the classical chain rule property:

$$\frac{\partial \phi(y,t)}{\partial y} = \frac{\partial \phi(y,t(s))}{\partial s} \cdot \frac{ds}{dy}. \tag{3.3}$$

For the case of the wake, a centerplane clustering is achieved through the use of a combination of hyperbolic tangents. The variation of the grid spacing between physical and computational domain is defined as:

$$\frac{1}{C}\frac{dy}{ds} = r + \left(\frac{r-d}{2}\right)\left[\tanh b(s-3/4) - \tanh b(s-1/4)\right]. \tag{3.4}$$

This equation represents a continuously derivable function that clusters the points on the center of the domain with the parameters r, d and b; these parameters are defined in figure

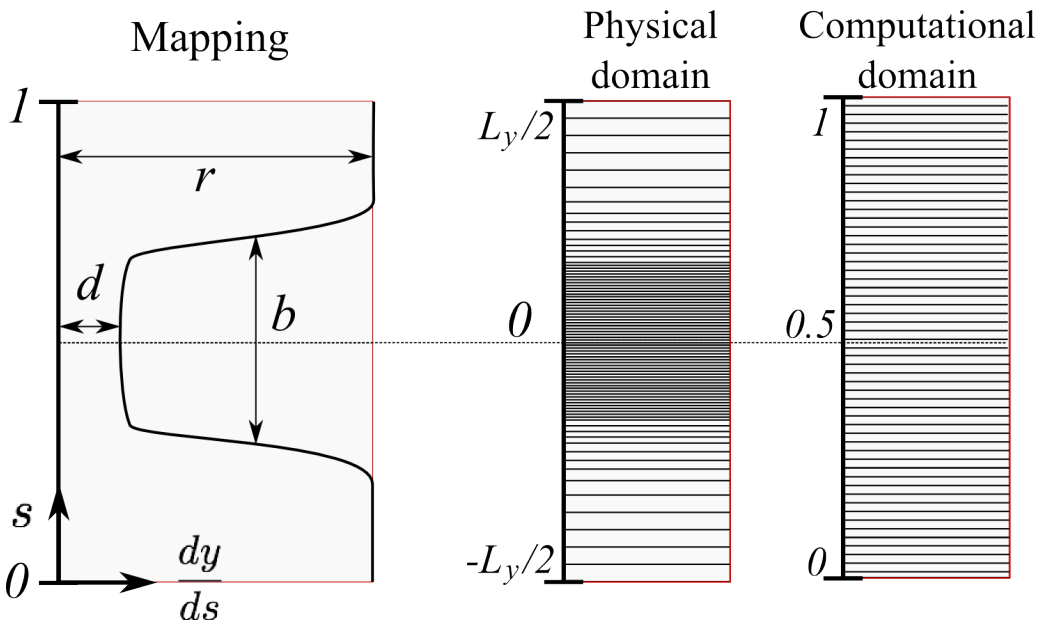

Figure 3.2: Mapping between non-uniform and uniform mesh. Left figure represents the function between the mapping and the physical domain. Illustration of the grid clustering in the physical and the homogeneous computational domain shown on the right.

3.2.

By integrating the above equation (3.4), we obtain:

$$y = C\left(rs + \left(\frac{r-d}{2b}\right)\left[ln\left(\cosh\left(b\left(s-0.75\right)\right)\right) - \cosh\left(b\left(s-0.25\right)\right)\right]\right), \tag{3.5}$$

where the constant C can be determined by evaluating the integral at $y(0) = 0$ and $y(1) = 1$.

Re-scaling the equation by the domain length in the y direction, L_y yields:

$$\frac{y}{L_y} = \frac{rs + \left(\frac{r-d}{2b}\right)\ln\left[\frac{\cosh b(s-3/4)\cosh b/4}{\cosh b(s-1/4)\cosh 3b/4}\right]}{r + \left(\frac{r-d}{b}\right)\ln\left[\frac{\cosh b/4}{\cosh 3b/4}\right]}. \tag{3.6}$$

By deriving the equation (3.6), we are able to obtain the adequate metrics to convert the variables back onto the original inhomogeneous domain.

3.3 Non-Reflecting Boundary Conditions

In compressible free shear flows, the boundary conditions are used to bound the computational domain. As such, the computational boundaries in the freestream should behave as if they were not there at all. The combined hyperbolic/parabolic nature of the governing equations implies that the information propagates at a finite speed within the domain. The propagation of the information must traverse the computational boundaries with limited spurious reflections.

The obvious solution of infinitely stretching the grid in the finite direction proves inadequate since the propagating waves/information must be resolved on the grid. The under-resolution of the wavelength (on a stretched grid) results in a spurious wave generation, which contaminates the computational domain. A variety of non-reflecting boundary conditions are available in the literature, which are based on identifying the characteristic lines of the flow at the boundaries. Formally, the concept of characteristic solutions to the Navier-Stokes equations is incorrect as it is not a purely hyperbolic equation set. For this reason, simpler models based on the Euler equations have been devised and retain their validity far from any high-shear regions.

The boundary condition implementation in the solver is based on the work by Thompson (1987) and Thompson (1990). Because of different normalization parameters used in the present work (recall Navier-Stokes equations (2.7)), a modification to the boundary conditions by Thompson (1990) was necessary and fully documented in the appendix D. For completeness, a brief summary of the one-dimensional method is presented for boundary conditions in the y direction. Using the Euler equations in non-conservative form, we isolate the spatial variables with gradients normal to the cross-wake boundary in the

y-direction. We have:

$$\frac{\partial \mathbf{U}}{\partial t} + \mathbf{A}\frac{\partial \mathbf{U}}{\partial y} + \mathbf{C} = 0, \tag{3.7}$$

where $\mathbf{U} = (\rho, u, v, w, p)^T$ represents the primary variables of the Euler equation, while $\mathbf{C}$ represents a matrix containing all the derivatives in the plane of the boundary. The matrix $\mathbf{A}$ contains the coefficients of the derivatives normal to the boundary, see definition of $\mathbf{A}$ in appendix D (equation (D.1)). The eigenvalue of $\mathbf{A}$ can be found from the relations:

$$\mathbf{l}_i\mathbf{A} = \lambda_i\mathbf{l}_i, \tag{3.8a}$$

$$\mathbf{A}\mathbf{r}_i = \lambda_i\mathbf{r}_i, \tag{3.8b}$$

where λ_i represents the eigenvalues along with their corresponding left ($\mathbf{l}_i$) and right ($\mathbf{r}_i$) eigenvectors. The eigenvalues and eigenvectors are listed in the appendix D for our non-dimensionalization used in the governing equation set. Naturally, the left and right eigenvectors are mutually orthogonal. The multiplication of equation (3.7) by the matrix containing the left eigenvector, assuming basic matrix properties, yields:

$$\mathbf{l}_i\frac{\partial \mathbf{U}}{\partial t} + \mathcal{L} + \mathbf{l}_i\mathbf{C} = 0, \tag{3.9}$$

where:

$$\mathcal{L} = \begin{cases} \lambda_i\mathbf{l}_i\frac{\partial \mathbf{U}}{\partial y} & \text{waves leaving the domain: } \lambda_i > 0 \text{ for typical outflow BCs} \\ 0 & \text{waves entering the domain: } \lambda_i < 0 \text{ for typical inflow BCs} \end{cases} \tag{3.10}$$

By determining the sign of eigenvalue λ_i, we determine if the information is leaving (positive) or entering (negative) the domain. If the information is exiting the domain, we compute the values of the non-conservative variables at the boundary using the information from within the computational domain. Alternatively, if the information is entering the domain (negative eigenvalue), the non-conservative variables are explicitly set to zero as we have no way to determine the incoming information.

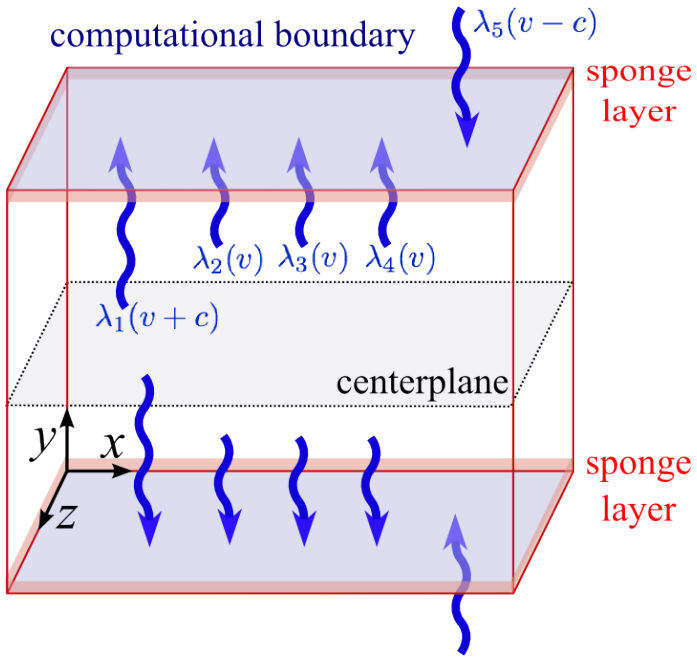

Figure 3.3: Illustration of the characteristics of the boundary conditions. The illustration corresponds to the case of outward directed subsonic flow normal to the finite boundaries in the y-direction.

Since an inviscid approximation is used at the boundaries to compute the characteristics, sponge layers are supplemented to the non-reflecting boundary conditions to assure that spurious waves are not reflected or generated. The sponge layer is a finite region inside the computational domain in which an extra damping term in the Navier-Stokes equations is used. The damping forces the flow back to the freestream state. The magnitude of the damping term is a third-order function that monotonically increases in strength as the boundary is approached. For the present simulations, a sponge layer of 15 grid points was used at all finite boundaries.

3.4 Numerical Solver Verification

A careful verification of the numerical solver was conducted, the details of the verification are explained here for archival purposes. The verification is an essential step in the development of a Navier-Stokes solver as it helps to identify and remove any computational mistakes. It also allows the user to gain confidence in the numerical results. The present solver was verified using two main tests: the evolution of the Taylor-Green vortex in the incompressible limit and the solution of the viscous shock. The details of the Taylor-Green verification can be found in standard fluid dynamics textbooks and are not repeated here for brevity. Here, we detail the verification of the solver using the laminar shock wave.

The shock discontinuity in the Euler equation is a discrete step function given the purely hyperbolic nature of the equation set. The additional viscosity and heat transfer terms in the Navier-Stokes equation smooth out this discontinuity. An analytical solution for the velocity and density variation through a weak shock exists for the one-dimensional Navier-stokes equation (Becker, 1922; Howarth, 1953). The details of the solution are found in appendix E. The viscous shock solution is verified sequentially in all three-directions, on the homogeneous and inhomogeneous grids. Any variation in the velocity or density profile through the shock is an unambiguous indication of a numerical error in the code. Figure 3.4 shows the comparison of the theoretical and numerical solutions of the shock on two-different grid resolutions.

In addition to these general tests, specific verifications of the non-reflecting boundary conditions were conducted by convecting a vortex through the computational boundaries. Additional validation tests were conducted by simulating decaying isotropic turbulence (see *e.g.,* Wu & Hickey, 2012), mixing layers and wakes (see chapter 4).

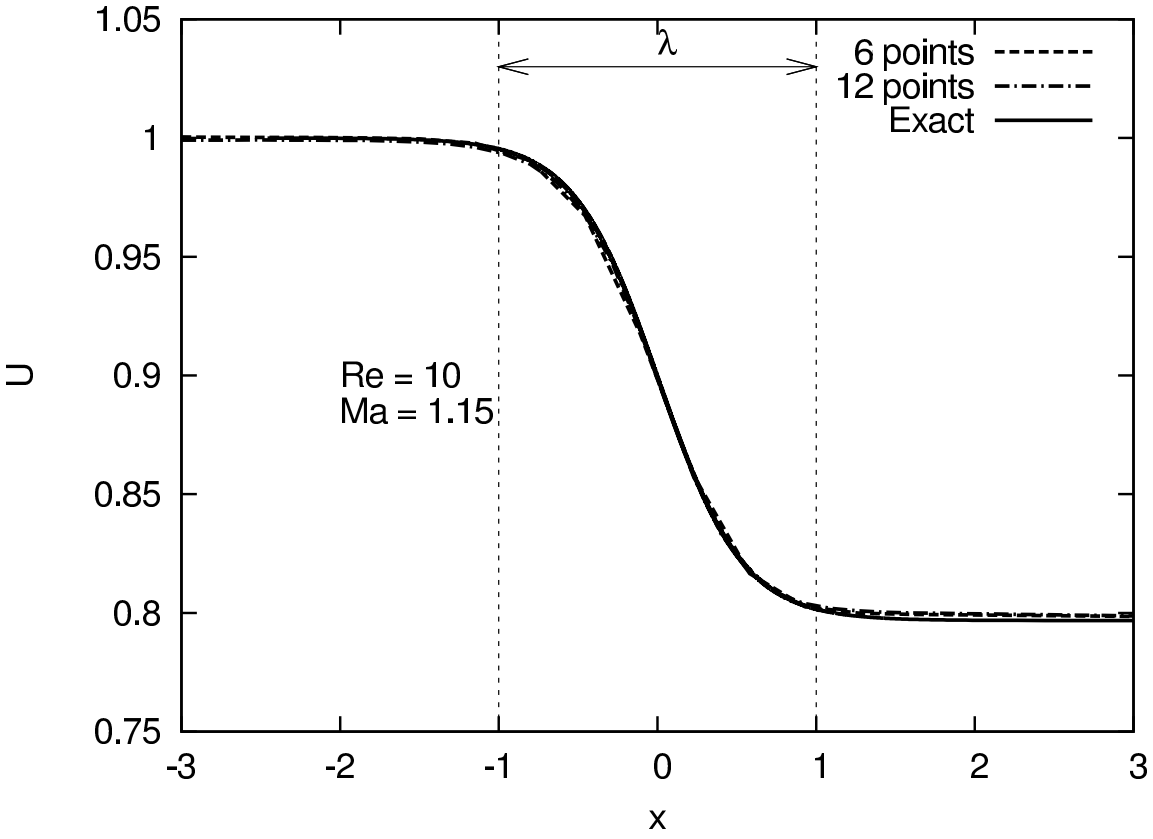

Figure 3.4: The effect of the resolution of the shock on the solution. The resolution corresponds to the number of grid points within the shock.

Chapter 4

Role of Coherent Structures in Multiple Self-Similar States of Turbulent Planar Wakes

4.1 Abstract

We study the nature of archetypal, incompressible, planar splitter-plate wakes, specifically, the effects of the exit boundary layer state on multiple approximate self-similarity. Temporally developing direct numerical simulations, at a Reynolds number of 1500 based on the mass-flux defect, are performed to investigate three distinct wake evolution scenarios: Kelvin-Helmholtz transition, bypass transition in an asymmetric wake and initially turbulent wake. The differences in the evolution and far wake statistics are analyzed in detail. The individual approximate self-similar states exhibit a relative variation of up to 48 % in the spread rate, in second-order statistics, and in peak values of the energy budgets terms. The self-similar multiplicity is related to the non-universality of the large-scale coherent structures, which maintain the memory of the initial conditions. Similar structural configurations among wakes may nonetheless lead to far wake statistical variations. In

the far wake, two distinct spanwise coherent motions are identified: (i) staggered, segregated spanwise rollers on either side of the centerplane, dominant in wakes transitioning via anti-symmetric instability modes; and, (ii) larger spanwise rollers spanning across the centerplane, emerging in the absence of a near wake characteristic length scale. The latter structure is characterized by strong spanwise coherence, cross-wake velocity correlations and a larger entrainment rate caused by deep pockets of irrotational fluid within the folds of the turbulent/non-turbulent interface. The mid-sized structures, primarily vortical rods, are generic for all initial conditions and are inclined at about $\pm 33^\circ$ to the downstream, shallower than the preferential $\pm 45^\circ$ inclination of the vorticity vector. The spread rate is driven by the inner wake dynamics, more specifically the advective flux of spanwise vorticity across the centerplane, which in turn depends on the large-scale coherent structures.

4.2 Introduction

In a series of wake experiments, Bonnet and co-workers (Bonnet *et al.* (1984, 1986); Bonnet & Chaput (1986)) investigated the influence of the splitter-plate exit boundary layer state on the evolution of the flow. In the far wake, they placed a fixed hot-wire at the location of the maximum turbulent fluctuations and measured the cross-correlation using a second probe with varying cross-wake separation. The measurements revealed a slight negative correlation in the fluctuating streamwise velocity for the case of a splitter-plate with turbulent trailing edge boundary layer, results convincingly replicated by our present simulations (see figure 4.1). This intriguing negative dip contrasts the laminar bluff-body wake data by Grant (1958) and, consequently, raises doubts on the universality of the characteristic structures in the far wake. The results of Bonnet *et al.* clearly manifest the well-known *memory effect* in free shear flows. We explore the influence of the generating

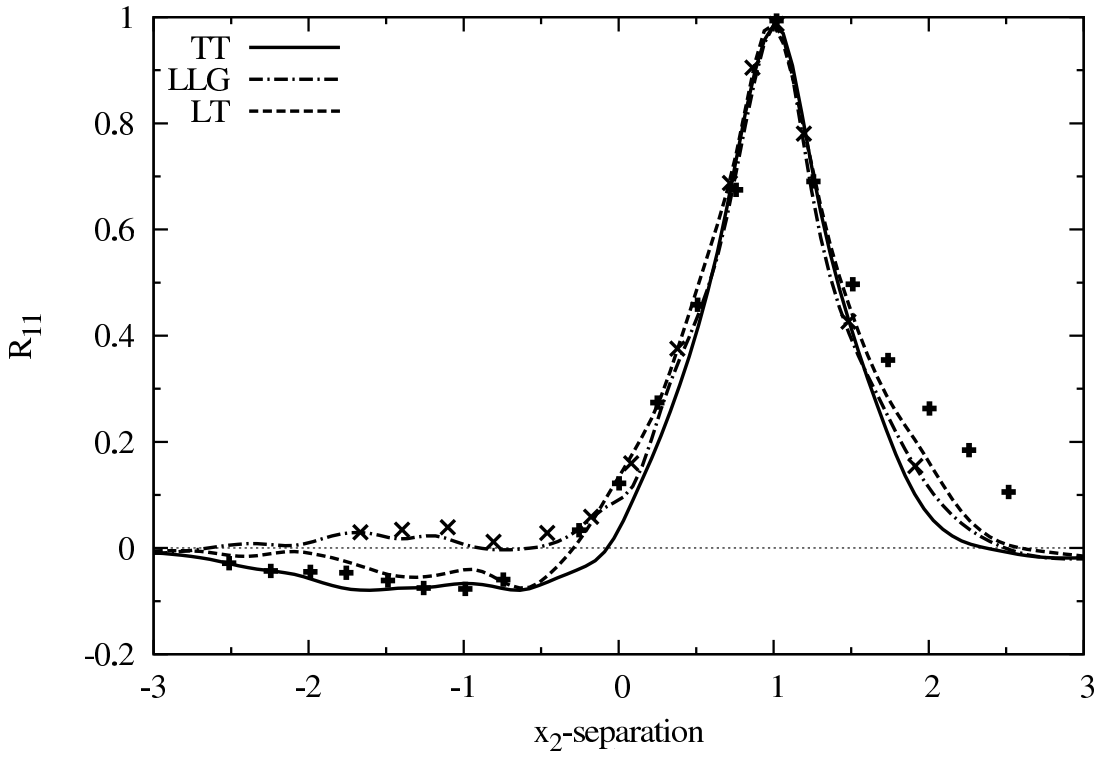

Figure 4.1: Two-point correlation of streamwise velocity fluctuations, R_{11}, with cross-wake separation. The x_2-separation is normalized with the location of the highest turbulent fluctuations. Our DNS data at $t = 250$: laminar Gaussian initial velocity profile (LLG), fully turbulent boundary layers (TT) and Blasius/turbulent boundary layers asymmetric wake (LT). Experimental data: cross - Grant (1958) low-Reynolds number bluff-body wake; and plus - Bonnet *et al.* (1986) turbulent splitter-plate.

conditions on the far field structures and the multiplicity of statistically self-similar states.

Multiplicity of self-similar states. Townsend (1949, 1976) proposed that each class of turbulent free shear flows should asymptotically approach a universal state, independent of the initial flow details. As they evolve, wakes - and any turbulent shear flow - should

gradually forget their starting characteristics and unscramble their initial features via nonlinear interactions to asymptotically tend toward the same statistical state. This seemingly reasonable hypothesis was conceptually attractive, and survived for a long time, until challenged by more detailed experimental and theoretical investigations. George (1989) showed that the governing equations admit multiple self-similar solutions in the far wake. Bevilaqua & Lykoudis (1978); Wygnanski *et al.* (1986); Marasli *et al.* (1992) and Zhou & Antonia (1995) demonstrated via careful experiments that different wake-generating bodies influence the spreading rate, Reynolds stresses, energy spectra, vorticity fluctuations and drag in both the near and far wakes. The memory effects of an axisymmetric wake were shown to persist until at least 600 momentum thicknesses downstream, possibly even farther (Johansson *et al.*, 2003). Memory effects are not limited to integral or first-order statistics. Lepore & Mydlarski (2009) observed an initial condition dependence of the inertial range scaling exponents of high-order scalar structure functions, despite similarity in the second-order statistics. Using direct numerical simulation (DNS) of initially turbulent planar wakes, Moser *et al.* (1998) showed that minute changes in the level of initial forcing resulted in large variations in the far wake spread rates and turbulence statistics. The multiplicity of the self-similar statistics could be reduced, although not entirely removed, when scaled with a non-dimensional parameter based on the spread rate. Despite an improved scaling, disparities between the forced and unforced cases persisted, particularly in the $\langle u_1 u_1 \rangle$ and $\langle u_1 u_2 \rangle$ profiles. Statistical multiplicity, imparted by different initial conditions, is also evident in mixing layer and jet experiments (*e.g.,* Hussain & Clark, 1977; Hussain & Zedan, 1978*a*,*b*).

Far wake structural universality? The existence of an archetypical far wake structure remains an open question (Brown & Roshko, 2011). Many previous works have questioned the idea of a universal far wake structure, independent of initial conditions

(Bevilaqua & Lykoudis, 1978; Bonnet *et al.*, 1986; Wygnanski *et al.*, 1986; Zhou & Antonia, 1995). The non-universality, or plurality of far wake structures (preferred terminology herein), is a clear possibility as a family of similarity solutions for the two-point velocity correlation exists (Ewing *et al.*, 2007). The classical structural understanding of the wake builds on the early work by Grant (1958) who proposed that the far field dynamics are governed by the combined action of spanwise vorticity (named *mixing-jet* by Grant) and pairs of counter-rotating vortices (double-roller eddy model). Grant's model was experimentally investigated through proper orthogonal decomposition by Payne & Lumley (1967) who inferred vortex pairs normal to the centerplane. The model was further refined by Mumford (1983) who showed a predominance of inclined double-rollers on each side of the centerplane. About half of the streamwise velocity fluctuations (Browne *et al.*, 1986) and 40 % of the total turbulent kinetic energy (Ferré *et al.*, 1990) are attributable to the inclined vortices. Breidenthal (1980), Browne *et al.* (1986) and Antonia *et al.* (1987), however, speculated that the mixing-jet and the double-roller vortices might be different observations of the same coherent structure in the form of closed-loop vortices spanning the entire wake width. Hayakawa & Hussain (1989) deduced, from a detailed study of the intermediate-wake with rakes of cross hot-wires, that outwardly kinked spanwise rolls are probably the primary coherent structure in the far wake. Using conditional sampling, Vernet *et al.* (1999) educed structures which are geometrically similar to horseshoes. The relative importance of the inclined vortical structures can be seen in the recent work by Philip & Marusic (2012). They proposed a simplified axisymmetric wake model, based on randomly inclined vortical structures, which is able to reproduce experimental wake statistics. The horseshoe legs have been interpreted (Cimbala *et al.*, 1988; Ferré *et al.*, 1990; Giralt & Ferré, 1993; Kopp *et al.*, 2002) as the observed double-roller eddies found by Grant (1958) while the heads of the structures have been shown to be the bulges at the

turbulent/non-turbulent interface (TNTI) (Kopp *et al.*, 2002). The connection at the head of the inclined rollers (hence forming a horseshoe) is conceptually appealing, but there is no preponderant, locally-spanwise stretching to sustain the head, which gets diffused with time, leaving the two strong legs. Furthermore, if the horseshoes originate from spanwise coherent rollers found in bluff-body and transitioning wakes as suggested by Hayakawa & Hussain (1989), their presence in screen or splitter-plate wakes must be understood. It is necessary to characterize the coherent far wake structures and, in particular, determine how they might be related to the statistical multiplicity.

Origin of far wake structures. Memory effects inherently imply a connection among the near, intermediate and far wake structures - but there is some evidence contradicting this notion. Two main hypotheses concerning the origin of the large-scale far wake structures are: pairing of coherent spanwise vortices and preferential amplification of new instability modes. The first hypothesis is that pairing of spanwise rollers, through Biot-Savart induction, occurs until a stable Karman street vortex is reached. The second suggests that pairing is not the principal mechanism of structure growth in the far wake. Instead, instability of the mean wake profile leads to the amplification of locally unstable modes (Taneda, 1959). Cimbala *et al.* (1988) proved the preponderance of the instability model, based primarily on the re-emergence of a turbulent vortex street (secondary Karman vortex street) after a quiescent period of less-organized flow. The instability based model has shortcomings, as the normalized mean velocity profile is insensitive to the initial conditions (Wygnanski *et al.*, 1986). One may infer that the large-scale far wake coherent structures - related to the locally unstable modes - may also be invariant to the initial conditions. Consequently, the instability based explanation might imply a de-coupling of the near and far fields - although some coupling is inescapable as the evolution of the resulting mode

must depend on the structure advecting from upstream. To address this conceptual problem, Wygnanski *et al.* (1986) hypothesized that the interaction of an unstable symmetric and anti-symmetric mode originating in the near wake may explain the emergence of the far field structures. Others have suggested that the near and far fields are connected by an oblique wave resonance which is very sensitive to initial conditions and freestream turbulence levels (Williamson & Prasad, 1993). The question of the origin of far wake structures remains, and is central to understanding statistical multiplicity in the far wake.

Statistical multiplicity, structural plurality and entrainment. The salient features of both statistical multiplicity and structural plurality can be seen at the turbulent / non-turbulent interface (TNTI). It has long been assumed that wakes, like mixing layers, jets and boundary layers, spread by entraining ambient, irrotational fluid via a two-step process: engulfment and nibbling. The entrainment process has been thought as a "pumping" (Papailiou & Lykoudis, 1974) mechanism by which the large-scale turbulent motion near the TNTI draws in irrotational fluid parcels, engulfing them into the folds of the TNTI; unlike the jet, there is no induced flow component to drive the large-scale entrainment in the wake (Philip & Marusic, 2012). Vorticity is then efficiently imparted to the irrotational engulfed fluid by viscous diffusion. This process results in the spreading of the wake and also the growth of the structures. Therefore, different spreading rates imply different entrainment rates. Any lack of structural universality should then result in notable differences in the TNTI. This seemingly reasonable hypothesis that has yet to be explored is discussed in the present work.

We investigate the effect of splitter-plate trailing-edge boundary layer states on self-similar wake statistics and structures. The wake of a zero-thickness plate represents an idealized case - without bluff-body effects, such as pressure gradient, trailing edge receptivity or changing leading edge stagnation point. We seek clarifications on the following

issues: (a) dependence of far wake statistical self-similarity on the initial condition; (b) universality, or lack thereof, of far wake coherent structures; and (c) connection between possible multiple statistical self-similar states and coherent structures. We perform direct numerical simulations of temporally evolving planar wakes. Four sets of limiting initial conditions are considered for the state of the boundary layers on the two sides at the trailing edge of a zero-thickness splitter-plate: (1) LLB: identical, fully laminar, Blasius profiles on both sides; (2) LLG: Gaussian velocity profile across the fully laminar wake; (3) TT: fully-developed, equilibrium, fully-resolved, instantaneous, flat-plate turbulent boundary layers on both sides; and (4) LT: laminar, Blasius profile on one side of the plate, and fully-developed turbulent boundary layer on the other. The asymmetric planar wake case (LT) provides a unique setup, as it shares characteristics of both the laminar and turbulent wakes (e.g. Thomas & Liu, 2004; Rai, 2010), evolving via the initiation and interaction of distinctly different structures on the two sides of the wake. A particular facet of LT is the likely influence of the turbulence on the laminar-side instability and transition. Aside from serving as an idealized setup for the study of wake-flow physics, the LT case has some relevance to wakes encountered in turbomachinery, wind turbine and aeronautical applications, where opposite pressure gradients on two sides of a lifting surface generates a wake from the merger of laminar and turbulent boundary layers (Wu & Hickey, 2012).

4.3 Numerical Considerations

Initial conditions. The states of the trailing edge boundary layers of an infinitely thin splitter-plate are taken as the initial conditions (ICs) of the temporally evolving wake. The ICs remove any trailing edge effects that would otherwise influence the flow, such as: pressure gradient, roughness of the generating body and trailing edge receptivity. We

study four different idealized ICs while maintaining all the other simulation parameters the same. The first case is a laminar Blasius boundary layer profile on both sides of the centerline (LLB). The second case is a Gaussian velocity profile (LLG), as would form via viscous diffusion after the merger of two laminar boundary layers. The Gaussian profile is defined as: $\langle u\,(x_2)\rangle = U_\infty - U_d \exp\left(-\ln(2)\,(x_2/b)^2\right)$, where U_∞, U_d and b are respectively the freestream velocity, the initial centerline defect and the wake half-width; $2b$ is the x_2 separation between the two points where the mean velocity defect is half its maximum. The initial conditions of both LLB and LLG are perturbed by low amplitude random noise ($\langle u_1\, u_1\rangle / U_d^2 = \mathcal{O}\left(10^{-6}\right)$) to initiate transition. A greater generality is achieved as the initial perturbations do not impose a length or time scale to the flow; instead, the instability modes undergo exponential growth. Two different laminar initial conditions are simulated to address issues raised in Papageorgiou & Smith (1989). Their work questioned the validity of initializing temporal simulations with a Gaussian velocity profile as the near wake Blasius-like profile has unstable modes with faster exponential energy growth (Papageorgiou, 1990). To clarify this issue, both the double Blasius and Gaussian initial conditions were simulated and compared (discussed in §4.4).

The third case (TT) represents a wake that is fully turbulent from its inception. The flow is initialized by statistically independent realizations of the flat-plate boundary layer DNS by Wu & Moin (2009, 2010). The simulations are taken at the around the station of momentum-thickness Reynolds number of $Re_\theta = 1300$ - farther into the fully turbulent region than previous wake studies (Moser *et al.*, 1998). The fourth case of an asymmetric wake (LT) is a fully developed turbulent boundary layer on one side of the plate and a laminar Blasius boundary layer on the other - similar to the setup in Thomas & Liu (2004) and Rai (2010). In LT and TT, no additional perturbations were added to the initial field.

Admittedly, initializing a temporal simulation with a spatially developing turbulent boundary layer DNS is unconventional. To assure that the non-periodicity of the initial velocity field did not cause globally aberrant results, we monitored the evolution of the maximum dilatation and verified that the TT case was domain size independent. In addition, we thoroughly validated the near and far field statistics with published experimental data (see validation in §4.4).

All the simulations are initialized with a unitary centerline velocity, U_d, and mass-flux defect, $\dot{m} = \int_{-\infty}^{\infty} [U_\infty - U(x_2)]\, dx_2$. Also, both constitutive boundary layers in LT (Blasius and turbulent boundary layers) have an identical mass-flux defect at the initial time-step. As the mass-flux and initial centerline defect are identical in all the cases, $\dot{m}$ and U_d are used to normalize the results. The characteristic length scale is defined as $\dot{m}/U_d$, whereas the time scale is $\dot{m}/U_d^2$. Throughout the paper, these characteristic scales are used to non-dimensionalize the results. The Reynolds number based on the mass-flux defect is $Re = 1500$. In the far wake, the Reynolds number based on the root-mean square of the maximum streamwise fluctuation and the Taylor scale is about $Re_\lambda = 90$.

Numerical method. Because the current work is the initial phase of our broader research program on supersonic wakes, the conservative form of the time-dependent compressible Navier-Stokes equations with skew-symmetric convective terms are solved in the incompressible limit. The slight compressibility removes the complications related to the coupling of the pressure and momentum equations at the cost of a more expensive computation. For all cases, the freestream Mach number is 0.3, which implies a finite propagation speed of the pressure waves. The incompressible approximation is acceptable because the compressibility effects (defined by the relative Mach number, $Ma_r = U_0/c_\infty$, where $U_\infty - U(x_2 = 0) = U_0$ is the maximum velocity defect) are initially small ($Ma_r = 0.3$) and

decrease monotonically as the flow evolves to a plateau of $Ma_r = \mathcal{O}\left(10^{-2}\right)$, while the fluctuating density remains small for the entire evolution, $\rho_{rms}/\rho_\infty = \mathcal{O}\left(10^{-7} - 10^{-5}\right)$. We can therefore assume that the results are essentially incompressible. The numerical method is based on a biased finite difference predictor/corrector scheme, which is centered over a time-step; the scheme is fourth-order accurate in space (third-order at the finite boundaries) and second-order accurate in time. The numerical scheme requires a higher spatial resolution to adequately capture the small scales of turbulence as it is more dispersive and dissipative than either the spectral or Padé methods. Fortunately, the over-resolution required for this method is offset by a computationally advantageous algorithm in terms of parallelizability and efficiency. The increased resolution also reduces the aliasing error caused by the higher-order non-linearities of the compressible Navier-Stokes equations; most importantly, the non-linearities in the convective terms of the momentum equations: $\partial \rho u_i u_j / \partial x_j$. The domain of our temporally evolving flow is periodic in the streamwise x_1 and spanwise x_3 directions. A non-reflective boundary condition, supplemented with sponge layers, is applied to the x_2 direction using the method by Thompson (1987, 1990) to assure that outwardly propagating perturbations leave the computational domain without reflection; the approach is based on the method of characteristics of the inviscid Euler equation.

Given the long evolution required to study the memory effects in wakes, temporal simulations were conducted to reduce the computational cost. These simulations *approximate* the spatial/temporal evolution of real planar wake flows, therefore, their inherent limitations need to be addressed. Firstly, the periodicity of the stream- and spanwise directions perpetuate perturbations along those axes, whereas in spatially evolving flows, these same perturbations are simply convected away. Secondly, as wakes from a thin splitter-plate are

formed, the boundary layers merge along a continuous line (or at a single point we consider a two-dimensional plane) near the trailing edge. In temporal simulations, the merger occurs simultaneously over the entire centerplane, which may limit the generality of our transitional investigation in §4.4.2. Despite these limitations, temporal simulations remain pertinent for the study of the memory effects in free shear flows.

Measured by a constant length scale, $\dot{m}/U_d$, the computational domain is $75 \times 45 \times 25$ (for LLB and LLG) in the streamwise, cross-wake and spanwise directions respectively - 50 % larger in the streamwise and 100 % larger in the spanwise direction compared to Moser *et al.* (1998). The spanwise domain length of TT and LT was limited to 20, which represents the lateral extent of two side-by-side, statistically independent, turbulent boundary layers of Wu & Moin. A total of four (two on each side) statistically independent boundary layer realizations were used for the IC of TT. A similar "stitching" of two independent boundary layers was successfully implemented to extend the spanwise computational domain in the LES by Ghosal & Rogers (1997). This approach was preferred to the doubling of a single boundary layer realization, which would have had a perfect matching at the intersection given the spanwise periodicity of the original simulation. The streamwise and spanwise dimensions were chosen to be large enough to permit a long self-similar evolution. For the entire simulation of all wakes, the computational domain is at least 2.5 and 8 wake half-widths in the spanwise and streamwise directions respectively. The number of grid points is 216 million ($1200 \times 450 \times 400$) for the transitional (LLG and LLB) and 173 million ($1200 \times 450 \times 320$) for the turbulent (LT and TT) ICs - about a decade greater than Moser *et al.* (1998) at a slightly lower Reynolds number ($Re = 1500$ compared to 2000 in Moser *et al.*). The domain size, resolution and Reynolds number are significantly larger than other wake simulations (Voke & Potamitis, 1994). The grid resolves -throughout the entire wake evolution- the turbulence down to at least the Kolmogorov scale (in the far

wake the maximal grid spacing is about 0.5 Kolmogorov scale). The time was advanced based on the acoustic CFL number, which was maintained below 0.35 for stability and temporal resolution. The grid spacing is homogeneous in the periodic directions (x_1 and x_3), and a hyperbolic tangent mapping is used in the x_2 direction. The code was validated in numerous steps by comparing our results with the analytical solution of the viscous shock and canonical incompressible turbulent flows (decaying isotropic turbulence and planar mixing layer). In addition to grid convergence tests, we assessed the influence of the domain size by simulating all cases on a smaller domain (identical resolution using 72 million points). Very comparable statistics in the near and intermediate wakes were obtained, but the smaller domain size eventually constrained the far wake evolution. The simulations were fully parallelized using up to 64 SPARC64 VII (2.52 GHz) processors on a Sun Enterprise M9000 cluster of the High Performance Computing Virtual Laboratory (HPCVL) located in Kingston, Ontario.

4.4 Towards Self-Similarity

We investigate planar wakes as they evolve towards self-similarity by comparing integral parameters, higher-order turbulence statistics, mechanisms of transition and energy budgets.

4.4.1 Integral parameters

Mean velocity profiles. The evolution of the mean streamwise velocity profiles is shown in figure 4.2. Prior to transition, the two laminar wakes (LLB and LLG) undergo a slow viscous decay of the centerline velocity defect. The locations of the pre-transitional inflection points in LLG remain constant at $x_2 = \pm 0.44$ and, as expected, the value of the

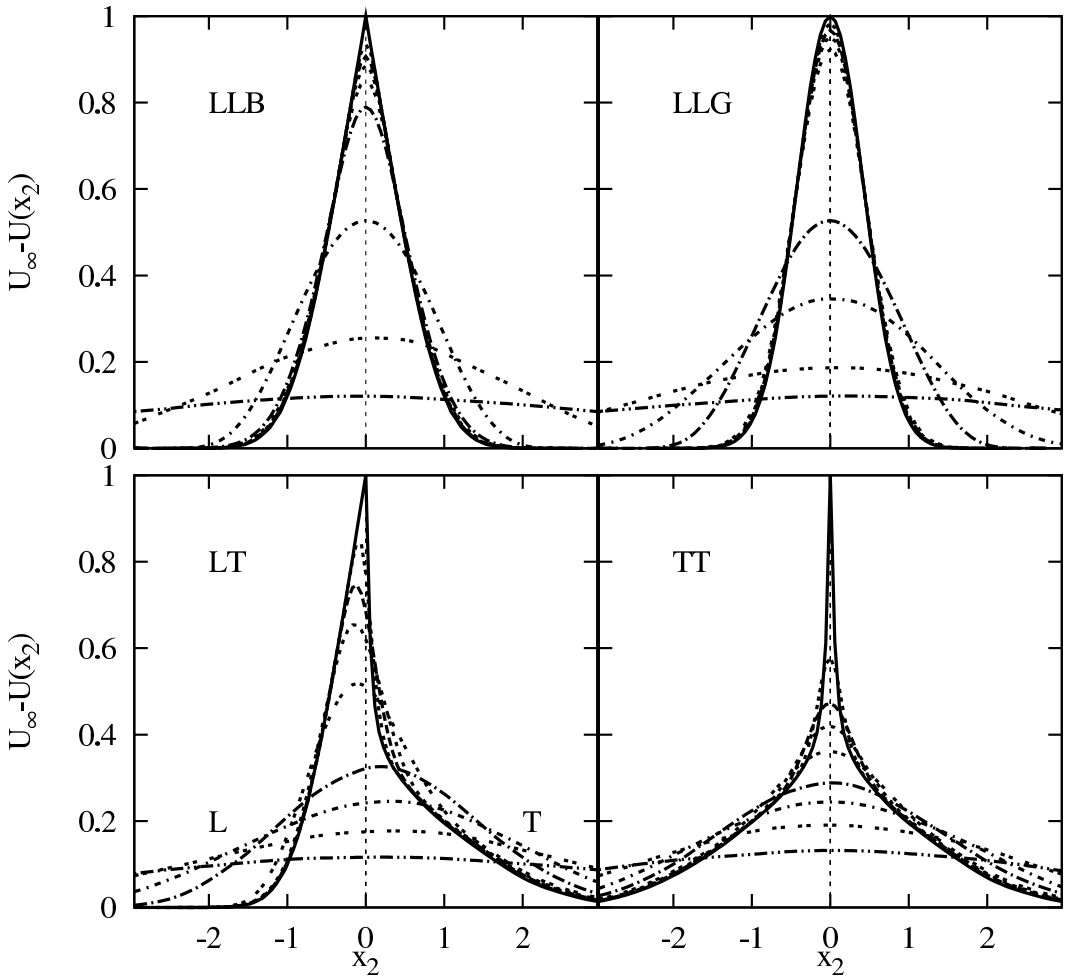

Figure 4.2: Evolution of the mean streamwise velocity profile. Clockwise from top left: LLB, LLG, TT and LT at $t = 0$, 4, 9, 13, 22, 44, 64, 108 and 234 (from top to bottom along the centerline).

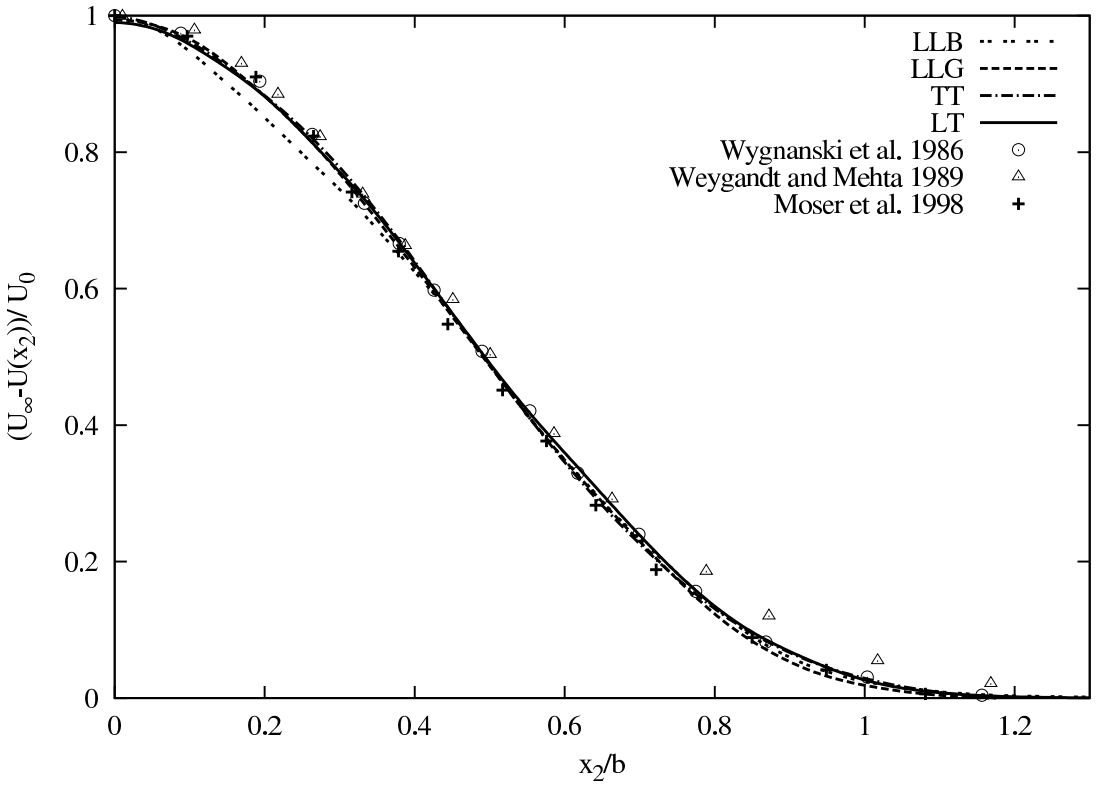

Figure 4.3: Normalized mean streamwise velocity profiles in the far wake (at normalized time 250) with symmetry about the centerplane.

peak mean shear monotonically decreases. In LLB at $t = 0$, the only change of curvature of the double Blasius velocity profile occurs at the centerplane and is indeterminate as the profile is not smooth at $x_2 = 0$. Through viscous decay (cross-diffusion) at the centerplane, the profile becomes smooth in the near wake of LLB, as experimentally observed by Sato & Kuriki (1961). The locations of the change of curvature on both sides of the LLB centerplane are continually displaced outward reaching a value of $x_2 = \pm 0.40$ immediately preceding the start of transition at around $tU_d^2/\dot{m} = 60$. The maximal shear remains approximately 40 % lower in LLB than in LLG. During transition of these two cases (roughly corresponding to time= $[40 - 55]$ (LLG) and $[60 - 80]$ (LLB)) the mean velocity

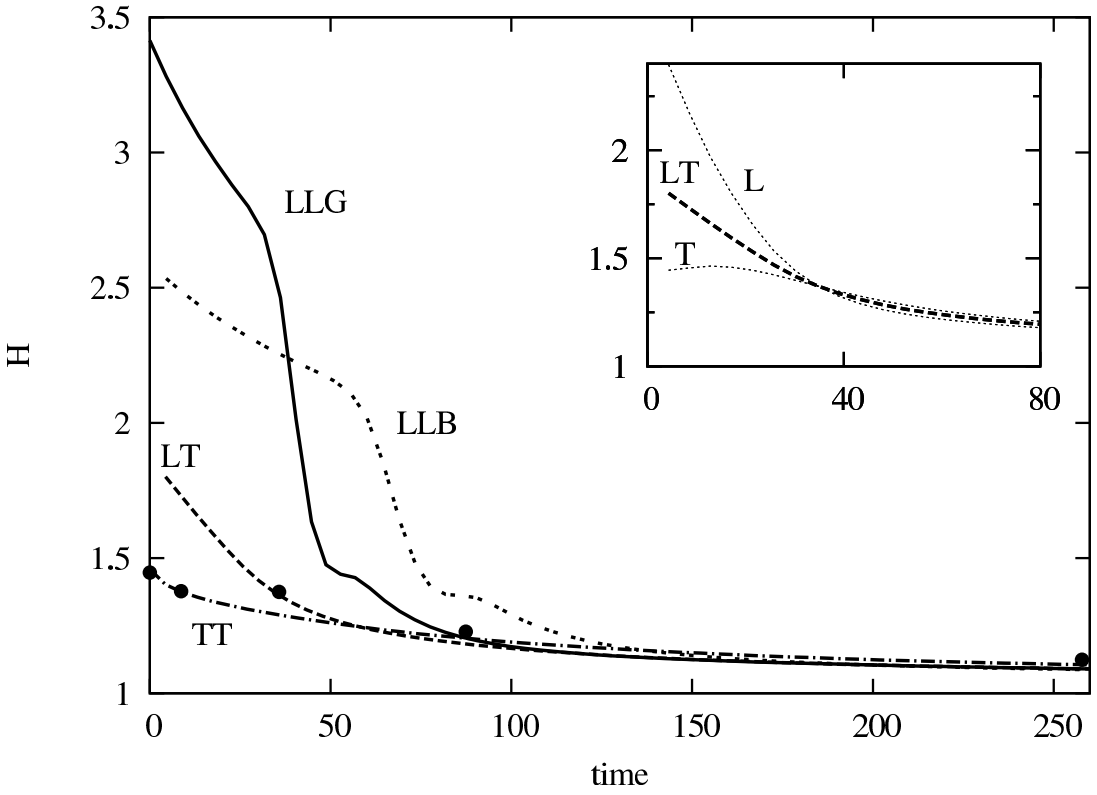

Figure 4.4: Evolution of the wake shape factor. The results compare favorably to experiments by Chevray and Kovasznay (1969) (circle), conducted in a similar setup and Re. The inset focuses on LT (thick dashed line, shape factor of entire profile); the individual shape factors of the laminar and turbulent half-wake (computed from $x_2 = 0$) are compared.

profiles undergo a rapid change, particularly at the outer edge, caused by the emergence of the transitional structures (discussed in §4.4.2); eventually both laminar ICs reach a universal profile, as seen at $t = 234$ in figure 4.2.

The centerline defect of TT undergoes a rapid change (in time) in the near field which is the result of a strong mean velocity gradient and an enhanced momentum transfer by turbulent fluctuations. To quantify the mean flow asymmetry in LT, we define a metric as:

$$AS(t) = \frac{\int_{-\infty}^{\infty} \left(U\left(x_2,t\right) - U\left(-x_2,t\right)\right)^2 dx_2}{\int_{-\infty}^{\infty} (U_\infty - U(x_2,t))^2 dx_2}, \tag{4.1}$$

where the metric is null for symmetric and unitary for perfectly anti-symmetric velocity profiles. The initial asymmetry of LT is 0.64 and monotonically decreases to a plateau at 0.0196 ± 0.0025 from $t = 150$; the value corresponds to the mean AS, along with the maximum deviation from the mean in the far wake. A similar far wake value is also found for the initially turbulent wake (TT: 0.014±0.01). The transitioning wakes have a more symmetric instantaneous velocity profile (AS of LLG=0.0025 $\pm 3.0E-5$; LLB= 0.002 $\pm 1.0E-5$). Interestingly, the location of maximum defect in the near field of LT shifts away from the centerline toward the laminar side, as previously noted by Thomas & Liu (2004), reaching a maximum (at around $t = 12$) of 0.38 when normalized by the wake half-width. After the transition of the laminar side, the maximum velocity defect gets pushed back towards the centerplane and overshoots onto the turbulent side between $t = [32 - 100]$. The phenomenological explanation of the shift of the maximal defect is found in the differing rates of momentum transfer in the turbulent and laminar half-wakes. On the turbulent side of LT, the principal mechanism of momentum transfer is through the turbulent fluctuations; the viscous stresses are relatively negligible. The fine-scale turbulent mixing reduces the gradient of the mean flow by transferring inward the high momentum fluid of the outer wake, resulting in an acceleration near the centerline (and a deceleration of the outer wake). The high cross-wake momentum transfer is enhanced by the strong gradient near the centerplane of the turbulent side. Prior to transition of the laminar side of LT, turbulent stresses are nonexistent; therefore, the momentum can only be transferred through lower viscous stresses. Hence, the acceleration of the mean flow (about the centerplane) is lower on the laminar than on the turbulent side. Consequently, the location of the maximum defect shifts away from the centerplane towards the laminar side. From $t = 32$, there is a slight secondary shift (under 0.1 when normalized by the wake half-width) of the maximum defect onto the turbulent side (see LT in figure 4.2 at

t =44 and 64). Since the turbulent mixing reduces the shear, the magnitude of the laminar side shear eventually surpasses that of the turbulent side. The concomitant stronger TKE production (discussed in §4.4.3) and cross-wake momentum transfer of the initially laminar half-wake causes the maximal defect to be pushed back over to the turbulent side. After this secondary shift, the maximum defect asymptotically returns toward the centerplane. No tertiary overshoot (back onto the laminar side) is possible as there are no mechanisms for preferential steepening of the mean flow gradient or TKE production on either side. Eventually, the initial asymmetry of the mean profile is lost (figure 4.2). The far wake symmetry of the mean flow profile implies an equilibrium of momentum transfer across the centerplane; presumably, large-scale structures may be responsible for this far field equilibrium. The time-averaged mean velocity profiles in the far field agree with published experimental and numerical data; see figure 4.3.

Wake shape factor. The identical nature of the far wake profile is further evidenced by the good collapse of the wake shape factor (figure 4.4) defined, as in the boundary layer, by the ratio of displacement to momentum thickness, $H = \delta^*/\theta$. The physical and mathematical interpretations of the shape factor parameters are fully analogous to the boundary layer and identical to the definition in Chevray & Kovasznay (1969). The wake displacement thickness is: $\delta^* = \int_{-\infty}^{\infty} \left(1 - U\left(x_2\right)/U_\infty\right) dx_2$; and the momentum thickness is: $\theta = \int_{-\infty}^{\infty} \frac{U(x_2)}{U_\infty}\left(1 - \frac{U(x_2)}{U_\infty}\right) dx_2$. Despite the very different initial conditions, all cases asymptotically tend towards $H \approx 1.0$ (Chevray & Kovasznay, 1969), confirming the invariance of the mean profile to the initial conditions as suggested by Wygnanski *et al.* (1986). The shape factor of LLB initially starts from the laminar boundary layer value of 2.59; the Gaussian velocity profile has a higher initial value (about 3.4). As for the boundary layer, the change in the shape factor is an unambiguous indicator of the transitional state of the flow. In LLG and LLB the onset of transition can be seen in the abrupt drops of the

slope at $t = 40$ and 60 respectively. The wake formed by the turbulent boundary layers (TT) initially has a H of 1.45 (Wu & Moin, 2010) and agrees - over the entire evolution - with experimental data of Chevray & Kovasznay (1969) for a turbulent flat-plate wake at $Re_\theta = 1580$. For LT, the H of each half-wake initially starts at 2.59 (Blasius layer) and 1.45 (turbulent layer); the H for the half-wakes of LT is defined as the ratio of displacement to momentum thickness computed from the initial centerplane ($x_2 = 0$). The steep drop in the shape factor of the laminar side implies a very rapid transition. As the drop of H is greater on the laminar side, the shape factor of each side (L and T) cross-over at $t = 35$ (inset in figure 4.4). The physical interpretation of the cross-over is ambiguous given our definition of the half-wake shape factor based on the initial centerplane ($x_2 = 0$), as opposed to the minimum velocity defect. Note that H of either side of LT follows a smooth monotonic progression in contrast to the abrupt drop observed in LLB and LLG during transition. The H of both half-wakes eventually collapse onto a single curve from about $t = 150$.

Wake spreading. Simplification of the governing equations shows that the lateral length scale (wake half-width) increases and the velocity scale (maximum defect) decreases as the square root of time (or distance in spatially evolving flows) assuming a self-similar evolution (see e.g. Lesieur (1997); Moser *et al.* (1998)). This scaling behavior has been proven for different generating bodies (Wygnanski *et al.*, 1986), types of imposed initial forcing (Moser *et al.*, 1998), and even compressibility (Bonnet *et al.*, 1984; Bonnet & Chaput, 1986). Figure 4.5 shows the evolution of the square of the wake half-width; the evolution of $1/U_0^2$ is very similar (not shown). The spread rate, $d\,b^2/d\,t$, is the slope which minimizes the L_2-norm of $b^2 U_d/\dot{m}$ as function of the non-dimensional time in the far wake. We recall that the wake half-width is defined as the total width of the wake at the location of half the maximum defect: $U_0/2 = U_\infty - U\,(x_2 = b/2)$. The spread rate

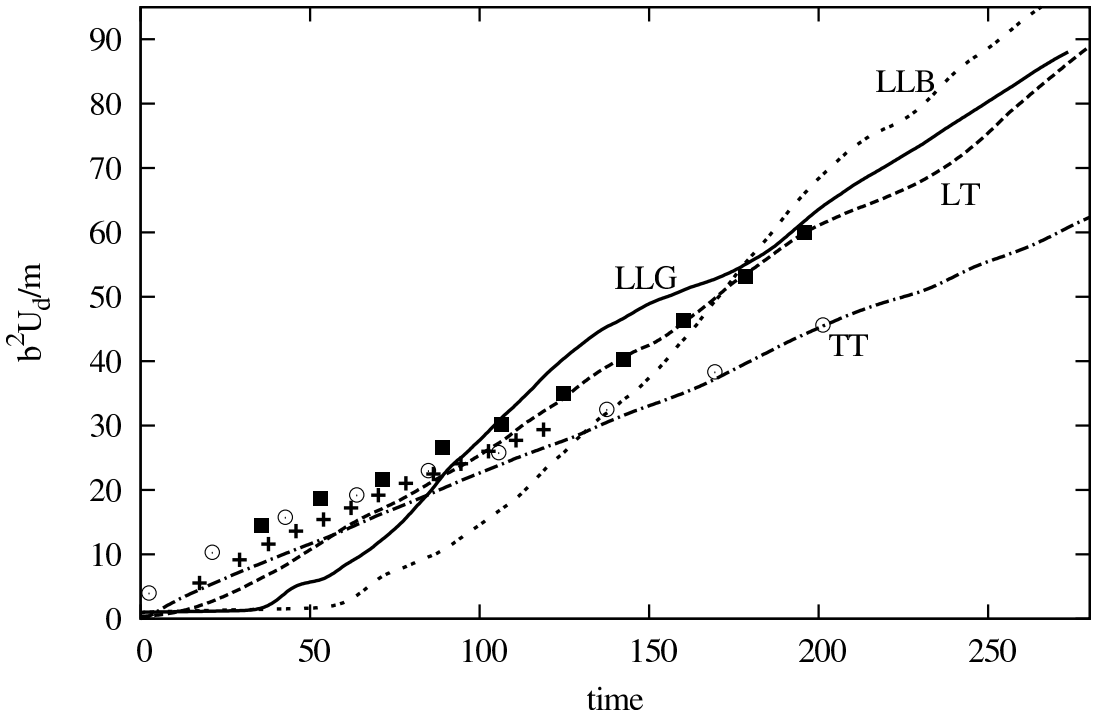

Figure 4.5: Evolution of the wake spreading. Thomas and Liu 2004: asymmetric wake (square), symmetric wake (circle) and Moser et al. 1998 (plus).

shows many differences among all four cases; the 48 % relative variation is comparable to that observed by Wygnanski *et al.* (1986) for wakes behind various generating bluff objects. The LLB and LLG wakes have the highest spread rate of all the cases studied: 0.36 and 0.34 respectively. The transitioning wakes undergo an early slow viscous spreading whence the primary anti-symmetric instability modes develop. As transition occurs, there is an increased three-dimensionality as rollers form and pair (see §4.4.2 for more details on transition). The concomitant transitional entrainment (in a mean flow sense, distinct from true entrainment, discussed later) for the LLB and LLG rapidly increases the spread rate (between $tU_d^2/\dot{m} = [65 - 150]$ (LLG) and $[100 - 200]$ (LLB)) before eventually levelling off to a constant state in the far wake. Some unexpected differences in the spread rate of

the two laminar wakes are observed - particularly in the near and intermediate regions - despite similar transitional characteristics such as the size and separation of rollers. The cause of this difference in the spread rate is unclear.

The TT wake has the lowest spread rate of all cases with 0.22, agreeing with the previous DNS (Moser *et al.*, 1998) ; experimental work by Thomas & Liu (2004) found 0.21 for a symmetric turbulent splitter-plate wake. We do note a slight offset of the curves in the near wake which is probably attributable to the minor differences in the setup, namely with regards to the Reynolds number and initial conditions. In contrast to the laminar wakes, where the pairing of coherent structures is a strong contributor to the lateral growth (as in the mixing layer and near wake (e.g. Winant & Browand, 1974; Ho & Huerre, 1984)), TT reaches a constant spread rate very early in the evolution of the flow. This would imply that the entrainment caused by the large-scale structures in TT and the turbulent boundary layer are very similar. The LT spread rate is intermediate between the laminar and turbulent cases at 0.34 which is slightly greater than the experimental value of 0.31 found by Thomas & Liu (2004); although the data collapse in the far wake. The trend in the spread rates for initially laminar and turbulent flows is in general agreement with previous studies in other types of flows, e.g. Hussain & Clark (1977).

4.4.2 Path to turbulence

The discussion of the transitional process is unavoidable to understand the memory effects in free shear flows. Admittedly, the temporal nature of our simulations (see limitations discussed in §4.3) limits the generality of our findings. Therefore, care should be used when inferring the structural make-up of experimental or spatially evolving transitional wakes from our results.

Freestream transition. The near wake evolution of the $\langle u_1 u_1 \rangle$ profiles is shown in

figure 4.6. The double peak, characteristic for the entire evolution for TT (and most of LT), changes into a single peak on the centerplane during the transition of the initially laminar wakes (LLB and LLG). The double peak of LLB and LLG is only regained in the fully developed far wake (see far wake profiles in figure 4.6); similar to the observations by Maekawa *et al.* (1992) for two-dimensional spatially evolving wakes. To gain insight into the modification of the streamwise Reynolds stress profile, the structural features of transition are investigated. Figure 4.8 shows slices of spanwise vorticity of LLB - nearly identical qualitative features are found in LLG (not shown): e.g. wavelength, emergence of structures, transitional mechanism. The spanwise coherent rollers, emerging from the two-dimensional anti-symmetric linear instability modes, can be seen in the first two panels. These rollers develop secondary instability along the span from the growth of a sub-harmonic mode (Lasheras & Meiburg, 1990) or through core dynamics (Schoppa *et al.*, 1995). The secondary instability kinks the rollers which connect with neighboring structures (figure 4.9 (top)) forming a distinctive pattern of connected rollers (Cimbala *et al.*, 1988; Lasheras & Meiburg, 1990; Julien *et al.*, 2003). The connection between the rollers is the first evidence of large-scale three-dimensionality in the wake. As these structures connect, the larger structures are located at the outer-edge of the wake, while smaller structures migrate towards the centerplane. The drifting of the smaller structures towards the centerplane at $t = 74$, in figure 4.8, is responsible for the formation of a single peak in the $\langle u_1 u_1 \rangle$ profile and the collapse of the $\langle u_1 u_2 \rangle$ profile, figure 4.7. Because of the different convection speeds of the structures, the rollers eventually pair as seen in multiple locations in panels $t = 87$ and 97 in figure 4.8. Eventually, the spanwise coherent rollers form a secondary, anti-symmetric Karman vortex street with the distinctive double peaks in the streamwise intensity profile. In addition to pairing, rib-like structures develop in the high strain regions between the transitional rollers, see figure 4.9 (bottom), as previously

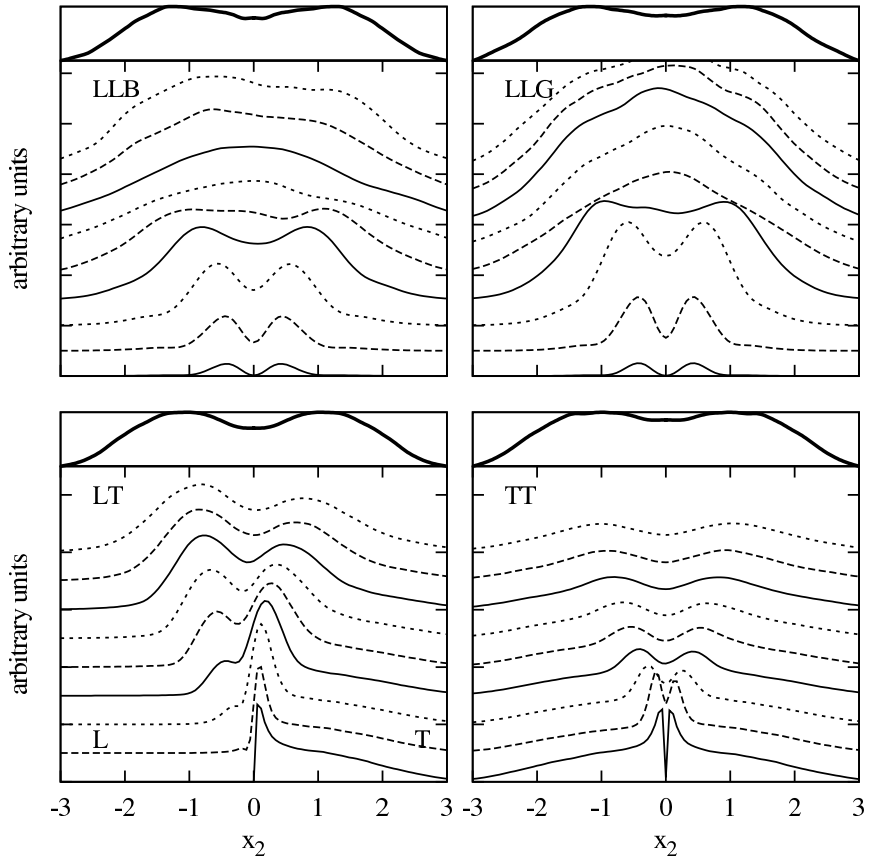

Figure 4.6: Profiles of $\langle u_1 u_1 \rangle$ in the transitional/near wake, identical scale used in all panels. Top line: comparative far wake averaged profile (on a different scale). LLB at times t =55, 59, 63, 67, 71, 75, 79 , 83, 87 and 91 (increasing from bottom to top); for LLG at t =32, 36, 40, 44, 48, 52, 56, 60, 64 and 68; for LT and TT at t =0, 4, 8, 12, 16, 20, 24, 28, 32 and 36.

observed in many experimental and numerical works.

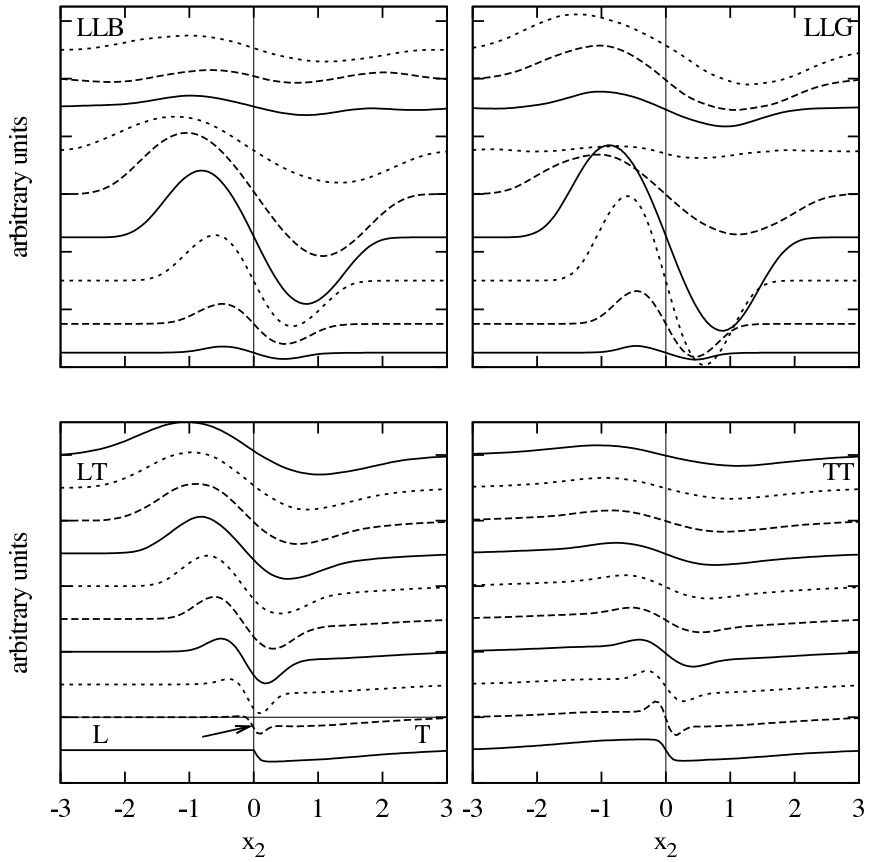

Figure 4.7: Profiles of $\langle u_1 u_2 \rangle$ in the transitional/near wake. LLB at times (increasing from bottom to top) t =55, 59, 63, 67, 71, 75, 79, 83, 87 and 91; LLG at t =32, 36, 40, 44, 48,52, 56, 60, 64 and 68; LT and TT at t =0, 4, 8, 12, 16, 20, 24, 28, 32, 36 and 40. Identical scale used in all panels.

Bypass transition in asymmetric wakes. Very little is known about the path to turbulence of the laminar side of an asymmetric wake. Do turbulent fluctuations simply "diffuse" across the centerplane to the laminar side? Does the laminar side undergo a transitional process with the exponential growth of Kelvin-Helmholtz instability modes? If so, what are the principal structures, if any? Some information can be inferred from statistics presented in the previous paragraphs. The wake shape factor reveals a very rapid onset of transition (figure 4.4), while the approximately constant spread rate (figure

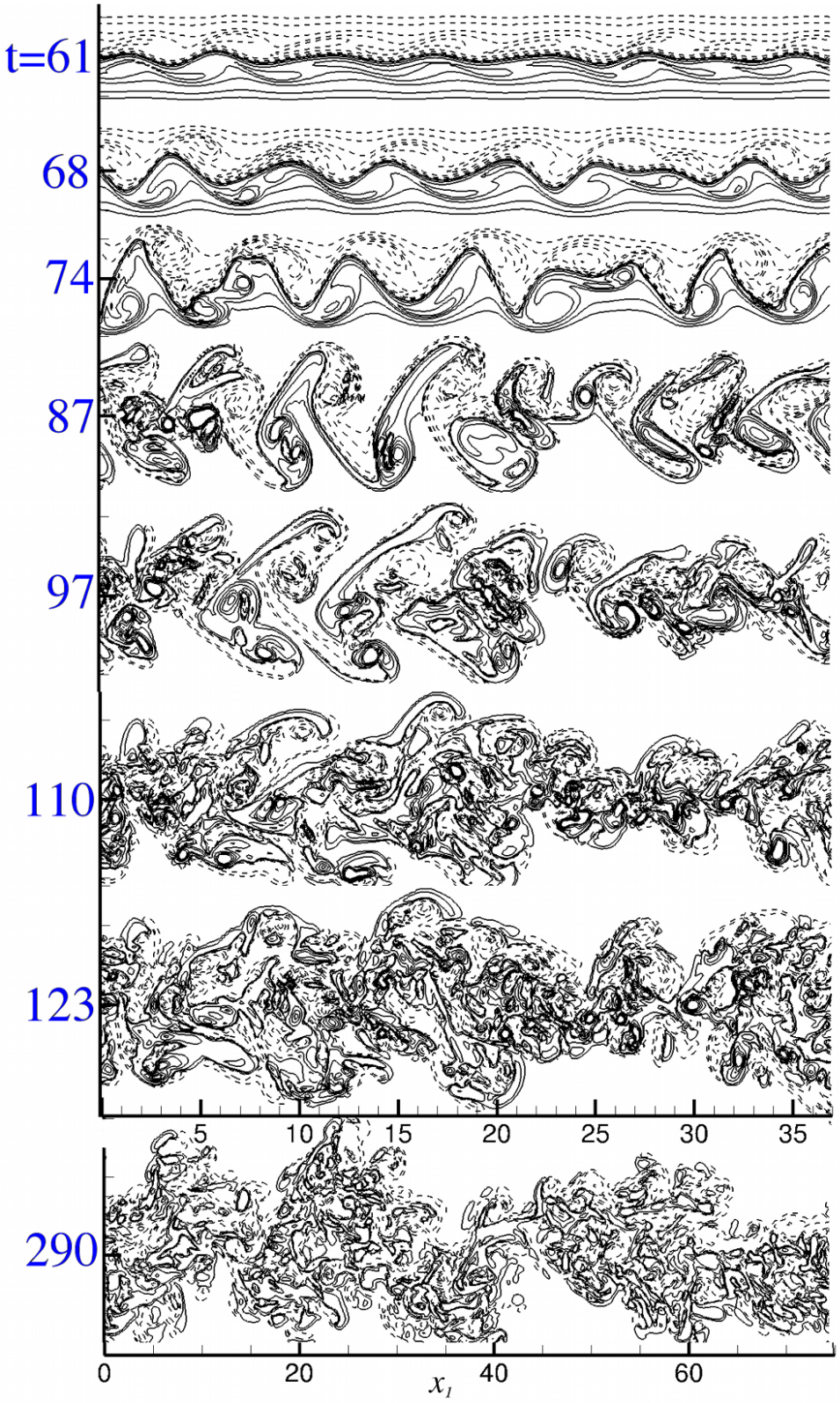

Figure 4.8: Pairing of the vortical structures in LLB. The slice (at $x_3 = L_z/2$) of spanwise vorticity contours at $\omega_3 = \pm 0.01, 0.05, 0.25, 0.5, 0.75$ and 1.0 (dashed contour - negative vorticity).

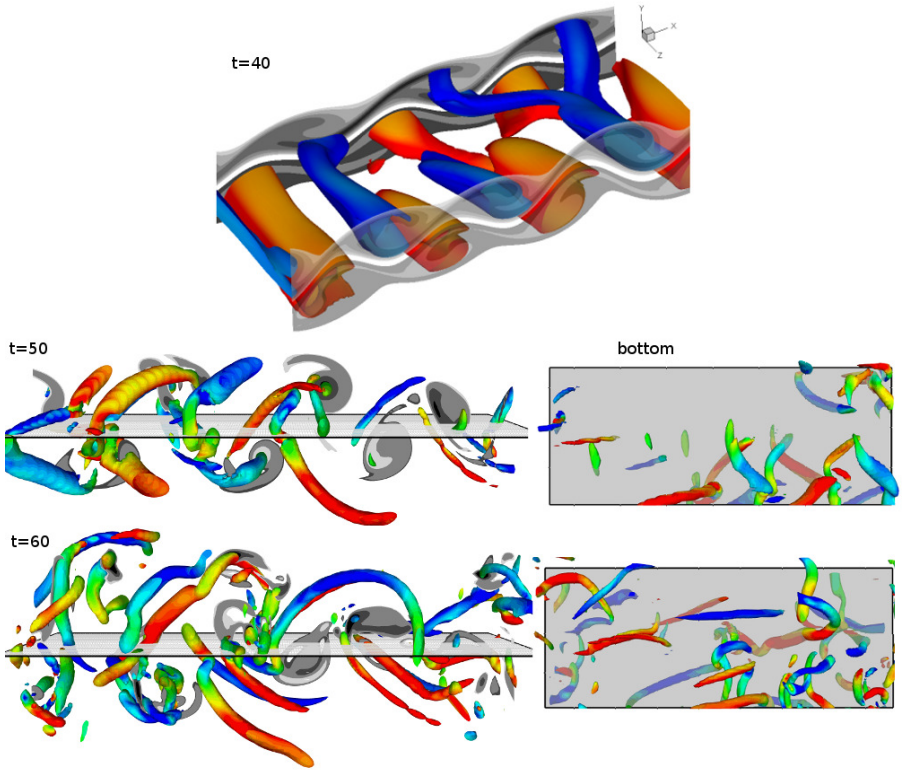

Figure 4.9: Transitional structures in LLG at $t = 40$, 50 and 60. The iso-surfaces of λ_2 are colored by spanwise vorticity (ω_3) in top figure and streamwise vorticity (ω_1) in the other figures. A slice of spanwise vorticity is overlaid in grayscale. Partial domain: $L_x/6$ and $L_z/5$

4.5) implies the absence of a predominant structural pairing as seen in the freestream transitioning wakes. The laminar side peak of the $\langle u_1 u_1 \rangle$ profile (figure 4.6), along with the rapid increase of the maximal shear stress component $\langle u_1 u_2 \rangle$ (figures 4.7 and 4.14), may hint at the emergence of transitional structures.

At $t = 6$, the slice of spanwise vorticity of LT, in figure 4.10, shows a clear perturbation of the Blasius boundary layer caused by the proximal disturbance of the turbulent half-wake. Along the centerplane, a slight negative Reynolds shear stress develops (without

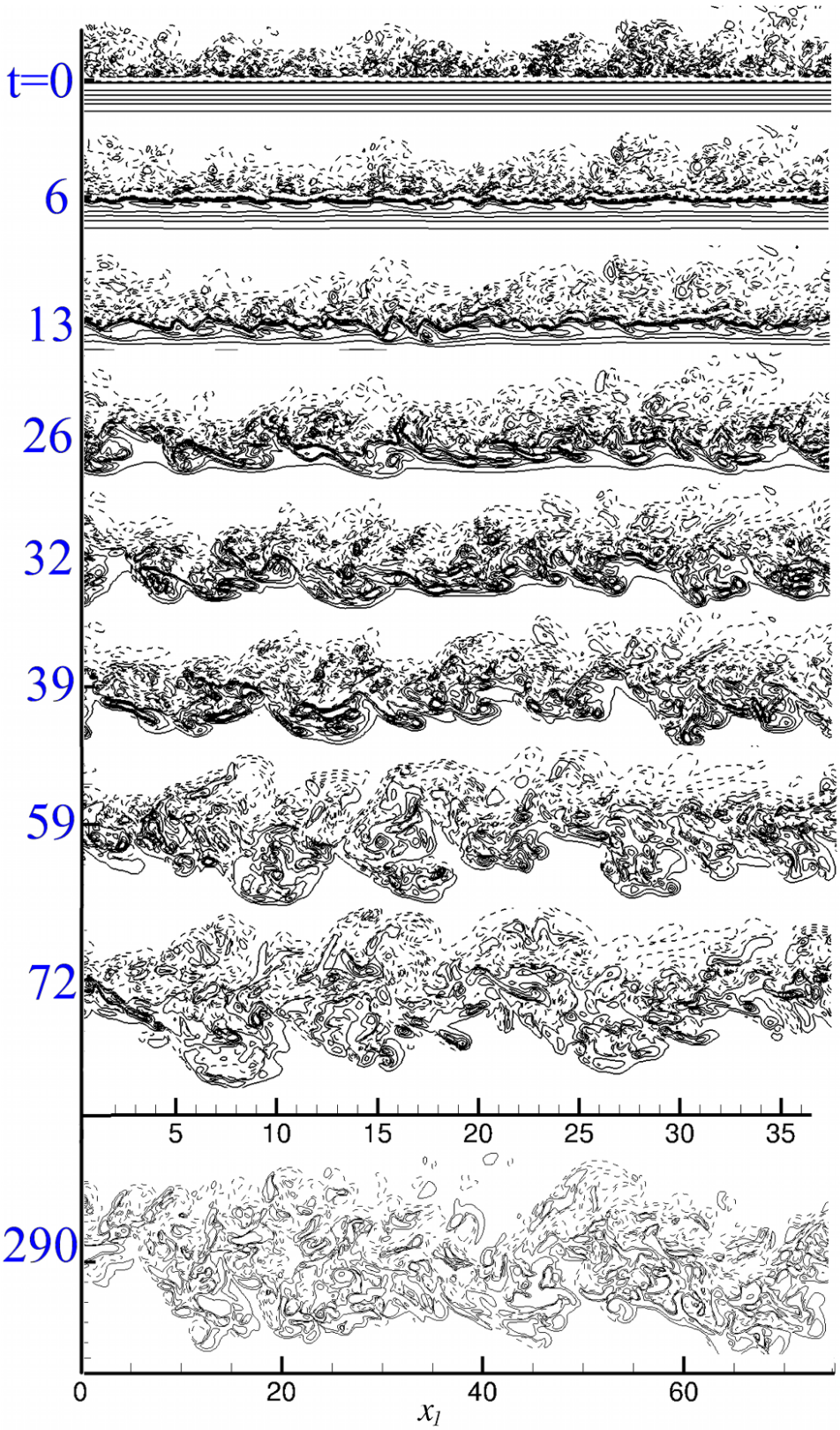

Figure 4.10: Pairing of the vortical structures in LT; spanwise vorticity at $\omega_3 = \pm 0.01, 0.05, 0.25, 0.5, 0.75$ and 1.0 (dashed contour - negative vorticity).

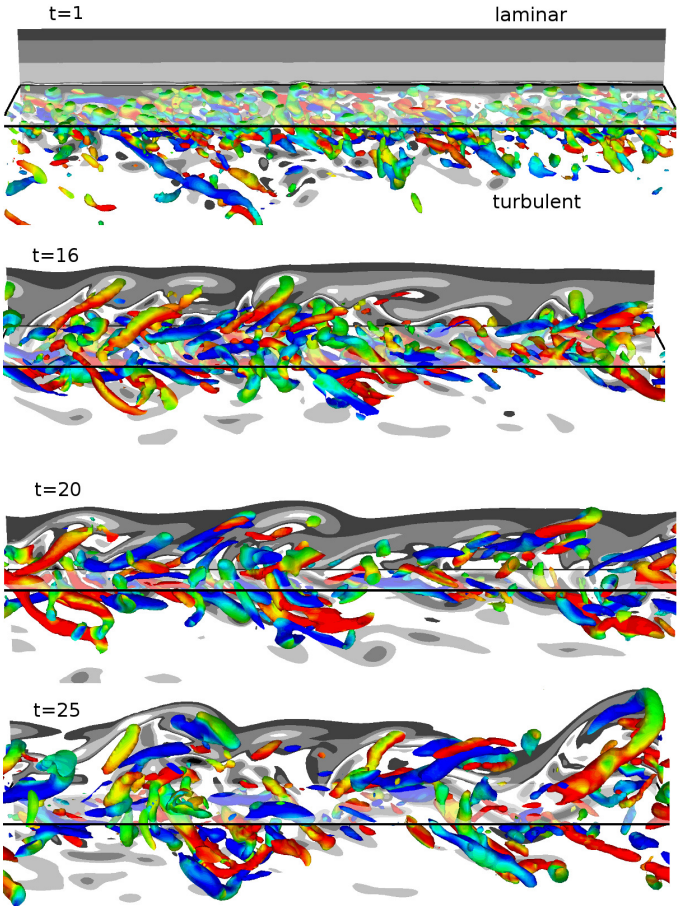

Figure 4.11: Transitional structures in LT at $t = 1$, 16, 20 and 25. Partial domain presented $L_x/6$ and $L_z/8$. The iso-surfaces of λ_2 are colored by streamwise vorticity (ω_1).

a distinctive positive peak on the laminar side), see arrow in figure 4.7 at $t = 4$. The negative Reynolds shear stress at $x_2 = 0$ is caused by the sweeping motion of the coherent structures within the turbulent boundary layer which is unobstructed by a non-slip wall at the centerplane. A positive peak in the $\langle u_1 u_2 \rangle$ profile emerges on the laminar side from $t = 8$ as coherent structures start to form during transition. The transitional structures of the laminar half-wake result in a larger Reynolds shear stress peak compared to the

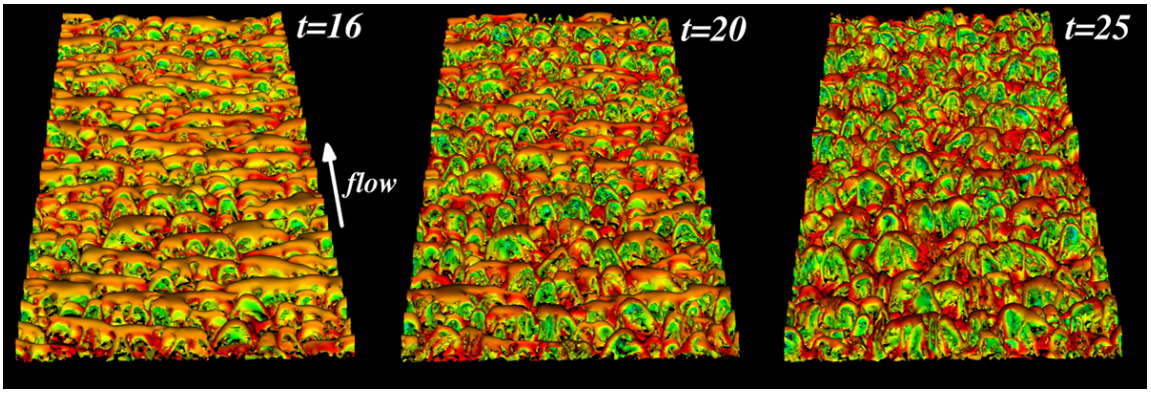

Figure 4.12: Transitional structures of the laminar side of LT. The structures are identified by the Q-criteria iso-surface (0.002) and colored by the streamwise velocity.

initially turbulent side (from time $t = 24$, figure 4.7); this order is maintained until a far wake equilibrium is reached. The initially small perturbation wavelength, λ (not to be confused with the Taylor micro-scale briefly discussed in §4.3), at $t = 6$ and 13 along the centerplane ($\lambda \approx 2$), gives rise to larger structures ($\lambda \approx \mathcal{O}(10)$ with positive spanwise vorticity) at $t = 26$ and 32 on the initially laminar side. The cores of these structures are nearly parallel to the centerplane (into the page in figure 4.10) but quickly develop kinks through the proximal disturbances of the turbulent half-wake. The kinks result in the emergence of loop-like structures in figure 4.11 which are organized with surprising spanwise alignment (see figure 4.12). The outwardly directed kinks, which form the heads, get advected faster than the legs because of the higher mean velocity of the outer wake and result in the formation of distinctive arrays of spanwise-aligned horseshoe-type vortices, seen in figure 4.22 at $t = 50$ (laminar side). The organized rows of horseshoe structures on the laminar side of LT are central to the transitional process as the spanwise fluctuations, u_3, remain a predominant component of the total TKE during transition (about half of TKE in LT; less than a fifth in LLG and LLB). The importance of the spanwise fluctuations

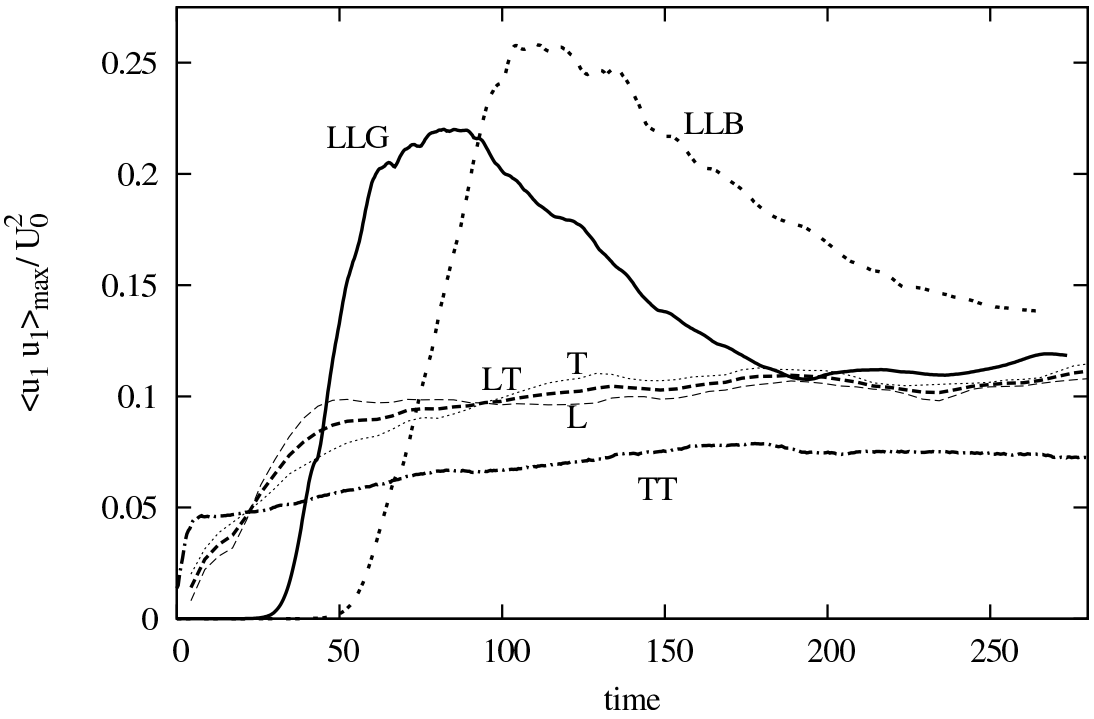

Figure 4.13: Evolution of the maximum normalized streamwise velocity fluctuation. Along with the average of both sides of the wake, the maximum on the laminar (L) and turbulent (T) sides of LT are shown.

(along with the short primary spanwise wavelength associated with $\langle u_3 u_3 \rangle$) suggests that the mid-size inclined structures play a central role in the transitional mechanism.

The organization and periodicity of the structures in LT recall some of the main features of a Kelvin-Helmholtz-type transition. But unlike LLG and LLB, the developing structures on the laminar side do not undergo a slow exponential growth; instead, they rapidly emerge in the near wake from a finite as opposed to an infinitesimal perturbation. The proximal disturbances of the turbulent half-wake cause the laminar side to bypass the typical Kelvin-Helmholtz transition which significantly expedites the transition process. In many ways, the process is analogous to the finite freestream perturbation of the boundary layer simulation in Wu & Moin (2009) which bypasses the Tollmien-Schlichting waves.

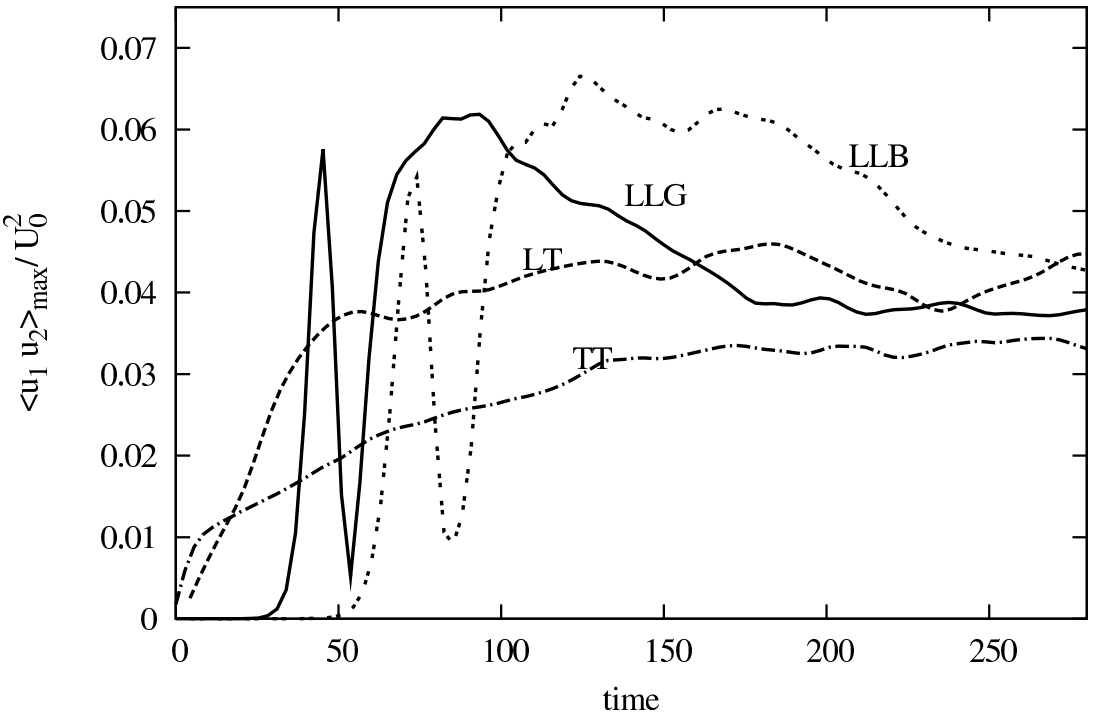

Figure 4.14: Evolution of the maximum Reynolds shear stress $\langle u_1 u_2 \rangle_{max} / U_0^2$.

4.4.3 Turbulence statistics and energy budgets

Evolution of Reynolds stresses. The evolution of the peak value of $\langle u_1 u_1 \rangle_{max} / U_0^2$ is shown in figure 4.13. The peak stresses are calculated by fitting a third-order polynomial function over 7 points the location of the maximum Reynolds stress. The peak values on both sides of the centerplane are averaged and normalized by the square of the maximum velocity defect. After a pre-transitional period characterized by very low turbulence intensity, the LLB and LLG fluctuations rapidly reach their highest values which correspond to the end of the pairing of the main transitional structures. Thereafter, the curves gradually settle down to an asymptotic state at about half of the maximum transitional values. The difference in the peak value between LLG and LLB is rather surprising particularly

considering the nearly identical evolution of the Reynolds shear stress, $\langle u_1 u_2 \rangle_{max} / U_0^2$, (figure 4.14) during the early stages of transition. Although, without normalization based on centerline velocity defect, the peak values of $\langle u_1 u_1 \rangle_{max}$ for LLG and LLB are inverted (0.027 and 0.020 respectively), suggesting that the variation in the maximal peak value may simply be a consequence of the delayed transition of LLB (as U_0 becomes smaller as the flow evolves).

The LT and TT wakes do not show a clear peak in the streamwise fluctuations or a distinctive change in the slope of the spread rate, which suggests, as noted previously, that these wakes do not undergo a characteristic structural pairing. This observation is further evidenced by a monotonic increase of the maximal Reynolds shear stress (figure 4.14) until a far field plateau is reached. The steep increase for TT in the near wake is primarily attributable to a rapid decay of the centerline defect (the normalizing term) and not to a marked increase of the streamwise fluctuations. A similar progression for LT has also been observed in an asymmetric laminar/turbulent mixing layer by Hussain & Zedan (1978*a*). The final self-similar value for $\langle u_1 u_1 \rangle_{max} / U_0^2$ ranges between 0.08 (in the TT wake) and 0.11 (in the LLG wake). The asymptotic values of the streamwise - and the shear Reynolds stresses - indeed depend on the initial conditions, as seen in Hussain and Zedan.

Normalized far wake statistics. We averaged the turbulence statistics in the homogeneous directions (x_1 and x_3) and over the approximate self-similar region (details follow) using snapshots at time intervals of $\Delta t \approx 4$ (between 18 and 36 snapshots within the self-similar domain). The sample size is enhanced by using the centerplane symmetry (also for LT in the far wake), as we effectively double our sample size and smooth out the higher-order statistics. The normalized Reynolds stresses fall within the scatter of published data on planar wakes. A good agreement of LT is obtained with the (zero-pressure gradient) asymmetric wake experiment by Thomas & Liu (2004) while LLG compares favorably with

the far wake data of Weygandt & Mehta (1989). Interestingly, the peaks of the streamwise fluctuations for LLG an LT are nearly equal, yet there is about a 10 % difference at the centerplane suggesting different structural organizations in the far wakes (discussed in §4.2). Slight disagreement was noted in $\langle u_2 u_2 \rangle / U_0^2$ which is caused by the continually increasing normalized cross-wake fluctuations observed in Moser *et al.* (1998) and Weygandt & Mehta (1989). Had their computational/experimental domain size permitted, a higher peak value of $\langle u_2 u_2 \rangle / U_0^2$ would presumably have been achieved. Similar to the lateral spread rate (in figure 4.5), TT has the lowest and LLG the highest turbulence intensity in the self-similar region (LLB did not reach a self-similar state within our computational domain). This order is maintained in all the second-order statistics apart from $\langle u_2 u_2 \rangle$. The high cross-wake velocity fluctuations in LT and TT are attributable to different large-scale organized motion in the far wake (discussed in section 4.5). The multiple approximate self-similar states show a relative variation of up to 40 % in the statistics. Obviously, by modifying the scaling parameters, as suggested by Moser *et al.* (1998), to include a non-dimensional factor to account for the spread rate, the variation among initial conditions is reduced. But, if the "universality" of the turbulence statistics is tied to the lateral spread rate, then there is a fundamental inconsistency which arises as the spread rate is intrinsically linked to the evolution of the wake. It therefore begs the question: "what dictates the multiple spread rates in the wake?". We contend that understanding the structural plurality will help us understand the multiple self-similar states in the wake.

Turbulent Kinetic Energy Budgets. The evolution of the integrated production and dissipation terms are shown in figure 4.16. These terms are computed by integrating the production and dissipation profiles at various temporal evolutions of the wake. The production terms of the transitioning wakes show two distinct maxima (at $t = 41$ and 61

for LLG) and one local minimum (at $t = 53$ in LLG). The first maximum at $t = 41$ represents the saturation of the principal mode; at this time, the rollers start to connect. The production sharply decreases as the rollers meander in the cross-wake direction through asymmetric mutual induction of neighboring rollers. The meandering results in the collapse of the $\langle u_1 u_2 \rangle$ profile (figures 4.7 and 4.14) and a concomitant drop in the integrated turbulence production. The local minimum (at $t = 53$ (LLG) and $t = 84$ (LLB)) corresponds to the average location of vortex pairing; analogous inferences were made in the structural pairing in a cylindrical jet (Zaman & Hussain, 1980). The second production peak occurs simultaneously with the peak of the normalized streamwise velocity fluctuation in figure 4.13. The integrated production in LT reveals that the coherent structures form, as evidenced by the increased production and dissipation during transition, but pairing does not occur. The peak production on laminar and turbulent sides do not occur simultaneously (inset of figure 4.16); the laminar side peak is delayed as the spanwise aligned vortical structures form. For TT, the integrated production and dissipation, not surprisingly, monotonically decrease (in magnitude) while the energy budget profiles preserve their overall form; see figure 4.17 ($t = 30$ and $t = 45$).

In the approximate self-similar region, the TKE budget terms for all wakes reach a self-preserving state; the statistics (normalized by U_0^3/b) are shown in figure 4.17. The profiles are qualitatively similar to Moser *et al.* (1998), but the peak values are greater here (about twice). As in Moser *et al.*, the peak production in all wakes (figure 4.18) occurs slightly below the wake half-width ($x_2 \approx 0.45b$). Although the general trends are qualitatively similar among the different IC, there is up to a 50 % variation in the normalized budget terms, particularly for the TKE dissipation. The peak production has a 25 % relative variation among the cases. The location of the maximum and minimum of the pressure-transport and dissipation profiles are independent of the initial conditions of the wake.

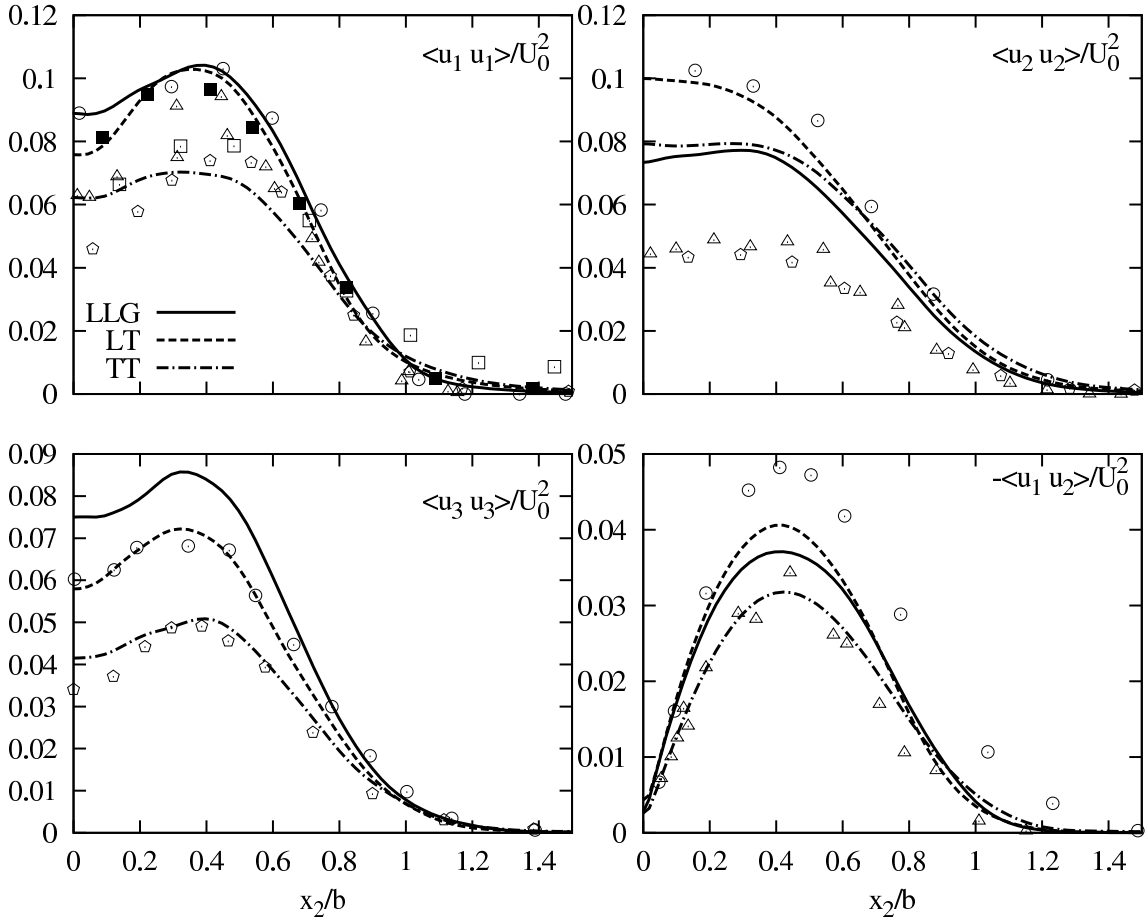

Figure 4.15: Second-order turbulence statistics in the approximate self-similar region. Clockwise from top-left = $\langle u_1 u_1 \rangle$, $\langle u_2 u_2 \rangle$,$-\langle u_1 u_2 \rangle$ and $\langle u_3 u_3 \rangle$ (quantities normalized by U_0^2). DNS data: LT (dashed), TT (dashed-dot) and LLG (full). Comparative data: Moser *et al.* 1998 (pentagone), Weygandt and Mehta 1989 (circle), Thomas and Liu 2004: asymmetric (full square), symmetric (empty square) and Chevray and Kovasznay 1969 (triangle).

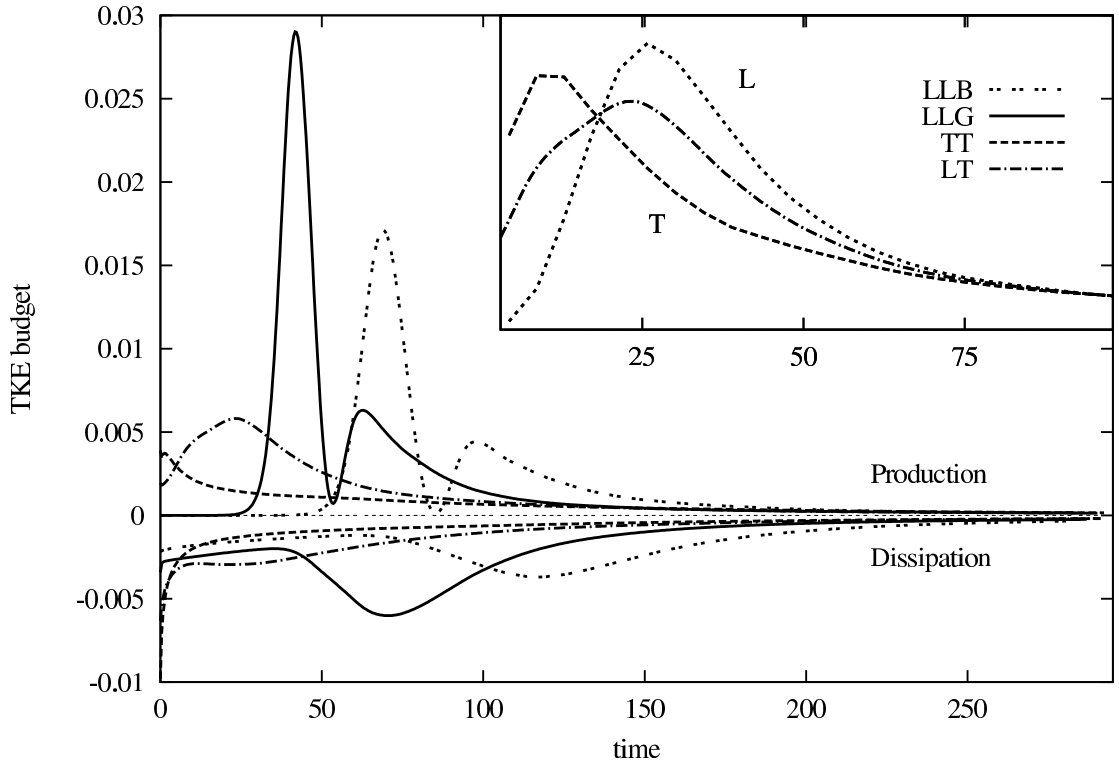

Figure 4.16: Evolution of integrated production and dissipation. Inset: production of each side of LT is compared with half the total integrated production of LT (dash-dotted line).

Defining self-similarity states. Insisting upon a complete dynamic-similarity in the far wake might preclude any finite wake simulation (or even a finite experimental setup for that matter). Instead, we adopt a pragmatic definition by Narasimha & Prabhu (1972) which removes some of the semantic ambiguity. We define approximate self-similarity in a turbulent wake flow as: "a region in which the distributions of mean velocity and the turbulent stresses exhibit similarity with essentially the same scale". From this definition, we may distinguish, as suggested by Bevilaqua & Lykoudis (1978), between a first-order self-similarity (equilibrium region for the mean and integral quantities) and a second-order self-similar region (equilibrium region for the Reynolds stresses). A necessary condition for

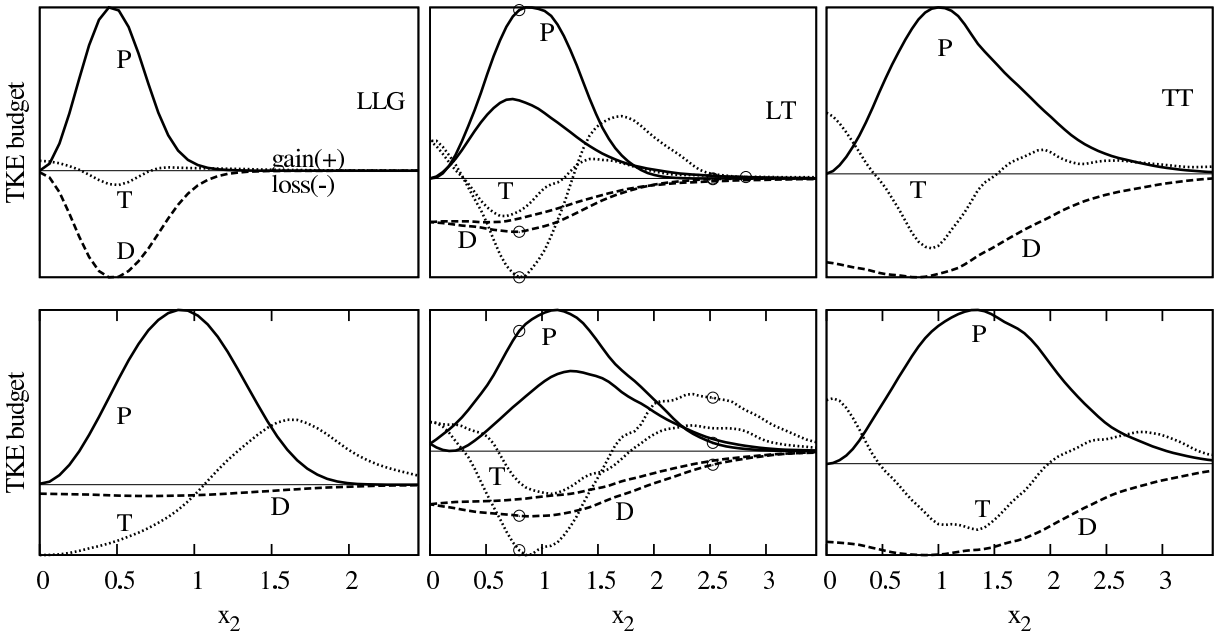

Figure 4.17: Profiles of the turbulent kinetic energy budget in the near/intermediate wake (in arbitrary units): production (P- full), dissipation (D- dashed) and pressure-transport (T- dotted). From left to right: LLG, LT and TT at $t = 30$ (top) and $t = 45$ (bottom). In LT, the laminar side is identified by the circle.

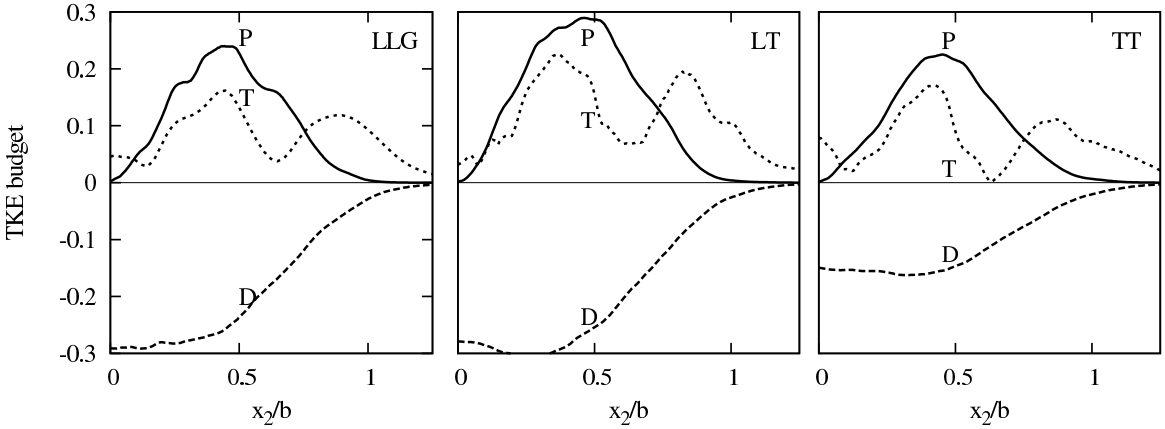

Figure 4.18: Profile of the normalized turbulent kinetic energy budget (U_0^3/b) in the self-preserving region: production (P - full), dissipation (D- dashed) and pressure-transport (T-dotted). The scale of the ordinate is identical in for all wakes.

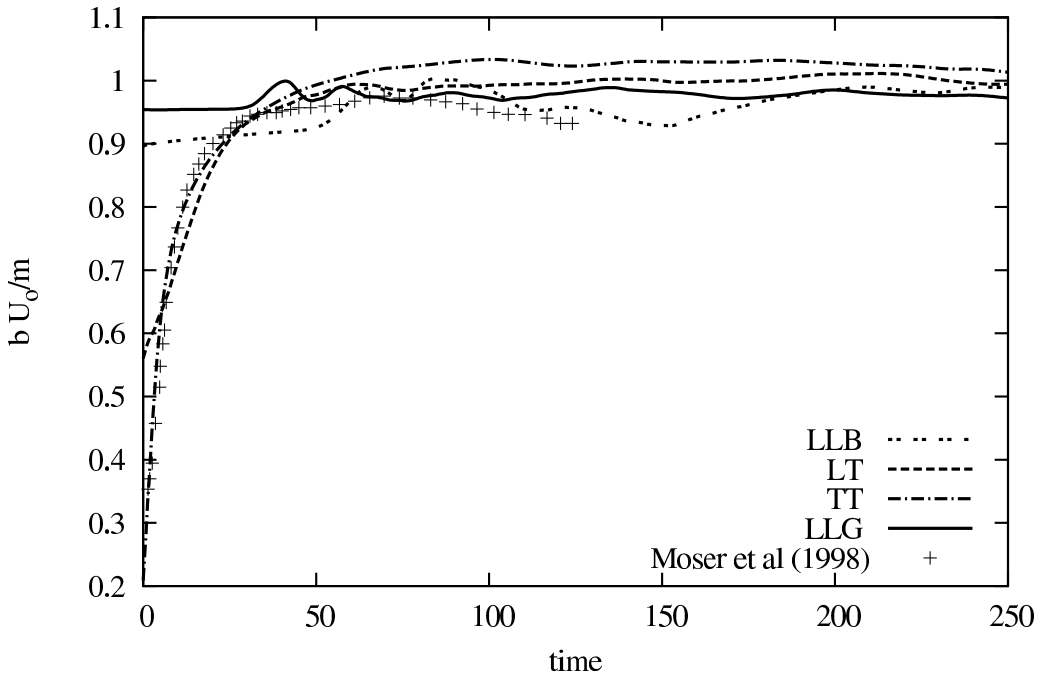

Figure 4.19: Evolution of spreading and the wake defect. DNS data: LLG (full line) ; LT (dash), TT (dash-dot) and LLB (double-dot). Comparative data: Moser *et al.* 1998 (plus)

the first-order self-similarity is the simultaneous evolution of the defect and the spreading (Moser *et al.*, 1998), such that: $bU_o/\dot{m} \approx cst$, see figure 4.19. For the Gaussian profile in LLG (in LLB the Gaussian-like profile is rapidly achieved), this parameter is not particularly insightful. For both TT and LT, we define the constant value as the average for $t > 125$. Using this far wake value ($bU_o/\dot{m} = 1.000$ (LT) and 1.021 (TT)), we define the first-order self-similarity as the time required to reach a tolerance range of ± 3 %. The first-order self-similarity is reached at $t = 45$ and $t = 48$ for the LT and TT respectively; interestingly, the bypass transition of LT reduces the time required to reach a first-order self-similar state.

We infer a region of approximate second-order self-similarity based on the plateau of

the maximal normalized Reynolds stresses, $\langle u_1 u_1 \rangle_{max} / U_0^2$, in figure 4.13. In order to judiciously confirm the choice of metric, we also verified the presence of a plateau in the streamwise fluctuations at the wake half-width. In addition, we qualitatively confirmed self-similarity by overlapping the normalized profiles at various far wake times. A final validation was done by verifying the presence of a plateau in the maximum normalized cross-wake velocity fluctuations, $\langle u_2 u_2 \rangle_{max} / U_0^2$. This last parameter is the most stringent criterion for second-order self-similarity, and many previous investigations (e.g. experimental (Weygandt & Mehta, 1989); numerical (Moser *et al.*, 1998)) noted a continual increase of this parameter in the far wake. For the LLG and LLB there is a well-defined plateau for $\langle u_2 u_2 \rangle_{max} / U_0^2$. In both LT and TT, an approximate plateau was reached; although we note a very slight monotonic increase. The ratio of $\langle u_2 u_2 \rangle_{max} / \langle u_1 u_1 \rangle_{max}$ increases linearly for LT and TT while in the other cases, it is nearly constant after transition. We contend that the statistical differences are a result of the dissimilar structural organization of the far wakes (detailed in §4.5 and §4.6). Defining the exact bounds of self-similarity is a rather subjective exercise (Moser *et al.*, 1998); based on our multiple metrics, we judge that approximate second-order self-similarity is reached at around $t = 210$ for LLG, $t = 150$ for LT, and $t = 160$ for TT. No self-similarity was achieved in LLB. The self-similarity was preserved until the end of all our computations i.e. $t = 290 - 300$. As for the mixing layer Bell & Mehta (1990), self-similarity is achieved most rapidly in the case of an initially turbulent boundary layer which recalls similar findings for screen wakes by Zhou & Antonia (1995). It was inferred that the absence of a near wake characteristic length scale - due to shedding or primary instability wavelength - results in a shorter time to reach a self-preserving state. In the following sections, we exclude LLB, as it did not reach a sufficient self-similarity state, and, furthermore, it shares many statistical and structural similarities with LLG.

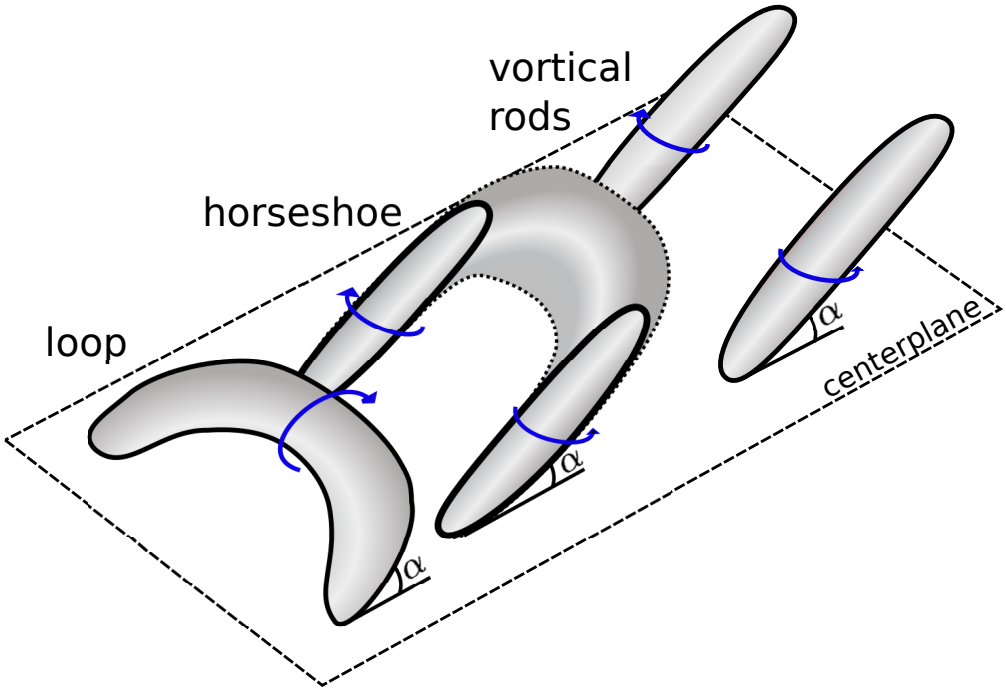

Figure 4.20: Conceptual geometry of loop, horseshoe and vortical rod structures.

4.5 Far Wake Structures

The far wake is made up of: inclined, mid-sized vortices and large-scale spanwise coherent motion. In this section, the nomenclature is defined, the instantaneous inclined vortices are visualized and the large-scale spanwise organized motion is extracted and interpreted.

4.5.1 Mid-size structures: rod vortices, loops, rings or horseshoes?

Nomenclature of far wake structures. A consensus on the characteristic mid-sized structures of the far wake has been difficult to reach, despite significant progress in experimental and computational methods. One of the main hindrances to a common understanding resides in the ambiguity and imprecision of the terms used to describe these structures. Loosely based on the nomenclature by Head & Bandyopadhyay (1981)

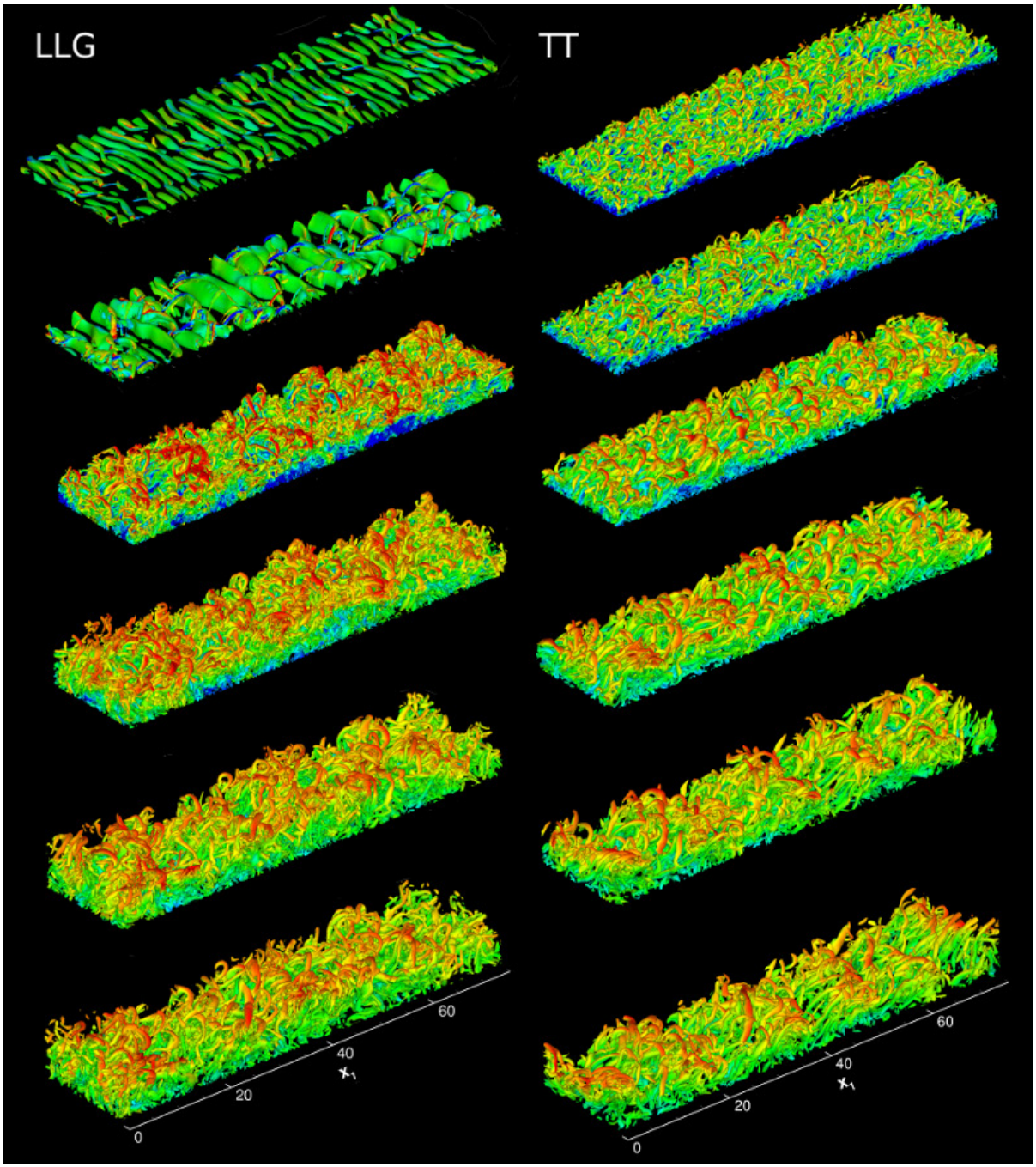

Figure 4.21: The λ_2 iso-surface ($\lambda_2 = -0.002$ except in top panels), colored with the instantaneous streamwise velocity of LLG (left) and TT (right). One side of wake shown at t =40 (30 in TT), 50, 100, 150, 200, 250.

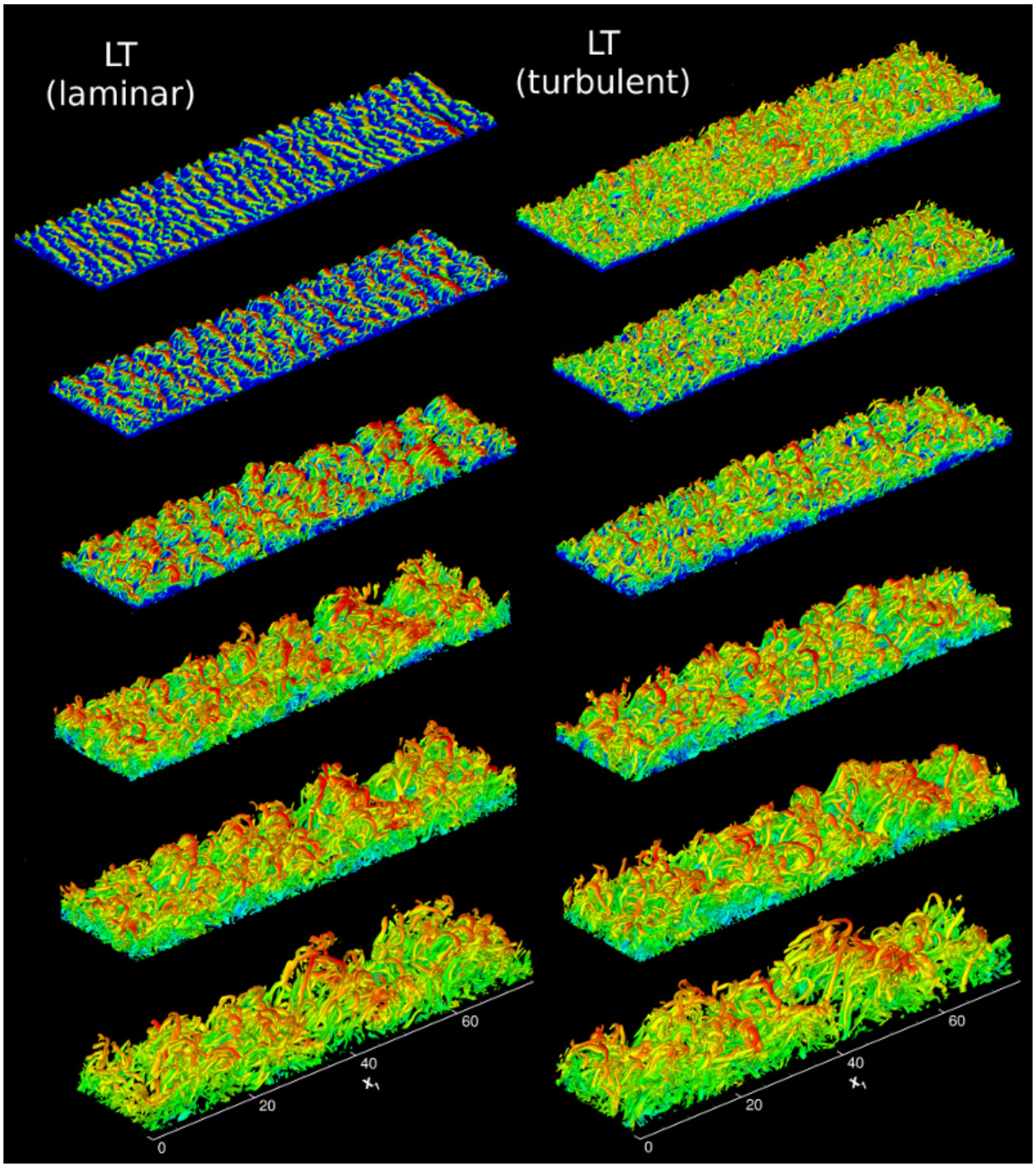

Figure 4.22: The λ_2 iso-surface ($\lambda_2 = -0.002$ except in top panels) colored with the instantaneous streamwise velocity of LT - laminar side (left) and turbulent side (right). The wake is shown at t =25, 50, 100, 150, 200, 250.

in wall bounded flows, a *loop* is a curved structure with a very low-aspect ratio and a predominant spanwise vortical component. A *ring* is an annulus-shaped structure resulting from the aggregation of closed -predominantly circular - vortex lines. A *horseshoe* is the structure formed from the elongation of a loop; the head connects two counter-rotating legs. A nuanced delineation between hairpin (primarily wall-bounded flows) and horseshoe structures is made. The hairpin has a smaller size relative to the characteristic length scale and the legs have a slight change of inclination near the head. The head of a horseshoe may become diffuse or dynamically unimportant; this occurs if there is no local spanwise stretching to maintain it or if the rotational component of the legs becomes dominant (through intense streamwise stretching, for example). The decay of the head, leaving only the counter rotating legs, results in the formation of a *vortical rod* pair. Note that in place of a well defined head, the vortical rod pair will still have spanwise vortex lines connecting both legs. But based on our definition, such structures are not horseshoes. An idealized loop, a horseshoe and a vortical rod pair are illustrated in figure 4.20.

Instantaneous structures. Instantaneous vortex structures, at various temporal locations, are shown in figure 4.21 using the λ_2-method (Jeong & Hussain, 1995). The transitional region of LLG is characterized by highly organized braids and spanwise rollers which evolve into highly disorganized streamwise-inclined vortical structures. The later the snapshot, the greater the disorganization. In the far wake, the mid-size structures show a surprising absence of organization which raises questions about the well-established belief that rib-like structures are simply arranged along the separatrix of neighboring rollers (Hussain & Hayakawa, 1987). The inclined rod vortices are the predominant instantaneous structures in the far field of LLG, as only a limited number of counter-rotating pairs of vortices are connected by a distinctive head. When using a more discriminant threshold of λ_2 (a lower value of λ_2), a clear predominance of the rod structures is observed.

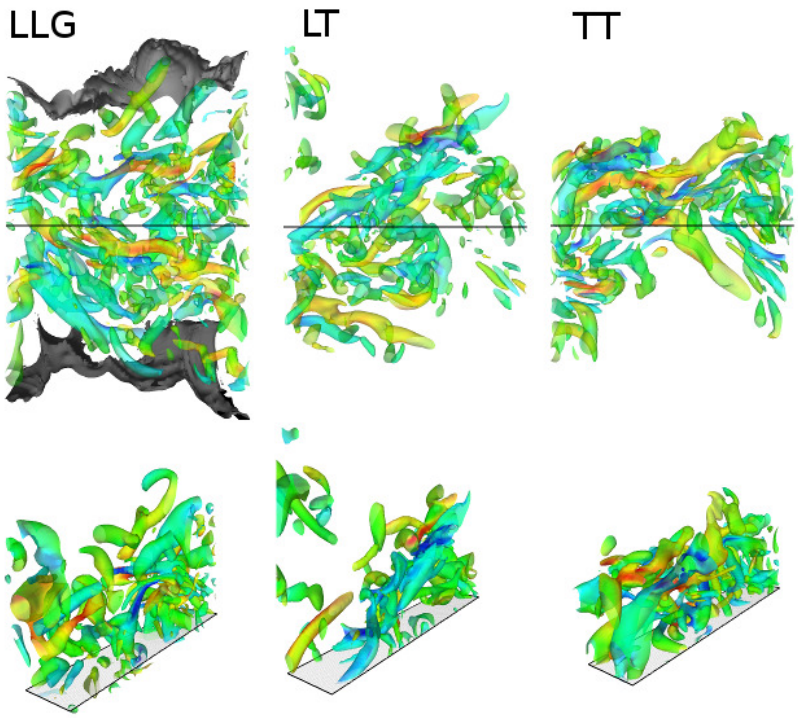

Figure 4.23: The λ_2 iso-surface ($\lambda_2 \approx -0.003$) colored with the instantaneous streamwise vorticity at time $t = 250$. Side view (top) and oblique view (bottom). Partial domain of $L_x/6$ and $L_z/8$. The turbulent/non-turbulent interface (TNTI) is shown for LLG, refer to section 4.7.2 for details on the identification of the TNTI.

In TT, the near wake is populated by lingering hairpin structures from the "forest of hairpins" of the original boundary layer DNS (Wu & Moin, 2009, 2010). The initial hairpin organization is gradually lost as the flow evolves. In the intermediate wake ($t = 100$ and 150), a number of horseshoe structures are clearly visible - slightly larger with an increased stance (increased spanwise separation between the legs) compared to the earlier hairpins. In the far wake, the number of horseshoes is greatly reduced and the underlying large-scale coherent motion modulates the structures (seen as spanwise bands of red colored flow

in figure 4.21) . These larger coherent structures stretch the horseshoe legs which form elongated vortical rod pairs in the far field. Unlike LLG, these inclined structures are approximately aligned along the regions of high shear between rollers.

Visualization of both sides of the asymmetric LT wake in figure 4.22 provides new and valuable insight into the transitional process. We recall that the laminar side of LT is characterized by a rapid onset of transition caused by aligned horseshoe structures (as discussed in §3.2 and figures 4.10, 4.11 and 4.12); the spanwise organization is maintained into the far field where the coherent motion modulates the vortical structures. The initially turbulent side of LT is nearly identical to TT, not surprising since it originates from the same turbulent boundary layer. Structural differences between the turbulent side of LT and TT start to become apparent from $t = 100$. Although the instantaneous structures are different, many far wake characteristic features of LT are similar to TT, namely, the large-scale organization and the long, streamwise-inclined vortical pairs.

In all cases, horseshoes are seldom observed in the far wake; the number continually decreases as the flow evolves. Between 3 and 8 distinctive horseshoes are found at time $t = 250$ (even fewer at $t = 280$) which represents far less than 1 % of the total number of structures in the flow; the number is even less if the threshold of the iso-surfaces becomes more discriminating. These figures would suggest that horseshoes are not the prototypical far wake structures as experimentally inferred (Hayakawa & Hussain, 1989; Ferré *et al.*, 1990; Vernet *et al.*, 1999). They appear to be residual structures from either the transitional mechanism (in LLG and LT) or from the hairpin structures of the boundary layer (in TT). The prototypical instantaneous structures are vortical rods inclined to the streamwise direction. No evidence of vortical rings, even as a singular event, was found. The close-up of the typical instantaneous structures in the far wake is shown in figure 4.23. The inhomogeneously sized structures fill up the entire wake between the top and bottom

turbulent/non-turbulent interfaces. The structures near the centerplane of LLG are small and confined to either side of the wake; in the outer wake, some larger, more energetic structures are observed. In LT and TT, larger structures are identified through out the wake - some even cross the centerplane. Despite a variety of structures, all wakes show a preferential inclination to the streamwise direction, slightly shallower than the expected inclination of $\pm 45°$.

4.5.2 Organization of spanwise coherent motion

Extraction of large-scale motion. Our understanding of the far wake large-scale structural organization has been derived primarily from cylinder wakes (e.g. Grant, 1958; Hussain & Hayakawa, 1987; Bisset *et al.*, 1990*a*); only a limited number of studies have broached the topic of the structural composition of splitter-plate wakes (e.g. Wygnanski *et al.*, 1986; Cimbala *et al.*, 1988; Moser *et al.*, 1998). As a result, the staggered anti-symmetric rollers, segregated on each side of the wake centerplane - forming a secondary Karman vortex street - is the only conceptual model available. This model, which originates from Grant (1958), has its limitations given the irreconcilable differences between the initially laminar and turbulent wakes, highlighted in figure 4.1. To identify the structural organization, an extraction technique is applied to the far wake. A two-dimensional Gaussian filter (with a standard deviation of $b/6$) is applied to the velocity components over each of the $x_1 - x_2$ slices. Thereafter, the filtered slices are averaged over the span. More elaborate techniques such as a conditional sampling based on quadrant analysis were also used, but the simple technique results in unambiguous structural identification.

Spanwise coherent motion: symmetric and anti-symmetric modes. Figure 4.24 shows the outcome of the extraction technique applied to an instantaneous flow field in the approximate self-similar region ($t = 290$). For clarity of the visualization, the weighted

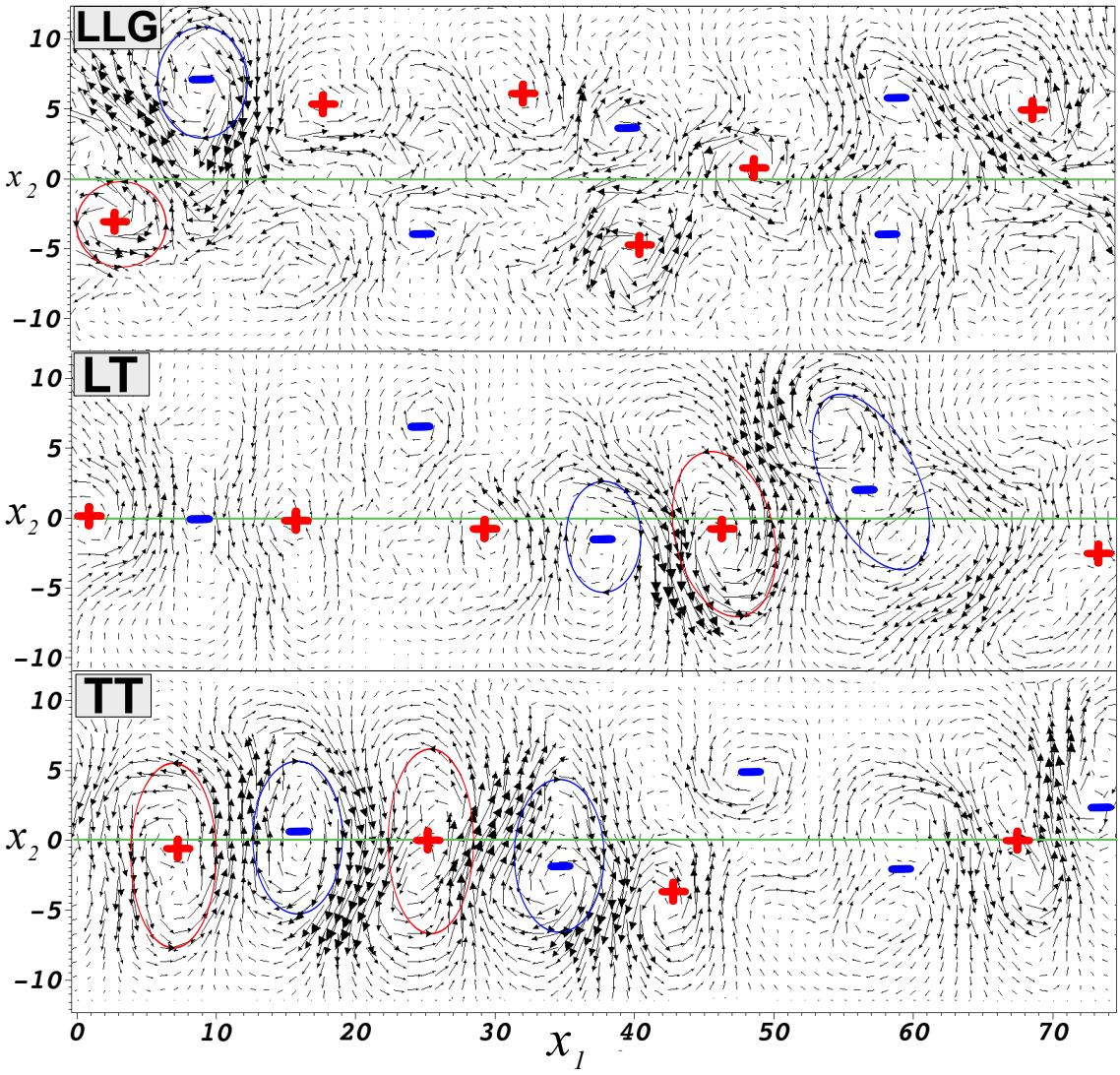

Figure 4.24: Vector field of the extracted large-scale structures in the far wake (at $t = 280$). The approximate center of the large-scale structures are identified by + and - for a positive and negative spanwise vorticity. Some characteristic rollers are identified to show the typical structural organization of the far wake.

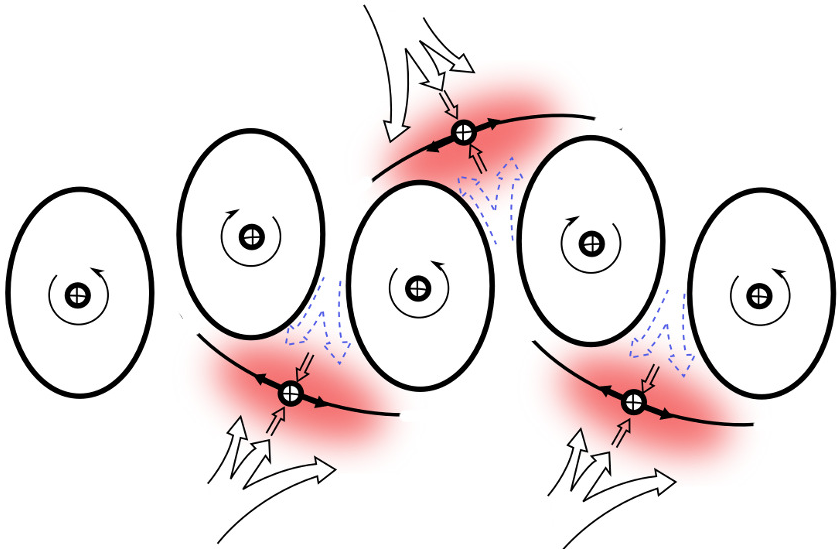

Figure 4.25: Conceptual model of spanwise coherent rollers in the far wake of LT and TT. The large rollers cross the centerline. The model differs from the classical staggered/segregated rollers from Hussain and Hayakawa (1987). Shaded area represents the region of highest turbulence production and arrows represent engulfment of non-turbulent fluid.

and conditioned velocity for Q2 and Q4 events are shown (typical rollers on the top side of the wake). To emphasize the structural differences among the wakes, the interpreted organization of the rollers is overlaid. The extracted features at other locations within the self-preserving region confirmed that the spatial organization and size of the rollers are not a one-time occurrence but instead are the typical large-scale organized motion in the self-similar wakes.

The extracted rollers in figure 4.24, nuance our previous understanding of the structural organization of the far wake; it has been generally accepted that the organized motion consists of staggered, segregated rollers (e.g. Grant, 1958; Cimbala *et al.*, 1988; Hussain & Hayakawa, 1987; Bisset *et al.*, 1990*a*). Two main types of structures are found: (i) slender, staggered rollers which are segregated to each side of the centerplane, as originally

proposed by Grant (1958); and (ii) large spanwise rollers which overlap the centerplane and may extend over the entire wake width. The staggered rollers reflect an anti-symmetric mode while the wake-spanning structures have properties similar to a symmetric mode. Our understanding of the symmetric mode is slightly different from the non-staggered, double row of vortices found in previous works (e.g. Robinson & Saffman, 1982; Wygnanski *et al.*, 1986). As a general observation, we note that slender, segregated rollers are predominant in the transitioning wake (LLG) whereas the large rollers are primarily found in initially turbulent wakes (TT and LT). Wygnanski *et al.* (1986) suggested that the interaction of symmetric and anti-symmetric modes explains the organization of the spanwise coherent structures. If the wake does not contain an anti-symmetric perturbation in the near-field (from anti-symmetric instability modes, shedding or trailing edge receptivity), the symmetric mode may develop, as noted for TT and LT.

Conceptual model of symmetric mode. The conceptual model of the far wake symmetric mode structures is shown with the help of an illustrative sketch in figure 4.25 - an adaptation of the classical anti-symmetric model by Hussain & Hayakawa (1987). In both symmetric and anti-symmetric cases, the high strain occurs along the separatrix between rollers. The high strain stretches the vortical rods which extracts turbulent kinetic energy from the mean flow. For the symmetric case, the core of the spanwise rollers are nearly aligned on the centerplane, in contrast to the anti-symmetric mode which has a strong offset between each row (the vortex cores are aligned at about $x_2 = \pm b/2$). Given the alignment and the proximity between neighboring rollers with opposite spins, large bands of strong cross-wake momentum form which explains the large peaks in the $\langle u_2 u_2 \rangle$ profiles for LT and TT; see figure 4.15. At the centerplane $x_2 = 0$, $\langle u_1 u_1 \rangle / U_0^2$ is greater than $\langle u_2 u_2 \rangle / U_0^2$ for LLG, whereas for both LT and TT, the latter term is greater. The inversion of the magnitude of the normal Reynolds stresses is a direct consequence of the

different structural make-up in the far wake.

Evidence of symmetric mode. Evidence of large-scale rollers overlapping the centerplane can be discerned from turbulent flat-plate wake data by Bonnet *et al.* (1984, 1986). By analysis of figure 4.25, it is obvious that a negative streamwise velocity correlation develops between the top and bottom of any roller. When the rollers overlap the centerplane, as in TT and LT, the negative streamwise velocity correlation is compounded between both rows of rollers. In their experiments, Bonnet *et al.* found a negative correlation when a hot-wire was fixed at the location of the maximum turbulent fluctuation and a second probe was traversed in the cross-wake direction; figure 4.1. The streamwise fluctuations of the anti-symmetric rollers become uncorrelated across the wake, as experimentally observed by Grant (1958). Our numerical findings agree with the experimental results for both the initially laminar (LLG) and turbulent (TT) cases; LT shares the characteristics of the initially turbulent wake which is consistent with the large-scale motion identified from our extraction algorithm. Note that other experimental works, notably Chevray & Kovasznay (1969), did not find any significant symmetric mode in the far wake of a turbulent splitter-plate.

4.6 Quantification of Far Wake Structures

The vorticity vector orientation is statistically investigated in the approximate self-similar region. The features of the prototypical mid-sized structures are quantified, and the origin of the spanwise rollers explained.

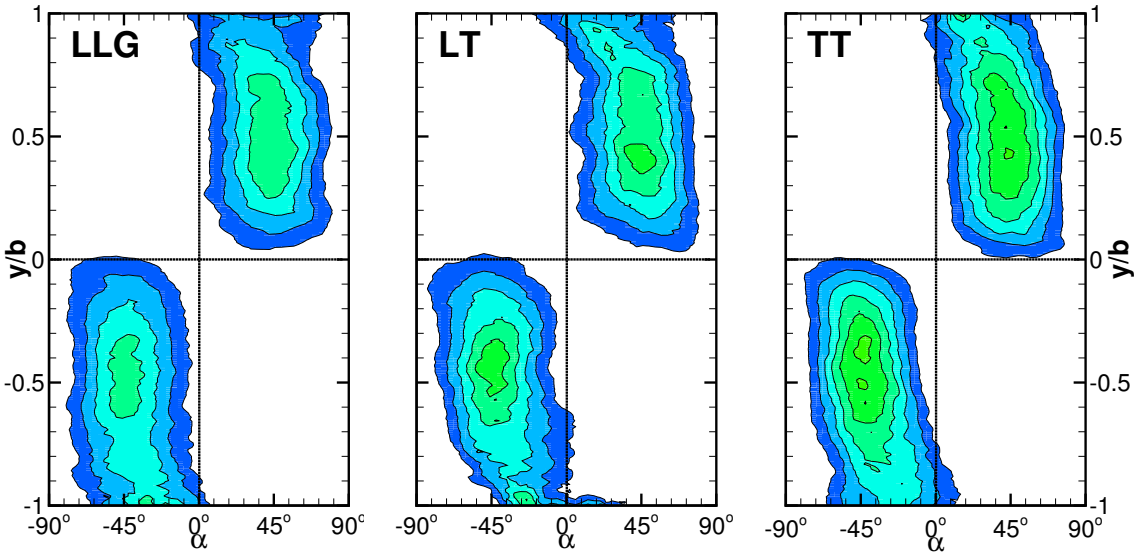

Figure 4.26: Weighted probability density function of the vorticity orientation in the $x_1 - x_2$-plane. The values of the contour lines are identical in all panels.

4.6.1 Mid-sized inclined structures

Streamwise inclination of vorticity vector. The far wake vorticity field provides an understanding of wake dynamics. To study the vortical inclination, the probability density function (pdf) is weighted by the local vorticity magnitude to discriminate the non-turbulent from the turbulent flow and to emphasize the dominant vortical motion. The fully converged statistics are accumulated over the approximate self-similar region (between 8 and 12 realizations for each wake). Figure 4.26 shows the weighted probability density of the vorticity orientation in the $x_1 - x_2$ plane (defined as $\alpha = \tan^{-1}(\omega_2/\omega_1)$; see figure 4.20). All the angles presented in this section (α, β and χ) are evaluated between $[-90°, 90°]$ as there is a near perfect periodicity over 180° (verified in all wakes), which increases the statistical significance of the results. The vorticity vector is preferentially inclined at $\pm 45°$ with respect to the streamwise direction on each side of the wake, similar to the vorticity

inclination of uniformly sheared turbulence (Vanderwel & Tavoularis, 2011). The highest probability density occurs just below $x_2 \approx \pm b/2$ for all the wakes, as previously noted by Bonnet *et al.* (1986) and Bisset *et al.* (1990*b*). To a close approximation, the stretching term is maximized when the vorticity vector is inclined at 45° to the mean flow which explains the peak production at this same location (see figure 4.18). The overall distribution of the pdf is similar among all the wakes suggesting that the preferential vorticity inclination is independent of the generating conditions; nonetheless, the magnitude of the peaks differs greatly. The highest peak, found in TT, suggests a greater homogeneity of the vortical inclination (and possibly also structural homogeneity). The probability function has a teardrop-type distribution; at the outer-edge of the wake, the highest probability density is tending toward $\alpha \approx 0$. A slight increase in the probability of spanwise vorticity is also observed at this location (not shown) - a result consistent with the experimental findings of Bisset *et al.* (1990*b*). It should be stressed that the increased spanwise vorticity at the outer wake does not imply the presence of horseshoe structures. Since the vortex lines must be continuous, it is natural that vorticity is spanwise at the outer-edge, as they are predominantly inclined at ±45° inside the wake.

Joint probability of vorticity orientation. To get a more complete picture of the spatial orientation of vorticity vectors, the joint probability density (jpdf) of α as a function of β (where $\alpha = \tan^{-1}(\omega_2/\omega_1)$ and $\beta = \tan^{-1}(\omega_3/\omega_2)$) at the wake half-width, $x_2 = b/2$, is presented in figure 4.27 (left). We use 60×60 uniformly spaced bins. The jpdfs share many commonalities among all cases. The wakes are characterized by an inverted V-shaped jpdf at the wake half-width (at $x_2 = +b/2$); on the opposite side, at the same distance from the centerplane (at $x_2 = -b/2$), the jpdfs are mirror images flipped about $\alpha = 0$. At the centerplane, the jpdfs form a perfectly symmetrical diamond shape. Note that, throughout the wake, if $\alpha \approx 0$, the vorticity vector is aligned with the spanwise direction,

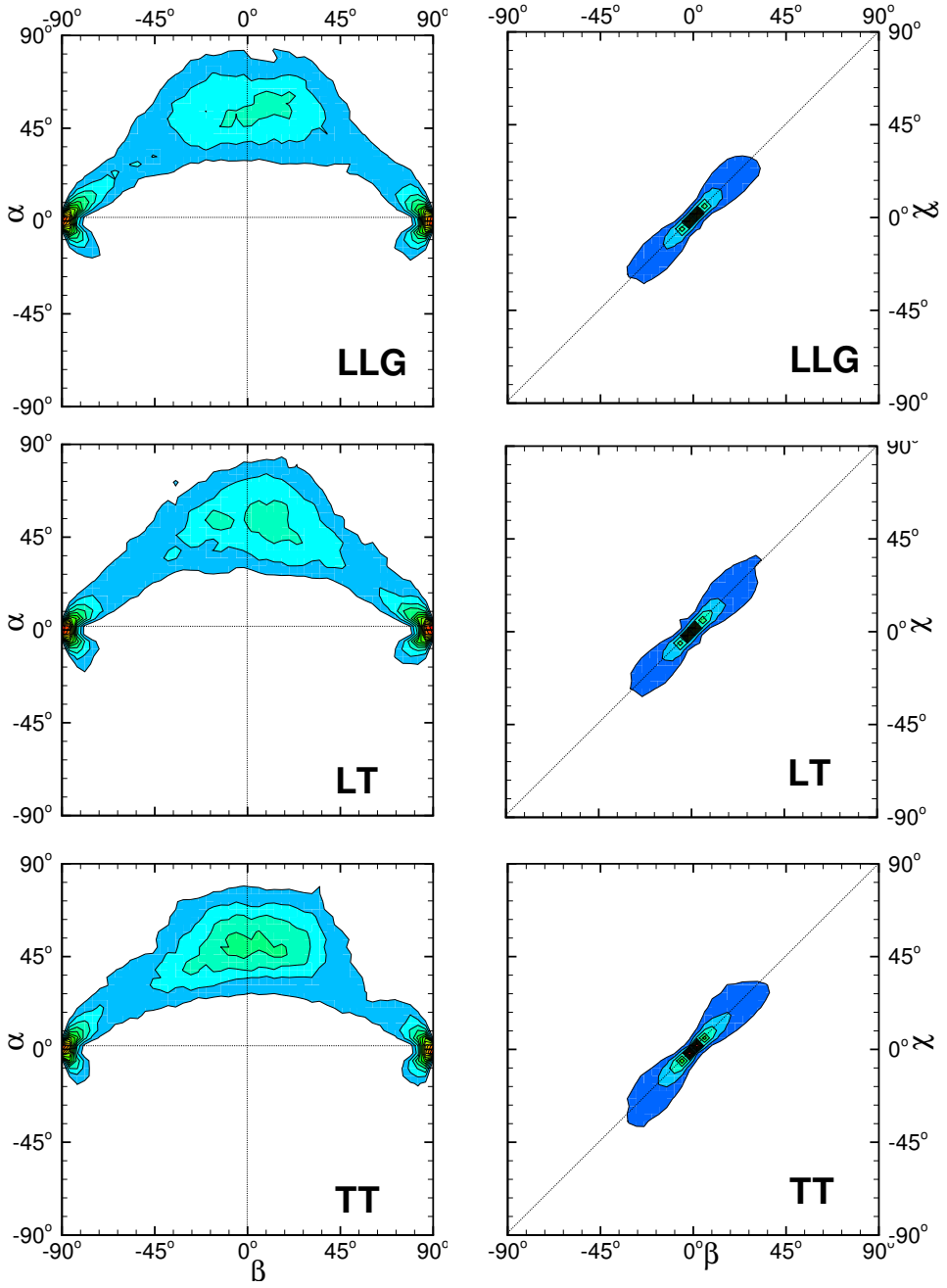

Figure 4.27: Weighted probability density function (pdf) of vorticity orientation at $y = 0.5b$ averaged over the self-similar region. Left figure: jpdf of α-β (orientation in plane $(x_1 - x_2)$ and $(x_3 - x_2)$) ; right figure: jpdf of β-χ (orientation in plane $(x_3 - x_2)$ and $(x_3 - x_1)$). Identical contour lines in all panels.

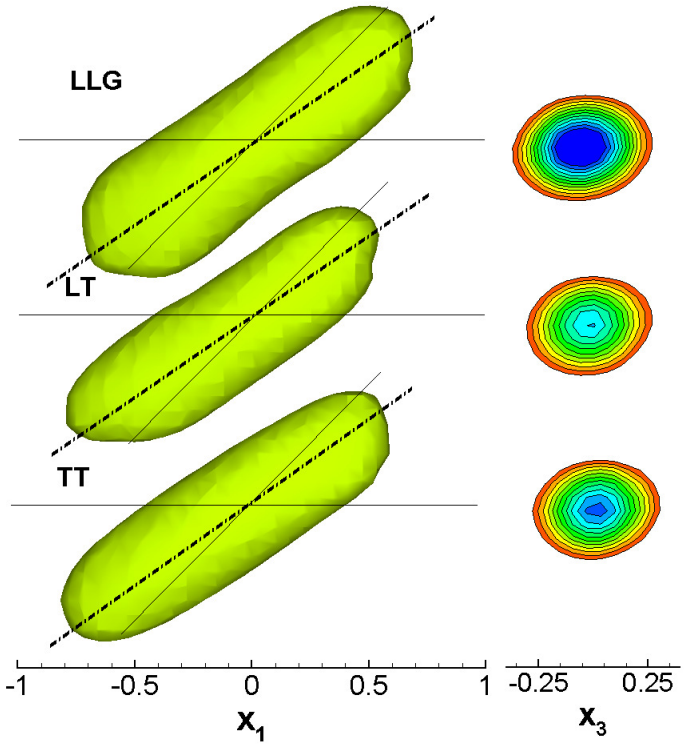

Figure 4.28: Constant iso-surface of λ_2 of the educed rod-like structure in the wake at $t = 250$. LLG, LT and TT shown with an identical threshold value of λ_2. Approximate vortex core inclination are indicated and compared with a reference slope at 45° (left). The slices of the vortex cores (perpendicular to incline) at $x_1 = 0$ are shown in the right column.

i.e. $\beta \approx \pm 90°$. This implies that if the vorticity has a negligible cross-wake component of vorticity (ω_2), the vorticity vector is preferentially spanwise aligned. Conversely, if there is a finite cross-wake vorticity component, the preferential orientation is $\alpha \approx \pm 45°$ and, on average, is centered in the $x_2 - x_3$-plane ($\beta \approx 0$). At the preferred streamwise inclination of $\alpha = \pm 45°$, β has a broad distribution with a high probability density over the range $\beta = -40°$ to $+40°$. This suggests high irregularity in the spanwise inclination of the

vorticity as can be seen in figures 4.21 and 4.22.

The jpdfs of the vector inclination in the spanwise and cross-wake directions (β and χ, where $\chi = \tan^{-1}(\omega_3/\omega_1)$) at the wake half-width (figure 4.27, right) are perfectly diagonal and centered at $(\beta, \chi) = (0, 0)$. At the same distance from the centerplane on the opposite side of the wake (at $x_2 = -b/2$), the jpdfs are aligned along the opposite diagonal; at the centerplane, the probability function forms an X-shaped distribution. The diagonally aligned pdfs imply a very high correlation between the orientations of the vorticity in the $x_2 - x_3$ and the $x_1 - x_3$ planes. The high correlation is at first rather surprising. On closer inspection, these results reveal a very important fact which could only be indirectly inferred from the instantaneous visualization, namely: the vorticity at the wake half-width is contained within perfectly straight tubes of vorticity. If the vortex lines were not perfectly straight and, say banana-shaped, the correlation between β and χ would not be as strong.

Eduction of vortical rods. The mid-sized inclined vortical structures, observed in figures 4.21 and 4.22, play an important role in the dynamics of the far wake, as they are responsible for up to 40 % of the turbulent kinetic energy (Ferré *et al.*, 1990). The shape and orientation of these prototypical rods are educed by applying a conditional sampling on λ_2. This allows a clearer interpretation of the structures compared to traditional velocity or vorticity based eduction techniques. Our eduction technique is based on the work of Jeong *et al.* (1997) which was developed to identify the near wall structures in a channel flow. The main steps of the eduction technique are:

1. identify the local minima of λ_2;
2. connect the minima and define the structural cores;
3. apply a conditional sampling on the structural cores;
4. ensemble average all acceptable structures.

The details of the eduction algorithm are as follows. For an instantaneous realization in the far wake, λ_2 is computed at every point. Up to 100 local minima of λ_2 are identified on each $x_2 - x_3$ slice; only the minima with $\lambda_2(x_1, x_2, x_3)$ below $-\langle\lambda_2(x_2)\rangle_{rms}$ are considered. Physically, these minima correspond to the central core of vortical structures. Two local minima are assumed to belong to the same structure if they are located within three grid points, in either x_2 or x_3, between two neighboring slices in the x_1 direction - a less restrictive criterion than used by Jeong *et al.* (1997). By connecting all the neighboring minima, the vortex core is identified. The identification technique fails in the case of a perfectly spanwise or cross-wake aligned vortex as it would represent a line on the $x_2 - x_3$-plane, not a single point; such vortices were observed and neglected as rare occurrences. A conditional sampling is applied to each cluster of points forming a vortex core. Three conditions are used to determine the acceptance of the structures: (1) a minimal length of the vortex core in the streamwise direction, chosen as 1/6 of the wake half-width (the minimal threshold was based on the visual identification of typical far field structures in the wake); (2) inclination in the $x_1 - x_2$-plane is $45° \pm 25°$; (3) inclination in the $x_2 - x_3$-plane is $\pm 25°$. The vortical inclination is calculated by simple linear regression over all points forming the vortex core. We further subsample the identified vortices with respect to their location within the wake (at the centerplane, half-width or outer-wake) and direction of the streamwise vorticity. We identify about 7000-15000 vortex cores per snapshot. The conditional sampling based on length reduces the number to about 1000 structures while the inclination constraints reduce the final number of structures to 50-175. The educed structures are then ensemble averaged.

Characterizing vortical rods. The educed structures are presented in figure 4.28. The results, subsampled at various locations in the wakes, are tabulated in table 4.1. The far wake prototypical structures are, as expected, rod-like structures inclined to the

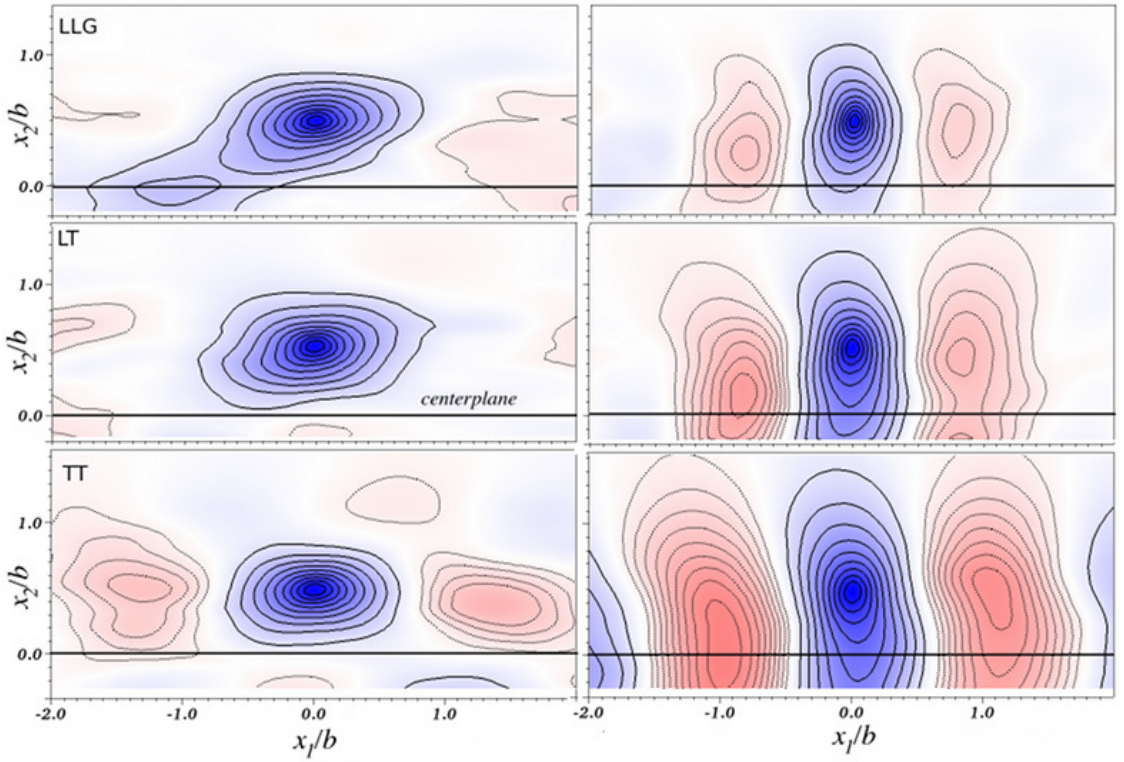

Figure 4.29: Two-point correlation maps in the x_1-x_2 plane at the wake half-width. Full lines (blue shading)- positive correlation from 0.1 with increments of 0.1. Thin lines (red shading) - negative correlations from -0.05 with increments of 0.05. Left column represents R_{u_1,u_1} and right column is the R_{u_2,u_2}. The statistics are averaged over at least 8 realizations in the self-similar domain.

streamwise direction. The structures are nearly perfectly aligned along the streamwise direction (some structures show slight sideways tilts of up to $\pm 8°$) and are inclined at about $\pm 30° - 35°$ to the downstream (from the horizontal, streamwise direction); when subsampled at various cross-wake locations, the streamwise inclination varies from 28° to 40° (see table 4.1). These results are fully consistent with the close-up view of the instantaneous structures in figure 4.23. Surprisingly, the angle of the rod-like structures differs rather

Table 4.1: Inclination angle from the streamwise direction of the educed structures. The value in the parenthesis represents the total number of structures accepted for eduction. The center corresponds to $[-b/2, +b/2]$; half-width: $[\pm b/4, \pm 3b/4]$; and outer-wake: $[\pm b/2, \infty$.

Location	**LLG**	**LT**	**TT**
Center	31.9° (122)	35.6° (125)	29.2°(166)
Half-width	40.1° (105)	31.6° (113)	29.9°(134)
Outer-wake	33.8° (62)	29.9° (59)	28.3°(66)

significantly from the principal axis of the mean strain-rate tensor or the preferential vorticity inclination, both at 45°. Although the inclination angle of the structures is consistent with the range $30° - 45°$ observed in the homogeneously sheared turbulence (Vanderwel & Tavoularis, 2011), it contrasts the previous experimental wake observations. Mumford (1983) found an inclination of 45° while others found inclination angles of up to 60° (LaRue & Libby, 1974*a*; Hayakawa & Hussain, 1989). Note that these experimental values were inferred through velocity or vorticity correlations and not from an eduction algorithm. The discrepancy between vorticity and structural inclination has been a reoccurring debate in wall bounded flows. Historically, the use of vortex lines has led to a misinterpretation of the hairpin structures Robinson (1991). Visualization techniques, such as λ_2 and Q-criteria, isolate the rotational from the shear component (Jeong & Hussain, 1995; Chakraborty *et al.*, 2005). For this reason, the DNS of channel flow by Zhou *et al.* (1999) noted that the vorticity was inclined to 50° while the structures had a local inclination of only 25°. A similar discrepancy between structural and vortical inclination is also noted in the case of the wake in spite of a significantly lower shear intensity than in wall bounded flows. It is therefore fair to infer that the shear is not the unique parameter which defines the structural inclination, as was suggested in Hayakawa & Hussain (1989).

4.6.2 Spanwise coherent motion

Large-scale spanwise rollers. We quantify the average size and spacing of the spanwise organized motion by investigating the two-point correlation maps in the x_1-x_2 plane with a fixed point at the wake half-width. The normalized correlation maps are averaged over the span and contain at least 8 instantaneous snapshots in the approximate self-similar region. The auto-correlation of the streamwise, R_{u_1,u_1} (left column), and cross-wake, R_{u_2,u_2} (right column), velocities are shown in figure 4.29. A clear structural difference can be seen in R_{u_1,u_1} between LLG and LT/TT. A band of strong positive correlation (with $R_{u_1,u_1} \approx 0.25$ at centerplane), inclined at 29°, is observed in LLG. In LT and TT the streamwise auto-correlation maps are elliptical with regions of negative correlations on either side and across the centerplane. The average size of the large-scale coherent motion can be inferred from the auto-correlation of the cross-wake velocity (left column) as the periodicity of the cross-wake velocity is a direct consequence of the spanwise coherent rollers. The LLG and LT wakes have a peak negative correlation at $x_1/b = \pm 0.82$ while the larger rollers in the TT case have a peak at $x_1/b = \pm 1.00$. Therefore, the spacing between two neighboring rollers is between 1.62b and $2.00b$. The separation of the peaks of the auto-correlation of TT is identical to Bonnet *et al.* (1984). Interestingly, the peak negative correlation of R_{u_2,u_2} is not located at the wake half-width ($x_2/b = 0.5$). The negative peaks are located closer to the centerplane at a distance of $x_2/b = -0.24, -0.33$ and -0.45 from the wake half-width, respectively for LLG, LT and TT. These results are a further indication of the larger roller size in LT/TT than LLG. As expected from the analysis in §4.5, the negative R_{u_2,u_2} clearly overlaps the centerplane for both LT and TT, while in LLG, albeit slightly negative, the correlation is significantly lower at the centerplane. The magnitude of the R_{u_2,u_2} peak indicates coherence and uniformity of the spanwise organized

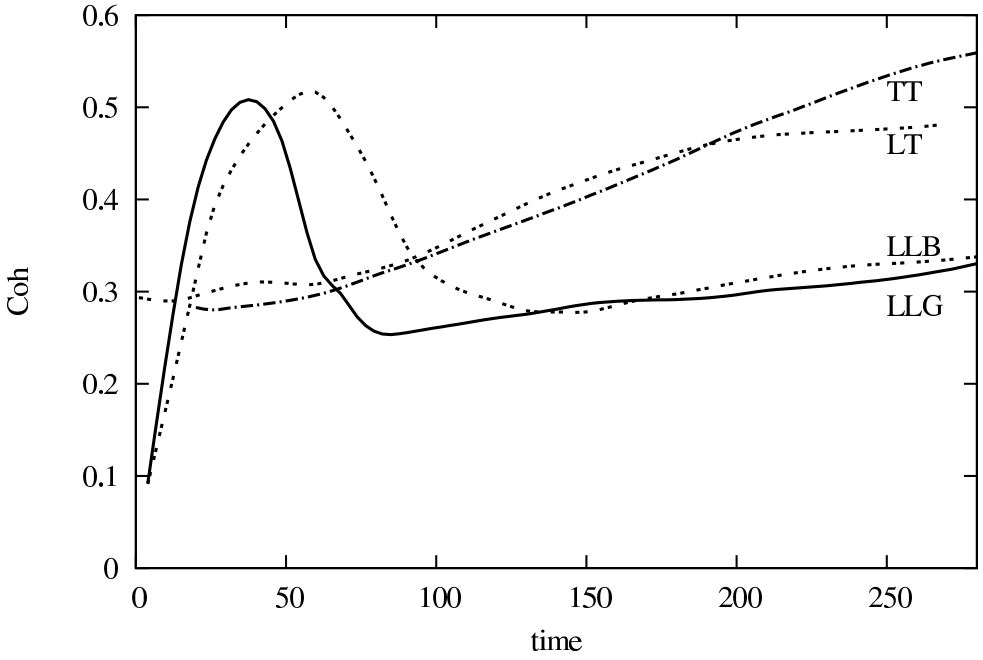

Figure 4.30: Evolution of the spanwise coherent energy, where Q represents the ratio of turbulent kinetic energy contained in the spanwise coherent motion over the total TKE energy.

motion: $R_{u_2u_2}$ = -0.22,-0.38 and -0.48 for LLG, LT and TT. Given the inherent lack of large-scale near field structures in TT, the higher level of structural organization is a rather unexpected finding.

Temporal evolution of spanwise coherence. Moser *et al.* (1998) suggested that the contribution of the spanwise coherent motion to the total kinetic energy approaches a constant ratio as the flow reaches an asymptotic state. The numerical results by Moser *et al.* (1998) only partially substantiate this claim as their computational domain limited the far wake evolution. The longer temporal evolution of the present simulations is better suited to evaluate this claim. By modifying the definition by Moser *et al.* (1998) (based on one-dimensional energy ratios in spectral space), we define the ratio of the spanwise averaged over the total turbulent kinetic energy as: $Coh = \langle u_i \rangle \langle u_i \rangle \,/\, \langle u_j u_j \rangle$, where the

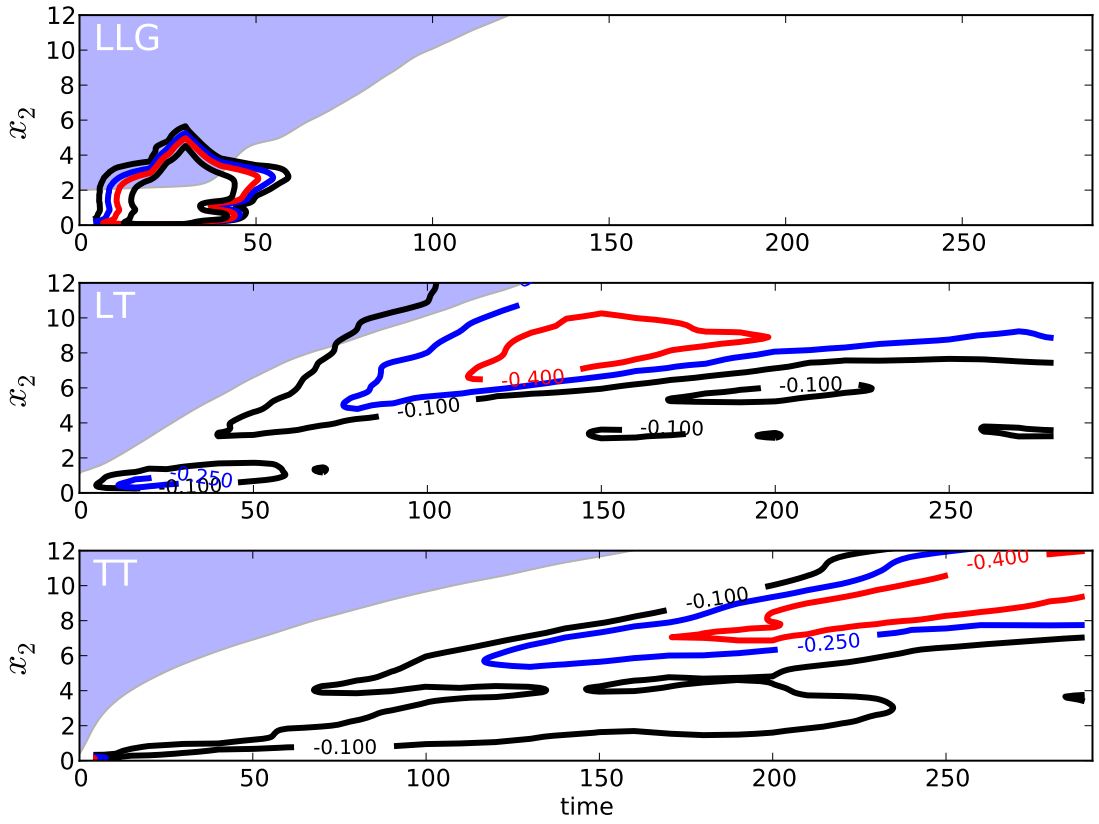

Figure 4.31: Evolution of the two-point correlation coefficient of the streamwise velocity $R^*_{u_1,u_1}$ fluctuations at symmetric distances from the centerplane. For clarity, only the negative contours are shown with increments of -0.1, -0.25 and -0.40. The shaded area represents the outer wake defined as one wake half-width from the centerplane. Auto-correlation in the outer wake are due to noise in the non-turbulent freestream.

brackets $\langle\cdot\rangle$ represents an ensemble average over the entire computational domain at a given time. Given a sufficiently wide domain, the spanwise averaging extracts the organized large-scale motion and offers a domain size independent method to evaluate the coherence of the TKE. Figure 4.30 shows that the evolution of LT is levelling out, whereas the other wakes appear to be slowly tending towards an asymptotic state, although as in Moser *et al.* (1998) an equilibrium evolution in the far wake was not achieved. In all cases, here 32-55 % (at $t = 300$) of the turbulence kinetic energy is found in spanwise coherent modes. As expected, the initially turbulent cases have monotonically increasing spanwise coherent energy which develops as the independent flow fields cross-correlate in the freestream. For the initially laminar wakes, there is a peak as the spanwise coherent rollers form during transition, followed by a sharp drop before a continual monotonic increase. Here, we note that both LT and TT have very similar levels of spanwise coherence over a large portion of the evolution, yet their spreading rates differ by 40 %. Contrary to the inference made by Moser *et al.* (1998), the present results suggest that spanwise coherence plays a secondary role in the spreading of the wake.

Origin of large-scale motion. Conceptually, turbulent splitter-plate wakes develop by cross-correlation between two statistically independent boundary layers (Bonnet *et al.*, 1984). As the trailing edge boundary layers are fully turbulent, dominated by small-scale turbulent motion, the near wake should be void of large-scale organization. Despite this simple logic, some experimental studies have noticed large-scale structures (e.g. Wygnanski *et al.*, 1986; Hayakawa & Hussain, 1989) while others only noted small-scale turbulence (e.g. Chevray & Kovasznay, 1969; Bonnet *et al.*, 1986; Moser *et al.*, 1998). The controversy regarding the presence of near wake large-scale structures in initially turbulent wakes persists. There are two main reasons: (1) experimental variability due to trailing edge receptivity or splitter-plate design (for example roughness (Althaus, 1990)); (2) inconsistent

definition of a spanwise coherent motion (the presence or absence of structural organization is generally inferred from flow visualization). As the influence of trailing edge effects is outside the scope of the present work, we address the origin of large-scale rollers in the splitter-plate wake. Since the prototypical far wake organized motion for TT and LT are symmetric and easily identifiable by an auto-correlation of the streamwise velocity with cross-wake separation (see §4.5), this metric is used to identify the origin of these structures in the near wake. The correlation coefficient with cross-wake separation at a symmetric distance from the centerplane is defined as:

$$R^*_{ij}(r,t) = \frac{\langle u_i(x_1,\ +r,\ x_3,t)\, u_j(x_1,\ -r,\ x_3,t)\rangle}{\left(u_i^{rms}(+r,t)u_j^{rms}(-r,t)\right)} \tag{4.2}$$

where r is the distance from the centerplane (no sum on repeated indices). Figure 4.31 shows the evolution of the correlation coefficient, calculated using snapshots at every $\Delta t = 10$. Interestingly, after transition of the LLG case (the auto-correlation is artificially high during transition because of low u_i^{rms}), the correlation between the top and bottom halves of the wake is very weak outside a thin strip around the centerplane. Conversely, in LT and TT, a negative correlation in the streamwise velocity (< -0.2) develops in the near wake and is maintained into the self-similar region. The negative correlation is a direct consequence of the large-scale organized motion. This is a particularly interesting finding given that the boundary layers on either side of the wake are initially statistically independent and void of any forcing. Since the evidence presented in figure 4.31 clearly reveals that the structural organization in turbulent splitter-plate wakes emerges from the near field, this raises many questions, namely: what is the origin of the symmetric mode in the initially turbulent wake? This question merits a deeper investigation.

4.7 Statistical Multiplicity and Structural Plurality

In §4.4, we show that initial conditions modify the path towards approximate self-similarity. In sections 4.5 and 4.6, we prove that the *memory* is maintained through the large-scale spanwise coherent motion; the mid-sized inclined structures being statistically similar for all initial conditions. Here, we connect the structural plurality to the multiplicity of the self-similar turbulence statistics. Firstly, we investigate the vorticity transport across the centerplane in order to understand the spread rate variations. Secondly, we study the changes to the entrainment and turbulent/non-turbulent interface (TNTI) caused by different large-scale structures, hence initial conditions.

4.7.1 Vorticity flux and spread rate

The circulation on either side of the centerplane is equal and of opposite sign - null over the entire wake. The circulation in each half-wake must decrease either by: (i) reduction of the centerplane defect; or (ii) advection of vorticity across the centerplane. The connection between transverse advection of spanwise vorticity and the spread rate of the self-similar wake is discussed.

For a temporally evolving wake, the mean momentum equation is:

$$\frac{\partial \left(U_\infty - U(x_2)\right)}{\partial t} = -\frac{\partial \left\langle u_1 u_2 \right\rangle}{\partial x_2} + \mu \frac{\partial^2}{\partial x_2^2} \left(U_\infty - U(x_2)\right) \tag{4.3}$$

During the self-similar evolution, the spreading and the centerline velocity defect evolve together, $bU_o/\dot{m} \approx cst$, verified in figure 4.19. Furthermore, we recall that for temporally evolving wakes, the mass-flux defect is constant, $\dot{m} = cst$ (Moser *et al.*, 1998). Using these simple relations, the left-hand side of equation (4.3) at the centerplane ($x_2 = 0$) is:

$$\frac{\partial U_0}{\partial t} = -\frac{U_0}{b}\frac{\partial b}{\partial t} + \frac{1}{b}\frac{\partial b U_0}{\partial t} \tag{4.4}$$

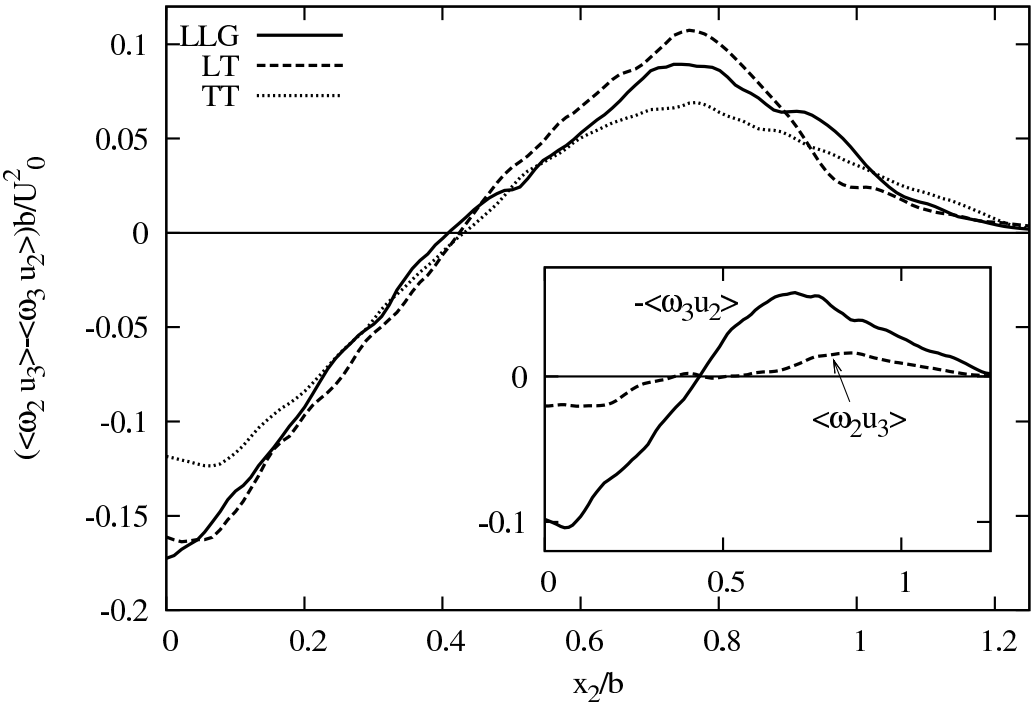

Figure 4.32: Correlation of vorticity and velocity: $\langle\omega_2 u_3\rangle - \langle\omega_3 u_2\rangle$ in the self-similar region. The individual profiles of $\langle\omega_2 u_3\rangle$ and $-\langle\omega_3 u_2\rangle$ for TT are shown in the inset.

where $U_0 = U_\infty - U\,(x_2 = 0)$. Since bU_o is constant, the spreading of an inviscid wake (without any new assumptions) is:

$$C\frac{\partial b^2}{\partial t} = -\left.\frac{\partial \langle u_1 u_2\rangle / U_0^2}{\partial x_2/b}\right|_{x_2=0} \tag{4.5}$$

where C is a constant dependant on the mass-flux defect. Consequently:

$$\frac{\partial b^2}{\partial t} \propto -\left.\frac{\partial \langle u_1 u_2\rangle / U_0^2}{\partial x_2/b}\right|_{x_2=0} \tag{4.6}$$

Since the spread rate in the far wake is constant ($\frac{\partial b^2}{\partial t} = cst$), we verified that the centerplane gradient of $\langle u_1 u_2\rangle / U_0^2$ is also constant. The average centerplane slope of the Reynolds shear stress is: 0.157 (LT and LLG), and 0.105 (TT). The difference in the slopes represents a relative variation of 40 %; this result is consistent with our findings for the spread rate (42

% relative variation between LLG/LT and TT). The proportionality between the spread rate and the centerplane slope of $\langle u_1 u_2 \rangle$ is also found in Moser *et al.* (1998) for the weakly forced wake (8 % difference based on the unforced case). For the strong forcing case, the difference is greater (about 20 %), although the statistics show "imperfect self-similarity" (Moser *et al.*, 1998), probably resulting from the limited computational domain size.

Using the following well-known vector identity for incompressible flows, we relate the Reynolds stresses to the vorticity flux and TKE (e.g. Brown & Roshko, 2011):

$$\frac{\partial u_i u_k}{\partial x_k} = \epsilon_{ijk}\omega_j u_k + \frac{\partial}{\partial x_i}\left(\frac{1}{2}u_k^2\right) \tag{4.7}$$

By averaging and assuming homogeneity in the x_1 and x_3 directions, we obtain:

$$\frac{\partial \langle u_1 u_2 \rangle}{\partial x_2} = \langle \omega_2 u_3 \rangle - \langle \omega_3 u_2 \rangle . \tag{4.8}$$

The second term of the right-hand side, representing the cross-wake advection of the spanwise vorticity, is the dominant component - the magnitude at the centerplane is over four times greater than the first term (see inset of figure 4.32). At $x_2 = 0$, (4.6) and (4.8) relate the wake spreading to the normalized transport of vorticity:

$$\frac{\partial b^2}{\partial t} \propto \frac{-b}{U_0^2}\left(\langle \omega_2 u_3 \rangle - \langle \omega_3 u_2 \rangle\right)_{x_2=0} \tag{4.9}$$

Figure 4.32 shows the right-hand side of (4.9). At $x_2 = 0$ the average is: -0.173 (LLG), -0.163 (LT) and -0.118 (TT). These results are broadly consistent with the variation of the spread rates (38 % relative variation between LLG and TT), although the slight discrepancy might be related to the limited statistical convergence of these higher-order statistics.

4.7.2 Entrainment and TNTI

Free shear flows are characterized by a thin sheet - the turbulent/non-turbulent interface (TNTI) - separating the rotational/turbulent from the irrotational/non-turbulent

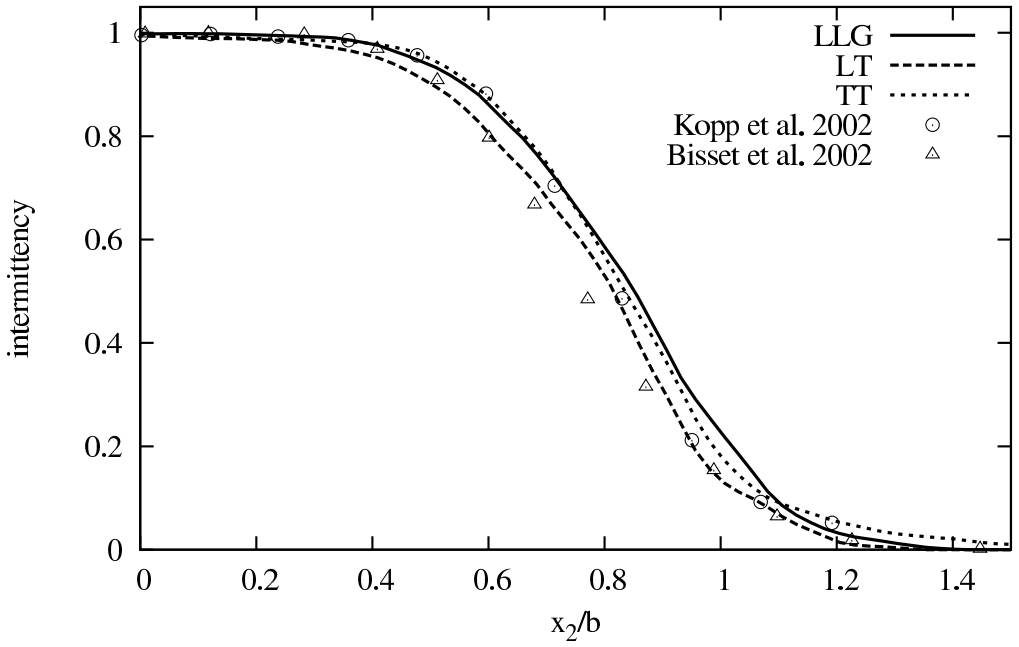

Figure 4.33: Intermittency factor based on the threshold of $d_1 = 5E-3$ at time $t = 250$. The results are compared with a cylinder wake (Kopp *et al.* 2002) and a numerical splitter-plate wake (Bisset *et al.* 2002).

regions. In order for a wake to spread, the irrotational freestream fluid must be entrained into the turbulent core through the TNTI. Two principal mechanisms of wake entrainment are: direct entrainment ("nibbling") and engulfment, the latter being governed by the large-scale structures (Bisset *et al.*, 2002; Philip & Marusic, 2012), although eventually "nibbled". We attempt to quantify the influence of the initial conditions on the entrainment and the contortions of the TNTI.

The entrainment rate is defined as dQ/dx_1 (e.g. Hussain & Clark, 1977) where the mass-flux defect is:

$$Q(x_1) = \int_{-\infty}^{\infty} \rho(U_\infty - U_1(x_1, x_2))dx_2 \tag{4.10}$$

In temporally evolving numerical simulations, the mass-flux defect is a preserved quantity

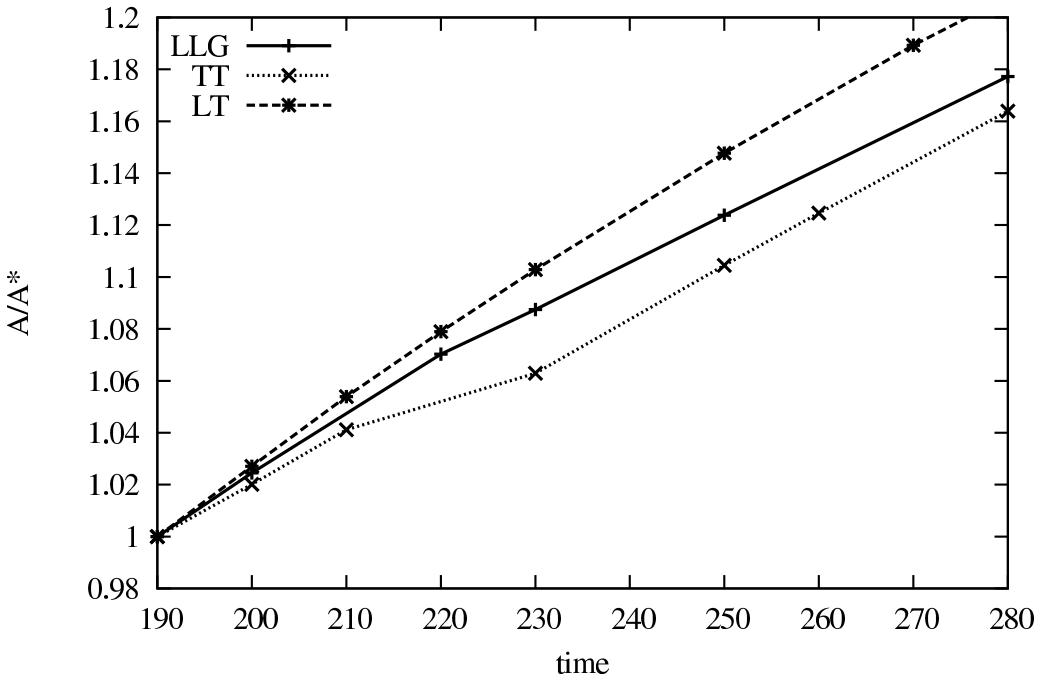

Figure 4.34: Evolution of the entrainment parameter, calculated using TNTI and normalized by the value at time $t = 190$ (A^*).

by design (Moser *et al.*, 1998). Therefore, we must use a different metric. Since entrainment is a process by which irrotational fluid becomes turbulent, we investigate the evolution, in time, of the volume of turbulent fluid :

$$A(t) = \int \int \int_{-\infty}^{\infty} \delta(x_1, x_2, x_3, t) dx_3 \; dx_2 \; dx_1 \tag{4.11}$$

where δ is a function equal to unity if the flow is turbulent (random vorticity) and zero otherwise. This metric is fully analogous to the intermittency-based entrainment measurements proposed by Townsend (1976). To distinguish between the turbulent and non-turbulent fluids, a thresholding technique is used. The flow is locally irrotational if:

$$\sqrt{\left(\frac{\partial \omega_1}{\partial x_1}\right)^2 + \left(\frac{\partial \omega_2}{\partial x_2}\right)^2 + \left(\frac{\partial \omega_3}{\partial x_3}\right)^2} < d_1, \tag{4.12}$$

where d_1 is a judiciously chosen threshold: $d_1 = 5 \times 10^{-3}$. To confirm that the spatial

derivatives of low-level vorticity do not correspond to a local maximum or minimum in an otherwise rotational flow, we add an additional constraint to assure irrotationality: $\sqrt{\omega_1^2+\omega_2^2+\omega_3^2} < d_2$, where d_2 is a threshold we conveniently define as function of d_1. It is precisely defined as: $d_2 = 10d_1$. This two-step detection technique is arguably more sensitive, although the results are practically identical to the well established detection technique based on vorticity magnitude alone. To validate our choice of metric, the intermittency profiles are compared to experimental and numerical data in figure 4.33. For a quantitative comparison, a curve fitting of the intermittency profiles was conducted. Based on a hyperbolic tangent function: $-\tanh\left((x-b^*)\,c\right)+1$, where b^* is the intermittency wake half-width, the fitting parameter of each wake is: $c = 4.018$ (LLG), 3.419(LT) and 4.184 (TT). It should be noted that the wakes generated from fully turbulent boundary layers (TT and LT) have a block of decaying isotropic turbulence in the freestream (Wu & Moin, 2009); only the portion of the domain without freestream turbulence is used for the entrainment calculations (about two-thirds of the streamwise domain).

The evolution of the turbulence volume (figure 4.34) show an unexpected trend over the self-similar domain. The very similar entrainment rates ($dA(t)/dt$) for TT (0.00201) and LT (0.00206), are higher than LLG (0.00179) from about $t > 220$. Interestingly, these results do not agree with the trend in spreading rates, we refer the reader to the discussion in §4.4.1 and figure 4.5. Since engulfment istherefore the predominant mechanism for entrainment, we investigate the main features of the TNTI to explain this result.

Characterization of the TNTI. As observed in the wake (Kopp *et al.*, 2002) and jet (da Silva & dos Reis, 2011; da Silva *et al.*, 2011), the TNTI contortions are caused by mid-sized inclined structures. But as seen in the vorticity slices and approximate TNTI in figures 4.35 and 4.36, the large-scale structures (particularly in LT and TT) modulate the mid-sized, inclined rollers and are responsible for creating the large pockets of engulfed

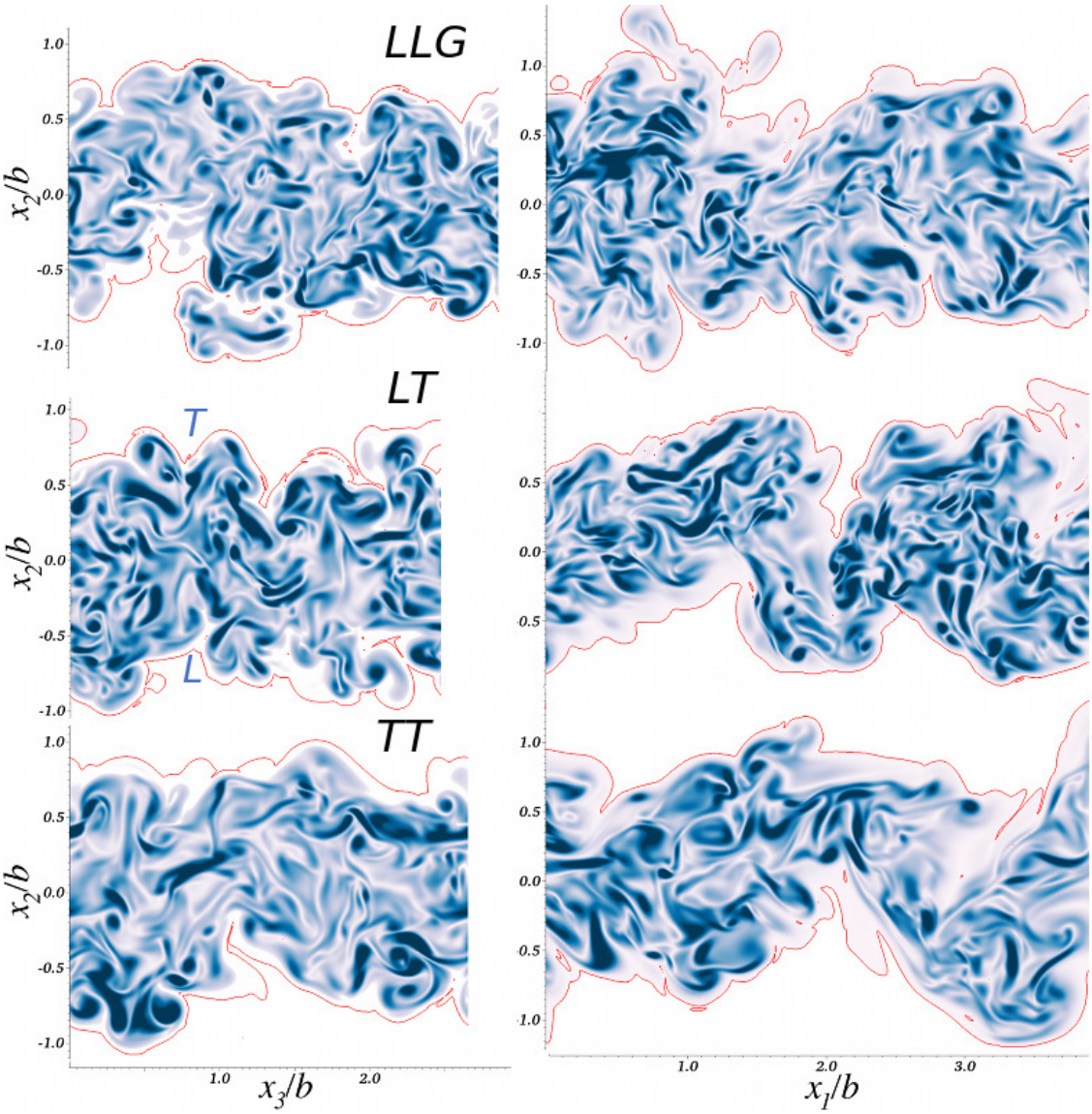

Figure 4.35: Instantaneous snapshot of vorticity magnitude at $t = 250$. Left column - $x_2 - x_3$ plane at $Lx/4$; right column - $x_1 - x_2$ plane at $Lz/2$. The outermost line represents the approximate turbulent/non-turbulent interface.

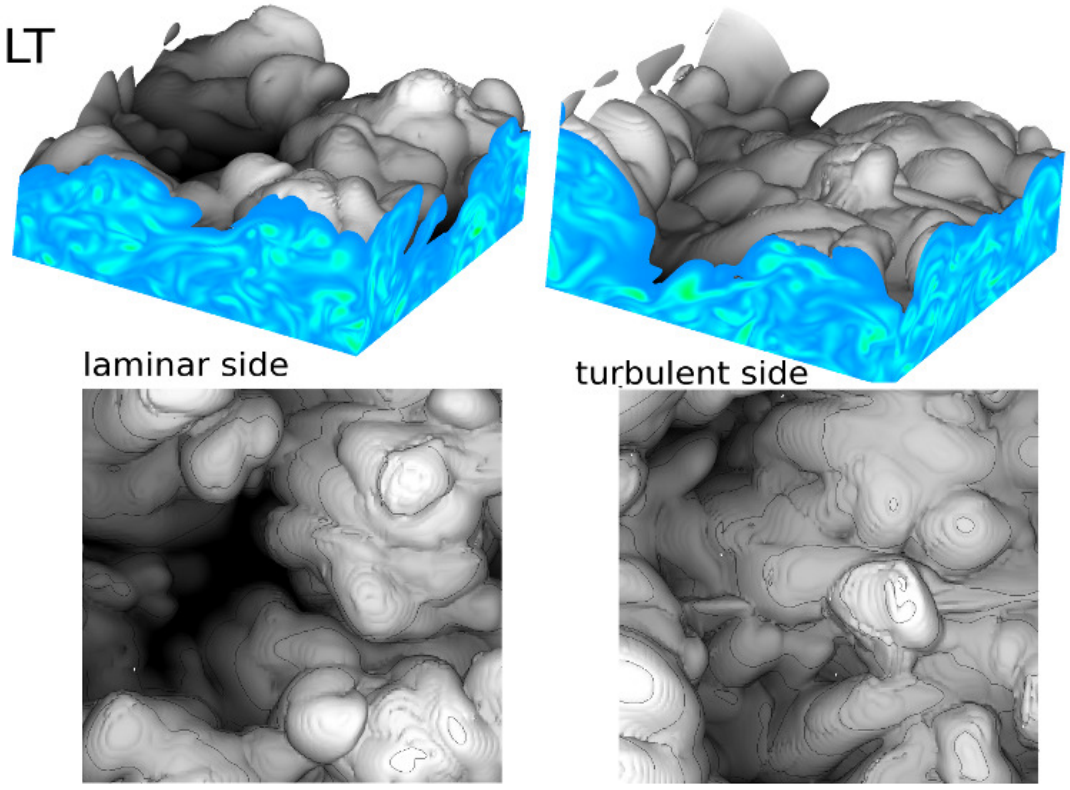

Figure 4.36: Visualization of the TNTI at time $t = 250$ over a small portion of the domain in LT (laminar side), LT (turbulent side). The side slices show the vorticity magnitude.

Table 4.2: Statistics of the TNTI at $t = 200$ / 250. Comparative statistics for the wake (Bisset *et al.*, 2002) and for the jet (da Silva & Pereira, 2008).

Statistics	**LLG**	**LT**	**TT**	**Wake**	**Jet**
Average height	0.896 / 0.867	0.840 / 0.841	0.874 / 0.871	0.79	-1.14
Variance	0.192 / 0.188	0.231 / 0.223	0.238 / 0.238	0.21	0.12
Skewness	-0.047 /-0.115	-0.116/-0.329	0.555 /0.455	0.03	0.09
Flatness	3.154/ 2.889	3.040/3.069	4.211 /3.916	3.28	2.95
Correlation	0.089 / 0.057	-0.080/-0.108	0.004 /-0.100	–	–

irrotational fluid. This is an important feature of the far wake dynamics as the mid-sized structures are decoupled from the initial conditions (see §4.5 and §4.6). In table 4.2, the average TNTI height, $\mathrm{H} = \langle \mathrm{h/b} \rangle$ is the ensemble average of h, the local distance between the TNTI and the centerplane (see figure 4.37) normalized by the wake half-width. The variance : $\sigma = \left\langle \mathrm{h'^2} \right\rangle^{0.5}$, where $\mathrm{h'} = \mathrm{H} - \mathrm{h/b}$ is the distance between H and the local TNTI. The skewness and flatness are respectively: $\left\langle \mathrm{h'^3} \right\rangle / \sigma^3$ and $\left\langle \mathrm{h'^4} \right\rangle / \sigma^4$. The higher the variance, the greater the possible entrainment through engulfment. Therefore, it comes as no surprise that the variance of the TNTI mirrors the trend in the entrainment rate among the wakes. The results in table 4.2 show an increased variance in the wake compared to the jet (da Silva & Pereira, 2008), which raises important questions regarding the relative importance of engulfment in both flows and the effect of the induced flow entrainment in the jet (Philip & Marusic, 2012). The skewness provides an indication on the degree of asymmetry of the TNTI about the average height. The strong positive skewness in TT suggests the predominance of large amplitude in the TNTI, possibly resulting from very large-scale contortions (recall figure 4.35). Alternatively, the negative skewness in LLG and LT implies the presence of deep pockets of irrotationality at the wake outer-edge. There is an unexplained discrepancy with the results by Bisset *et al.* (2002) (especially in the skewness), which could be related to the lower resolution and smaller computational domain of their simulation.

To investigate the influence of the large-scale rollers on the corrugations, the correlation between the top and bottom TNTIs is computed. At a each (x_1, x_3) location, a positive unitary value is assigned if the TNTI is above the mean (towards the outer wake) and a negative unitary value if it is below. Here, we neglect the overhanging TNTI. At each (x_1, x_3) location, a single value of h is assigned to each side of the wake. In figure 4.37, point A is 1, while points A', B and B' are -1. The values are correlated with the exact

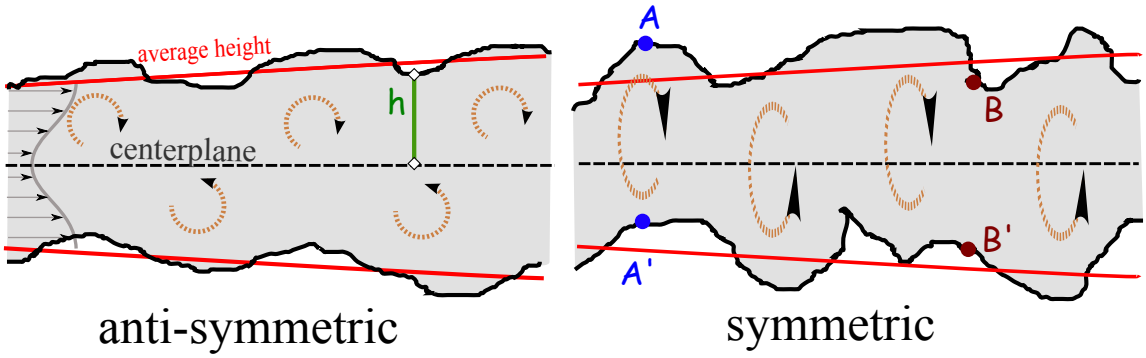

Figure 4.37: Sketches of the TNTI emphasizing the anti-symmetric and symmetric modes.

same (x_1, x_3) location on the opposite sides of the wake. In figure 4.37, points A and A' are negatively correlated while B and B' are positively correlated. The correlation reveals a small, positive correlation between the top and bottom TNTIs for LLG. Interestingly, LT and TT have a negative correlation which increases (in absolute terms) as the flow evolves; at $t = 280$, TT and LT respectively have a correlation of -0.16 and -0.13, while LLG is only 0.035. This finding is consistent with the previous results showing the predominant influence of the large-scale rollers modulating the structures in LT and TT, which then modify the TNTI.

Features of the TNTI contortions. The size of the bulges are estimated using an auto-correlation of the TNTI height in the streamwise and spanwise directions. The correlation varies greatly in time, although a consistent two-point correlation peak (with an auto-correlation of 0.1-0.15) is found at $x_1/b = 1.6 - 2.0$ and $x_3/b = 1.3 - 1.5$. These values are similar for all the wakes and consistent with the streamwise separation of the large-scale structures calculated by two-point velocity correlations in figure 4.29. The pdf of the tangent angle to the TNTI surface is shown in figure 4.38. The interface angle is calculated at each point by fitting a third-order polynomial, passing through 11 grid

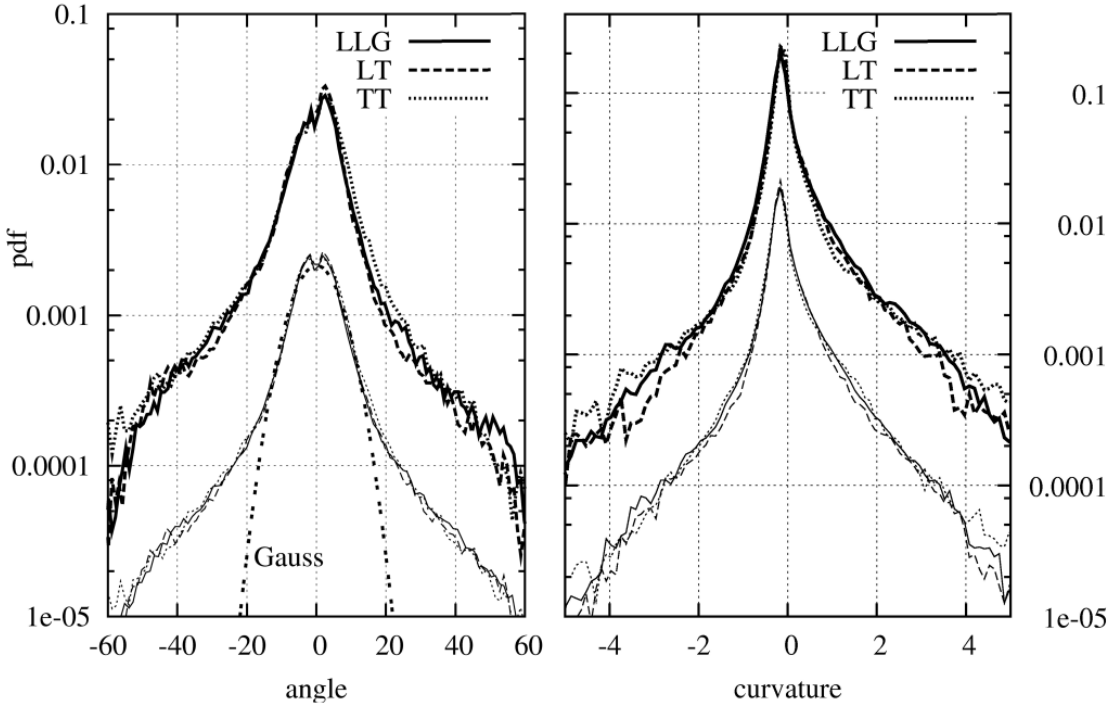

Figure 4.38: The pdf of the TNTI inclination angle (left) and curvature (right) in the streamwise (thick lines) and spanwise directions (thin lines - offset by a decade to ease the comparison) at time $t = 250$. A comparative Gaussian curve is shown in the left panel.

points (5 grid points on each side) along the spanwise or streamwise directions. The large number of grid points and low-order polynomial fit acts as a smoothing. Surprisingly, the pdfs are nearly identical for all wakes; although, the similarities among cases are partially a result of the choice logarithmic scale. As expected, the pdf has a slightly skewed positive peak with a broad-tailed, non-Gaussian distribution. In the streamwise direction (thick lines), the tails of the pdfs show a slight asymmetry as large angles (beyond $\pm 20°$) have a negative orientation. Previous experimental work showed a preferential angle of $+48°$ for the upstream edge while the downstream edge was inclined to $-66°$ (LaRue & Libby, 1976), hence corroborating the shift towards the large negative angles found here.

In the spanwise (thin lines), the pdf is perfectly symmetrical about zero because of the spanwise homogeneity. The TNTI curvature is calculated from the second derivative of the polynomial function passing through each point (figure 4.38, left). Similar to the tangent angle, the curvature shows a striking similarity among all the wakes in both the streamwise and spanwise directions. The peak is negatively shifted while the stronger positive tail is indicative of very deep valleys in the TNTI. The density functions in both the streamwise and spanwise directions are quantitatively similar.

4.8 Discussion and Concluding Remarks

We studied four prototypical wakes with different initial conditions (bottom-top): laminar-laminar with a Gaussian (LLG) and double Blasius (LLB), turbulent-turbulent (TT) and laminar-turbulent (LT) velocity fields. The study reaffirmed a well-known fact: wakes maintain some memory of their origin. We extended this conclusion to show that the multiplicity of approximate self-similar states is associated with a plurality of the far wake large-scale coherent structures. It has been often argued that a very large domain (possibly even an infinite domain) may be needed to reach a truly universal asymptotic state, independent of its origin. The investigation of such an idealized flow is inherently impossible because of the physical constraints of any experimental or computational setup. In the present work, we do not claim to settle the debate surrounding the possible existence of a universal, asymptotic state. Instead, we infer, from our approximate self-similar states, the statistical and structural nature of the far wake (and possibly even in the asymptotic, equilibrium region of the wake) - a reasonable conclusion given the large computational domain and time evolution of our simulations.

Self-similar multiplicity. Independently, each wake eventually reaches an approximate self-preserving state - even in the case of the initially asymmetric wake - but these states are not universal. In §4.4, we carefully tracked the path to self-similarity in all wakes. We investigated the evolution of the structures and the statistics in the Kelvin-Helmholtz transition (LLG and LLB), bypass transition (LT) and the merging of two statistically independent turbulent boundary layers (TT). In the approximate self-similar state, the initial condition dependence is evidenced by significant variations in spread rates (48 % relative variation), Reynolds stresses (40 % relative variation in peak values) and in TKE energy budget terms (up to 50 % relative variation). These variations occur despite an invariance of the mean flow profile. The multiplicity of the self-similar statistics is direct evidence of the long-term initial-condition dependence in the wake. Hence, it comes as no surprise that published experimental and numerical wake data show a large scatter in fully converged statistical quantities. Admittedly, a modified velocity and length scale based on the lateral spread rate (Moser *et al.*, 1998), reduces the variation among the turbulence statistics. Although mathematically sound, this scaling parameter is an intrinsic quantity tied to the wake evolution; therefore, it raises an important question: what leads to spreading rate variations in unforced planar wakes? It is our belief that part of the answer lies in understanding the plurality of far wake structures.

Prototypical structures. The far wake is made up of two distinct types of coherent structures: mid-sized, energetic, streamwise inclined vortical rods and large-scale spanwise rollers. In contrast to many recent works, we conclude that inclined vortical rods are the dominant prototypical mid-sized structures in the far field; horseshoes make up much less than 1 % of the total structures. The horseshoes are residual structures from the transitional process (LLG and LLB) or evolve from the hairpins in the initial boundary layers (TT), possibly also a structural feature of transition. Disintegration of the horseshoes

results from a combination of intense stretching of the legs by the large-scale rollers and the lack of a sustaining, locally-spanwise stretching of the head. Consequently, the head becomes diffuse and dynamically inactive, leaving counter-rotating, inclined rod-like legs as the dominant structures. Despite the disappearance of the head, vortex lines connecting the legs of course exist, a fact which has led many workers to misinterpret the outer wake spanwise vortex lines as evidence of horseshoes. Based on a λ_2-eduction technique, we found that mid-sized inclined structures are independent of the initial conditions and preferentially inclined at $\pm 30^\circ - 35^\circ$ in the streamwise direction. The inclination of the rods is shallower than the results from previous investigations (LaRue & Libby, 1974*b*; Hayakawa & Hussain, 1989) but is broadly consistent with recent PIV results of homogeneously sheared flow (Vanderwel & Tavoularis, 2011). The vorticity vector has a preferential inclination of $\pm 45^\circ$, which maximizes the stretching term and the TKE production.

Memory effects in large-scale organization. We found that the memory effects in the wake are maintained by a plurality of characteristic large-scale rollers - a clear possibility given the existence of a family of solutions to the governing equations of the two-point velocity correlations (Ewing *et al.*, 2007). Two types of spanwise coherent structures are identified among the wakes investigated (although we do not preclude the existence of other types of coherent structures): (i) small, staggered rollers, segregated on each side of the wake; and (ii) large rollers spanning the entire wake width. The former conform to the classical far wake organization of a secondary Karman vortex street and appear in bluff-body or freestream transitioning wakes. The latter, predominant in LT and TT, emerges from a symmetric mode which is excited during the evolution of the wake. The effects of these wake spanning rollers have been measured in experimental auto-correlation statistics (Bonnet *et al.*, 1986) but have not, until now, been described in detail. We found that a symmetric mode originates early in the near field, for both LT and TT, and is maintained

into the self-similar region. This mode is concealed by the superposition of a stronger anti-symmetric mode in the transitioning wakes (LLG and LLB). When the wakes evolve without a defined length scale (related to forcing, shedding or instability wavelength - all of which are anti-symmetric), the symmetric mode is dominant in the far wake. Incidentally, a side investigation of the linear stability characteristics of an approximate turbulent profile suggests the emergence of an unstable symmetric mode. But such a finding, and more specifically the inherently flawed assumption of linearity of the momentum equations in a fully turbulent velocity profile, warrants a further investigation.

Although we are able to explain some features of the far wake, many lingering questions remain and some new questions are raised by our study. There has been a longstanding belief that the inclined structures in the wake are energized by a continual straining along the separatrix between adjacent rollers (see e.g. Hussain & Hayakawa (1987)). Such a reasonable hypothesis has led many researchers to infer that mid-sized structures are inclined to maximize turbulent production, hence: 45° to the streamwise direction. This conceptual understanding is incompatible with the findings from our eduction technique which shows a shallower streamwise inclination of the structures. Another important question is the relation between the "sweep" motion from quadrant analysis of the boundary layer and the origination of the symmetric mode. Because of the lack of a centerplane wall in the wake (as opposed to the boundary layer), the so-called "sweep" motions are unconstrained and cross the centerplane; this cross-wake motion acts to correlate the initially independent boundary layers on either side of the centerplane. At present, the mechanisms behind the cross-correlation of the statistically independent boundary layers are unclear. Another puzzling question regards the discrepancy in the statistics between LT and TT. Both wakes show a similar large-scale structural organization and spanwise coherence, yet the resulting self-similar statistics and spread rates are drastically different; the turbulence statistics of

LT have more in common with LLG than with TT. Does this imply that different self-similar states may exist despite a similarity in the structures of the far wake? To elucidate this fundamental question, a further investigation, possibly with external forcing, would be needed.

Statistical multiplicity and structural plurality. Finally, we related the structural plurality to the statistical multiplicity in the approximate self-similar state by investigating: (i) the spanwise vorticity flux at the centerplane; and (ii) the entrainment and turbulent/non-turbulent interface (TNTI). We showed that the spread rate and the slope of the Reynolds shear stress $\langle u_1 u_2 \rangle$ at the centerplane are linked. The relative variation in the spread rates among the cases simulated was reflected by the centerplane slope of the Reynolds shear stress. We further extended the result to show that the spread rate is proportional to the advective transport of spanwise vorticity patches across the centerplane of the wake. Consequently, the spread is governed by the inner wake dynamics and is only indirectly affected by the outer wake. This conclusion can be seen in the decoupling of the spread rate from the entrainment rate. The entrainment is primarily driven by the engulfment of irrotational flow which is enhanced by the large-scale symmetric mode structures in the far wake. The consequence of the wake-spanning coherent structures in TT and LT leads to the formation of large pockets of irrotationality (quantitatively measured by the high variance of the TNTI) and the strong correlation between the TNTIs on both sides of the centerplane.

Chapter 5

Compressibility Effects in the Transition of High-Speed Planar Wakes

5.1 Abstract

The effects of compressibility on the transition of the high-speed planar wake is investigated through linear stability analysis and direct numerical simulations at initial relative Mach numbers of 0.3, 0.8, 1.2 and 2.0 and for Reynolds numbers up to 3000 based on the initial velocity defect and wake half-width. The staggered configuration of the emerging transitional structures of the planar wake is dictated, when no external forcing is applied, by the linear stability mode with the greatest exponential growth. The wavelength of this two-dimensional, anti-symmetric mode increases approximately linearly with the Mach number, and at $Ma_r = 2.0$ is 18 % longer than at $Ma_r \to 0$. Trivially, the longer wavelength results in rollers with a greater streamwise separation and larger circulation - a configuration which modifies both statistics and structures of transition. Assuming incompressible and inviscid vortex dynamics, the Biot-Savart induced cross-wake momentum transfer increases linearly with increased streamwise separation and circulation of the

rollers. Obviously, the compressibility effects modify the domain of influence of these structures. The velocity gradients of the local Mach number promote an increased cross-wake and reduced streamwise communication. The reduced streamwise domain of influence impedes the roller pairing and, for $Ma = 2.0$, the pairing is completely suppressed. In the absence of pairing, the rib structures connecting rollers on either side of the wake develop very distinct features compared to the low-speed wake. The effects from the most unstable mode are also observed in the increasing ellipticity of the rollers which rotate during the roll-up process. In addition to the structural understanding of the wake, the study of influence of compressibility on the convection velocity, Reynolds stress anisotropy and shocklet formation are thoroughly discussed.

5.2 Introduction

The understanding of high-speed transitional wakes is of great interest in scramjet engines, aero-optic laser diffraction and transonic turbomachinery. At the heart of this interest lies the desire to modify, predict and/or control the large-scale coherent structures originating during transition. From an engineering perspective, these highly anisotropic structures are important for their mixing enhancement potential as they are the main contributor to the large-scale mixing (Brown & Roshko, 1974), a generally desired attribute for high-speed fuel injector systems. At the same time, these structures are the primary source of aeroacoustic disturbances resulting from the large pressure gradients and vortical reconnection (Sandham, 1994; Virk *et al.*, 1995; Bastin *et al.*, 1997) which, downstream, may lead to combustion oscillations in supersonic propulsion systems (Choi *et al.*, 2005). In order to control these conflicting characteristics, the effects of compressibility on the transitional high-speed wake need to be understood fully.

Characterizing compressibility effects. Insight into compressibility effects are gained through the study of the high-speed mixing layer - one of the simplest and ubiquitous free shear flows. The most intriguing effect is the reduced lateral spreading with increased convective Mach number. From early experiments, it was clear that the reduced turbulent kinetic energy (TKE) explains the lower spread rate; density variations have a second-order effect (Brown & Roshko, 1974) . What is less clear is the exact mechanism by which the compressibility limits the TKE growth. From the governing equations, the evolution of TKE for a compressible flow is:

$$\frac{dK}{dt} = P + \Sigma^d - \bar{\epsilon}_s - \bar{\epsilon}_d \tag{5.1}$$

where P, Σ^d,$\bar{\epsilon}_s$ and $\bar{\epsilon}_d$ are respectively the production, pressure-dilation correlation, solenoidal- and dilational-dissipation. Early works attributed the lower turbulent kinetic energy to a negative pressure-dilation and dilatational-dissipation terms in shear flows (Zeman, 1990, 1991; Sarkar *et al.*, 1991). But, outside zones of large gradients (such as shocks), the dilation alone cannot account for the extent of the TKE reduction. Breidenthal (1992) proposed a novel structural explanation for the reduced spread rate using a sonic-eddy model to account for the reduced entrainment of high-speed flows. The insight gained from modern computational simulations has allowed more recent investigations to conclude that the reduction of the pressure-strain term implicitly inhibits the turbulence production (Blaisdell *et al.*, 1993; Vreman *et al.*, 1996; Freund *et al.*, 2000*b*; Pantano & Sarkar, 2002; Foysi & Sarkar, 2010) by reducing the transfer among velocity components. Naturally, this modifies the near field anisotropy of the flow (Pantano & Sarkar, 2002).

Fewer studies have specifically tackled the issue of compressibility in the planar wake.

This is partly because the compressibility effects, characterized by the relative Mach number $Ma_r = U_o/c_\infty$ (where U_o is the centerline velocity defect and c_∞ the freestream speed of sound), are not constant and, therefore, more difficult to isolate than in the mixing layer. The variability of the compressibility effects also raises an important inconsistency in the scaling of the wake. If compressibility inhibits the spread rate through a reduction of the pressure-strain term (as in the case of the mixing layer), then the wake half-width appears to be an ill suited non-dimensionalization parameter as the compressibility decreases with the wake evolution. Alternatively, if the spread rate is invariant to the relative Mach number (in the mid and far wake when compressibility may still be non-negligible), a structural based explanation must be sought to explain the discrepancy with the mixing layer. Even though the wake tends toward a fully incompressible state as the defect becomes null, the asymptotic state of the high-speed wakes may nonetheless differ from its low-speed counterpart. Since free shear flows maintain a "memory" of their origin, it can be inferred that a differing far wake structural organization and statistics found by Bonnet *et al.* (1991) may be tied to the near wake evolution. Consequently, the effects of compressibility on the transitional mechanisms of the planar wake need to be well understood.

Transition of planar wakes. As for all shear flows, the compressibility has a stabilizing effect in the wake (Behrens, 1968; Demetriades, 1971, 1978); a finding confirmed by hydrodynamic stability calculations (Gold, 1963; Lees & Gold, 1966; Chen *et al.*, 1990; Papageorgiou, 1990; Watanabe & Maekawa, 2004). In contrast to the obliquity of the primary instability mode in the high-speed mixing layer (above $Ma_c = 0.6$), a two-dimensional anti-symmetric mode is found to be dominant for all Mach numbers (Chen *et al.*, 1990; Watanabe & Maekawa, 2004). This result was contradicted by Papageorgiou (1990) who questioned the validity of the parallel flow assumption inherent in the temporal stability

calculations (Chen *et al.*, 1990; Watanabe & Maekawa, 2004) and showed that a three-dimensional wave inclined at 60° has the highest growth rate for spatially evolving wakes with a Gaussian velocity profile at $Ma_\infty = 3.0$. The obliquity of a transitional mode was experimentally found by Lysenko (1999) by artificially forcing a splitter-plate wake at $Ma_\infty = 2.0$. Although, from their experiment, it is unclear why the oblique perturbation undergoes the largest growth. It could be one of the following reasons: (1) the growth of the most unstable oblique mode, as found by (Papageorgiou, 1990); (2) or, as hypothesized by Lysenko (1999); Lysenko *et al.* (2008), a receptivity of an inclined symmetric mode which emerges at $Ma_r > 1.2$ (Chen *et al.*, 1990; Watanabe & Maekawa, 2004); (3) or, a secondary acoustic mode which resonates between the sonic lines of the wake as in the boundary layer (Gill, 1965; Mack, 1990); (4) or a, triadic non-linear interaction as observed in the H-type transition in the boundary layer (Hebert, 1988) or the incompressible wake (Wu, 1996). The debate surrounding the origin of the three-dimensional modes remains unanswered and central to the understanding the transitional mechanism of the planar wake.

Structures in high-speed flows. In idealized free shear flows, the transitional structures emerge from the length scale imposed by the fastest growing instability mode. There has been some debate on the presence (or absence) of transitional spanwise coherent rollers. Kendall (cited in (Laufer, 1975)) noted a clear absence of structures in the transitional region. More recently, experiments by Clemens & Smith (1998) found that the high-speed wake shares many structural similarities with its incompressible counterpart, most importantly in terms of the two-dimensionality of the transitional rollers connected by rib-like structures. Experimentally, it is difficult to establish if the two-dimensionality is the result of the linear growth of the most unstable mode or if it originates from the receptivity of

the unsteady Kutta condition (Barone & Lele, 2005) or the two-dimensional convective instability in the base flow (Sandham & Sandberg, 2009). What is clear is that the wake and the transitional structures are highly sensitive to the splitter-plate design (Althaus, 1990). In the intermediate and far wake, the two-dimensionality of the structures has been well established (Bonnet & Chaput, 1986; Nakagawa & Dahm, 2006) with a Strouhal number of 0.3 (Behrens & Ko, 1971; Gai *et al.*, 2002).

Direct numerical simulations of idealized wakes have been used to help clarify the transitional mechanisms. Using a laminar base flow with eigenmode perturbations, Chen *et al.* (1990) and Watanabe & Maekawa (2004) showed many qualitatively similarities to the low-speed wake: two-dimensional and staggered spanwise rollers connected by rib-like structures. This apparent structural invariance to the Mach number contrasts the emergence of Λ-type structures of the high-speed mixing layer (Kourta & Sauvage, 2002; Ma *et al.*, 2009). When the base flow was perturbed with broadband random fluctuations (Watanabe & Maekawa, 2004), an oblique mode shortly dominates the early wake evolution before being overtaken by the growth of the primary two-dimensional mode (see Watanabe & Maekawa (2004), fig. 5(a)) - clearly an unexpected finding based on linear stability results. Unfortunately, the available direct numerical simulations of high-speed planar wakes (Chen *et al.*, 1990; Watanabe & Maekawa, 2004) are inadequate to understand fully the origin of the three-dimensional modes. More specifically, if they are caused by an oblique principal mode, or if it caused by the receptivity of a secondary symmetric mode. The reasons for the inadequacy of existing DNS simulations are the (1) limited stream- and spanwise computational domains (L_x twice the most unstable wavelength Chen *et al.* (1990)) cannot capture the symmetric instability mode which is over twice the streamwise wavelength at $Ma = 2.0$. (2) the low Reynolds number of the simulations ($Re = 300$ (Chen *et al.*, 1990) and up to $Re = 1000$ (Watanabe & Maekawa, 2004)) limits the growth

of the oblique instability mode, which is shown herein to be very sensitive to viscous effects. These shortcomings invite a closer investigation of transitional mechanisms with modern-day computational resources with a canonical setup, free of trailing edge effects. Given the recent surge in high quality simulations of supersonic axisymmetric wakes (Sandberg & Fasel, 2006; von Terzi *et al.*, 2009; Meliga *et al.*, 2010; Sandberg, 2011), planar wake simulation results are needed.

Our understanding of transitional high-speed planar wakes is far from complete. In this work, we seek to contribute to the understanding of the influence of compressibility on transition as well as the onset of three-dimensionality in the wake. We shed light on some lingering questions: What is the effect of compressibility on the structures in the transitional flow? Do shocklets appear in the wake and do they modify the dynamics of transition? Can the convective velocity of the structures be estimated by an isentropic assumption? The present investigation rests on a combined study of the linear stability analysis and high quality direct numerical simulations of the transitional high-speed wake to gain insight into the flow physics. The work is divided as follows. The numerical details of the linear stability analysis and numerical simulations are presented in the §5.3. The stability results are detailed in §5.4 and, based on these findings and an idealized understanding of the wake, we infer the structural features of the non-linear stage of transition in §5.5. These theoretical results are supplemented by our direct numerical simulations of the transitional high-speed wakes in §5.6. The structural organization and the evolution of the rollers is detailed in §5.7.

5.3 Numerical Details

5.3.1 Viscous linear stability theory

A viscous, compressible linear stability analysis tool was developed to study the transitional characteristics of the high-speed wake, based on the previous work by Chen *et al.* (1990) and Watanabe & Maekawa (2004). A periodic disturbance, with a given stream- and spanwise wavelength, is applied to a laminar base flow. The temporal growth of the perturbation is computed from the linearized three-dimensional Navier-Stokes equations (conservation of mass, momentum and energy) in non-conservative form. In order to assure the validity of our linear assumption, we impose a very low-amplitude disturbance with respect to the base flow. The fluctuations are of the form : $\mathbf{\Phi} = \hat{\mathbf{\Phi}} \exp^{i(\alpha x + \beta y - \omega t)}$, where $\mathbf{\Phi}$ represents a vector of the primitive variables: $[\rho, u, v, w, T]$. For a temporal stability calculation, α and β are real and respectively the stream- and spanwise wavenumber, while ω is complex with the imaginary part representing the temporal growth rate of the given perturbation. Assuming a parallel flow, we consider the stability characteristics of an initial Gaussian velocity profile: $U(y) = U_\infty - U_0 \exp(-\ln(2) y^2)$, where U_∞ and $U_0 = \ln(2)$ are the freestream velocity and centerline defect. These values are chosen to validate our results with the previous investigations (Chen *et al.*, 1990; Watanabe & Maekawa, 2004). The thermodynamic variables are related through the equation of state where the non-dimensionalized static pressure was assumed to be constant in the cross-wake. The initial temperature (and consequently the density) distribution was determined by using the Crocco-Busseman relation with a unitary Prandtl value. In the cross-wake direction, a hyperbolic tangent stretching was used to convert the doubly infinite domain to a finite computational domain defined on $\zeta = [0, 1]$ using the spectral mapping techniques by Cain *et al.* (1984). The linearized equation set can be solved as a simple eigenvalue problem of

the form $\mathcal{L}\hat{\mathbf{\Phi}} = \omega\hat{\mathbf{\Phi}}$ where $\mathcal{L}$ is a linear operator acting on the eigenvector $\hat{\mathbf{\Phi}} = \left[\hat{\rho}, \hat{u}, \hat{v}, \hat{w}, \hat{T}\right]$ for a given eigenvalue, ω. The eigenvalue with the largest imaginary part represents the maximal growth of the imposed perturbations. By investigating the resulting real part of the eigenvectors of the equation, we differentiate between the symmetric (varicose) and anti-symmetric (sinuous) modes. The complete mathematical formulation of the problem can be found in Watanabe & Maekawa (2004) and is not repeated for sake of brevity. Numerically, the eigenvalue calculations are performed using the LAPACK scientific library. A gradient-based SLSQP optimizer, implemented through the pyOpt package (Perez *et al.*, 2012), was used to reduce the computational time required to identify the optimal growth over the solution domain. We confirmed the validity of our linear stability code by comparing our results with previously calculated linear stability statistics from Chen *et al.* (1990) and Watanabe & Maekawa (2004). The complete Python code is available in appendix H.1.

5.3.2 Direct numerical simulation details

5.3.2.1 Governing equations

The equation set for the time-dependent compressible Navier-Stokes equations, written in conservative form, consists of the equation for the conservation of mass, momentum and total energy along with an additional passive scalar equation. The equations are non-dimensionalized by the freestream velocity, $\mathbf{U} = U_\infty$ and the initial wake half-width, $\mathbf{L} = b_0$. The other parameters are non-dimensionalized with the freestream values. The corresponding non-dimensional pressure and energy are respectively: $p = p^*\rho_0 c_0^2/\gamma$ and $E = E^*/\rho_0\mathbf{U}^2$, while the Reynolds, Prandtl and Mach numbers:

$$Re = \frac{\rho_0 \mathbf{U}\mathbf{L}}{\mu_0}; \qquad Pr = \frac{\mu_0 c_p}{\kappa_0}; \qquad Ma = \frac{\mathbf{U}}{c_0} \tag{5.2}$$

The non-dimensionalized governing equation set is:

$$\frac{\partial \rho}{\partial t} + \frac{\partial \left(\rho u_i\right)}{\partial x_i} = 0$$

$$\frac{\partial \left(\rho u_i\right)}{\partial t} + \frac{\partial}{\partial x_j}\left(\rho u_i u_j + p/\left(\gamma Ma^2\right)\delta_{ij}\right) = \frac{1}{Re}\frac{\partial \sigma_{ij}}{\partial x_j}, \tag{5.3a}$$

$$\frac{\partial E}{\partial t} + \frac{\partial}{\partial x_i}\left[\left(Eu_i + p/\left(\gamma Ma^2\right)\right)\right] = \frac{1}{PrRe\left(\gamma-1\right)Ma^2}\frac{\partial}{\partial x_i}\left(\kappa\frac{\partial T}{\partial x_i}\right) + \frac{1}{Re}\frac{\partial u_j \sigma_{ij}}{\partial x_i} \tag{5.3b}$$

where $\sigma_{ij} = \mu\left(\frac{\partial u_i}{\partial x_j} + \frac{\partial u_j}{\partial x_i} - \frac{2}{3}\frac{u_k}{x_k}\delta_{ij}\right)$. The above equation set is closed with the normalized equation of state: $p = \rho T$. The energy term in the last equation corresponds to the total energy which is the sum of the internal and kinetic energy, such that: $E = \frac{p}{(\gamma-1)\gamma Ma^2} + \frac{1}{2}\rho\left(u_i u_i\right)$. The viscosity is uniquely function of the temperature of the fluid and follows a power law of the form: $\mu = T^{0.76}$.

5.3.2.2 Numerical scheme

We developed and validated a predictor/corrector finite difference solver, which was used to compute the compressible Navier-Stokes equations. The spatial scheme is fourth-order accurate inside the domain with a one-sided, third-order scheme at the finite boundaries. The high-order MacCormack-like scheme was chosen as the biased stencil on the convective terms provides a robust and efficient method to deal with the high gradients (without adding artificial viscosity) while offering acceptable dispersion and dissipative qualities. The over-resolution required to account for the slightly inferior numerical qualities (compared to spectral or Padé schemes, for example) is offset by the computational efficiency, parallelisability and small memory footprint. The time-dependent compressible Navier-Stokes equations are solved in conservative form with skew-symmetric convective terms for robustness and to reduce the aliasing errors. The time was advanced using a

Ma	Re	Grid size	Domain size	$\eta/\Delta x\|_{min}$
0.8	3000	$1600 \times 496 \times 596$	$67.9 \times 20 \times 26.1$	0.61
2.0	3000	$1792 \times 496 \times 696$	$78.3 \times 20 \times 29.9$	0.88

Table 5.1: Characteristics of the numerical simulations of the transitional wake. The $\eta/\Delta x|_{min}$ represents the minimal value over the domain, during the entire transitional simulation.

second-order explicit scheme in which the time-step was set by an imposed acoustic Courant number. The numerical code was extensively verified against the analytical solution of a viscous shock, Taylor-Green vortex and decaying compressible isotropic turbulence. Validation with experimental wake data in the incompressible-limit was performed in Hickey *et al.* (2012).

5.3.2.3 Grid, boundary and initials conditions

A homogeneous grid was used in the stream- and spanwise directions. In the cross-wake direction, the grid was clustered about the centerline using a hyperbolic tangent mapping. The grid resolution was chosen to resolve down to the Kolmogorov scale for the entire evolution of the wake. As the flow is temporally evolving, periodic boundary conditions were set in the streamwise (x) and spanwise (z) directions. In the cross-wake direction (y), non-reflecting boundary conditions (Thompson, 1990), supplemented with sponge layers, were used to attenuate spurious numerical oscillations at the boundaries. The domain size was selected to be eight times the most unstable anti-symmetric wavelength in the streamwise direction and four times the most unstable oblique symmetric mode in the spanwise direction. Consequently, the domain sizes are Mach number dependent. In the cross-wake, the domain height was chosen large enough to accommodate at least six wake half-widths at all times during the simulation. The very large computational domain was

justified by the need to enhance the sampling of higher-order statistics, to reduce the dependence of the domain size on the developing instability modes and to allow the growth of the long-wavelength oblique varicose mode.

The simulations are temporally evolving. Although temporal simulations remain of great scientific interest, they fall short in faithfully reproducing the transition of wake flows. On the one hand, the temporal simulations require a parallel flow assumption which is not entirely valid in the case of transitional wakes. In addition, the instability modes are unable to grow spatially, as would occur in a spatial simulation or experimental setup, and are constrained by the computational domain. A final issue concerns the infinite propagation in the stream- and spanwise direction of acoustical, vortical and entropic perturbations. These perturbations then recontaminate the computational domain, whereas in the spatial case, they are simply advected out of the domain. Despite these valid concerns, the study of temporal transition of free shear flow remains valuable in understanding transitional mechanism. Many temporal studies of high-speed free shear flows have shown convincing quantitative matching of experimental results (*e.g.,* Pantano & Sarkar, 2002). In addition, the temporal wake evolves without a receptive trailing edge and therefore we are able to isolate the intrinsic wake transition from the wake generating body. Furthermore, given the lengthy transition caused by the increasing stability of the high-speed wake, we are able to simulate higher Reynolds number flows than could be afforded by a spatial simulation.

The wakes were simulated at a constant Reynolds number of 3000, based on the initial wake half-width and initial velocity defect, at two different initial relative Mach numbers: $Ma = 0.8$ and 2.0 (herein, the wakes are identified by their initial relative Mach number; for clarity, the subscript "r" from Ma_r is dropped). To resolve fully all the scales of turbulence, a grid of 473 and 619 million nodes (respectively for $Ma = 0.8$ and 2.0) was needed, see the numerical details in table 5.1. A laminar initial velocity profile was used:

$\langle u(y)\rangle = U_\infty - U_d \exp(-\ln(2)y/b)^2$ where U_∞, U_d and b are respectively the freestream velocity, the initial deficit velocity and the initial wake half-width. Admittedly, the choice of a Gaussian, instead of a double Blasius profile, may inhibit the development of near wake instability modes originating from a double boundary layer profile (Papageorgiou & Smith, 1989; Papageorgiou, 1990). In Hickey *et al.* (2012), the evolution of a Gaussian and double Blasius wake profiles were compared in the incompressible limit, other than a delayed transition, the main characteristic structures and statistics remain surprisingly similar. Based on these conclusions, we deemed that an initial Gaussian profile allows for the greatest generality for the study of the temporally evolving wake. The laminar base flow velocity and temperature fields were related through the Crocco-Busemann relationship. The initial wake profile is perturbed by broadband velocity fluctuations for the components in x- and y-directions with an rms value of 1.5 % of the velocity deficit, in order to break the symmetry about the centerline. The broadband perturbations have a greater generality but result in a longer transition compared to specific mode forcing. The initial wake half-width was unity resulting in a constant mass-flux defect of $\dot{m} \approx 1$. The computations were conducted at the High Performance Computing Virtual Laboratory (HPCVL) in Kingston, Ontario using up to 64 processors which required a wall clock time of about 45 days per simulation. In addition to these computations, we conducted numerous lower Reynolds number simulations at $Re = 1500$ on a constant computational domain (L_x, L_y, L_z= 50, 25, 12.5) and grid (56 million grid points) for Mach numbers of 0.3, 0.8, 1.2 and 2.0. These fully resolved simulations are used to validate the generality of our results at different relative Mach numbers. Grid convergence and resolution validations are presented in appendix G.

5.4 Linear Stability of Transitional High-Speed Wakes

Given the symmetry of the laminar base flow, two classes of instability modes arise. The anti-symmetric (or sinuous) mode is defined at the centerline as $\hat{u} = 0$ and $d\hat{v}/dy = 0$ while the symmetric (or varicose) mode is defined as $\hat{v} = 0$ and $d\hat{u}/dy = 0$. Both modes have exponentially unstable components in the two-dimensional planar wake.

5.4.1 Sinuous instability mode

As in the incompressible wake, the highest exponential growth is achieved for a purely two-dimensional, anti-symmetric (sinuous) perturbation for all Mach numbers. This perturbation results in the formation of two alternating rows of staggered spanwise coherent rollers, sharing many characteristics with the classical Karman vortex street in the wake of a bluff body. From previous investigations (Chen *et al.*, 1990; Watanabe & Maekawa, 2004), an increasing Mach number decreases the maximal exponential growth of the primary disturbance. Between the freestream Mach numbers of $Ma = 0.01$ and $Ma = 2.0$, the exponential growth rate is reduced by 25 %, see figure 5.1; a modest decrease compared to the very drastic drop in growth rates observed in the mixing layer (a reduction of about 18 % from the incompressible growth rate at $Ma_c = 0.4$ and 72 % at $Ma_c = 1.2$ (Sandham & Reynolds, 1990)). The viscosity has a slightly stabilizing effect on the high-speed wake. The stabilizing effect of viscosity is minimal compared to the inflectional instability of the mean profile. As noted by Watanabe & Maekawa (2004), there is less than 2 % difference between growth rate at $Re = 1000$ and the fully inviscid case for all Mach numbers studied, see figure 5.1. Overshadowed in the previous studies is the striking correlation between the growth rate and the wavelength of the most unstable mode. The wavelength of the most unstable mode is similarly about 18 % longer at a Mach number of 2.0 compared to the

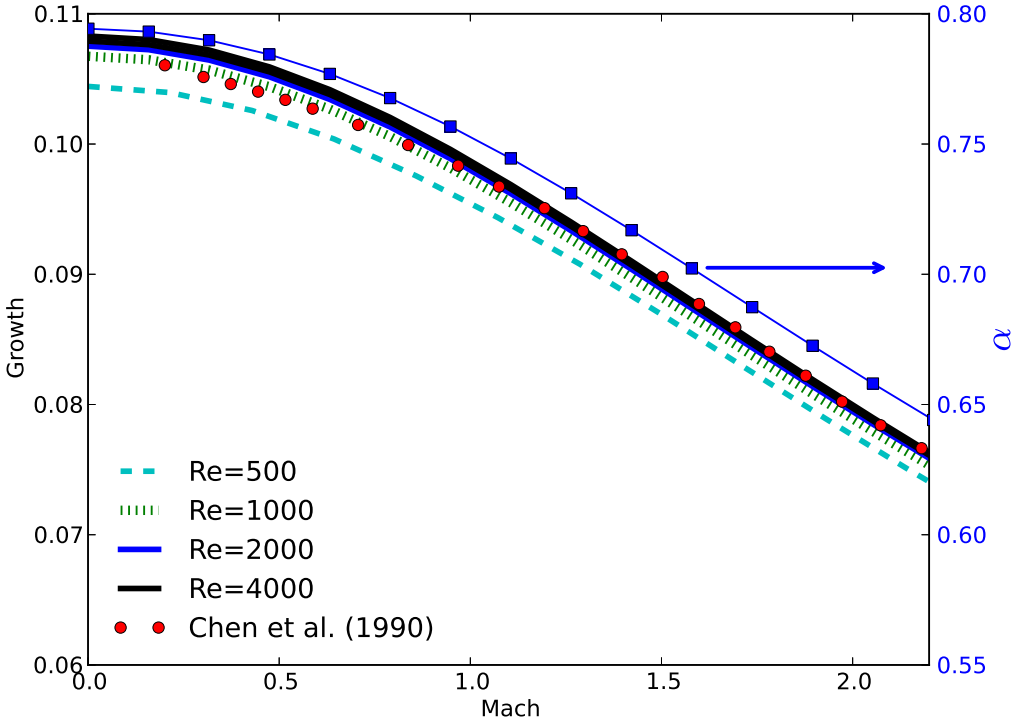

Figure 5.1: Influence of compressibility and viscosity on the maximal growth rate of the instability modes (two-dimensional, anti-symmetric mode). The maximal exponential growth for Reynolds numbers of 500, 1000, 2000 and 4000 are compared with the inviscid results by Chen *et al.* 1990.

incompressible baseline. The concomitant effects of an increased wavelength are discussed in the following sections and is central to our understanding of high-speed wake transition.

5.4.2 Varicose instability mode

The symmetric (varicose) mode plays a secondary role in the transitional mechanism of the high-speed wake, as the growth rate is less than a third of the primary anti-symmetric instability. Nonetheless, the importance of the symmetric mode cannot be neglected as it

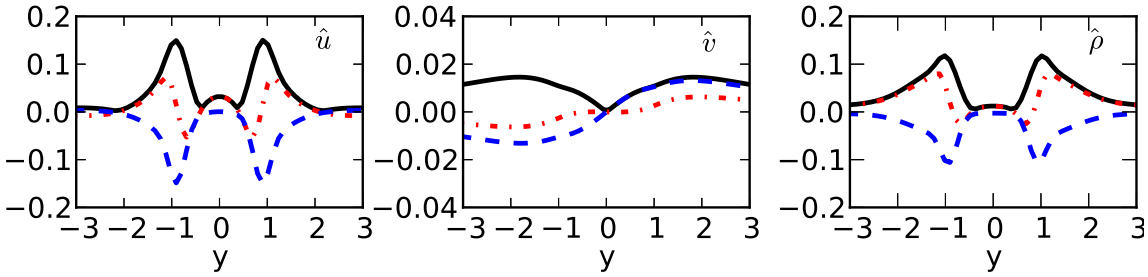

Figure 5.2: Eigenvector of the most unstable mode at Re =10000 at Ma=1.92 (α= 0.239, β =0.264). The real (red line, dashed-dot), imaginary (blue line, dashed) and the magnitude (black line, full) are presented for u, v and ρ.

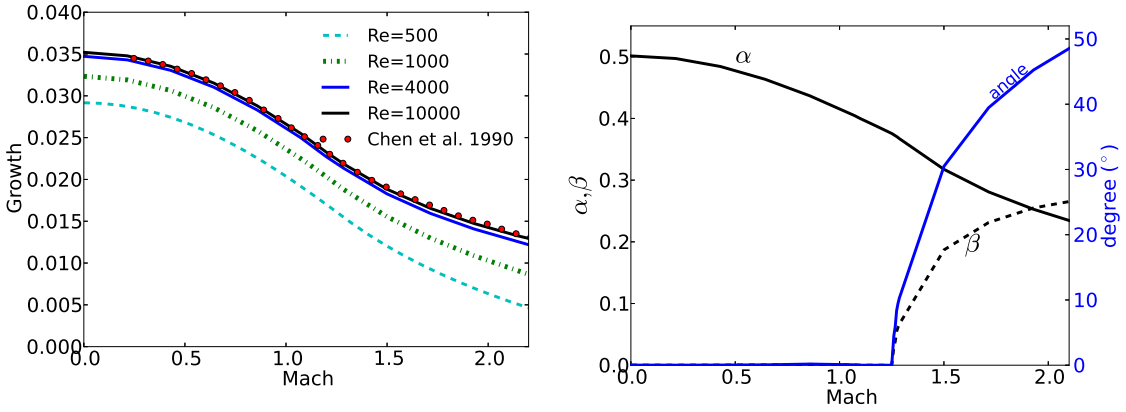

Figure 5.3: Influence of compressibility and viscosity on the varicose (two- and three-dimensional, symmetric perturbation) mode in the high-speed wake. The viscosity has a strong stabilizing effect on the growth (top). The stream-/spanwise wavenumbers of the most unstable symmetric mode for Re = 10000 are presented along with the corresponding angle of the optimal disturbance.

may modulate the anti-symmetric mode, as noted in the incompressible case by Wygnanski *et al.* (1986). For completeness, figure 5.2 shows the eigenvectors of the most unstable varicose mode. The influence of this mode is particularly important as it shifts from a purely two-dimensional to an oblique perturbation at around $Ma = 1.2$ (see figure 5.3) as previously observed by Chen *et al.* (1990) and Watanabe & Maekawa (2004). These findings recall the onset of three-dimensionality in the transitional high-speed mixing layer above a convective Mach number of 0.6. Similar to the primary mode, the symmetric instability is damped by both viscous and compressibility effects. The viscous effects play an important role in impeding the growth of this mode. Figure 5.3 shows that at $Re = 1000$, the exponential growth rate is 10 % lower than the inviscid case at $Ma = 0.001$ - at Mach number 2.0, it is 30 % lower. The varicose mode is nearly completely suppressed for Reynolds numbers under 250. In addition to the stabilizing effect of viscosity, the wavelength of the symmetric mode is over twice the streamwise length of the sinuous mode over all the Mach numbers investigated. The combined effects of an inhibited growth rate caused by viscosity and the longer instability wavelength may have hindered the observation of the emergence of this three-dimensional mode in the previous direct numerical simulations of transitioning high-speed wakes. The previous simulations were conducted at $Re = 300$ (Chen *et al.*, 1990) and 1000 (Watanabe & Maekawa, 2004) on computational domains which were clearly too small to capture the varicose modes. As a result, the effects of the three-dimensional symmetric mode were probably inhibited. These observations invite a new investigation, at higher Reynolds number and on a larger domain in order to accommodate the longer wavelengths.

5.5 Features of Non-Linear Stage of Transition

In free shear flows, the wavelength imposed by the fastest growing instability mode characterizes the length scale of the emerging transitional structures. Based on the results from linear stability theory §5.4 (assuming no external forcing), it comes as no surprise that the rollers are purely two-dimensional with an increasing wavelength with the Mach number of the flow. The increased wavelength of the primary instability mode leads to two, seemingly trivial, features of the high-speed wake transition: (1) increased streamwise separation between neighboring rollers on the same row; (2) increased circulation of each roller (as the circulation is function of the length of a shear layer). For a fixed wake half-width of the base flow, b, the compressibility decreases the ratio of the cross-wake to streamwise separation, h/λ, where h represents the cross-wake separation between rows (which is, to a close approximation, function of the wake half-width, b) and λ the streamwise separation between neighboring rollers. In the present section, we consider, in a very idealized setting, the consequences of the increasing streamwise separation and circulation of the rollers. These effects are first considered in the purely incompressible case, thereafter, the effects of compressibility are taken into account.

5.5.1 Effect of roller separation in the incompressible limit

The stability of the staggered array of spanwise vortices, forming a Karman vortex-like street, has been shown to be unstable to infinitesimal perturbations for two-dimensional vortex filaments in the inviscid case - except for the well-known neutrally stable configuration of $h/\lambda = 0.28055$. Using an inviscid hollow vortex model, Crowdy & Green (2011) showed a cross-over point at an aspect ratio of $h/\lambda = 0.34 - 0.36$. Above this threshold, the pairing occurs between neighboring roller on the same row, as typically observed in most

low-speed transitioning wakes. Below this threshold, it occurs between rollers on opposite sides of the centerplane (merger between rollers with opposite circulation). The stability properties of such flows were considered in Llewellyn Smith & Crowdy (2012).

Here, we consider the influence of the separation ratio h/λ on the induced velocity in a staggered vortex array. Assuming a streamwise separation, λ, the circulation of each spanwise coherent roller is: $\Gamma_r = \gamma\lambda$, where γ represent the strength of the idealized vortex sheet. The streamwise separation of the rollers is directly related to the instability wavelength (which is tied to the Mach number of the wake). The lateral cross-wake separation of the rollers varies with the lateral spreading of the wake.

Assuming a two-dimensional inviscid flow, the magnitude of the induced velocity caused by a single vortex filament (representing an idealized roller) is: $\vec{v} = \frac{\Gamma_r}{2\pi\vec{r}}$, where $\vec{r}$ is the distance from the center of the point vortex filament of circulation Γ_r; the induced velocity is aligned perpendicular to the radius vector at each point. The principal contributions to the cross-wake induced velocity component is caused by the two neighboring rollers (noted with indices 1 and 2 in figure 5.4) on either side of the centerplane; the rollers further away have a secondary effect on the induced velocity. Figure 5.4 illustrates the principal dimensions. Through simple trigonometric considerations, the velocity components in the y-direction are:

$$v_y = v_{y_1} + v_{y_2} = v_1 \frac{\lambda/4}{r_1} + v_2 \frac{\lambda/4}{r_2} \tag{5.4}$$

By introducing the formulation for the induced velocity, we obtain:

$$v_y = \frac{\lambda^2\gamma}{8\pi}\left(\frac{1}{r_1^2} + \frac{1}{r_2^2}\right) \tag{5.5}$$

By simple geometric consideration, we have $r_i^2 = \lambda^2\left(\left(\frac{y \pm b/2}{\lambda}\right)^2 + \frac{1}{16}\right)$, where y is the cross-wake position. With a formal definition of the induced cross-wake velocity, the integration of $2\int_0^\infty \rho v_y dy$ represents the induced cross-wake momentum caused by two neighboring

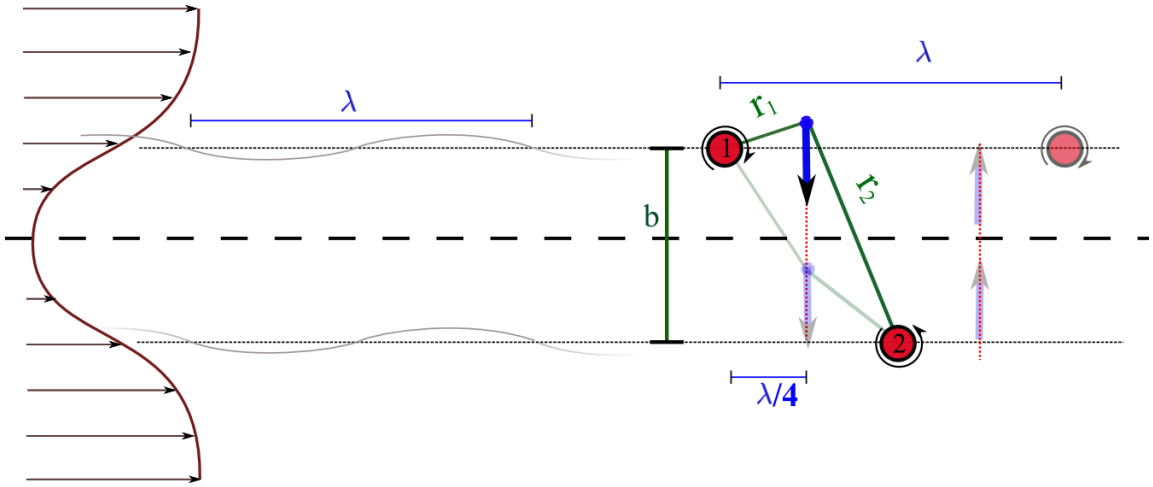

Figure 5.4: Illustration of the induced cross-wake velocity resulting from and increased wavelength and circulation of spanwise coherent rollers in the high-speed wake.

rollers (assuming symmetry of the wake centerplane), we simplify the equation:

$$\int_0^\infty \rho v_y dy = \frac{\rho\gamma\lambda}{2\pi}\left[-\tan^{-1}\left(\frac{4(b/2-y)}{\lambda}\right)+\tan^{-1}\left(\frac{4(b/2+y)}{\lambda}\right)\right]_0^\infty = \rho\gamma\lambda/2 \qquad (5.6)$$

This result shows that the induced cross-wake momentum is linearly dependant on the wavelength of the perturbation assuming a constant lateral separation of the rollers. As a result of $\lambda \propto Ma$, the cross-wake momentum transfer is proportional, assuming the validity of Biot-Savart induction to compressible flows, to the Mach number of the flow. This is a rather simple yet counter intuitive finding as it implies an increased momentum transfer with increasing Mach number - a clear contrast to the well-established compressibility effects found in the mixing layer. Unfortunately, this simple result is not valid when the compressibility effects cannot be neglected. The influence of compressibility on the domain of influence in the wake are discussed in the following sub-section.

5.5.2 Domain of influence in the transitional compressible wake

The study of the dynamics and stability of a staggered array of vortices with compressibility, is an important, yet unresolved problem with direct aeronautical applications (Crowdy & Green, 2011). Prior works have addressed stability characteristics of a two-dimensional, single-layer, hollow vortex array (Ardalan *et al.*, 1995) and of a compressible Stuart vortex array(Meiron *et al.*, 2000; O'Reilly & Pullin, 2003). The stability characteristics of the compressible Karman street remains unknown and of particular interest in the non-linear stage of transition of the high-speed wake. Although it is tempting to infer the stability features from incompressible vortex dynamics, this approach is invalid in high-speed flow as the domain of influence of each roller is no longer global. The classic Biot-Savart induction law is not directly applicable to compressible flows, partly because of the dilatational component of the flow, but more importantly, because the induced velocity follows the characteristic lines (Smits & Dussauge, 2006) which are modified by the mean flow gradient. To address this issue, the domain of influence of a perturbation in a high-speed wake is studied in order to infer the domain of influence of a high-speed roller.

The path of communication in compressible flows follows the characteristic lines. In a high-speed free shear flow, the mean Mach gradient changes the paths of the characteristic wavefronts. As a result, communication between two neighboring rollers is hindered, possibly even completely cut-off. Despite the simplicity of the approach, the geometric evaluation of the ray paths have been shown by Papamoschou (1994) to offer a good qualitative and quantitative comparison with the characteristic based computations from the linearized equations of motion. In order to investigate the compressibility effects on the communication paths in the high-speed wake, we extend the analysis of the mixing layer by Papamoschou (1993); Papamoschou & Lele (1993); Papamoschou (1994) to consider

the symmetric profile of the high-speed wake. Assuming a constant speed of sound, the generalized form of Snell's law relating the direction of acoustic propagation to the local Mach number is:

$$\sin\theta = \frac{\sin\theta_o}{1 + (Ma - Ma_o)\sin\theta_o} \tag{5.7}$$

where θ is the angle from the vertical and the subscript "$_o$" represents the Mach number and angle at the origin (Ma_o, θ_o). Based on classical ray tracing theory, the trajectory can be defined as a simple ordinary differential equation in two-dimensions :

$$\frac{dx}{dt} = U(y) - a\sin\theta; \qquad \frac{dy}{dt} = \pm a\cos\theta \tag{5.8}$$

Herein, we are interested in understanding the path of information propagation. For simplicity, we assume a laminar Gaussian distribution of velocity - a valid assumption even during transition. We developed a two-dimensional ray tracing tool using an explicit time advancement based on a fourth-order Runge-Kutta scheme, similar to Papamoschou (1993). Figure 5.5 shows the path of propagation of a perturbation emitted from a source at the centerplane (left) and at the wake half-width (right). For the computations, we neglect the effect of wave dispersion or attenuation.

The path of communication is greatly influenced by the mean flow Mach number gradient, figure 5.5. There is a clear increased cross-wake information transfer while the streamwise communication is inhibited. With increasing Mach numbers, an important region of near-silence develops upstream (to the left) of the source while a region of weak acoustic intensity develops downstream of the source (to the right). We recall that the acoustic intensity is calculated by the separation between two adjacent traces (Papamoschou, 1993): the closer two adjacent traces are to each other, the stronger the signal. The constitutive shear layers of the wake act as a waveguide, as such, the perturbations within the wake are internally reflected, raising the possibility of the emergence of an acoustic instability modes

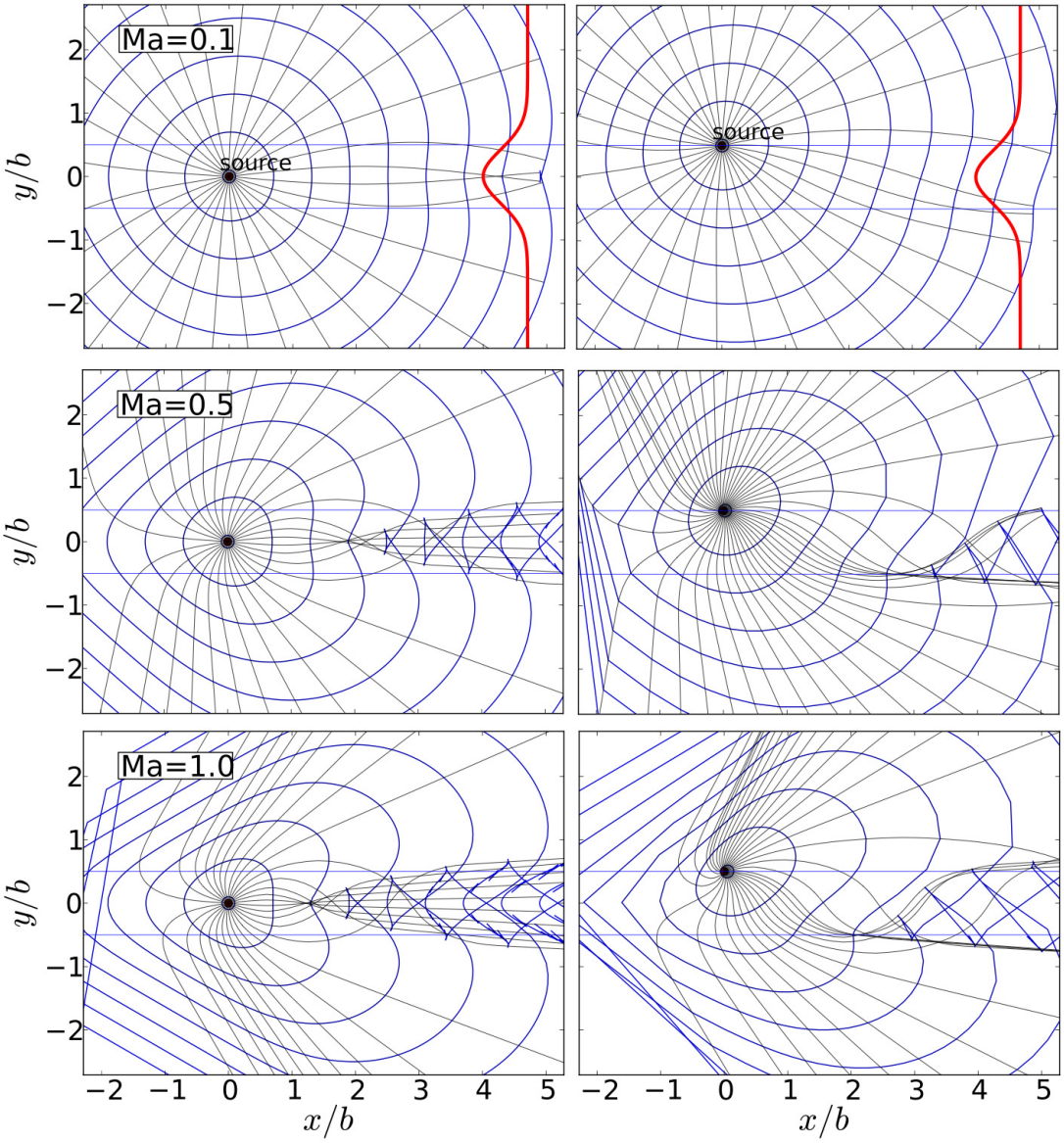

Figure 5.5: Propagation path of acoustic disturbance in wake for laminar wakes at $Ma_r = 0.0$, 0.5 and 1.0 (rows top to bottom) for a source at the centerline (left) and at the inflection point of the mean velocity profile (right). The contour lines represent the wavefronts.

as in the boundary layer (Mack, 1975, 1990). Interestingly, the information which does exit the waveguide is preferentially inclined to the freestream with an increasing streamwise orientation with Mach number, recalling the findings of acoustic waves in the freestream by Watanabe & Maekawa (2004) and Maekawa *et al.* (2006).

5.6 Numerical Simulation of Transitional High-Speed Wake

5.6.1 Defining compressibility effects

The global compressibility effect is defined as the relative Mach number Ma_r, which is the ratio of the centerline velocity defect to the freestream speed of sound: $Ma_r = Ma_\infty - Ma_o = \frac{U_\infty - U_0}{c_\infty}$. Unlike for the mixing layer, the level of compressibility in the wake decays with its evolution; the decay in time of Ma_r is shown in figure 5.6. Given a long enough evolution, the relative Mach number - and the velocity defect for that matter - asymptotically tend toward zero and the wake essentially becomes incompressible. This is not to say that the far wake of the compressible and incompressible wakes are identical. Bonnet *et al.* (1991) and Gatski & Bonnet (2009) noted clear differences in turbulence statistics in the far field between low- and high-speed wakes, the most notable difference is the peak turbulence intensity which is located further from the centerplane with increasing compressibility. Since the mean compressibility is small in the far wake, the differences are most likely caused by the "memory effects" which get imparted to the flow in the near wake. A comprehensive study of the memory effects in incompressible wakes can be found in Hickey *et al.* (2012).

During the pre-transitional evolution, the centerline defect decreases faster, the lower the Reynolds number and the greater the initial Mach number of the flow. This comes as no surprise as the pre-transitional decay is a purely viscous phenomenon. During the start

of the non-linear stage of transition, which roughly corresponds to the abrupt change of slope in figure 5.6 (left) at the time $[40-50]$ ($Ma=0.8$) and $[70-85]$ ($Ma=2.0$), the relative Mach number decays at an increasing rate with the Mach number. The maximum slope of the relative Mach number with respect to time is: -0.035 ($Ma=0.8$) and -0.057 ($Ma=2.0$). The trend is consistent in the lower Mach number case simulations: -0.012 ($Ma=0.3$), -0.028 ($Ma=0.8$), -0.035 ($Ma=1.2$) and -0.036 ($Ma=2.0$).

The turbulent Mach number characterizes the compressibility effects due to turbulent fluctuations and is defined as: $Ma_t=\langle u'\rangle_{max}/c_\infty$. The maximum turbulent Mach number is reached during transition and corresponds to: 0.1396 ($Ma=0.8$) and 0.307 ($Ma=2.0$). For the low-Re cases: 0.049, 0.128, 0.183 and 0.250 respectively for $Ma=0.3$, 0.8, 1.2 and 2.0. In the far wake, the turbulent Mach monotonically decreases with intensity of the fluctuation which follows a decay law, as in the incompressible case of: $\mathcal{O}\left(t^{-1/2}\right)$. Given the initial level of compressibility of the flow, these turbulent Mach numbers are rather small, and *a priori*, should not contain any shocklets (discussed in more detail in §5.6.7). To put into context, Sandham & Reynolds (1990) did not observe any shocklets for three-dimensional mixing layers with a unitary convective Mach number. Passot & Pouquet (1987) noted that a turbulent Mach number of 0.3 was the approximate threshold for shocklet formation in decaying isotropic turbulence in two-dimensional simulations; higher turbulence Mach numbers are required for three-dimensional simulations (Lee *et al.*, 1991; Samtaney *et al.*, 2001).

5.6.2 Evolution of transitional turbulence statistics

The maximal Favre averaged turbulence statistics are presented in figure 5.7. Other than the delayed transition, the qualitative evolution of all simulations remains similar. Viscous effects are small but non-negligible between the simulations at Re=1500 (dashed

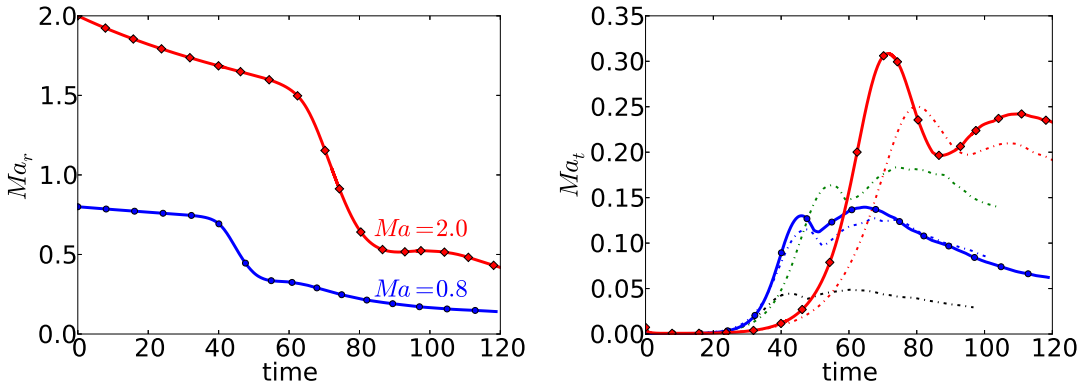

Figure 5.6: Evolution of the relative Mach number (left) and of the maximal turbulent Mach number (right).

lines) and 3000 (full lines), although the relative difference between both Reynolds numbers increases with Mach number. All wakes show a well defined peak in vv and uv during the non-linear stage of the transition. As for the incompressible cases, the peaks in the streamwise and spanwise normal stresses are rather blunt, and slowly decay to a far field plateau which is about half of the peak value (Hickey *et al.*, 2012). One of the principal quantitative differences in the turbulence statistics is found in the peak values reached during transition. A 53 % relative difference in the normalized cross-wake peak is observed between $Ma = 0.8$ and 2.0. Interestingly, at lower Reynolds numbers, the peak value are approximately constant (and show no clear monotonic trend) for Ma between 0.3 and 1.2, while the peak at $Ma = 2.0$ is almost 19 % higher. As will be discussed in the next sections, this discrepancy between the low and high Mach number peaks is related to the slightly different structural mechanisms of transition compounded with the increased anisotropy of turbulent statistics with Mach number.

The figure 5.8 shows the normalized profiles of production, dissipation and transport.

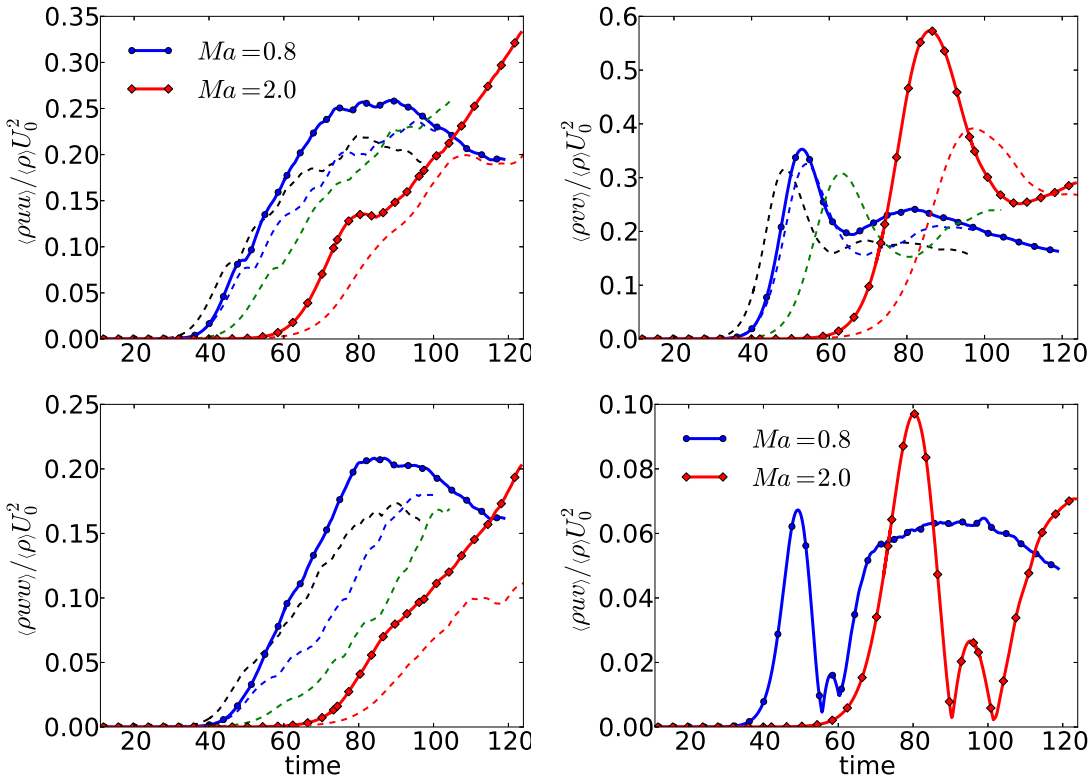

Figure 5.7: Evolution of the maximal Favre averaged normalized Reynolds stresses. The dashed lines are for the $Re = 1500$ cases for Ma=0.3, 0.8, 1.2 and 2.0.

The normalized production profiles nearly overlap with identical peaks located at $y/b = \pm 0.45$ at both Mach numbers. A large discrepancy is found in the transport term which is very sensitive to the compressibility effects. For the higher Mach number, the centerplane transport term remains a significant positive contributor to the turbulent kinetic energy (TKE) at both chosen location during transition.

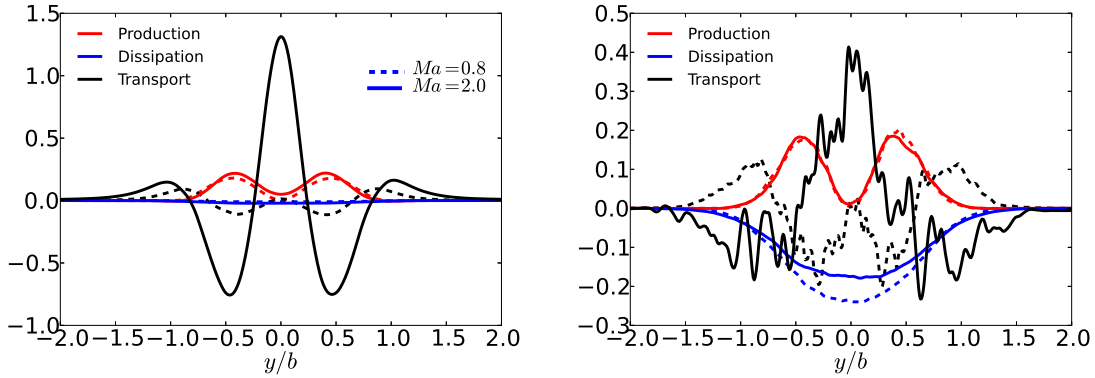

Figure 5.8: Normalized turbulent kinetic energy budget terms during transition at the peak $\langle vv \rangle$ (left: $Ma = 0.8$ at $t = 50$; $Ma = 2.0$ at $t = 80$) and at the approximate peak $\langle uu \rangle$ (right: $Ma = 0.8$ at $t = 80$; $Ma = 2.0$ at $t = 122$). The normalization parameter is U_0^3/b.

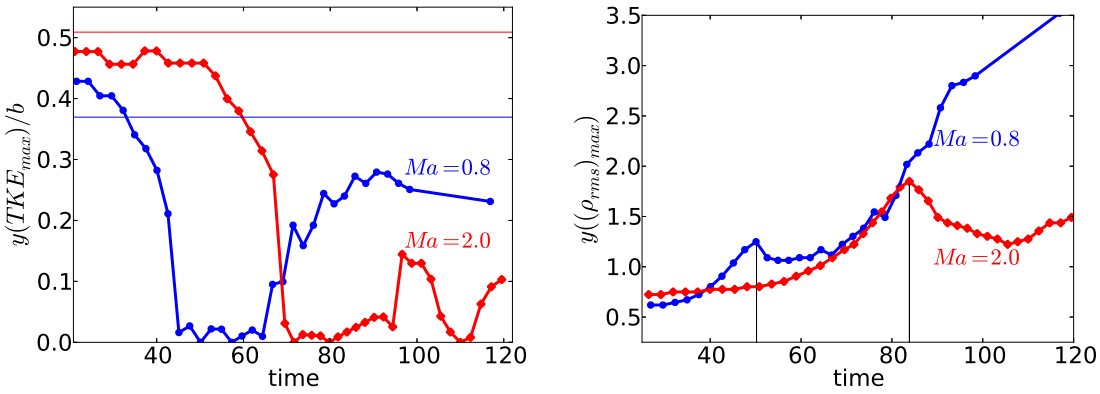

Figure 5.9: Evolution of the normalized cross-wake location of the maximum turbulent kinetic energy (left). The horizontal lines correspond to the far wake values found by Bonnet *et al.* (1991). The evolution of the location of the maximum density fluctuations (right).

5.6.3 Location of the maximal turbulence intensity

The far wake turbulence statistics by Bonnet *et al.* (1991) and Gatski & Bonnet (2009) show a clear outward shift of the location of the normalized TKE peak with increasing Mach number. The peak shifts from about $y_{max}/b = 0.36$ at $Ma = 0.5$ up to $y_{max}/b = 0.51$ at $Ma = 2.0$, where b is the wake half-width. Since the effects of compressibility are negligible in the far wake, these statistical features must be imparted to the flow in the near field (where the compressibility effects are important) and maintained through the memory effects of the wake. During the early stages of transition, a long plateau is observed with the normalized peak TKE located at $y/b = 0.403$ and 0.431, respectively for $Ma = 0.8$ and 2.0; a similar monotonic trend in the peak location is captured by the lower Re-simulations. As rollers develop, the typical double peaks of the TKE profile is lost and the maximum turbulence intensity is located about the centerplane, as seen in figure 5.9 (left); the double-peak is soon regained after transition. In order to understand the structural features of transition, we investigate the location of the maximum density fluctuation, which can be considered to be an approximate surrogate for the average cross-wake location of the spanwise rollers during transition. Figure 5.9 (right) shows a very distinct peak at $t = 50$ and 83 for $Ma = 0.8$ and 2.0 respectively. These peaks correspond to the exact time of the peak in $\langle \rho v v \rangle \,/\, \langle \rho \rangle \, U_0^2$, see figure 5.7. The larger the Mach number of the wake, the farther this peak is located from the centerplane (y_{peak}=1.35 ($Ma = 0.8$) and 1.85 ($Ma = 2.0$)). These features will be more thoroughly addressed in section 5.7.

5.6.4 Spectral distribution of TKE

The evolution of the spectral distribution of the turbulent kinetic energy at the wake half-width is shown in figure 5.10. The peaks are visible in all the velocity components

to a varying degree. The spectral peaks are found at $\kappa = 1.46$, 3.12 and 4.87; and 1.26, 2.26, 3.46 and 5.68, respectively for $Ma = 0.8$ and 2.0 (we recall that $\kappa^2 = \alpha^2 + \beta^2$). The primary wavenumbers correspond acceptably well to the theoretical results obtained from linear stability analysis (note that wavenumber of the linear stability results must be multiplied by two given the different definition of the wake half-width) which are: κ =1.50 ($Ma = 0.8$) and 1.30 ($Ma = 2.0$). Interestingly, the secondary peaks are not exact integers of the primary modes suggesting that they may be the result of secondary instability modes of the wake. Note that they do not correspond to the most unstable sinuous perturbation, which have a lower wavenumber than the primary anti-symmetric instability mode. The energetic modes diffuse and the wavelength increases as the wake undergoes transition. For $Ma = 0.8$, the secondary peaks are completely lost between $t = 42$ and 50. Between $t = 50$ and 62, only the primary rollers can be identified in the spectrum and, once the wake transitions, the primary peak is completely lost, although, presumably regained in the far wake. At $Ma = 2.0$, the rollers are more resilient to the scrambling of the turbulent fluctuations occurring during transition. A clear peak is observed until approximately $t = 115$, which corresponds to a very late stage of transition, recall figure 5.7. Although not presented, the spectral energy distribution in the spanwise direction is void of any energetic peak during transition.

5.6.5 Evolution of Reynolds stress anisotropies

The explanation of a reduced production in compressible flows has often been tied to the reduction of the pressure-strain term which inhibits the redistribution of the TKE among the various turbulent components. As a result, the increased compressibility leads to an increased anisotropy, which we investigate during the transition of the wake. The

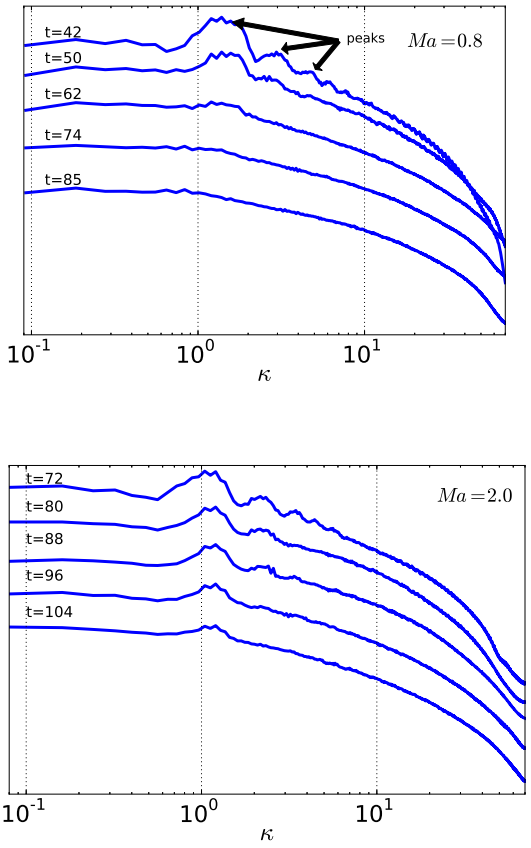

Figure 5.10: Spectral distribution of the turbulent kinetic energy at the wake half-width. The spectrums are offset by two decades between each line.

Reynolds stress anisotropy tensor is defined as:

$$b_{ij} = \frac{R_{ij} - \frac{1}{3}R_{kk}\delta_{ij}}{R_{kk}} \tag{5.9}$$

where R_{ij} represents the ij component of the Favre averaged Reynolds stress which is integrated in the cross-wake direction. In the high-speed mixing layer, Pantano & Sarkar (2002) showed a monotonic increase of the magnitude of the normal terms with increasing convective Mach number, but only in the near field. A similar result is observed for the

Table 5.2: Peak values of the Favre averaged Reynolds stress anisotropy for the near wake evolution.

	Present DNS		Mixing layer		
Ma	0.8	2.0	0.3	0.7	1.1
b_{11}	0.320	0.328	0.26	0.29	0.36
b_{22}	0.339	0.356	-0.16	-0.19	-0.22
b_{33}	-0.284	-0.288	–	–	–
b_{12}	-0.235	-0.211	0.19	0.19	0.19

transitional wake, see figure 5.11 and table 5.2. Unlike the mixing layer, the wake undergoes a return-to-isotropy after transition. The anisotropy in the far wake becomes negligible as the centerline defect - hence, the mean shear - tends towards zero. In the transitional region, all the peak values of the normal terms show a slight monotonic increase in magnitude with Mach number, while b_{12} has shows a clear decrease; a similar trend is observed among the lower-Reynolds number simulations. The most significant effect of compressibility is noted in the pre-transitional anisotropy where the difference between b_{11} and b_{22} increases, rather significantly, with the Mach number of the flow. These results are very similar to the observation in the high-speed mixing layer (Pantano & Sarkar, 2002). The importance of the anisotropy can be seen in the recent advances in turbulence modelling for second-order closure. Recent lower-order turbulence models (Yoshizawa *et al.*, 2012) have attempted to capture the Reynolds stress anisotropy, which in turn results in a reduced spread rate in the high-speed mixing layer.

5.6.6 Transitional convection velocity

The velocity of convecting structures in free shear flows plays a central role in the entrainment of stagnant fluid into the turbulent flow. In bluff-body wakes, any modification

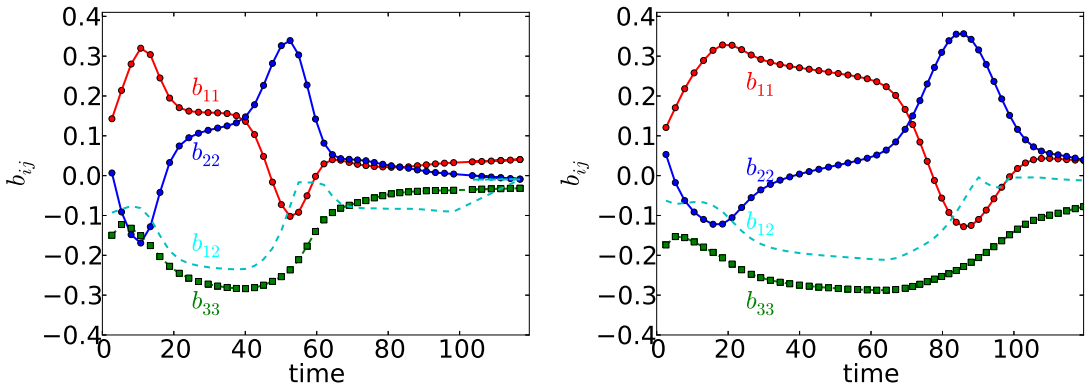

Figure 5.11: Evolution of the integrated Favre averaged anisotropy for Ma_r =0.8 (left) and 2.0 (right)

to the convective velocity is therefore tied to the base pressure (Kastengren *et al.*, 2007) and consequently the total drag of a body. The effects of compressibility on the convection velocity of free shear flows have been subject to much debate, especially for the mixing layer. It has been suggested that at high convective Mach numbers, the isentropic approximation does not capture the velocity of convecting structures (Clemens & Mungal, 1995)- the convection velocity is either higher or lower depending on the sub- or supersonic nature of the co-flowing streams. Other workers have suggested (Thurow *et al.*, 2008) that the experimental difficulties of computing this velocity may explain the non-isotropic convection velocity results.

Any modification to the convection velocity caused by the compressibility effects in the transitioning wake would greatly modify the dynamics of the flow and this issue needs to be addressed for completeness. Different approaches to the computation of the convective velocity have been proposed. To investigate Taylor's hypothesis, del Alamo & Jimenez

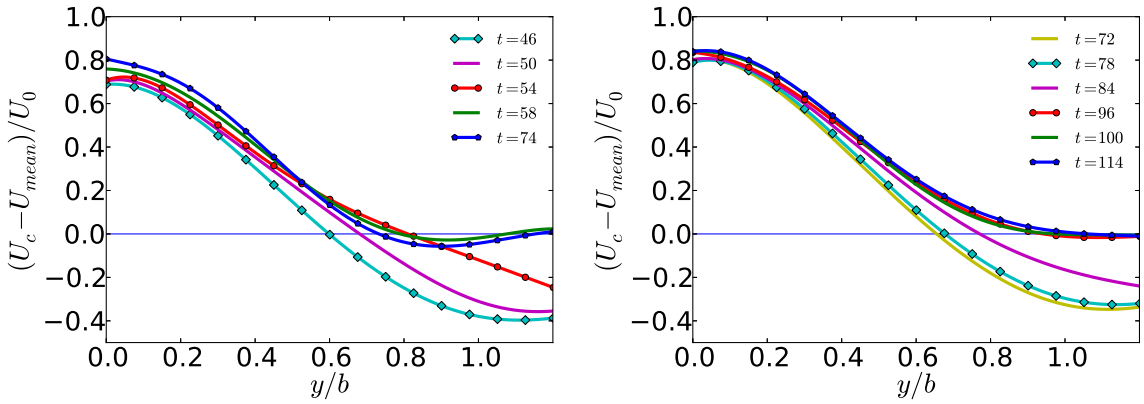

Figure 5.12: Convection velocity at various temporal locations during transition of the wake. A fourth-order polynomial is used to interpolate all the discrete convective velocity for clarity. The convection velocity is based on the separation distance which maximizes the two-point correlation of density, ρ, with $\tau = 4$. Figures for $Ma_r = 0.8$ (left) and 2.0 (right).

(2009) computed the convective velocity in spectral space, Hussain & Clark (1981*b*) proposed the frequency-wavenumber spectrum peak while Demetriades (1976) suggested a spatial-temporal correlation approach. In the present work, this latter approach is used by finding the streamwise separation, δx, which maximizes the peak cross-correlation coefficient for a given temporal separation τ. Therefore, the convection velocity of the structures is defined as:

$$U_c = \frac{\delta x}{\tau} \tag{5.10}$$

As the δx is confined to the finite grid, we must judiciously choose a minimal temporal separation, τ which allows enough resolution to adequately determine the convection velocity. If τ is too small, the convection velocity becomes limited by the spatial resolution of the simulation. Alternatively, if τ is too large, the convection velocity becomes an average

value of little physical interest and the inherent parallel flow assumption in this approach becomes questionable. For the current cases, $\tau = 4$ was chosen as a baseline, it should be noted that the results remain unchanged for $\tau = 8$. The density is used to identify the maximal cross-correlation coefficient, although other components such as velocity, pressure and scalar field have also been computed using the same procedure and yield very similar results.

Figure 5.12 presents the difference between the local convection and mean velocity normalized by the centerline defect. As the instantaneous convection velocity represents an averaged value over a finite time window ($\tau = 4$), the means and centerline velocities are computed over the same temporal span. The convection velocity at the centerline differs drastically from the mean flow, the identified structures convect at significantly faster speed than the mean centerline velocity. This result should come as no surprise since any structure which drifts (from the top or bottom side of the wake) toward the centerplane will naturally have a higher velocity. Similarly at the outer edge of the wake, the structures have a lower velocity than the mean during transition; after transition, the convection velocity becomes equal to the mean. Interestingly, the convection velocity is invariant to the Mach number of the wake, a result which comes as a surprise given the large centerplane discrepancy between the magnitude of the transport term, recall figure 5.8.

5.6.7 Shocklet formation

Shocklets are the term used to describe a localized discontinuity caused by fluctuating fields of turbulent eddies (Lee *et al.*, 1991). They are known to occur in decaying isotropic turbulence (Lee *et al.*, 1991; Samtaney *et al.*, 2001) and in mixing layer (Sandham &

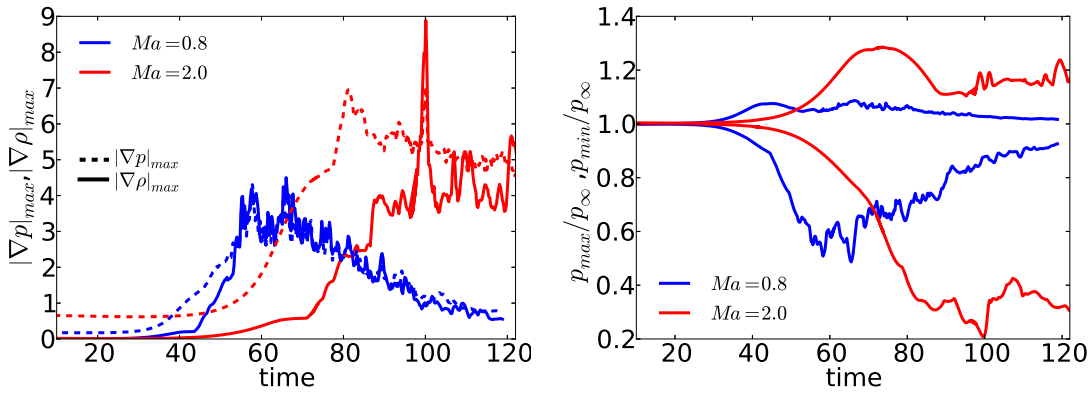

Figure 5.13: Evolution of the magnitude of the maximum pressure and density gradient (left) and the minimum and maximum pressure (right).

Yee, 1989; Papamoschou, 1995; Vreman *et al.*, 1996; Freund *et al.*, 2000*b*,*a*). In the two-dimensional mixing layer simulations, the shocklets appear at Ma_c=0.7 (Sandham & Yee, 1989); for three-dimensional simulations, a higher convective Mach number is needed, about Ma_c=1.2 (Vreman *et al.*, 1996). In the case of the wake, Clemens & Smith (1998) observed eddy-induced shocklets in the near field wake ($Ma_r > 0.9$). These observations were primarily based on the inspection of PLS images from a freestream transitioning wake at $Ma_\infty = 3$. The presence of shocklets in the transitioning wake has the potential of greatly modifying the dynamics of the flow, as shocks promote a rapid change from kinetic to internal energy. Given the low relative and turbulent Mach numbers during the non-linear stage of transition, it comes as no surprise that shocklets are not observed in the present transitioning wakes. Nonetheless, the evolution of the maximum local pressure, $(\partial p/\partial x_i \cdot \partial p/\partial x_i)^{1/2}$, and density, $(\partial \rho/\partial x_i \cdot \partial \rho/\partial x_i)^{1/2}$, derivatives are shown in figure 5.13. Despite an important peak at $t = 100$, no clear evidence of a shocklet was observed in the instantaneous velocity field.

5.7 Structural Features of Wake Transition

5.7.1 Formation and shape of rollers

Based on the flow visualization, Clemens & Mungal (1995) showed that the compressibility effects modify the shape of the rollers in the mixing layer; as the Mach number is increased, the rollers change from a circular to polygonal shape. Messersmith & Dutton (1996) showed - using a more rigorous statistical approach - that the structures become elongated and compressed with increasing compressibility. In the wake, the experimental (Clemens & Smith, 1998) and numerical (Chen *et al.*, 1990; Watanabe & Maekawa, 2004) visualizations show initially circular rollers which deform and tend toward an elliptical shape, although from the results, it is difficult to assess if it is a transitional or a compressibility effect. To gain an overall understanding of the transitional structures in the planar wake, a slice of the magnitude of the density gradient, at various times, is shown in figures 5.14 and 5.15. These figures, especially figure 5.15, highlight the limitations of temporal simulations. The primary instability wavelength, as computed from the linear stability theory, dictates the streamwise extent of the computational domain. As the flow evolves and the principal wavelength becomes longer, the domain can no longer support an integer number of structures. This results in the breakdown of some emerging structures as seen in the middle of the domain from $t = 93$ in figure 5.15. These localized breakdowns should not limit the generality of our findings but need to be mentioned in the analysis.

The two-dimensional slice provides a local and instantaneous representation of the roller shape. Although the rollers are predominantly two-dimensional, there is a non-negligible variation of the shape at different spanwise locations (this will become obvious in discuss the three-dimensional structural visualizations in figures 5.22 and 5.23). These spanwise variations are attributable to the internal core dynamic instabilities, underlying

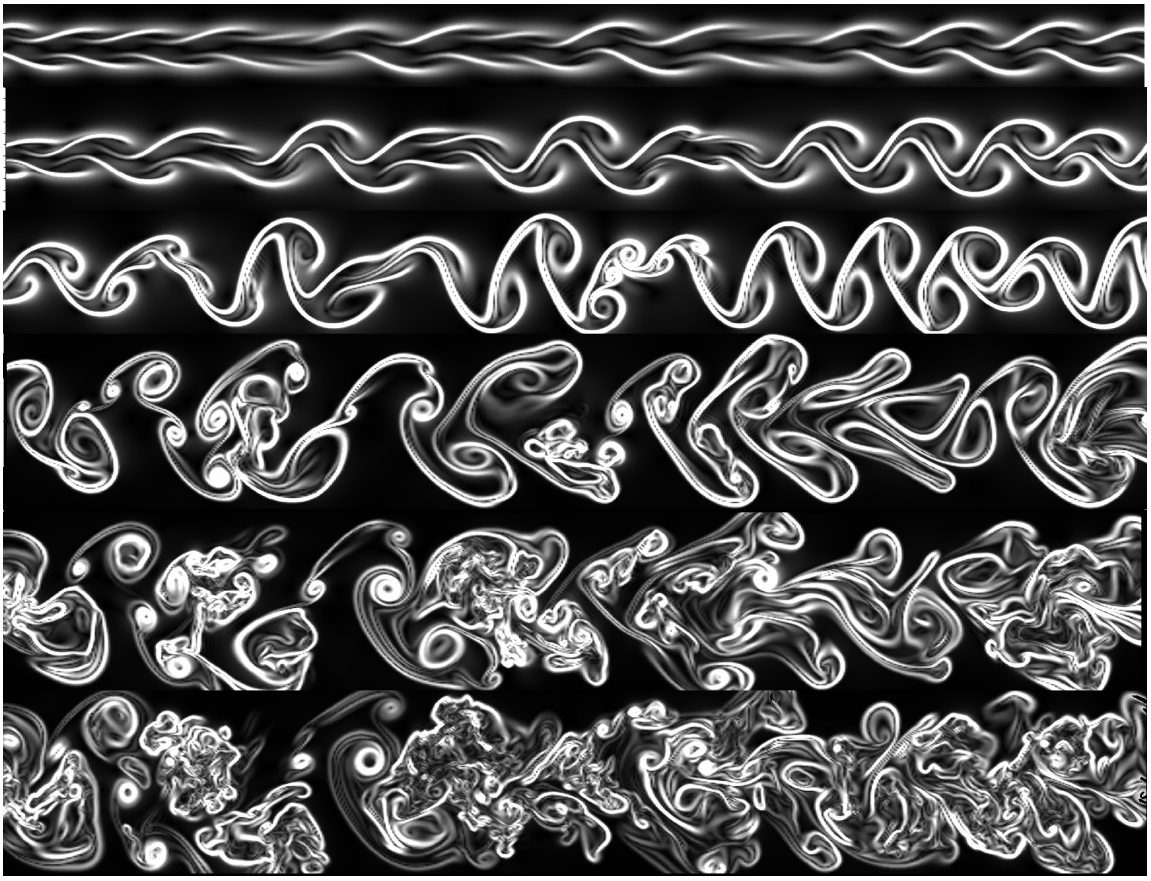

Figure 5.14: Magnitude of the density gradient during transition for $Ma_r = 0.8$ at times (top to bottom): 41, 46, 51, 56, 62 and 76.

three-dimensional instability modes or simply inhomogeneities in the spanwise direction. Therefore, we seek to generalize the effect of compressibility on the evolution of a prototypical roller during transition. To this effect, an eduction technique based on the Q-criteria was developed (results are very similar when using density or λ_2 to identify the structures).

In the first step, we agnostically average the flow in the spanwise direction and locate the mean vortex axis location by identifying the local peaks in the averaged Q-criteria. We visually confirm that these peaks correspond to the approximate location of the axis of

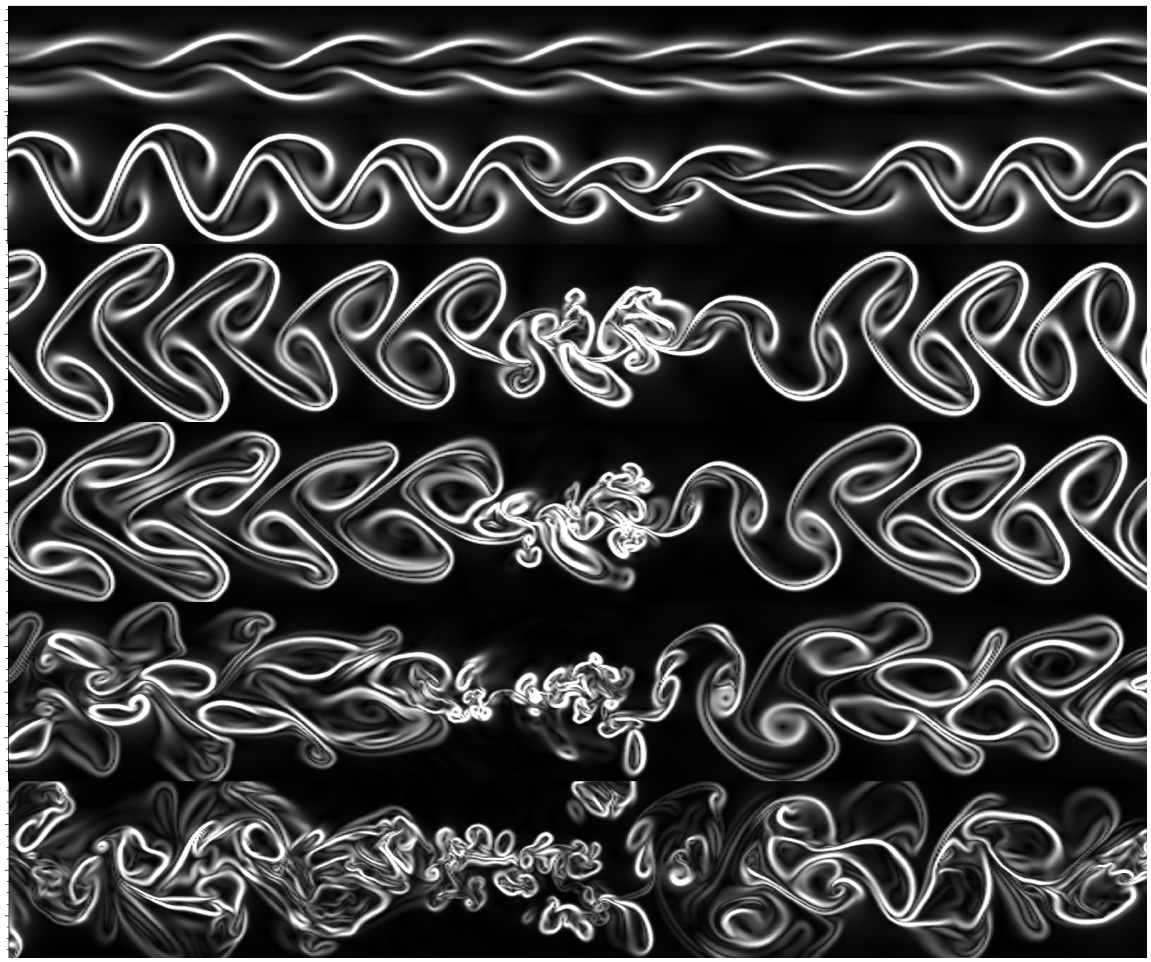

Figure 5.15: Magnitude of the density gradient during transition for $Ma_r = 2.0$ at times (top to bottom): 66,78, 93, 109 and 122.

the rollers. In the second step, the rollers are extracted in the spanwise direction using a window of $b/2 \times b/2$ (in the x-y plane) around each identified peak. Each roller is remapped, using a second-order Lagrangian polynomial, onto a homogenous grid (in the x-y plane; z is already homogeneous) with a higher resolution (71×71 for a computational domain of $b \times b$). The $x-y$ slices at each z location are first correlated to the spanwise averaged slice.

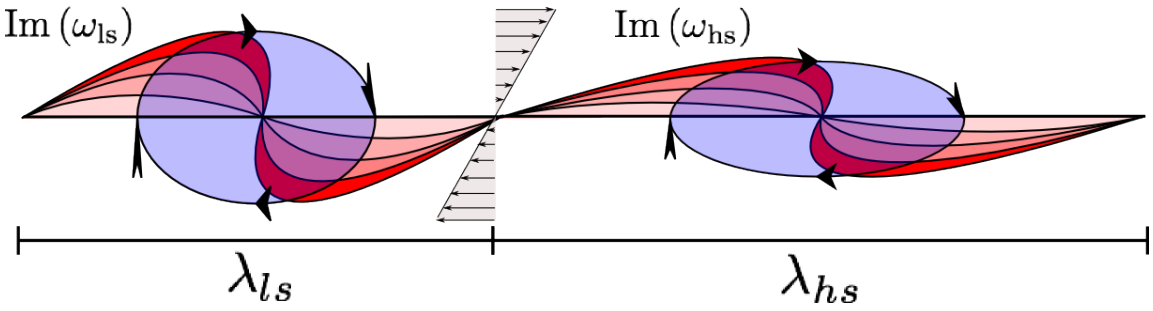

Figure 5.16: Conceptual image of the growth of a sinusoidal perturbation in a shear layer. The wavelength, λ, increases and the growth $Im(\omega)$ decreases. In a shear flow, the perturbations in a low speed wake (ls) will have a more circular while the high-speed wake (hs) roller will be more elliptical.

By offsetting the slice by up to 12 grid points in each direction (which represents a maximal offset of about $b/6$ in x and y-directions), we identify the offset which maximizes the auto-correlation coefficient. The spanwise average, with the optimal offset, is computed with the slices which have an above average correlation coefficient. A bootstrapping technique is used. The new spanwise average roller (with optimal offset) is used to re-correlate all the slices, which are offset to maximize the correlation; again, only the above average correlation coefficient slices are used for the spanwise average. After 3 loops, we obtain a highly correlated coherent structure. The evolution of the prototypical rollers during transition are unambiguously educed and presented in figures 5.17 and 5.19. In order to confirm the validity of the educed features, figures 5.18 and 5.20 show the evolution of a typical roller from a single slice of spanwise vorticity.

The effects of compressibility on the roller formation of the planar wakes is illustrated in figure 5.4. The increased ellipticity is a result of the combined effects of an increased wavelength and a reduced growth rate with increasing Mach number. Given an infinitesimal sinusoidal perturbation within a shear layer, shown in figure 5.16, $Im(\omega)$ defines the linear

grow of the perturbation in time. As the perturbation grows, the shear pushes the vorticity toward the center point of the sinusoidal perturbation, hence forming the rollers. Naturally, the larger the growth rate, the faster the roll-up process. In transitional wakes, it follows that the growth rate of the most unstable mode is proportional to the conjugate diameter of the resulting elliptical structure, while the transverse diameter is characterized by the wavelength of the instability. Since the growth rate and wavelength are negatively coupled in the wake (recall figure 5.1), it comes as no surprise that the higher Mach number - hence lower growth and longer wavelength - leads to an increased ellipticity of the transitional structures.

The increasing ellipticity with Mach number is evidenced by the educed rollers in figures 5.17 and 5.19 as well as by the two-dimensional slices of vorticity in figures 5.18 and 5.20. The present findings are in agreement with Messersmith & Dutton (1996) who suggested that compressibility elongates the coherent structures in the mixing layer. Unlike our conceptual understanding of the roll-up, the rollers show a clear asymmetry with vorticity preferentially initially congregating on the side closest to the outer-edge of the wake. This is the result of a continual reduction of the inner wake shear (relative to the inflectional point shear layer) which is a direct consequence of the reduction of the centerline defect, whereas the shear at the outer-edge of the wake remains constant as it is characterized by the freestream velocity. As the roll-up process evolves, the location with the greatest vorticity rotates at the outer radius of the roller, this phenomenon is very clearly seen in figures 5.17 and 5.19. Interestingly, the rotation of the maximum vorticity mirrors the local peak in the location of the maximum density fluctuations (at times $t = 50$ and 83 for Ma =0.8 and 2.0, respectively) in figure 5.9. This result indicates that the evolution of the roll-up process can be inferred from the average statistics in the wake.

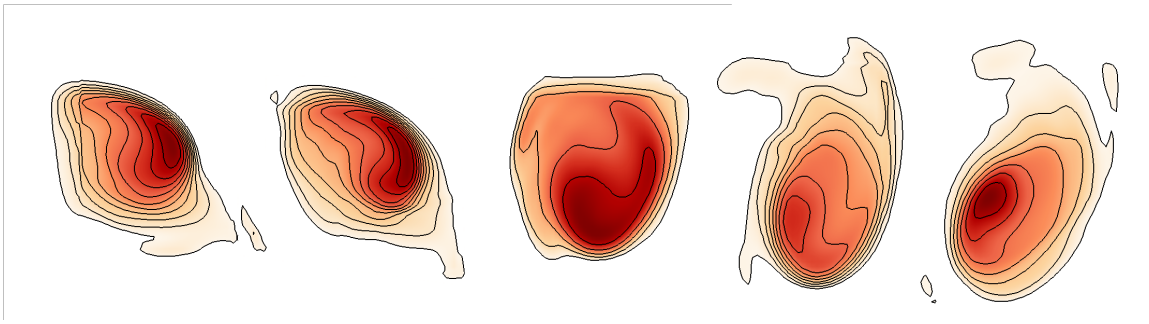

Figure 5.17: Evolution of the spanwise educed structure for $Ma = 0.8$ (at around $x = 46$) at times from left to right: 46, 48, 52, 54 and 56.

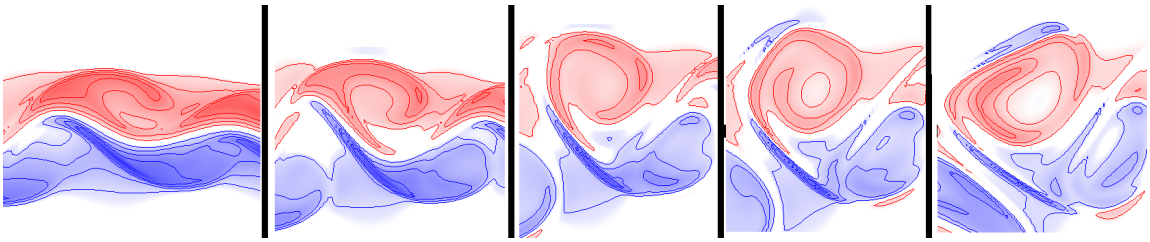

Figure 5.18: Formation of a roller from an instantaneous slice of the spanwise vorticity for the low-Mach number case ($Ma = 0.8$). Contour lines are: $\omega_z = \pm$ 0.25, 0.5, 0.75 and 1.0.

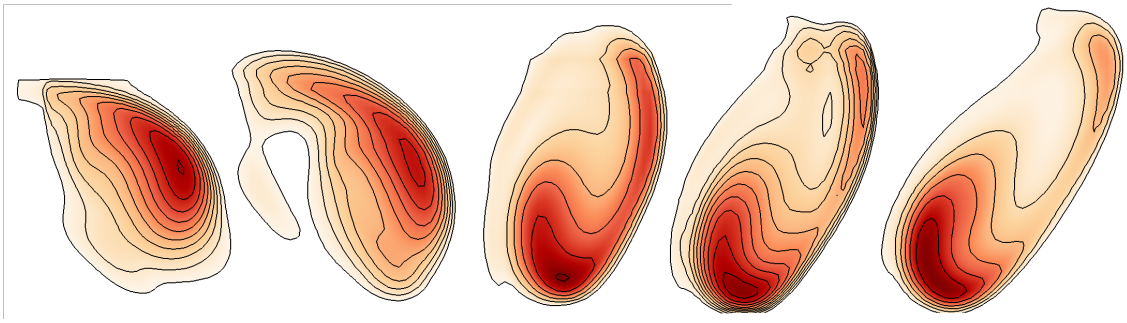

Figure 5.19: Evolution of the spanwise educed structure for $Ma = 2.0$ (at around $x = 42$) at times from left to right: 76, 84, 88, 90 and 92.

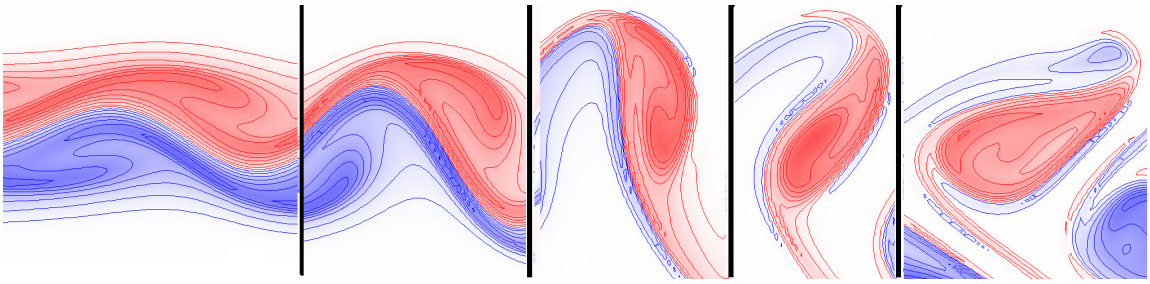

Figure 5.20: Formation of a roller from an instantaneous slice of the spanwise vorticity for the higher-Mach number case ($Ma = 2.0$). Contour lines are: $\omega_z = \pm$ 0.05, 0.15, 0.3, 0.45 0.6 and 0.75.

5.7.2 Evolution of roller configuration during transition

The effects of compressibility on the structural configuration of the rollers are investigated. The evolution of the streamwise separation of the rollers, λ, is presented in figure 5.21 (left). It is defined as the first positive peak of the two-point correlation with streamwise separation of the cross-wake velocity (λ is invariant to the use of other velocity or thermodynamic components) at the wake half-width. In order to identify unambiguously the first positive peak, the minimal correlation coefficient was set to -0.15 for the first negative peak and 0.1 for the first positive peak. For that reason, the values for $t > 76$ ($Ma = 0.8$) and $t > 98$ ($Ma = 2.0$) are not presented as the peaks in the streamwise correlation are too weak. As expected from the linear stability theory, the increasing Mach number results in a longer streamwise separation of the rollers. The plateau of λ during linear stage and the roller formation stage, conforms surprisingly well with the calculated wavelength of the primary instability mode from §5.4.2 (recall that the wake half-width of the linear stability calculations is twice that of the DNS): $\lambda_{linear} = 4.18$ compared to $\lambda_{DNS} = 4.12$ for the case at Ma=0.8. For the higher Mach number case, the difference is slightly greater ($\lambda_{linear} = 4.83$ compared to $\lambda_{DNS} = 5.24$). It should be noted that the monotonically increasing wavelength with Mach number is also observed for the lower-Re despite the constant computational domain size. The connection and pairing of rollers can be seen in the increase of the streamwise separation in $Ma = 0.8$. As the pairing does not occur simultaneously for all rollers, there is an incremental roller separation from $t > 60$ ($Ma = 0.8$). Interestingly, there is no noticeable increase in the length scale for $Ma = 2.0$; a result corroborated by the spectral analysis in figure 5.10.

The evolution of the wake half-width, b, is shown in figure 5.21 (left). The initial linear stage of the wake evolution is characterized by low spread rates (up $t = 40$ for $Ma = 0.8$

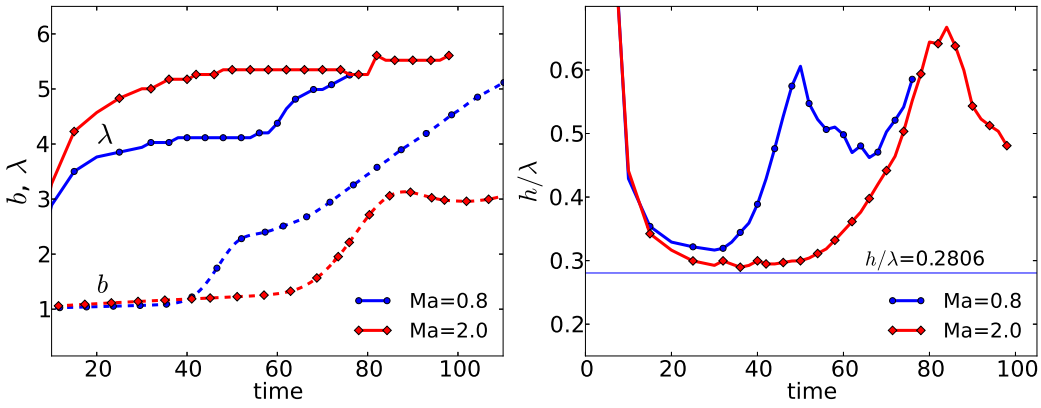

Figure 5.21: Evolution of the size of the spanwise rollers during transition. The separation length of the first positive peak in the two-point correlation of the cross-wake velocity was used to estimate the size of the rollers (left). Evolution of the ratio of the cross-wake to streamwise separation of rollers with comparative line of the neutrally stable configuration (right).

and $t = 65$ for $Ma = 2.0$). At the start of the non-linear stage, a very rapid lateral spreading occurs during which the rollers form and rotate; recall figures 5.17 and 5.19. The spread rate during the roller formation stage decreases - albeit very slightly- with Mach number ($db/dt = 0.1155$ and 0.1058; for $Ma = 0.8$ and 2.0, respectively). It should be noted that the lower-Re cases did not reveal a clear monotonic trend with Mach number. After the roller formation and rotation, the lateral spreading levels off. In the $Ma = 2.0$, there is even a slight, temporary decrease in the lateral length scale of the wake caused by the rotation of the elliptical rollers. As the transverse axis of the roller is oriented in the cross-wake direction, the wake half-width is maximized; as 180° rotation is completed and the transverse axis becomes parallel to the streamwise direction, the wake half-width is reduced, albeit, temporarily.

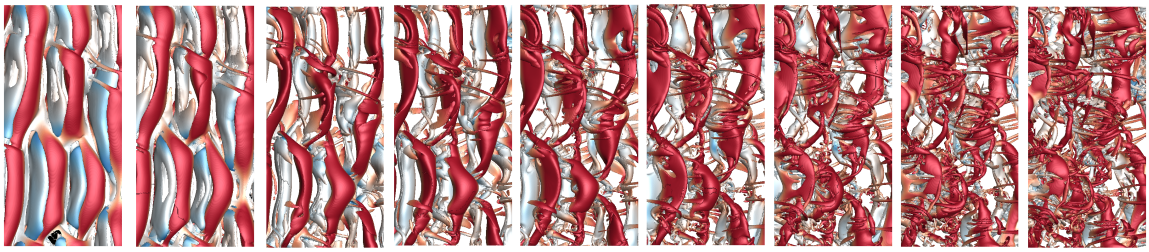

Figure 5.22: Top-view of the transition of Ma =0.8 during transition at t =48, 50, 54, 56, 58. 60, 62, 64, 66 and 68. Iso-surfaces of the Q-criteria (0.04) colored by the streamwise velocity.

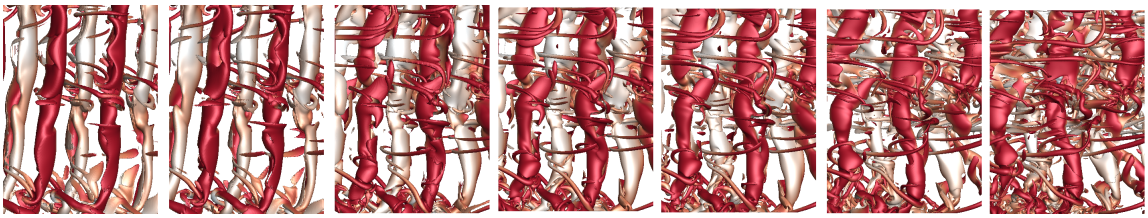

Figure 5.23: Top-view of the transition of Ma =2.0 during transition at t =88, 90, 94, 96, 98. 100, 104 and 108. Iso-surfaces of the Q-criteria (0.04) colored by the streamwise velocity.

The ratio of the cross-wake to streamwise roller separation, h/λ, (discussed in §5.5) is shown in figure 5.21 (right). For the cross-wake separation, we use the location of the maximum density fluctuations (figure 5.9). As expected, the ratio of h/λ decreases with increasing Mach number during the roller formation stage. As the rollers rotate, the density fluctuation peaks get pushed to the outer-edge of the wake. The increase in the ratio h/λ is maximized for elliptical structures when the transverse axis of the rollers is perpendicular to the streamwise axis, hence, explaining the peaks at $t \approx 50$ ($Ma = 0.8$) and $t \approx 84$ ($Ma = 2.0$).

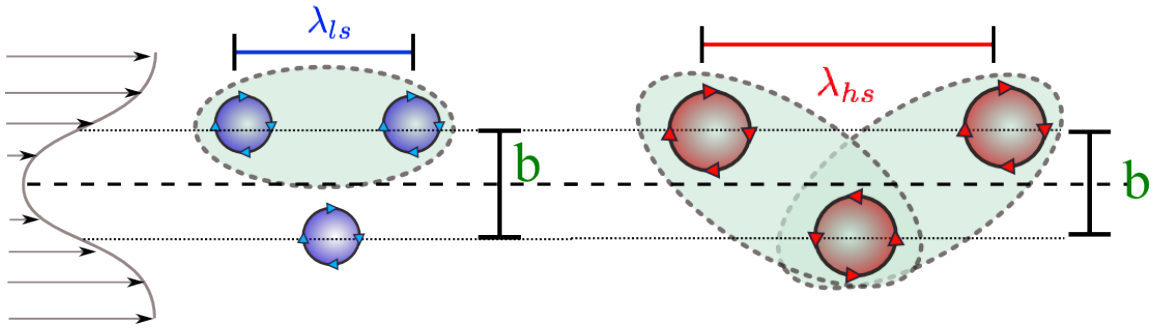

Figure 5.24: Illustrative effects of compressibility on the domain of influence of the rollers. In typical low-speed wakes (ls), communication occurs primarily between neighboring along the same row (left). In higher speed wakes (hs), the domain of influence is predominantly in the cross-wake direction (right).

5.7.3 Visualization of the rollers and ribs

The top-view visualization of the rollers, in figures 5.22 and 5.23, offers a different perspective to understand of the effects of compressibility on the vortex array configuration. The cumulative effects of the increased streamwise roller separation (section 5.4 and previous subsection) and an inhibited streamwise communication between rollers on the same row (section 5.5) drastically modifies the interaction between the rollers. As the compressibility effects become more important, there is an increasing cross-wake and reduced streamwise interaction, see illustration 5.24, which eventually impedes the pairing of rollers. This inhibited pairing is observed in figure 5.23 and in the corresponding statistics of the streamwise separation 5.21 (left). Presumably, in the fully turbulent region, pairing or amalgamation of turbulent rollers occurs but, unlike the $Ma = 0.8$ case in figure 5.22, it is not a transitional feature.

The increased cross-wake communication, longer roll-up time and the inhibited structural pairing in the high-speed wake promote the formation of well-organized rib structures

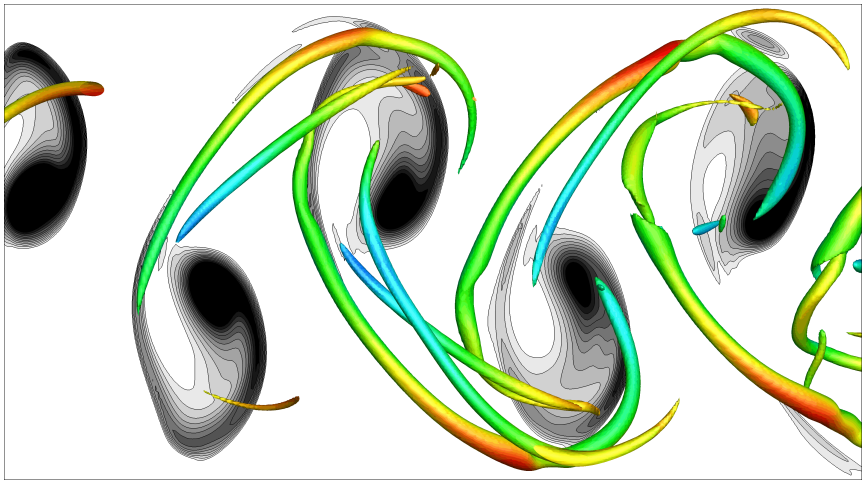

Figure 5.25: Organization of the rib vortices (iso-surface of Q=0.5) with respect to the spanwise rollers at $Ma = 2.0$ at $t = 92$. The rollers are identified by a two-dimensional contour plot of the Q-criteria.

which connect rollers on the opposite side of the centerplane. Figure 5.25 shows the organization of the rib structures with respect to the two-dimensional rollers in the case of $Ma = 2.0$. The rib-structures are highly organized and survive through-out transition - a clear contrast to the incompressible and low-speed wakes. The very-well organized rib structures are a striking feature of the experimental work by Clemens & Smith (1998). The increased stability of the high-speed rollers results in the transition of the secondary rib-structures before the principal rollers become fully turbulent. Signs of rib breakdown events can be inferred from experimental visualizations by Clemens & Smith (1998) and from the numerical work by Watanabe & Maekawa (2004). The breakdown of the rib structures is a topic of future study (Hickey *et al.*, 2013*a*).

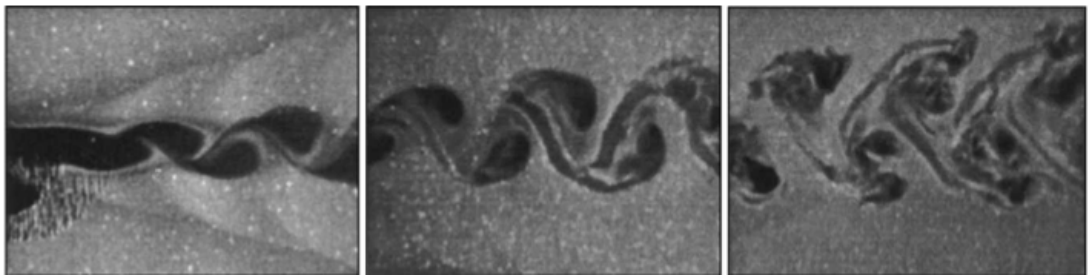

Figure 5.26: Roller visualization from Clemens & Smith (1998) for a planar wake at $Ma = 3.0$.

5.8 Discussion and Conclusions

The objective of our work is to gain a deeper understanding of the effects of compressibility on the transition of planar wakes. Using linear stability theory, we investigated the characteristic length and time scales of high-speed wake transition. These theoretical results were supplemented by high quality direct numerical simulations covering the range of initial Mach numbers from 0.3 to 2.0. Many previous investigations have downplayed the importance of compressibility in wake flows. It is true, at least qualitatively, that the increasing Mach number does little to modify the general features of transition - the flow remains two-dimensional, rollers are qualitatively similar and secondary structures are also present. This similarity is especially striking considering the drastic effects of compressibility in the transitioning mixing layer. In the present work, we highlight the insidious effects of compressibility on the emerging structures, along with the concomitant effects on the statistics, in the transition of the plane wake.

The cause of the structural differences in the transitional wake stem from a reduced growth rate and an increased wavelength of the primary instability mode. Two trivial consequences result from the increased wavelength: (1) the streamwise separation between

each roller is increased; and (2) rollers develop with an increased circulation. Assuming incompressibility, we showed that the net result of an increased separation and circulation of the rollers is an increased cross-wake momentum transfer. Naturally, these incompressible results bear little significance to the high-speed flows as the characteristic lines, and consequently the entrained flow, are no longer directly function of the distance from the vorticity filament, as assumed for incompressible flow. Based on a geometric interpretation of the characteristic lines in the wake, we showed that with increasing Mach number, the communication is reduced between neighboring rollers along the same row. From these results, we infer that the compressibility effects lead to an increased cross-wake domain of influence, which modifies the path to transition.

Direct numerical simulations support our claims inferred from theoretical considerations. The simulation results revealed that the increased streamwise separation and impeded communication eventually inhibits the structural pairing - an important feature of low-speed wake transition. This lack of pairing is clearly highlighted by our structural visualization in the $Ma = 2.0$ case. The secondary structures, connecting ribs, have drastically different features depending if the principal rollers pair or not. In the high Mach number case, the ribs undergo a vortex breakdown that precedes the transition to turbulence of the principal rollers. This transitional feature, which is discussed in our future work (Hickey *et al.*, 2013*a*), provides a new mechanism for control in the transition of the high-speed wake.

Our work also sheds light on the increasing ellipticity of the transitional structures in the high-speed free shear flows. The ellipticity of the structures is a result of the linear stability characteristics; as the growth rate is reduced and the wavelength increased, the resulting structures become increasingly elliptical. The developed eduction technique clearly reveals the step-by-step roll-up of the rollers during transition; the modification

to the roll-up process is particularly striking. In high-speed wakes, the ellipticity of the rollers results in a sustained lateral spreading of the wake as they rotate about themselves. When the transverse axis of the elliptical roller is perpendicular to the streamwise axis, there is a local maximum in the spread of the wake. As the elliptical rollers continue their rotation, there is a temporary decrease in the wake half-width when the transverse roller axis is aligned in the streamwise direction.

The simulation results clarify some lingering questions regarding high-speed wake transition. From our results, the convection velocity remains invariant to the freestream Mach number of the wake, in accordance to the conclusion by Thurow *et al.* (2008). Shocklets do not play a significant role in the transition of the planar wake at $Ma = 2.0$. Although, it should be noted that in the present simulation, the laminar viscous centerline velocity decay and the very slow growth of the normal modes mean that the non-linear stage of transition started at a relative Mach number of 1.5 - the peak TKE occurs at an even lower Mach number. A higher transitional Mach number would be necessary to observe shocklets in the wake. The anisotropy of the Reynolds stresses tensor is modified by the compressibility effects, although the modifications to the anisotropy tensor are greatest in the very early stages of transition. As the wake transitions, there is a return-to-isotropy, which is invariant to the initial level of compressibility in the wake. The emergence of three-dimensionality remains an important question of the plane wake. This issue cannot be settled from our results and will necessitate further investigations.

Chapter 6

Vortex Breakdown in Transitional High-Speed Wakes

6.1 Abstract

We report on the identification and explanation of vortex breakdown events of secondary rib structures in the transition of high-speed planar wakes. The effects of compressibility impart changes to the transitional statistics and structures in the wake. The wavelength of the primary instability mode increases and the growth rate decreases with the freestream Mach number of the flow. As a result, the emerging array of staggered spanwise coherent structures has an increased streamwise separation and the rollers have an increased ellipticity. The streamwise-aligned rib structures connect neighboring rollers between either sides of the wake, therefore, any changes to the primary rollers due to compressibility directly affect the evolution of the secondary rib structures. Direct numerical simulations of transitioning high-speed planar wakes at $Ma = 2.0$ have revealed multiple vortex breakdown events of the ribs prior to the full transition of the principal rollers. The topology of the vortex breakdown is explained by studying the velocity trajectory in

phase plane about a stagnation point. Using critical point theory, we show that a reduced axial velocity of a vortex results in a breakdown through the formation of an outwardly spiralling vortex; a *spiral source*. Applying the same theory to a vortex with a strong positive axial velocity gradient leads to the formation of a *spiral sink*. Through the analysis of the vector field, we show evidence supporting our theoretical framework to explain the observed vortex breakdown events. The understanding and explanation of the breakdown mechanism in the transitional wake have many potential applications for high-speed mixing enhancements and flow control.

6.2 Introduction

Compressibility has a well-known stabilizing effect in most canonical high-speed turbulent flows such as: boundary layers, jets, wakes and mixing layers. The increased stability in the transitional regime results in a delayed onset of turbulence and modifications of the transitional structures. The case of the high-speed planar wake is particularly instructive as the overall features of transition remain, in many ways, similar to the incompressible wake (Clemens & Smith, 1998). The planar wake is most unstable to a two-dimensional, anti-symmetric perturbation - irrespective of the Mach number of the flow (Chen *et al.*, 1990; Watanabe & Maekawa, 2004; Hickey *et al.*, 2013*b*). The primary instability mode imparts the length scale from which the staggered array of spanwise coherent rollers emerges. This two-dimensional array recalls the general organization of the Karman vortex street. The primarily two-dimensional transition represents a clear break from the three-dimensionality of other canonical high-speed free shear flows such as the mixing layer (Sandham & Reynolds, 1991; Kourta & Vitale, 2002). The compressibility effects in the wake transition are arguably more nuanced than other shear flows, yet important

nonetheless.

In both the low- and high-speed wakes, the principal axis of strain is inclined to $\pm 45^{\circ}$ to the direction of the flow and leads to the formation of streamwise inclined rib vortices between the spanwise coherent rollers. The insidious effects of compressibility are rooted in the nearly linear increase of the instability wavelength and decrease of the growth rate with Mach number (Chen *et al.*, 1990; Watanabe & Maekawa, 2004; Hickey *et al.*, 2013*b*). These seemingly unimportant features of high-speed wake transition result in two important modifications to the transitional wake structures: (1) increasing ellipticity of the rollers (with a larger total circulation); (2) increased cross-wake influence of the rollers because of an increasing streamwise separation (with the same cross-wake separation). The combined effect of both flow features leads to drastically different structural dynamics (Hickey *et al.*, 2013*b*). The structural pairing - a distinctive feature of low-speed transition - is inhibited at higher freestream Mach numbers. The increased stability of the roller array results in the vortex breakdown of the inclined ribs prior to the full transition of the primary rollers. In the present work, we show the vortex breakdown of the rib structures through fully resolved direct numerical simulations. The breakdown mechanism is explained using critical point theory of an idealized, inviscid vortex. The vector field around the stagnation point supports the theoretical foundation of the vortex breakdown. By identifying the large-scales structures, we show the roller organization which promotes the breakdown of the ribs. The breakdown of secondary structures prior to the transition of the principal mode opens the path to novel mixing enhancement strategies for high-speed laminar wakes.

The study of vortex breakdown has received considerable attention in classical reviews (Hall, 1972; Leibovich, 1978) as well as in more recent investigations (Brøns *et al.*, 1999; Serre & Bontoux, 2002; Husain *et al.*, 2003; Ruith *et al.*, 2003). Most of the works have studied the breakdown mechanisms in incompressible flows; recently, some attention has

turned to the study of shock-induced vortex breakdown (Kalkoran & Smart, 2000; Zhang *et al.*, 2009). The observation of the breakdown in the secondary rib structures of high-speed wakes has, to the knowledge of the authors, not been addressed in the literature, although experimental visualization by Clemens & Smith (1998) (see figures 2 and 3) of high-speed wake transition - though difficult to identify unequivocally - shows some evidence of vortex breakdown events. Recent works, studying mixing layer transition in stratified flows (Mashayek & Peltier, 2012a,b) discuss the possibility of a stagnation point instability mechanism in two-dimensional flows, which shares some of the characteristics of the present vortex breakdown.

6.3 Numerical Framework

Direct numerical simulations of temporally evolving planar wakes were conducted using an alternatively biased fourth-order finite difference code, which solves the governing equations in conservative form with skew-symmetric convective terms for robustness, discussed in detail in Hickey *et al.* (2013b) (hereafter, HHW). The non-dimensional governing equations of mass, momentum and energy are supplemented with the equation of state. The numerical code was validated with canonical test cases in high-speed flow and with planar wakes in the incompressible limit in Hickey *et al.* (2012). The simulations were conducted at $Re = 3000$ based on the initial wake defect and wake half-width at initial relative Mach numbers of 0.8 and 2.0. Since the vortex breakdown was only observed in the higher Mach number case, the emphasis in the present work is placed on the latter simulation. The domain is doubly periodic in the homogeneous directions (x and z) with non-reflecting boundary conditions based on local inviscid characteristic velocities in the cross-wake direction (y). To remove all spurious oscillations, the boundary condition was

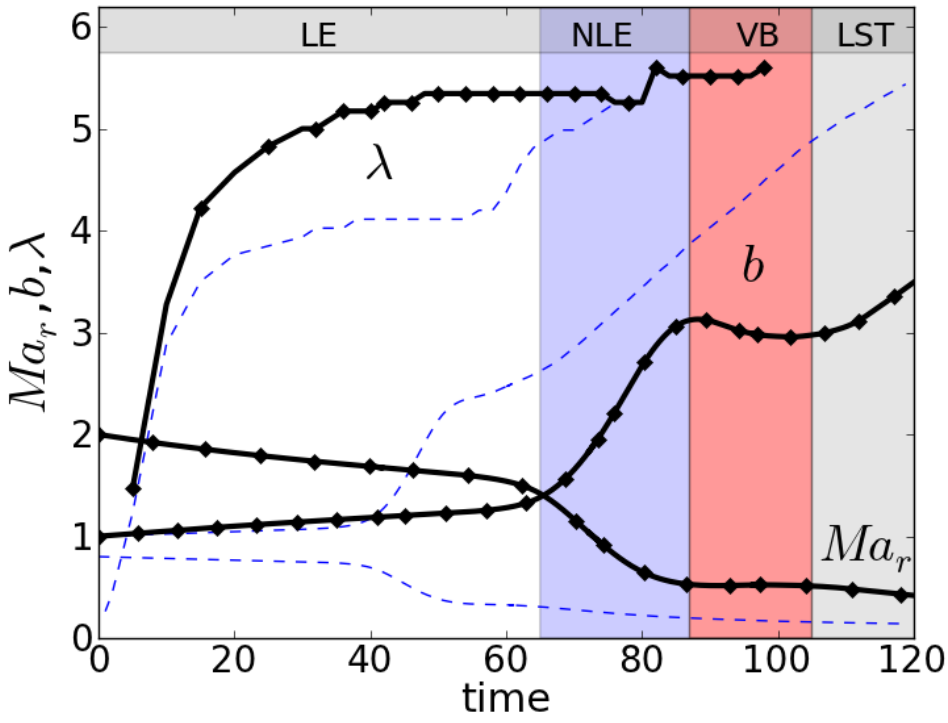

Figure 6.1: Evolution of the relative Mach number (Ma_r), roller size (λ) and wake half-width (b). Wake with $Ma_r = 2.0$ (full lines with diamonds) and comparative wake at $Ma_r = 0.8$ (dashed lines). Approximate regions of transition are shown: linear evolution (LE), non-linear evolution/roll-up stage (NLE), vortex breakdown (VB) and late-stage transition (LST). The reader should bear in mind that the NLE and VB (and also LST) stages overlap.

supplemented with a sponge layer (third-order exponential function) over at least 15 grid points. For the purpose of our further studies on large-scale structures in the transitional wake, a large computational domain was used: $78.3 \times 20 \times 29.9$ in x, y and z respectively. The spanwise extent was purposefully chosen to accommodate the development of large wavelength oblique modes. To resolve down to the Kolmogorov scale, 619 million grid points were necessary ($1792 \times 496 \times 696$). A careful grid convergence study was conducted to assure the invariance of the transitional statistics from the grid resolution. It should be noted that the vortex breakdown was also observed on the coarser grid. Herein, we report on the finest simulated grid. In addition, a series of lower Reynolds number simulations were conducted to assure the consistency of the results, although in these flows, clear evidence of a vortex breakdown was not observed. The flow is initialized with a laminar Gaussian profile on which low-intensity random fluctuations are superimposed; the initial thermodynamic properties are set with Crocco-Busemann relation assuming a constant pressure wake. The initial broadband random fluctuations are chosen to break non-physical symmetries that may arise from an idealized laminar computational setup. As such, no preferential wavelength is amplified and all unstable modes may develop concurrently which permits a greater generality of the obtained results.

6.4 Summary of High-Speed Wake Transition

Here, we summarize the main features of high-speed wake transition; a more detailed report can be found in HHW, or Hickey *et al.* (2011). Compressibility effects in single density wake flows are characterized by the relative Mach number, $Ma_r = U_0/c_\infty$, where U_0 and c_∞ are respectively the centerline defect and the freestream speed of sound. The evolution of Ma_r is shown in figure 6.1. Unlike the mixing layer, the compressibility

effects decay with the evolution of the wake. The influence of compressibility is most important in the early stages of transition, while the evolution of the far wake is essentially incompressible. Given this fact, no shocklets are observed during the entire wake transition even with an initial Mach number of 2.0. The maximum turbulent Mach number, $Ma_t = u'_{max}(t)/c_\infty$, peaks just above 0.3. For such a low Ma_t, no shocklets are expected.

The compressibility effects are seen in a reduction of the exponential energy growth of the most unstable mode. As a result, the onset of transition is delayed, the higher the Mach number of the wake. The delayed transition can be seen in the evolution of the wake half-width, b, in figure 6.1. In addition to a longer transition time, compressibility effects are observed in the increasing wavelength of the most unstable mode. The primary instability wavelength increases approximately linearly with Mach number, as shown in HHW; the imprint left by the longer wavelength modifies the spacing and size of the emerging spanwise rollers in the non-linear evolution stage. The streamwise spacing of the rollers, calculated from the first positive peak in the two-point correlation of the cross-wake velocity with streamwise separation (λ), is shown in figure 6.1. As a consequence of an increasing wavelength and reduced growth rate, there is an increased ellipticity of the rollers (which have a larger total circulation) and an increased cross-wake path of communication, see HHW for more details. These features hinder the roller pairing, which, for high enough Mach numbers, is completely inhibited. The obvious differences resulting from the compressibility effects are seen in the structural organization of the transitioning wake, see figure 6.2. Since the pairing between neighboring rollers is inhibited in the high Mach number case, the ribs develop intricate structures connecting rollers on opposite sides of the wake. As the elliptical rollers rotate, the strain field around the ribs is modified which results in a vortex breakdown of the structures. This breakdown is of interest in the present work.

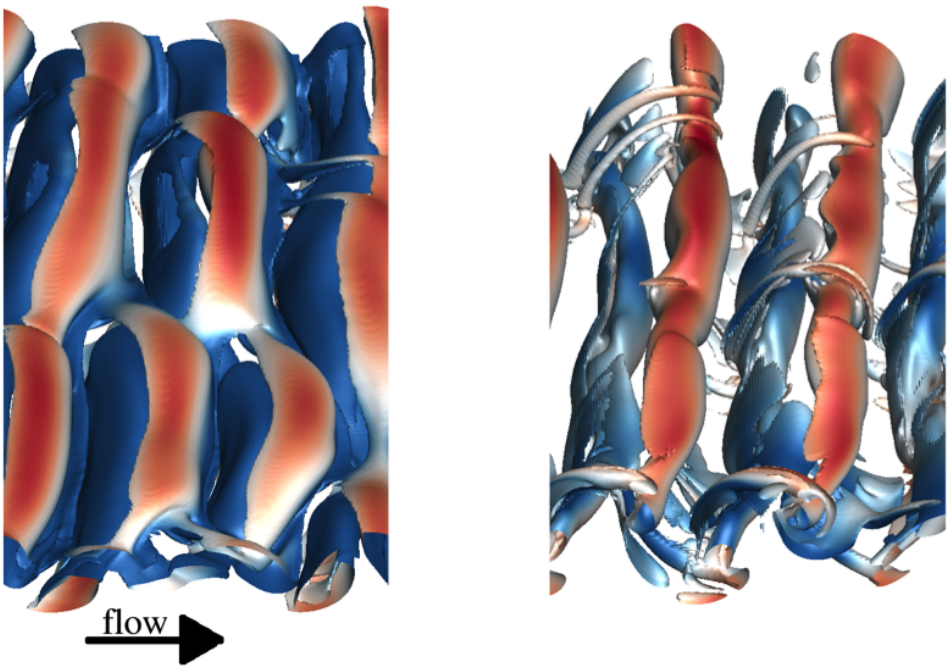

Figure 6.2: Visual comparison of the roller interaction and rib structures between the $Ma = 0.8$ (left) and $Ma = 2.0$ (right) cases using the iso-surface of the Q-criteria.

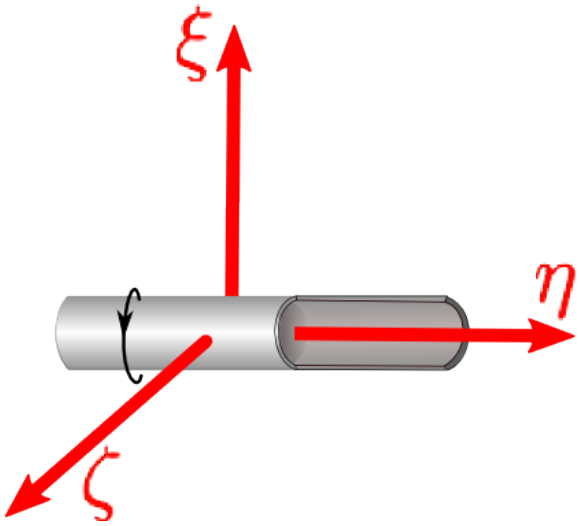

Figure 6.3: Local cartesian coordinate system for the study of the trajectory about a critical point.

6.5 Vortex Breakdown and Critical Point Theory

The sequence of the vortex breakdown events from our direct numerical simulation is shown in figure 6.4. According to Leibovich (1978), a vortex breakdown refers to a: "disturbance characterized by the formation of an internal stagnation point on the vortex axis, followed by reversed flow in a region of limited axial extent". Naturally, as the vortex breakdown occurs, the structure undergoes a very abrupt and rapid change. Since the vortex breakdown implies the presence of a stagnation point, we infer the topology of the resulting structure based on critical point theory.

For simplicity, we assume an idealized vortical structure aligned along the positive η-direction in an arbitrary Cartesian coordinate system with axes: η, ξ, ζ (see figure 6.3). Instead of considering the velocity as function of space and time, we are interested in analyzing the trajectories in phase space. As such, we isolate the location as a function of the velocity. The corresponding streamlines can be written as an ordinary differential equation set (*e.g.,* Brøns *et al.*, 1999):

$$\frac{d\eta\,(t)}{dt} = u^*; \qquad \frac{d\xi\,(t)}{dt} = v^*; \qquad \frac{d\zeta\,(t)}{dt} = w^*. \tag{6.1}$$

The star superscript indicates that the velocities are in the local Cartesian coordinate system of the vortex. Therefore, u^* is the component of the velocity in the η-direction; v^* in the ξ-direction and w^* in the ζ-direction. Following the theoretical development by Zhang *et al.* (2009), we consider the centerline of the vortex to be a critical point in the homogeneous system of ordinary differential equations. Therefore, we can expand the

velocity components about the critical point as a Taylor series:

$$u^* = u_0^* + \eta\frac{\partial u^*}{\partial \eta} + \xi\frac{\partial u^*}{\partial \xi} + \zeta\frac{\partial u^*}{\partial \zeta} + \mathcal{O}\left(\eta^2, \xi^2, \zeta^2\right), \tag{6.2a}$$

$$v^* = v_0^* + \eta\frac{\partial v^*}{\partial \eta} + \xi\frac{\partial v^*}{\partial \xi} + \zeta\frac{\partial v^*}{\partial \zeta} + \mathcal{O}\left(\eta^2, \xi^2, \zeta^2\right), \tag{6.2b}$$

$$w^* = w_0^* + \eta\frac{\partial w^*}{\partial \eta} + \xi\frac{\partial w^*}{\partial \xi} + \zeta\frac{\partial w^*}{\partial \zeta} + \mathcal{O}\left(\eta^2, \xi^2, \zeta^2\right). \tag{6.2c}$$

Naturally, we assume that η, ξ and ζ are small. The expansion can be simplified if we consider a plane perpendicular to the vortex axis: ξ - ζ plane. In this plane, the center of the vortex represents a stagnation point which implies that: $v_0^*(\eta, 0, 0) = w_0^*(\eta, 0, 0) = 0$. By considering the trajectories of the velocity in the ξ-ζ plane about the critical point (see figure 6.3) and by neglecting the higher-order terms, we have:

$$\frac{d\xi}{dt} = \left(\xi\frac{\partial v^*}{\partial \xi} + \zeta\frac{\partial v^*}{\partial \zeta}\right)_c, \tag{6.3a}$$

$$\frac{d\zeta}{dt} = \left(\xi\frac{\partial w^*}{\partial \xi} + \zeta\frac{\partial w^*}{\partial \zeta}\right)_c, \tag{6.3b}$$

or, in phase space:

$$\frac{d\zeta}{d\xi} = \frac{w^*}{v^*} = \frac{\left(\xi\frac{\partial w^*}{\partial y} + \zeta\frac{\partial w^*}{\partial \zeta}\right)_c}{\left(\xi\frac{\partial v^*}{\partial \xi} + \zeta\frac{\partial v^*}{\partial \zeta}\right)_c}. \tag{6.4}$$

The subscript c is to recall that the derivatives are computed about the centerline of the vortex. The trajectory in the plane perpendicular to the vortex axis is determined by two main parameters: the trace, $\tilde{p} = \frac{dv^*}{d\xi} + \frac{dw^*}{d\zeta}$, and the determinant, $\tilde{q} = \frac{dv^*}{d\xi}\cdot\frac{dw^*}{d\zeta} - \frac{dw^*}{d\xi}\cdot\frac{dv^*}{d\zeta}$, of the linear ordinary differential equation set, see *e.g.* Kreyszig (1998) for more details on critical point theory. Since we are considering a critical point of a vortex aligned in the η direction, it is clear that $\tilde{q}$ must be positive (since $-\frac{dw^*}{d\xi}\cdot\frac{dv^*}{d\zeta} > \frac{dv^*}{d\xi}\cdot\frac{dw^*}{d\zeta}$ if the vortex has $\omega_\eta > 0$). As a result, the eigenvalues are complex conjugates and the trajectory is spiral. The direction of the spiral trajectory about the critical point is determined by the trace of the linear ordinary differential equation (6.4). In other words, the direction of the

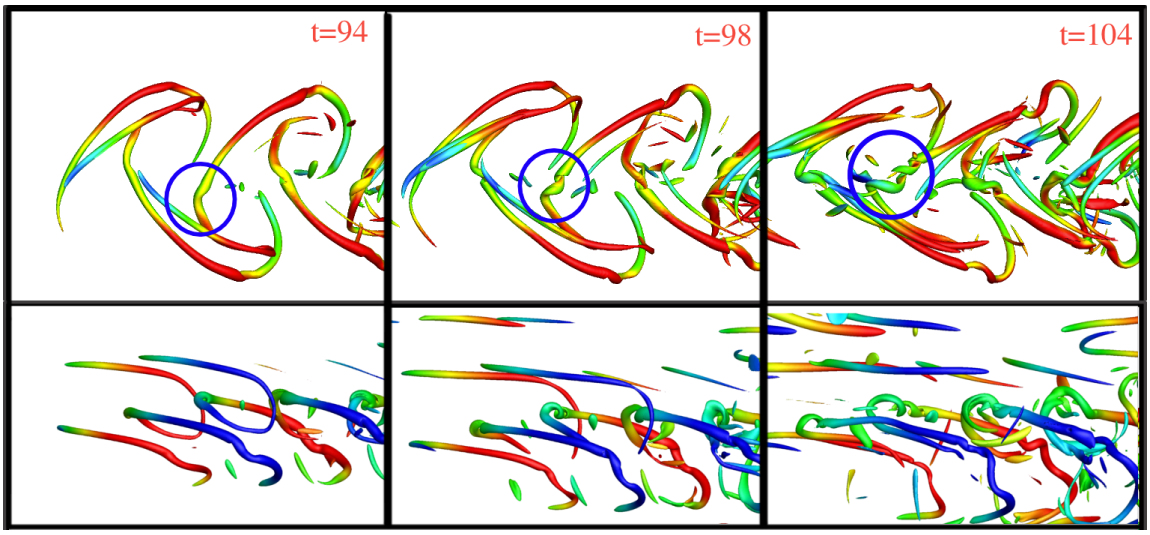

Figure 6.4: Evolution of the rib vortices and their breakdown during the non-linear stages of planar wake transition using the Q-criteria. Side view (top row) and top view (bottom row) at times 94, 98 and 104.

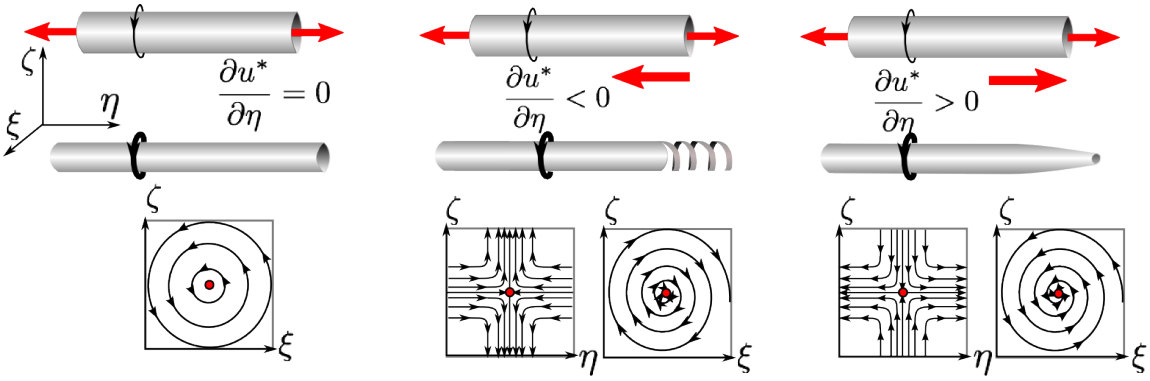

Figure 6.5: Effect of centerline velocity gradients on the breakdown of the vortex assuming that $Ma < 1$. If $\tilde{p} = 0$, we have a stable rotational vortex (left); if $\tilde{p} > 0$, we have an outward spiralling breakdown (middle) and if $\tilde{p} < 0$ we have an inward spiralling / kink formation (right).

trajectory is determined by the sign of:

$$\tilde{p} = \left(\frac{dv^*}{d\xi} + \frac{dw^*}{d\zeta} \right)_c . \tag{6.5}$$

The above equation can be rewritten in terms of other variables with the continuity equation:

$$\frac{\partial \rho}{\partial t} + \frac{\partial \rho u^*}{\partial \eta} + \frac{\partial \rho v^*}{\partial \xi} + \frac{\partial \rho w^*}{\partial \zeta} = 0 \tag{6.6}$$

Since we are evaluating $\tilde{p}$ at the stagnation point, we have $v^* = w^* = 0$, therefore, equation (6.5) becomes:

$$\tilde{p} = \frac{-1}{\rho} \left(\frac{d\rho}{dt} + \frac{d\rho u^*}{d\eta} \right)_c = - \left(\frac{1}{\rho} \frac{d\rho}{dt} + \frac{du^*}{d\eta} + \frac{u^*}{\rho} \frac{d\rho}{d\eta} \right)_c . \tag{6.7}$$

Inspired by Zhang *et al.* (2009), we assume an isentropic speed of sound: $c^2 = \frac{\partial p}{\partial \rho}$. Neglecting the variation in time and with the simplified Euler equation for the η velocity component, $u^* \frac{\partial u^*}{\partial \eta} = -\frac{1}{\rho} \frac{\partial p}{\partial \eta}$, the equation becomes:

$$\tilde{p} = \left(Ma^2 - 1 \right) \frac{du^*}{d\eta} \tag{6.8}$$

The above result suggests that the trajectory in the plane perpendicular to the vortical axis depends primarily on the component of the axial velocity gradient in the axial direction, but also on the Mach number of the flow. For a subsonic flow, if $\frac{du^*}{d\eta} < 0$, the trajectory is a spiral source; if $\frac{du^*}{d\eta} > 0$, it is a spiral sink. See figure 6.5 for illustrative examples. Physically, the spiral source in the ξ-ζ plane corresponds to the spiral breakdown of a vortex. The spiral sink represents vortex stretching along the axial direction. The flow trajectories are inverted in the supersonic case since the sign of the coefficient becomes positive. In the present simulation, the vortex breakdown occurs at $Ma_r \approx 0.5$ (recall figure 6.1) therefore, we will only be considering the subsonic case.

Following a similar development in the meridional plane (η-ζ plane), we observe the emergence of a *saddle point*. Depending on the value of $\frac{du^*}{d\eta}$ along the vortex axis, two

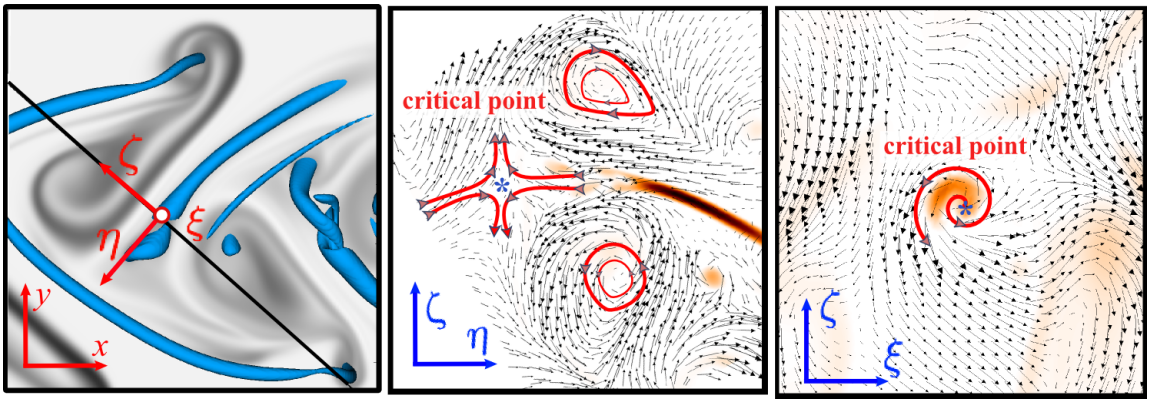

Figure 6.6: Vortex breakdown at $t = 98$. Left: The iso-surface of the Q-criteria ($Q = 0.25$) identifies the rib structures and the corresponding local coordinate system (η,ξ,ζ); the contour plane in η-ξ shows a slice (cutting through the meridional plane of the rib) of the passive scalar field concentration. Middle: Vector field in the η-ζ plane. Right: Vector field in the ξ-ζ plane. The shaded regions in the middle and right panels represent the rib vortex.

types of saddle points may emerge. See figure 6.5 for an illustration of both planes and the corresponding topology of the vortex.

6.6 Investigation of the Rib Breakdown

The simplification of the trajectory about the critical point shown in the previous section can be used to explain the spiral breakdown of the rib structures in the wake. The strain field between two neighboring rollers is maximized for an inclination of $\pm 45^\circ$ to the streamwise direction. As a result, pairs of counter-rotating streamwise inclined vortices emerge between the rollers. These ribs are characteristic of all wakes, irrespective of the Mach number of the flow, see figure 6.2. In the higher Mach number wakes, the increased cross-wake communication and inhibited roller pairing yields very distinctive rib vortices

which connect rollers on either side of the wake, see figure 6.4 at time $t = 94$. As the rollers rotate, the rib vortices are energized through the induced straining. Eventually they disintegrate due to vortex breakdown, see times $t = 98$ and 104 in figure 6.4.

To verify the theoretical development of the previous section, figure 6.6 shows the vector field of the perpendicular and meridional planes of the vortex breakdown event. The meridional plane (figure 6.6 middle panel) shows a clear saddle point. As the rib vortex approaches the stagnation point, the axial velocity, u^*, decreases. Therefore, in this subsonic case (recall that $Ma_r \approx 0.5$ at $t = 98$), a spiral source should be observed in the perpendicular plane of the rib. Figure 6.6 (right panel) clearly shows the corresponding spiral vector field, supporting our theoretical argument in the previous section.

The question now turns to the origin of the stagnation point in the high-speed wakes. As found in HHW, at higher Mach numbers, the rollers become elliptical and strongly asymmetric. As the rollers rotate, the strain field is modified and a stagnation point emerges once the transverse axis of the rollers is inclined to approximately $\pm 45^\circ$ to the streamwise direction. At this rotation, a strong induced velocity is created between neighboring rollers on either side of the wake. The jet formed between these two rollers impinges on the induced flow from a third neighboring roller, which causes a stagnation point. The strain field and stagnation point formation are illustrated in figure 6.7.

6.7 Discussion and Conclusions

We present evidence of a previously unknown breakdown mechanism of the rib structures during the transition of high-speed planar wakes. The breakdown of the rib vortices in the transition of the planar wake with initial relative Mach number of 2.0, is observed as the rollers rotate about themselves. Although the breakdown is only noted in the

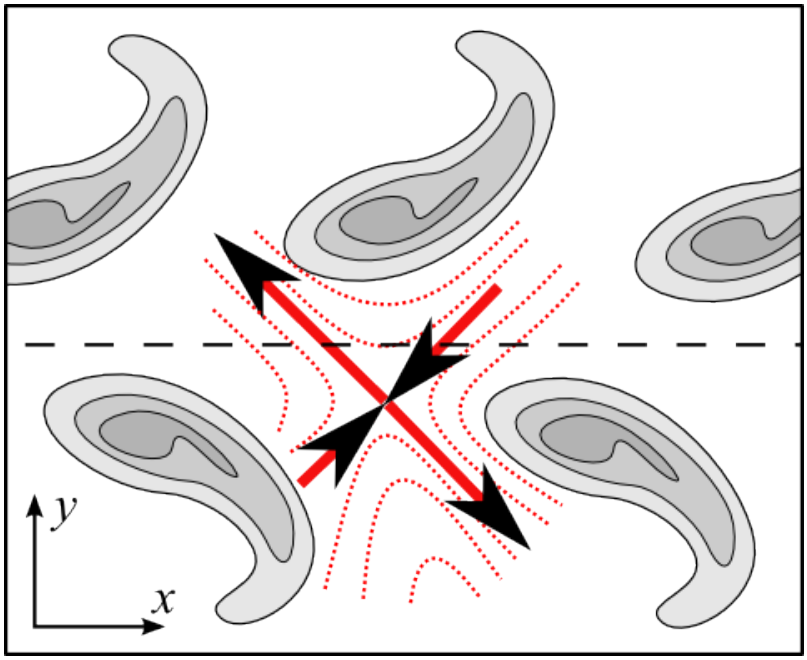

Figure 6.7: Illustration of the stagnation point in relation to the rotating elliptical rollers.

high-speed wakes, it is not a direct consequence of the compressibility effects. Instead, it indirectly results from the effects of compressibility on the formation of the transitional structures in the planar wake. In the present work, we show, using critical point theory, that an outwardly spiralling vortex breakdown occurs as a stagnation point between the rollers is approached. The stagnation point occurs as the elliptical rollers rotate about their spanwise axis. The rollers on either side of the wake induce a very strong jet-like flow along the axis of the rib. This jet is countered by the induced flow of a neighboring roller which leads to the formation of a stagnation point. As the rib approaches the critical point, breakdown ensues. Interestingly, experimental mixing layer investigations have revealed a "kink" formation in the rib structures at higher subsonic convective Mach numbers (Clemens & Mungal, 1995; Olsen & Dutton, 2003). Given the similar propensity

for elliptical structures with increasing Mach number in the mixing layer, it appears possible that a similar stagnation point may emerge and could be the source of this "kink" formation. Further detailed studies would need to be conducted to verify this claim.

Chapter 7

Discussion and Conclusions

This dissertation presents a comprehensive study of canonical planar wakes in the subsonic and supersonic regimes. Despite the simplicity of this flow, the advent of powerful computational tools has done relatively little to further our understanding of the wake. Compared to other constitutive flows such as the boundary layer, channel, jet or mixing layer, the planar wake has not received much attention. Actually, a considerable amount of our understanding of the wake results from dated experimental works. It is for this reason that a fresh, new, physics-based study on the nature of the canonical planar wake was conducted. Resting on the use of very-large scale direct numerical simulations and supplemented by theoretical considerations, the present study was undertaken in order to address many lingering questions for both the subsonic and supersonic cases. The results of this study are presented in chapters 4 to 6; detailed conclusions and discussions are found at the end of each of these chapters. Here, we recall the main contributions of the work, draw broader conclusions and offer paths for future inquiries.

The complete development, verification and validation of a computational fluid dynamics solver for high-speed flows was an integral part of this doctoral work. The numerical implementation and verification is discussed in detail in chapter 3. Whereas most high-speed

codes rely on compact (such as Padé schemes) or spectral methods for spatial derivatives, we opted for a modified MacCormack scheme. By undertaking a study of the numerical properties of the scheme, we gained a firm understanding of the advantages, and, became aware of the limitations of this numerical method. The massive parallelizability afforded by the local stencil allowed us to compensate the less desirable dispersive and dissipative characteristics by a much higher grid count. The over-resolution was beneficial as it reduced the aliasing error, allowed for a very precise study of the turbulent/non-turbulent interface (chapter 4) and helped to limit errors caused by the high gradients in the flow, which would otherwise require special considerations. The development of this code will also have a lasting value as it will be used by future students in Dr.Wu's group at the Royal Military College of Canada.

In chapter 4, we conducted a series of numerical simulations for the incompressible planar wake in order to characterize and understand the lack of universality in the self-similar statistics. Using four different exit boundary layer states, we showed that each flow independently reaches a self-similar state, but these states are not universal - even when properly scaled. The explanation of this memory effect is central to the understanding of the far wake. We showed that mid-size, rod-like structures are universal and inclined to $\pm 30°$–$35°$ to the streamwise direction, a finding which contradicts the prevailing notion that horseshoes are the archetypical far wake structures. We showed that vortex lines may lead to a misinterpretation of the mid-sized structures but the dynamically relevant structures are, in fact, rods. The memory effects are maintained by the plurality of large-scale structural organization. Two types of large-scale structures were identified, although we admit that other structural organizations may also exist. The anti-symmetric structures correspond to slender, segregated, alternating rollers; this structural model has been the

long-standing conceptual basis for the understanding of far wakes. We revealed the existence of a symmetric mode, which emerges in the absence of a near wake anti-symmetric disturbance (caused by instability modes, shedding and/or trailing edge receptivity). The symmetric rollers are larger and cross the centerplane, a finding that explains a quarter-century old inconsistency first identified by Bonnet *et al.* (1984).

The effects of compressibility in the transition of high-speed wakes are studied in chapters 5 and 6 using linear stability theory, geometric interpretation of characteristic lines and direct numerical simulations. The increased wavelength and the reduced growth rate with increasing Mach number of the most unstable mode define the emerging structural characteristics of the transitional vortex array. The effect of compressibility on the instability modes results in an increased ellipticity and streamwise separation of the rollers, which eventually inhibits the large-scale pairing. We have addressed many important issues in the transition of high-speed wakes: the validity of the isotropic approximation of the convection velocity, the slight increase in the Reynolds stress anisotropy with Mach number and the absence of shocklets for transitioning wakes - at least up to $Ma = 2.0$. The eduction of the structures has given us a clear understanding of the influence of compressibility on the roller formation and the roll-up process. The rotation of elliptical structures modifies the internal dynamics of the wake. As the transverse axis of the rollers becomes perpendicular to the streamwise direction, there is a local peak in the wake spreading. This peak is followed by a temporary reduction of the wake half-width (only for $Ma = 2.0$) once the rollers complete a 180° rotation. The ellipticity also results in the formation of a stagnation point between the rollers which leads to the breakdown of the rib structures prior to the transition of the principal rollers.

7.1 Future Work

Many issues remain unresolved and new questions have come to light as a result of the present investigation. The following topics are, from the perspective of the author, fundamental questions that need to be addressed in future studies:

- **Existence of far wake universality.** The possible existence of a universal state could not be assessed in the present work because of computational limitations. Instead, we inferred, from the self-similar state, the nature of the asymptotic wake. Very recent work by Redford *et al.* (2012) contends that the axisymmetric wake eventually reaches a universal statistical and structural state. Is the same true for the planar wake? What changes occur to the self-similar wake in order to reach an asymptotic state? How do the structures reach a universal state? Although it may seem that such questions are purely academic, they may help reveal the intrinsic physics governing the far wake dynamics.

- **Modelling the memory effects in the wake.** The present investigation convincingly demonstrates that the far wake turbulence is influenced by nearly indelible memory effects originating from the near field. This is seen, for example, in the drastic spread rate variation among wakes with identical mean flow properties. It is therefore obvious that when modelling the effects of turbulence, the local mean flow does not provide all the information. For example, how can the memory effects be incorporate in existing turbulence models? Are there other statistical parameters which are surrogates for the varying structural organization of the wake? From an engineering perspective, these questions continue to be of great interest.

- **Memory effects in high-speed wakes.** In the incompressible wake, the memory

effects were obvious given the multiplicity of self-similar states. From our analysis of the transition in the high-speed planar wake, and based on experimental evidence (Bonnet *et al.*, 1991; Gatski & Bonnet, 2009), we inferred that the effects of compressibility are imparted to the flow and maintained through the memory effects. But because of our computational limitations, we did not achieve a self-similar evolution in the high-speed wake. The far field structural make-up of the high-speed wake needs to be characterized. Do the far wake structures increase in size with the Mach number? What are the effects of an inhibited pairing on the far wake statistics? These fundamental questions still need to be addressed.

- **Stability of a staggered array of rollers with compressibility.** The classical study by von Karman (1911) highlights, with elegance, the stability characteristics of a staggered array of vortex filaments. Recent theoretical works, using a hollow vortex assumption instead of an idealized filament (Crowdy & Green, 2011; Llewellyn Smith & Crowdy, 2012), have contributed to a better understanding of the stability characteristics of a vortex array. All these works rest on the validity of the Biot-Savart induction theorem and, therefore, assume incompressibility. The compressible counterparts to these stability calculations are of great importance not only from a theoretical, but also from an engineering perspective.

- **Flow control of transitional structures.** In chapter 6, we showed that the breakdown of secondary structures precedes the transition to turbulence of the primary rollers. This interesting finding could be employed to precipitate or delay the breakdown of the rib structures. To accomplish such flow control, many problems need to be addressed. The breakdown was shown to result from the organization of rotating elliptical rollers. Therefore, the exact mechanism by which the breakdown may be

controlled remains unclear. One idea may be to apply an asymmetric forcing to a laminar wake in order to obtain an asynchronous rotation of the rollers on either side of the wake. As a result, the formation of a stagnation point may be controlled, with a concomitant effect on the breakdown.

These questions, and many others discussed at the end of chapters 4 to 6, remain unanswered. They lie at the intersection of physics, mathematics and engineering. The answer to these questions remains the key to addressing important problems such as the quantification of the minimal separation distance between aircrafts, proper modelling of wake/boundary layer interaction in numerical computations in turbomachinery and many more problems of great interest and importance.

Bibliography

2012 *Aeronautical Information Manual, Federal Aviation Administration, U.S. Department of Transportation*. U.S. Department of Transportation.

del Alamo, J. & Jimenez, J. 2009 Estimation of turbulent convection velocities and corrections to Taylor's approximations. *J. Fluid Mech.* **640**, 5–26.

Althaus, W. 1990 Experimental investigation of vortex formation in the wake of a flat plate for subsonic and supersonic freestream Mach numbers. *Exp. Fluids* **9**, 267–272.

Antonia, R. A. & Browne, L. W. B. 1986 Anisotropy of the temperature dissipation in a turbulent wake. *J. Fluid Mech.* **163**, 393–403.

Antonia, R. A., Browne, L. W. B., Bisset, D. K. & Fulachier, L. 1987 A description of the organized motion in the turbulent far wake of a cylinder at low Reynolds number. *J. Fluid Mech.* **184**, 423–444.

Ardalan, K., Meiron, D.I. & Pullin, D. I. 1995 Steady compressible vortex flows: the hollow-core vortex array. *J. Fluid Mech.* **301**, 1–17.

Bandyopadhyay, P.R. 2005 Modification of Vehicle Wake Vortices. *Tech. Rep.*. Naval Undersea Warfare Center.

Barone, M. F. & Lele, S. 2005 Receptivity of compressible mixing layer. *J. Fluid Mech.* **540**, 301–335.

Bastin, F., Lafon, F. & Candel, S. 1997 Computation of jet mixing due to coherent structures: the plane jet case. *J. Fluid Mech.* **335**, 261–304.

Batchelor, G. K. 1967 *An Introduction to Fluid Dynamics*. Cambridge Univ Press.

Becker, R. 1922 Stosswelle und detonation. *Zeitschrift für Physik A Hadrons and Nuclei* **8** (1), 321–362.

Behrens, W. 1968 Far wake behind cylinders at hypersonic speed: II. stability. *AIAA J.* **6 (2)**, 225–232.

Behrens, W. & Ko, D. R. S. 1971 Experimental stability studies in wakes of two-dimensional slender bodies at hypersonic speeds. *AIAA J.* **9 (5)**, 851–857.

Bell, J. H. & Mehta, R. D. 1990 Development of a two-stream mixing layer from tripped and untripped boundary layers. *AIAA J.* **28(12)**, 2034–2042.

Bevilaqua, P. M. & Lykoudis, P. S. 1978 Turbulence memory in self-preserving wakes. *J. Fluid Mech.* **89**, 589–606.

Bingham, R. 2007 On the crest of a wake. *Nature* **445**, 721–722.

Bisset, D. K., Antonia, R. & Browne, L.W.B. 1990*a* Spatial organization of large structures in the turbulent far wake of a cylinder. *J. Fluid Mech.* **218**, 439–461.

Bisset, D. K., Antonia, R. A. & Britz, D. 1990*b* Structures of large-scale vorticity in a turbulent far wake. *J. Fluid Mech.* **218**, 463–482.

Bisset, D. K., Hunt, J. C. R. & Rogers, M. M. 2002 The turbulent/non-turbulent interface bounding a far wake. *J. Fluid Mech.* **451**, 383–410.

Blaisdell, G.A., Mansour, N.N. & Reynolds, W.C. 1993 Compressibility effects on the growth and structure of homogeneous turbulent shear flow. *J. Fluid Mech.* **256**, 443–485.

Bonnet, J.-P. & Chaput, E. 1986 Large-scale structures visualization in a high-Reynolds number turbulent flat plate wake at supersonic speeds. *Exp. Fluids* **4**, 350–356.

Bonnet, J.-P., Delville, J. & Garem, H. 1986 Space and space-time longitudinal velocity correlations in the turbulent far wake of a flat plate in incompressible flow. *Exp. Fluids* **4**, 189–196.

Bonnet, J.-P., Delville, J., Sapin, S., Sullivan, P. & Yeru, R. 1991 Compressibility effects in turbulent far wakes. In *Eigth Symposium on Turbulent Shear Flows*.

Bonnet, J.-P., Jayaraman, V. & Alziary de Roquefort, T. 1984 Structure of a high-Reynolds number turbulent wake in supersonic flow. *J. Fluid Mech.* **143**, 277–304.

Breidenthal, R. 1980 Response of plane shear layers and wakes to strong three-dimensional disturbances. *Phys. Fluids* **23**, 1929–1934.

Breidenthal, R. 1992 Sonic eddy - a model for compressible turbulence. *AIAA J.* **30(1)**, 101–104.

Broderick, A. J., Bevilaqua, P., Crough, J., Gregory, F., Hussain, F., Jeffers, B. F., Newton, D. W., Nguyen, D. P., Powell, J., Spain, A. T., Stone, R. P. & Willcox, K. 2008 *Wake Turbulence: An Obstacle to Increased Air Traffic Capacity*. The National Academies Press.

Brøns, M., Voigt, L.K. & Sørensen, J.N. 1999 Streamline topology of steady axisymmetric vortex breakdown in a cylinder with co- and counter-rotating end-covers. *J. Fluid Mech.* **401**, 275–292.

Brosh, A & Kussoy, M. 1983 An experimental investigation of the impingement of a planar shock wave on an axisymmetric body at Mach 3. *Tech. Rep.*. NASA Technical Memorandum 84410.

Brown, G.L. & Roshko, A. 1974 On density effects and large structure in turbulent mixing layers. *J. Fluid Mech.* **64**, 775–816.

Brown, G. L. & Roshko, A. 2011 Turbulent shear layers and wakes. In *Turbulence Colloquium Marseille 2011*. 50th anniversary of 1961 Marseille meeting.

Browne, L.W.B., Antonia, R. A. & Bisset, D. K. 1986 Coherent structures in the far field of a turbulent wake. *Phys. Fluids* **29(11)**, 3612–3618.

Cain, A. B., Ferziger, J. H. & Reynolds, W. C. 1984 Discrete orthogonal function expansions for non-uniform grids using the fast Fourier transform. *J. Comput. Phys.* **56**, 272–286.

Chakraborty, P., Balachandar, S. & Adrian, R. J. 2005 On the relationships between local vortex identification schemes. *J. Fluid Mech.* **535**, 189–214.

Chapman, C. J. 2000 *High-speed flow*. Cambridge University Press.

Chen, J.H., Cantwell, B. J. & Mansour, N. N. 1990 The effect of Mach number on the stability of a plane supersonic wake. *Phys. Fluids A* **2**, 984–1004.

Chevray, R. & Kovasznay, L. S. G. 1969 Turbulence measurements in the wake of a thin flat plate. *AIAA J.* **7**, 1641–1643.

Choi, J.-Y., Ma, F. & Yang, V. 2005 Combustion oscillations in a scramjet engine combustor with transverse fuel injection. *Proc. Combust. Inst.* **30**, 2851–2858.

Chung, T. J. 2002 *Computational Fluid Dynamics*. Cambridge Univ Press.

Cimbala, J. M., Nagib, H. & Roshko, A. 1988 Large structure in the far wakes of two-dimensional bluff bodies. *J. Fluid Mech.* **190**, 265–298.

Clemens, N. & Mungal, M. 1995 Large-scale structure and entrainment in the supersonic mixing layer. *J. Fluid Mech.* **284**, 171–216.

Clemens, N. T. & Smith, M.F. 1998 Observations of a supersonic flat plate wake transition. *AIAA J.* **36 (7)**, 1328–1330.

Crowdy, D.G. & Green, C. C. 2011 Analytical solutions for von Karman streets of hollow vortices. *Phys. Fluids* **23** (12), 126602.

Curran, E. & Murthy, S. 2000 *Scramjet Propulsion*. American Institute of Aeronautics and Astronautics.

Demetriades, A. 1971 Observations on the transition process of two-dimensional supersonic wakes. *AIAA J.* **9** (11), 2128–2134.

Demetriades, A. 1976 Turbulence correlations in a compressible wake. *J. Fluid Mech.* **74** (02), 251–267.

Demetriades, A. 1978 Transition to turbulence in two-dimensional wakes. *AIAA J.* **16** (6), 587–591.

Desikan, S. L., N. & Kurian, J. 2006 Strut-based gaseous injection into a supersonic stream. *J. Propul. Power* **22 (2)**, 474–478.

Ewing, D., George, W. K., Rogers, M. & Moser, R. 2007 Two-point similarity in temporally evolving plane wakes. *J. Fluid Mech.* **577**, 287–307.

Ferré, J. A., J. A., Mumford, J. C., Savill, A. M. & Giralt, F. 1990 Three-dimensional large-eddy motions and fine-scale activity in a plane turbulent wake. *J. Fluid Mech.* **210**, 371–414.

Foysi, H. & Sarkar, S. 2010 The compressible mixing layer: an LES study. *Theor. Comput. Fluid Dyn.* **24**, 565–588.

Freund, J. B., Lele, S.J. & Moin, P. 2000*a* Compressibility effects in a turbulent annular mixing layer. Part 2. mixing of a passive scalar. *J. Fluid Mech.* **421**, 269–292.

Freund, J. B., Lele, S. J. & Moin, P. 2000*b* Compressibility effects in a turbulent annular mixing layer. Part 1. turbulence and growth rate. *J. Fluid Mech.* **421**, 229–267.

Gai, S. L., Hughes, D. P. & Perry, M.S. 2002 Large-scale structures and growth of a flat plate compressible wake. *AIAA J.* **40**, 1164–1169.

Gatski, T.B. & Bonnet, J.P. 2009 *Compressibility, Turbulence and High Speed Flow*. Elsevier Science.

George, W. K. 1989 *The self-preservation of turbulent flows and its relation to initial conditions and coherent structures*. Advances in Turbulence, Berlin, Springer.

Ghosal, S. & Rogers, M. M. 1997 A numerical study of self-similarity in a turbulent plane wake using Large-Eddy Simulation. *Phys. Fluids* **9**, 1729–1739.

Gill, A. E. 1965 Instabilities of "top-hat" jets and wakes in compressible fluids. *Phys. Fluids* **8**, 1428.

Giralt, F. & Ferré, J. A. 1993 Structure and flow patterns in turbulent wakes. *Phys. Fluids* **A 5**, 1783–1789.

Gold, H. 1963 Stability of laminar wakes. PhD thesis, California Institute of Technology.

Gottlieb, David & Turkel, Eli 1976 Dissipative two-four methods for time-dependent problems. *Math. Comput.* **30** (136), 703–723.

Grant, M. L. 1958 The large eddies of turbulent motion. *J. Fluid Mech.* **4**, 149–190.

Hall, M. G. 1972 Vortex breakdown. *Annu. Rev. Fluid Mech.* **4**, 195–218.

Hayakawa, M. & Hussain, F. 1989 Three-dimensionality of organized structures in a plane turbulent wake. *J. Fluid Mech.* **206**, 375–404.

Head, M. R. & Bandyopadhyay, P. 1981 New aspects of turbulent boundary-layer structure. *J. Fluid Mech.* **107**, 297–338.

Hebert, T. 1988 Secondary instability of boundary layers. *Annu. Rev. Fluid Mech* **20**, 487–526.

Hickey, J.P., Blakie, S., Gray, C. & Wu, X. 2010 Further studies on the statistics and structures of flat-plate boundary layer with passing wakes. *Int. J. Heat Fluid Flow* **31** (3), 315–326.

Hickey, J.P., Hussain, F. & Wu, X. 2013*a* Vortex breakdown in transitional high-speed wake. *Phys. Fluids* **(to be submitted)**.

Hickey, J.-P., Blakie, S., Gray, C. & Wu, X. 2009 Further studies on the statistics and structures of flat-plate boundary layer with passing wakes. In *Sixth International Symposium on Turbulence and Shear Flow Phenomena*, pp. 169–174.

Hickey, J.-P., Hussain, F. & Wu, X. 2011 Coherent structures in the transition of compressible planar wakes. In *Seventh International Symposium on Turbulence and Shear Flow Phenomena*, pp. 1–6.

Hickey, J.-P., Hussain, F. & Wu, X. 2012 Role of coherent structures in multiple self-similar states of turbulent planar wakes. *J. Fluid Mech.* **(submitted and in first revision)**.

Hickey, J.-P., Hussain, F. & Wu, X. 2013*b* Compressibility effects in the transition in the high-speed planar wakes. *J. Fluid Mech.* **(to be submitted)**.

Hixon, R. 1997 Evaluation of a high-accuracy MacCormack-type scheme using benchmark problems. *Tech. Rep.*. NASA (ICOMP9703).

Ho, C. M. & Huerre, P. 1984 Perturbed free shear layers. *Annu. Rev. Fluid Mech.* **16**, 365–422.

Howarth, L. 1953 *Modern development in fluid dynamics - High speed flow*. Oxford University Press.

Husain, H.S., Shtern, V. & Hussain, F. 2003 Control of vortex breakdown by addition of near-axis swirl. *Phys. Fluids* **15**, 271.

Hussain, A. & Clark, AR 1981*a* On the coherent structure of the axisymmetric mixing layer: a flow-visualization study. *J. Fluid Mech.* **104**, 263–294.

Hussain, A.K.M.F. & Clark, A. R. 1977 Upstream influence on the near field of a plane turbulent jet. *Phys. Fluids* **20**, 1461–1472.

Hussain, A.K.M.F. & Hayakawa, M. 1987 Eduction of large-scale organized structures in a turbulent plane wake. *J. Fluid Mech.* **180**, 193–229.

Hussain, A. K. M. F. & Clark, A. R. 1981*b* Measurements of wavenumber-celerity spectrum in plane and axisymmetric jets. *AIAA J.* **19 (1)**, 51–51.

Hussain, A. K. M. F. & Zedan, M. F. 1978*a* Effects of the initial condition on the axisymmetric free shear layer: Effect of the initial fluctuation level. *Phys. Fluids* **21**, 1475–1481.

Hussain, A. K. M. F. & Zedan, M. F. 1978*b* Effects of the initial condition on the axisymmetric free shear layer: Effects of the initial momentum thickness. *Phys. Fluids* **21**, 1100–1112.

Jeong, J. & Hussain, F. 1995 On the identification of a vortex. *J. Fluid Mech.* **285**, 69–94.

Jeong, J., Hussain, F., Schoppa, W. & Kim, J. 1997 Coherent structures near the wall in a turbulent channel flow. *J. Fluid Mech.* **332**, 185–214.

Johansson, P. B. V., George, W. K. & Gourlay, M. J. 2003 Equilibrium similarity, effects of initial conditions and local reynolds number on the axisymmetric wake. *Phys. Fluids* **15 (3)**, 603–617.

Julien, S., Lasheras, J. & Chomaz, J.-M. 2003 Three-dimensional instability and vorticity patterns in the wake of a flat plate. *J. Fluid Mech.* **479**, 155–189.

KALKORAN, I. J. & SMART, M. K. 2000 Aspects of shock wave-induced vortex breakdown. *Prog* **36**, 63–95.

VON KARMAN, T. 1911 Über den mechanismus des widerstandes den ein bewegter körper in einer flüssigkeit erfärt. *Nachrichten von der Gesellschaft der Wissenschaften zu Göttingen, Mathematisch-Physikalische Klasse* pp. 509–517.

KASTENGREN, A. L., DUTTON, J. C. & ELLIOT, G. S. 2007 Large-scale structure visualization and convection velocity in supersonic blunt-base cylinder wakes. *Phys. Fluids* **19**, 015103.

KOPP, G. A., GIRALT, F. & KEFFER, J. A. 2002 Entrainment vortices and interfacial intermittent turbulent bulges in a plane turbulent wake. *J. Fluid Mech.* **469**, 49–70.

KOURTA, A. & SAUVAGE, R. 2002 Computation of supersonic mixing layers. *Phys. Fluids* **14-11**, 3790–3798.

KOURTA, A. & VITALE, E. 2002 Analysis and control of cavity flow. *Phys. Fluids* **20** (7), 077104.

KREYSZIG, E. 1998 *Advanced Engineering Mathematics*. John Wiley & Sons.

KUNDU, PK & COHEN, IM 2004 *Fluid Mechanics*. Elsevier Academic Press.

KUSSOY, M.I. & HORSTMAN, K. C. 1992 Intersecting shock-wave/turbulent boundary-layer interactions at mach 8.3. *Tech. Rep.*. NASA Technical Memorandum 103909.

LARUE, J. C. & LIBBY, P. A. 1974*a* Temperature and intermittency in the turbulent wake of a heated cylinder. *Phys. Fluids* **17**, 873–890.

LaRue, J. C. & Libby, P. A. 1974*b* Temperature fluctuations in the plane turbulent wake. *Phys. Fluids* **17**, 1956–1967.

LaRue, J. C. & Libby, P. A. 1976 Statistical properties of the interface in the turbulent wake of a heated cylinder. *Phys. Fluids* **19**, 1864–1875.

Lasheras, J. C. & Meiburg, E. 1990 Three-dimensional vorticity modes in the wake of a flat plate. *Phys. Fluids A* **2**, 371–381.

Laufer, J. 1975 New trends in experimental turbulence research. *Annu. Rev. Fluid Mech.* **7**, 307–326.

Lee, S., Lele, S. K. & Moin, P. 1991 Eddy shocklets in decaying compressible turbulence. *Phys. Fluids* **3**, 658–664.

Lees, L. & Gold, H. 1966 Stability of laminar boundary layer and wakes at hypersonic speeds. In *Proceedings of the international Symposium on Fundamental Phenomena in Hypersonic Flow*, p. 310. Cornell University Press.

Leibovich, S. 1978 The structure of vortex breakdown. *Annu. Rev. Fluid Mech.* **10** (1), 221–246.

Lepore, J. & Mydlarski, L. 2009 Effect of the scalar injection mechanism on passive scalar structure functions in a turbulent. *Phys. Rev. Lett.* **103**, 034501–1– 034501–4.

Lesieur, M. 1997 *Turbulence in Fluids (3rd rev.)*. Kluwer Academic Publishers.

Liao, J.C., Beal, D. N., Lauder, G. V. & Triantafyllou, M. S. 2003 The Karman gait: novel body kinematics of rainbow trout swimming in a vortex streets. *J. Exp. Biol.* **206**, 1059–1073.

Llewellyn Smith, S.G. & Crowdy, D.G. 2012 Structure and stability of hollow vortex equilibria. *J. Fluid Mech.* **691**, 178–200.

Lysenko, V. I. 1999 Experimental studies of stability and transition in high-speed wakes. *J. Fluid Mech.* **392**, 1–26.

Lysenko, V. I., Semenov, N. V. & Smorodskii, B. V. 2008 Stability of a supersonic flat-plate wake: Comparison of numerical and experimental results. *Fluid Dyn.* **43 (6)**, 869–872.

Ma, H. D., Pan, H. L. & Wang, Q. 2009 *Numerical Simulations of Transitional and Turbulent Flows in Plane Mixing Layers*. Springer.

MacCormack, R. W. 1969 The effect of viscosity in hypervelocity impact cratering. *AIAA J.* **69**, 354–361.

Mack, L. M. 1975 Linear stability theory and the problem of supersonic boundary-layer transition. *AIAA J.* **13**, 278–289.

Mack, L. M. 1990 On the insvicid acoustic-mode instability of supersonic shear flows. Part 1: Two-dimensional waves. *Theor. Comput. Fluid Dyn.* **2**, 97–123.

Maekawa, H., Mansour, N. N. & Buell, J. C. 1992 Instability mode interactions in a spatially developing plane wake. *J. Fluid Mech.* **235**, 223–254.

Maekawa, H., Takiguchi, T. & Watanabe, D. 2006 Acoustic wave generation in a compressible wake. *JSME Int J., Ser. B* **49 (4)**, 1086.

Mahesh, K., Moin, P. & Lele, S. 1996 The interaction of a shock wave with a turbulent shear flow. *Tech. Rep.*. Stanford University.

Marasli, B., Champagne, F. & Wygnanski, I. 1992 Effect of travelling waves on the growth of a plane turbulent wake. *J. Fluid Mech.* **235**, 511–528.

Martin, C., Seibert, M., Neill, J. D., Schiminovich, D., Forster, K., Rich, R. M., Welsh, B. Y., Madore, B. F., Wheatley, J. M., Morrissey, P. & Barlow, T. A. 2007 A turbulent wake as a tracer of 30,000 years of Mira's mass loss history. *Nature* **448**, 780–783.

Mashayek, A. & Peltier, W. R. 2012*a* The zoo of secondary instabilities precursory to stratified shear flow transition. Part 1: Shear aligned convection, pairing, and braid instabilities. *J. Fluid Mech.* **708**, 5 – 44.

Mashayek, A. & Peltier, W. R. 2012*b* The zoo of secondary instabilities precursory to stratified shear flow transition. Part 2: The influence of stratification. *J. Fluid Mech.* **708**, 45–70.

Meiburg, E. & Lasheras, JC 1987 Comparison between experiments and numerical simulations of three-dimensional plane wakes. *Phys. Fluids* **30**, 623.

Meiron, DI, Moore, DW & Pullin, DI 2000 On steady compressible flows with compact vorticity; the compressible Stuart vortex. *J. Fluid Mech.* **409** (1), 29–49.

Meliga, P., Sipp, D. & Chomaz, J.-M. 2010 Effect of compressibility on the global stability of axisymmetric wake flows. *J. Fluid Mech.* **660**, 499526.

Messersmith, NL & Dutton, JC 1996 Characteristic features of large structures in compressible mixing layers. *AIAA J.* **34** (9), 1814–1821.

Moin, P. 2010 *Fundamentals of Engineering Numerical Analysis*. Cambridge University Press.

Moser, R. D., Rogers, M. M. & Ewing, D. W. 1998 Self-similarity of time-evolving plane wakes. *J. Fluid Mech.* **367**, 255–289.

Mumford, J. C. 1983 The structure of the large eddies in fully developed turbulent shear flows. Part 2. The plane wake. *J. Fluid Mech.* **137**, 447–456.

Nakagawa, M. & Dahm, W. J. A. 2006 Scaling properties and wave interaction in confined supersonic turbulent bluff-body wake. *AIAA J.* **44 (6)**, 1299–1310.

Narasimha, R. & Prabhu, A. 1972 Equilibrium and relaxation in turbulent wakes. *J. Fluid Mech.* **54**, 1–17.

Olsen, M.G. & Dutton, J.C. 2003 Planar velocity measurements in a weakly compressible mixing layer. *J. Fluid Mech.* **486**, 51–77.

O'Reilly, G. & Pullin, D. I. 2003 Structure and stability of the compressible Stuart vortex. *J. Fluid Mech.* **493**, 231254.

Pantano, C. & Sarkar, S. 2002 A study of compressibility effects in the high-speed turbulent shear layer using direct simulation. *J. Fluid Mech.* **451**, 329–371.

Papageorgiou, D. T. 1990 Linear instability of the supersonic wake behind a flat plate aligned with a uniform stream. *Theor. Comput. Fluid Dyn.* **1 (6)**, 327–348.

Papageorgiou, D. T. & Smith, F. T. 1989 Linear instability of the wake behind a flat plate placed parallel to a uniform stream. *J. Fluid Mech.* **208**, 67–89.

Papailiou, D.D. & Lykoudis, P.S. 1974 Turbulent vortex streets and the entrainment mechanism of the turbulent wake. *J. Fluid Mech.* **62**, 11–31.

Papamoschou, D. 1993 Zone of influence in the compressible shear layer. *Fluid Dyn. Res.* **11**, 217–228.

Papamoschou, D. 1994 Characteristics of the linearized equations of motion for a compressible fluid. *Phys. Fluids* **6**, 3–5.

Papamoschou, Dimitri 1995 Evidence of shocklets in a counterflow supersonic shear layer. *Phys. Fluids* **7** (2), 233–235.

Papamoschou, D. & Lele, S. 1993 Vortex-induced disturbance field in a compressible shear layer. *Phys. Fluids* **4**, 1412–1419.

Passot, T. & Pouquet, A. 1987 Numerical simulation of compressible homogeneous flows in the turbulent regime. *J. Fluid Mech.* **181**, 441–466.

Payne, F. & Lumley, J. 1967 Large eddy structure of the turbulent wake behind a circular cylinder. *Phys. Fluids* **9**, S194–S196.

Perez, R. E., Jansen, P. W. & Martins, J. R. 2012 pyOpt: a Python-based object-oriented framework for nonlinear constrained optimization. *Struct. Multidiscip. Optim.* **45** (1), 101–118.

Philip, J. & Marusic, I. 2012 Large-scale eddies and their role in entrainment in turbulent jets and wakes. *Phys. Fluids* **24**, 055108.

Piomelli, U. 2009 Course notes: Mech 935 turbulence simulations (fall semester 2009). Queens University at Kingston.

Piponniau, S., Dussauge, J.-P., Debieve, J.F. & Dupont, P. 2009 A simple model for low-frequency unsteadiness in shock-induced separation. *J. Fluid Mech.* **629**, 87–108.

Pope, S. 2000 *Turbulent Flows*. Cambridge University Press.

Rai, M.M. 2010 A computational investigation of symmetric and asymmetric turbulent wakes. In *AIAA 40th Fluid Dynamics Conference and Exhibit (AIAA 2010-4602)*.

Redford, J. A., Castro, I. & Coleman, G. 2012 On the universality of turbulent axisymmetric wakes. *J. Fluid Mech.* **710**, 419–452.

Robinson, A. C. & Saffman, P. G. 1982 Three-dimensional stability of vortex arrays. *J. Fluid Mech.* **125**, 411–427.

Robinson, SK 1991 Coherent motions in the turbulent boundary layer. *Annu. Rev. Fluid Mech.* **23**, 601–639.

Rona, A., Spisso, I., Bernardini, M. & Pirozzolli, S. 2009 Comparison of optimized high-order finite-difference schemes for computational aeroacoustics. In *47th AIAA Aerospace Sciences Meeting Including The New Horizons Forum and Aerospace Exposition*.

Ruith, M. R., Chen, P., Meiburg, E. & Maxwothy, T. 2003 Three-dimensional vortex breakdown in swirling jets and wakes: direct numerical simulations. *J. Fluid Mech.* **486**, 331–371.

Samtaney, R., Pullin, D. I. & Kosovic, Branko 2001 Direct numerical simulation of decaying compressible turbulence and shocklet statistics. *Phys. Fluids* **13**, 1415–1430.

Sandberg, R. D. 2011 Stability analysis of axisymmetric supersonic wakes using various basic states. In *2011 J. Phys.: Conf. Ser. 318 032017*.

Sandberg, R. D. & Fasel, H. 2006 Numerical investigation of transitional supersonic axisymmetric wakes. *J. Fluid Mech.* **563**, 1–41.

Sandham 1989 A numerical investigation of the compressible mixing layer. PhD thesis, Stanford University.

Sandham, N. 1994 The effect of compressibility on vortex pairing. *Phys. Fluids* **6(2)**, 1063–1073.

Sandham, N. D. & Reynolds, W. 1990 Compressible mixing layer : Linear theory and direct simulation. *AIAA J.* **28(4)**, 618–624.

Sandham, N. D. & Reynolds, W. C. 1991 Three-dimensional simulation of large-eddies in the compressible mixing layer. *J. Fluid Mech.* **224**, 133–158.

Sandham, N. D. & Sandberg, R. D. 2009 Direct numerical simulation of the early development of a turbulent mixing layer downstream of a splitter plate. *J. Turbul.* **10-1**, 1–17.

Sandham, N. D. & Yee, H. C. 1989 A numerical study of a class of TVD schemes for compressible mixing layers. *Tech. Rep.*. National Aeronautics and space administration.

Sarkar, S., Erlebacher, G. & Hussaini, M.Y. 1991 Direct simulation of compressible turbulence in a shear flow. *Theoret. Comput. Fluid Dyn.* **2**, 291–305.

Sato, H. & Kuriki, K. 1961 The mechanism of transition in the wake of a thin flat plate placed parallel to a uniform flow. *J. Fluid Mech.* **11**, 321–352.

Schoppa, W., Hussain, F. & Metcalfe, R. W. 1995 A new mechanism of small-scale transition in a plane mixing layer: core dynamics of spanwise vortices. *J. Fluid Mech.* **298**, 23–80.

Schulte, V. & Hodson, HP 1998*a* Prediction of the becalmed region for LP turbine profile design. *J. Turbomach.* **120**, 839.

Schulte, V. & Hodson, HP 1998*b* Unsteady wake-induced boundary layer transition in high lift LP turbines. *J. Turbomach.* **120**, 28.

Segal, C. 2009 *The Scramjet Engine: Processes and Characteristics*. Cambridge University Press.

Serre, E. & Bontoux, P. 2002 Vortex breakdown in a three-dimensional swirling flow. *J. Fluid Mech.* **459** (1), 347–370.

Shu, C.-W. & Osher, S. 1989 Efficient implementation of essentially non-oscillatory shock-capturing schemes, II. *J. Comput. Phys.* **83**, 32–78.

da Silva, C.B., dos Reis, R. & Pereira, J.C. 2011 The intense vorticity structures near the turbulent/non-turbulent interface in a jets. *J. Fluid Mech.* **685**, 165190.

da Silva, C. B. & Pereira, J. C. 2008 Invariants of the velocity-gradient, rate-of-strain, and rate-of-rotation tensors across the turbulent/non-turbulent interface in jets. *Phys. Fluids* **20**, 055101.

da Silva, C. B. & dos Reis, R. J. 2011 The role of coherent vortices near the turbulent/non-turbulent interface in a planar jet. *Phil. Trans. R. Soc. A* **369**, 738–753.

Smits, A. J. & Dussauge, J.-P. 2006 *Turbulent shear layers in supersonic flow*. Springer Verlag.

Sod, GA 1978 A survey of several finite difference methods for systems of nonlinear hyperbolic conservation laws. *J. Comput. Phys.* **27**, 1–31.

Tam, C. W. & Webb, J. C. 1993 Dispersion-relation-preserving finite difference scheme for computational acoustics. *J. Comput. Phys.* **107**, 262–281.

Taneda, S. 1959 Downstream development of the wakes behind cylinders. *J. Phys. Soc. Jpn.* **14**, 843–848.

von Terzi, D.A., Sandberg, R.D. & Fasel, H.F. 2009 Identification of large coherent structures in supersonic axisymmetric wakes. *Comp. Fluids* **38** (8), 1638–1650.

Thomas, F. O. & Liu, X. 2004 An experimental investigation of symmetric and asymmetric turbulent wake development in pressure gradient. *Phys. Fluids* **16**, 1725–1745.

Thompson, K. W. 1987 Time dependent boundary conditions for hyperbolic systems. *J. Comput. Phys.* **68**, 1–24.

Thompson, K. W. 1990 Time-dependent boundary conditions for hyperbolic systems, ii. *J. Comput. Phys.* **89**, 439–461.

Thurow, B.S., Jiang, N., Kim, J.H., Lempert, W. & Samimy, M. 2008 Issues with measurements of the convective velocity of large-scale structures in the compressible shear layer of a free jet. *Phys. Fluids* **20** (6), 066101–066101.

Townsend, A 1956 *The structure of turbulent shear flow*. Cambridge University Press.

Townsend, A. A. 1949 The fully developed turbulent wake of a circular cylinder. *Australian Journal of Scientific Research* **2(4)**, 451– 468.

Townsend, A. A. 1976 *The structure of turbulent shear flow*. Cambridge University Press.

Vanderwel, C. & Tavoularis, S. 2011 Coherent structures in uniformly sheared turbulent flow. *J. Fluid Mech.* **689**, 434–464.

Vernet, A., Kopp, G. A., Ferré, J. A. & Giralt, F. 1999 Three-dimensional structure and momentum transfer in a turbulent cylinder wake. *J. Fluid Mech.* **394**, 303–337.

Virk, D., Hussain, F. & Kerr, RM 1995 Compressible vortex reconnection. *J. Fluid Mech.* **304**, 47–86.

Voke, P. R. & Potamitis, S. G. 1994 Numerical simulation of a low-Reynolds number turbulent wake behind a flat-plate. *Int. J. Numer. Methods Fluids* **19**, 377–393.

Vreman, A. W., Sandham, N. D. & Luo, K. H. 1996 Compressible mixing layer growth rate and turbulence characteristics. *J. Fluid Mech.* **320**, 235–258.

Watanabe, D. & Maekawa, H. 2004 Three-dimensional evolution of structure and acoustic wave and generation in a compressible plane wake. *Fluid Dyn. Res.* **34**, 145–165.

Weygandt, J. H. & Mehta, R. D. 1989 Asymptotic behavivor of a flat plate wake. *Tech. Rep.*. Stanford University (JIAA Tr-95).

White, M. F. 1999 *Fluid Mechanics*. McGraw-Hill.

Whittlesey, Robert W, Liska, Sebastian & Dabiri, John O 2010 Fish schooling as a basis for vertical axis wind turbine farm design. *Bioinspiration & Biomimetics* **5** (3), 035005.

Williamson, C. H. K. & Prasad, A. 1993 A new mechanism for oblique wave resonance in the 'natural' far wake. *J. Fluid Mech.* **256**, 269–313.

Winant, C. D. & Browand, F. K. 1974 Vortex pairing: the mechanism of turbulent mixing-layer growth at moderate reynolds number. *J. Fluid Mech.* **63**, 237–255.

Wu, X. 1996 On an active resonant triad of mixed modes in symmetric shear flows: a plane wake as a paradigm. *J. Fluid Mech.* **317**, 337–368.

Wu, X. & Hickey, J.P. 2012 Visualization of continuous stream of grid turbulence past the Langston turbine cascade. *AIAA J.* **50 (1)**, 215–224.

Wu, X., Jacobs, R., Hunt, J. C. R. & Durbin, P. A. 1999 Simulation of boundary layer transition induced by periodically passing wakes. *J. Fluid Mech.* **398**, 109–153.

Wu, X. & Moin, P. 2009 Direct numerical simulation of turbulence in a nominally zero-pressure-gradient flat-plate boundary layer. *J. Fluid Mech.* **630**, 5–41.

Wu, X. & Moin, P. 2010 Transitional and turbulent boundary layer with heat transfer. *Phys. Fluids* **22**, 085105.

Wygnanski, I., Champagne, F. & Marasli, B. 1986 On the large-scale structures in two-dimensional, small-deficit, turbulent wakes. *J. Fluid Mech.* **168**, 31–71.

Xie, S.-P., Liu, W. T., Liu, Q. & Nonaka, M. 2001 Far-reaching effects of the Hawaiian islands on the Pacific ocean-atmosphere systems. *Science* **2057**.

Yoshizawa, A., Abe, H., Matsuo, Y., Fujiwara, H. & Mizobuchi, Y. 2012 A Reynolds-averaged turbulence modeling approach using three transport equations for the turbulent viscosity, kinetic energy, and dissipation rate. *Phys. Fluids* **24**, 075109.

Zaman, K. B. M. Q. & Hussain, A. K. M. F. 1980 Vortex pariring in a circular jet under controlled excitation: Part 1. general jet response. *J. Fluid Mech.* **101**, 449–491.

Zeman, O. 1990 Dilatation dissipation: The concept and application in modeling compressible mixing layers. *Phys. Fluids* **A(2)**, 178–188.

Zeman, O. 1991 On the decay of compressible isotropic turbulence. *Phys. Fluids* **A(3)**, 951–955.

Zhang, S., Zhang, H. & Shu, C. W. 2009 Topological structure of shock induced vortex breakdown. *J. Fluid Mech.* **639**, 343–373.

Zhou, J., Adrian, R., Balachandar, S. & Kendall, J. 1999 Mechanisms for generating coherent packets of hairpin vortices in channel flow. *J. Fluid Mech.* **387**, 353–396.

Zhou, Y. & Antonia, R. A. 1995 Memory effects in a turbulent plane wake. *Exp. Fluids* **19**, 112–120.

Part I

Appendices

Appendix A

Governing Equations: Expanded Form

The equations developed in chapter 2 are presented here in expanded form:

Conservation of mass:

$$\frac{\partial \rho}{\partial t} + \frac{\partial \rho u}{\partial x} + \frac{\partial \rho v}{\partial y} + \frac{\partial \rho w}{\partial z} = 0 \tag{A.1}$$

Conservation of momentum:

$$\frac{\partial \rho u}{\partial t} + \frac{\partial \rho uu}{\partial x} + \frac{\partial \rho uv}{\partial y} + \frac{\partial \rho uw}{\partial z} = -\frac{1}{\gamma Ma^2}\frac{\partial p}{\partial x} + \frac{1}{Re}\left(\frac{\partial \tau_{11}}{\partial x} + \frac{\partial \tau_{12}}{\partial y} + \frac{\partial \tau_{13}}{\partial z}\right) \tag{A.2}$$

$$\frac{\partial \rho v}{\partial t} + \frac{\partial \rho vu}{\partial x} + \frac{\partial \rho vv}{\partial y} + \frac{\partial \rho vw}{\partial z} = -\frac{1}{\gamma Ma^2}\frac{\partial p}{\partial y} + \frac{1}{Re}\left(\frac{\partial \tau_{21}}{\partial x} + \frac{\partial \tau_{22}}{\partial y} + \frac{\partial \tau_{23}}{\partial z}\right) \tag{A.3}$$

$$\frac{\partial \rho w}{\partial t} + \frac{\partial \rho wu}{\partial x} + \frac{\partial \rho wv}{\partial y} + \frac{\partial \rho ww}{\partial z} = -\frac{1}{\gamma Ma^2}\frac{\partial p}{\partial z} + \frac{1}{Re}\left(\frac{\partial \tau_{31}}{\partial x} + \frac{\partial \tau_{32}}{\partial y} + \frac{\partial \tau_{33}}{\partial z}\right) \tag{A.4}$$

Conservation of energy:

$$\begin{aligned}\frac{\partial E}{\partial t} + \frac{\partial Eu}{\partial x} + \frac{\partial Ev}{\partial y} + \frac{\partial Ev}{\partial z} &= -\frac{1}{\gamma Ma^2}\left(\frac{\partial pu}{\partial x} + \frac{\partial pv}{\partial y} + \frac{\partial pw}{\partial z}\right) \\ &+ \frac{1}{PrRe\,(\gamma-1)\,Ma^2}\left(\frac{\partial}{\partial x}\left(\kappa\frac{\partial T}{\partial x}\right) + \frac{\partial}{\partial y}\left(\kappa\frac{\partial T}{\partial y}\right) + \frac{\partial}{\partial z}\left(\kappa\frac{\partial T}{\partial z}\right)\right) + \\ &\frac{1}{Re}\left(\frac{\partial \tau_{11}u}{\partial x} + \frac{\partial \tau_{12}v}{\partial x} + \frac{\partial \tau_{13}w}{\partial x} + \frac{\partial \tau_{21}u}{\partial y} + \frac{\partial \tau_{22}v}{\partial y} + \frac{\partial \tau_{23}w}{\partial y} + \frac{\partial \tau_{31}u}{\partial z} + \frac{\partial \tau_{32}v}{\partial z} + \frac{\partial \tau_{33}w}{\partial z}\right)\end{aligned} \tag{A.5}$$

Passive transport:

$$\frac{\partial \rho\phi}{\partial t} + \frac{\partial \left(\rho\phi\right) u}{\partial x} + \frac{\partial \left(\rho\phi\right) v}{\partial y} + \frac{\partial \left(\rho\phi\right) w}{\partial z} = \frac{1}{ReSc}\left[\frac{\partial}{\partial x}\left(\mu\frac{\partial\phi}{\partial x}\right) + \frac{\partial}{\partial y}\left(\mu\frac{\partial\phi}{\partial y}\right) + \frac{\partial}{\partial z}\left(\mu\frac{\partial\phi}{\partial z}\right)\right] \tag{A.6}$$

In the above equations, the shear stresses are expanded to:

$$\tau_{11} = \mu\left[2\frac{\partial u}{\partial x} - \frac{2}{3}\left(\frac{\partial u}{\partial x} + \frac{\partial v}{\partial y} + \frac{\partial w}{\partial z}\right)\right] \tag{A.7a}$$

$$\tau_{22} = \mu\left[2\frac{\partial v}{\partial y} - \frac{2}{3}\left(\frac{\partial u}{\partial x} + \frac{\partial v}{\partial y} + \frac{\partial w}{\partial z}\right)\right] \tag{A.7b}$$

$$\tau_{33} = \mu\left[2\frac{\partial w}{\partial z} - \frac{2}{3}\left(\frac{\partial u}{\partial x} + \frac{\partial v}{\partial y} + \frac{\partial w}{\partial z}\right)\right] \tag{A.7c}$$

$$\tau_{12} = \tau_{21} = \mu\left(\frac{\partial u}{\partial y} + \frac{\partial v}{\partial x}\right) \tag{A.7d}$$

$$\tau_{13} = \tau_{31} = \mu\left(\frac{\partial u}{\partial z} + \frac{\partial w}{\partial x}\right) \tag{A.7e}$$

$$\tau_{23} = \tau_{32} = \mu\left(\frac{\partial v}{\partial z} + \frac{\partial w}{\partial y}\right) \tag{A.7f}$$

To reduce the manipulations in the Navier-Stokes solver, the above equations may be rewritten in matrix form such that:

$$\frac{\partial \mathbf{U}}{\partial t} + \frac{\partial \mathbf{A}}{\partial x} + \frac{\partial \mathbf{B}}{\partial y} + \frac{\partial \mathbf{C}}{\partial z} = 0 \tag{A.8}$$

where we define:

$$\mathbf{U} = \begin{bmatrix} \rho \\ \rho u \\ \rho v \\ \rho w \\ E \\ \phi \end{bmatrix} \tag{A.9}$$

$$\mathbf{A} = \begin{bmatrix} \rho u \\ \rho uu + \tilde{p} - \tilde{\tau_{11}} \\ \rho uv - \tilde{\tau_{21}} \\ \rho uw - \tilde{\tau_{31}} \\ u\left(E + \tilde{p}\right) + q_1 - \tilde{\tau_{11}} u - \tilde{\tau_{12}} v - \tilde{\tau_{13}} w \\ \rho\phi u - \frac{1}{ReSc}\mu\partial\phi/\partial x \end{bmatrix} \tag{A.10}$$

$$\mathbf{B} = \begin{bmatrix} \rho v \\ \rho uv - \tilde{\tau_{12}} \\ \rho vv + \tilde{p} - \tilde{\tau_{22}} \\ \rho vw - \tilde{\tau_{32}} \\ v\left(E + \tilde{p}\right) + q_2 - \tilde{\tau_{21}} u - \tilde{\tau_{22}} v - \tilde{\tau_{23}} w \\ \rho\phi v - \frac{1}{ReSc}\mu\partial\phi/\partial y \end{bmatrix} \tag{A.11}$$

$$\mathbf{C} = \begin{bmatrix} \rho w \\ \rho wu - \tilde{\tau_{13}} \\ \rho wv - \tilde{\tau_{23}} \\ \rho ww + \tilde{p} - \tilde{\tau_{33}} \\ w\left(E + \tilde{p}\right) + q_3 - \tilde{\tau_{31}} u - \tilde{\tau_{32}} v - \tilde{\tau_{33}} w \\ \rho\phi w - \frac{1}{ReSc}\mu\partial\phi/\partial z \end{bmatrix} \tag{A.12}$$

We redefine the shear stresses as:

$$\tilde{\tau_{11}} = \frac{\mu}{Re}\left[2\frac{\partial u}{\partial x} - \frac{2}{3}\left(\frac{\partial u}{\partial x} + \frac{\partial v}{\partial y} + \frac{\partial w}{\partial z}\right)\right] = \frac{\mu}{Re}\frac{4}{3}\frac{\partial u}{\partial x} - \frac{\mu}{Re}\frac{2}{3}\frac{\partial v}{\partial y} - \frac{\mu}{Re}\frac{2}{3}\frac{\partial w}{\partial z} \tag{A.13a}$$

$$\tilde{\tau_{22}} = \frac{\mu}{Re}\left[2\frac{\partial v}{\partial y} - \frac{2}{3}\left(\frac{\partial u}{\partial x} + \frac{\partial v}{\partial y} + \frac{\partial w}{\partial z}\right)\right] = \frac{\mu}{Re}\frac{4}{3}\frac{\partial v}{\partial y} - \frac{\mu}{Re}\frac{2}{3}\frac{\partial u}{\partial x} - \frac{\mu}{Re}\frac{2}{3}\frac{\partial w}{\partial z} \tag{A.13b}$$

$$\tilde{\tau_{33}} = \frac{\mu}{Re}\left[2\frac{\partial w}{\partial z} - \frac{2}{3}\left(\frac{\partial u}{\partial x} + \frac{\partial v}{\partial y} + \frac{\partial w}{\partial z}\right)\right] = \frac{\mu}{Re}\frac{4}{3}\frac{\partial w}{\partial z} - \frac{\mu}{Re}\frac{2}{3}\frac{\partial v}{\partial y} - \frac{\mu}{Re}\frac{2}{3}\frac{\partial u}{\partial x} \tag{A.13c}$$

$$\tilde{\tau_{12}} = \tilde{\tau_{21}} = \frac{\mu}{Re}\left(\frac{\partial u}{\partial y} + \frac{\partial v}{\partial x}\right) = \frac{\mu}{Re}\frac{\partial u}{\partial y} + \frac{\mu}{Re}\frac{\partial v}{\partial x} \tag{A.13d}$$

$$\tilde{\tau_{13}} = \tilde{\tau_{31}} = \frac{\mu}{Re}\left(\frac{\partial u}{\partial z} + \frac{\partial w}{\partial x}\right) = \frac{\mu}{Re}\frac{\partial u}{\partial z} + \frac{\mu}{Re}\frac{\partial w}{\partial x} \tag{A.13e}$$

$$\tilde{\tau_{23}} = \tilde{\tau_{32}} = \frac{\mu}{Re}\left(\frac{\partial v}{\partial z} + \frac{\partial w}{\partial y}\right) = \frac{\mu}{Re}\frac{\partial v}{\partial z} + \frac{\mu}{Re}\frac{\partial w}{\partial y} \tag{A.13f}$$

where:

$$\tilde{p} = \frac{p}{(\gamma Ma^2)} \tag{A.14a}$$

$$q_1 = -\frac{\kappa}{PrRe\,(\gamma-1)\,Ma^2}\frac{\partial T}{\partial x} \tag{A.14b}$$

$$q_2 = -\frac{\kappa}{PrRe\,(\gamma-1)\,Ma^2}\frac{\partial T}{\partial y} \tag{A.14c}$$

$$q_3 = -\frac{\kappa}{PrRe\,(\gamma-1)\,Ma^2}\frac{\partial T}{\partial z} \tag{A.14d}$$

We can rewrite the above equations in fully expanded form as:

$$\mathbf{A} = \begin{bmatrix} \rho u \\ \rho uu + \tilde{p} - \frac{\mu}{Re}\frac{4}{3}\frac{\partial u}{\partial x} + \frac{\mu}{Re}\frac{2}{3}\frac{\partial v}{\partial y} + \frac{\mu}{Re}\frac{2}{3}\frac{\partial w}{\partial z} \\ \rho uv - \frac{\mu}{Re}\frac{\partial u}{\partial y} - \frac{\mu}{Re}\frac{\partial v}{\partial x} \\ \rho uw - \frac{\mu}{Re}\frac{\partial u}{\partial z} - \frac{\mu}{Re}\frac{\partial w}{\partial x} \\ u\,(E+\tilde{p}) + q_1 - u\frac{\mu}{Re}\frac{4}{3}\frac{\partial u}{\partial x} + u\frac{\mu}{Re}\frac{2}{3}\frac{\partial v}{\partial y} + u\frac{\mu}{Re}\frac{2}{3}\frac{\partial w}{\partial z} - v\frac{\mu}{Re}\frac{\partial u}{\partial y} - v\frac{\mu}{Re}\frac{\partial v}{\partial x} - w\frac{\mu}{Re}\frac{\partial u}{\partial z} - w\frac{\mu}{Re}\frac{\partial w}{\partial x} \\ \rho\phi u - \frac{\mu}{ReSc}\frac{\partial \phi}{\partial x} \end{bmatrix} \tag{A.15}$$

$$\mathbf{B} = \begin{bmatrix} \rho v \\ \rho uv - \frac{\mu}{Re}\frac{\partial u}{\partial y} - \frac{\mu}{Re}\frac{\partial v}{\partial x} \\ \rho vv + \tilde{p} - \frac{\mu}{Re}\frac{4}{3}\frac{\partial v}{\partial y} + \frac{\mu}{Re}\frac{2}{3}\frac{\partial u}{\partial x} + \frac{\mu}{Re}\frac{2}{3}\frac{\partial w}{\partial z} \\ \rho vw - \frac{\mu}{Re}\frac{\partial v}{\partial z} - \frac{\mu}{Re}\frac{\partial w}{\partial y} \\ v\left(E+\tilde{p}\right) + q_2 - u\frac{\mu}{Re}\frac{\partial u}{\partial y} - u\frac{\mu}{Re}\frac{\partial v}{\partial x} - v\frac{\mu}{Re}\frac{4}{3}\frac{\partial v}{\partial y} + v\frac{\mu}{Re}\frac{2}{3}\frac{\partial u}{\partial x} + v\frac{\mu}{Re}\frac{2}{3}\frac{\partial w}{\partial z} - w\frac{\mu}{Re}\frac{\partial v}{\partial z} - w\frac{\mu}{Re}\frac{\partial w}{\partial y} \\ \rho\phi v - \frac{\mu}{ReSc}\frac{\partial \phi}{\partial y} \end{bmatrix} \tag{A.16}$$

$$\mathbf{C} = \begin{bmatrix} \rho w \\ \rho wu - \frac{\mu}{Re}\frac{\partial u}{\partial z} - \frac{\mu}{Re}\frac{\partial w}{\partial x} \\ \rho wv - \frac{\mu}{Re}\frac{\partial v}{\partial z} - \frac{\mu}{Re}\frac{\partial w}{\partial y} \\ \rho ww + \tilde{p} - \frac{\mu}{Re}\frac{4}{3}\frac{\partial w}{\partial z} + \frac{\mu}{Re}\frac{2}{3}\frac{\partial v}{\partial y} + \frac{\mu}{Re}\frac{2}{3}\frac{\partial u}{\partial x} \\ w\left(E+\tilde{p}\right) + q_3 - u\frac{\mu}{Re}\frac{\partial u}{\partial z} - u\frac{\mu}{Re}\frac{\partial w}{\partial x} - v\frac{\mu}{Re}\frac{\partial v}{\partial z} - v\frac{\mu}{Re}\frac{\partial w}{\partial y} - w\frac{\mu}{Re}\frac{4}{3}\frac{\partial w}{\partial z} + w\frac{\mu}{Re}\frac{2}{3}\frac{\partial v}{\partial y} + w\frac{\mu}{Re}\frac{2}{3}\frac{\partial u}{\partial x} \\ \rho\phi w - \frac{\mu}{ReSc}\frac{\partial \phi}{\partial z} \end{bmatrix} \tag{A.17}$$

Appendix B

Linear Stability Theory for High-Speed Flows

The linearized Navier-Stokes equations in non-conservative form are written as (Watanabe & Maekawa, 2004):

$$\frac{\partial \rho'}{\partial t} + u_1 \frac{\partial \rho'}{\partial x_1} + u_2' \frac{\partial \rho}{\partial x_2} + \rho \left[\frac{\partial u_1'}{\partial x_1} + \frac{\partial u_2'}{\partial x_2} + \frac{\partial u_3'}{\partial x_3} \right] = 0 \tag{B.1a}$$

$$\begin{aligned} & \rho \frac{\partial u_1'}{\partial t} + \rho u_1 \frac{\partial u_1'}{\partial x_1} + \rho u_2' \frac{\partial u_1}{\partial x_2} + \frac{1}{\gamma Ma^2} \left(T \frac{\partial \rho'}{\partial x_1} + \rho \frac{\partial T'}{\partial x_1} \right) \\ = \quad & \frac{1}{Re} \mu \left(\frac{4}{3} \frac{\partial^2 u_1'}{\partial x_1^2} + \frac{\partial^2 u_1'}{\partial x_2^2} + \frac{\partial^2 u_1'}{\partial x_3^2} + \frac{1}{3} \frac{\partial^2 u_2'}{\partial x_1 \partial x_2} + \frac{1}{3} \frac{\partial^2 u_3'}{\partial x_1 \partial x_3} \right) \\ & + \frac{1}{Re} \left(\mu' \frac{\partial^2 u_1}{\partial x_2^2} + \frac{\partial \mu}{\partial x_2} \left(\frac{\partial u_1'}{\partial x_2} + \frac{\partial u_2'}{\partial x_1} \right) + \frac{\partial \mu'}{\partial x_2} \frac{\partial u_1}{\partial x_2} \right) \end{aligned} \tag{B.1b}$$

$$\begin{aligned} & \rho \frac{\partial u_2'}{\partial t} + \rho u_1 \frac{\partial u_2'}{\partial x_1} + \frac{1}{\gamma Ma^2} \left(T \frac{\partial \rho'}{\partial x_2} + T' \frac{\partial \rho}{\partial x_2} + \rho \frac{\partial T'}{\partial x_2} + \rho' \frac{\partial T}{\partial x_2} \right) \\ = \quad & \frac{1}{Re} \mu \left(\frac{\partial^2 u_2'}{\partial x_1^2} + \frac{4}{3} \frac{\partial^2 u_2'}{\partial x_2^2} + \frac{\partial^2 u_2'}{\partial x_3^2} + \frac{1}{3} \frac{\partial^2 u_1'}{\partial x_1 \partial x_2} + \frac{1}{3} \frac{\partial^2 u_3'}{\partial x_2 \partial x_3} \right) \\ & + \frac{1}{Re} \left(\frac{\partial \mu}{\partial x_2} \left(-\frac{2}{3} \frac{\partial \mu'}{\partial x_1} + \frac{4}{3} \frac{\partial u_2'}{\partial x_2} - \frac{2}{3} \frac{\partial u_3'}{\partial x_3} \right) + \frac{\partial \mu'}{\partial x_1} \frac{\partial u_1}{\partial x_2} \right) \end{aligned} \tag{B.1c}$$

$$\begin{aligned}
&\rho\frac{\partial u_3'}{\partial t}+\rho u_1\frac{\partial u_3'}{\partial x_1}+\frac{1}{\gamma Ma^2}\left(T\frac{\partial \rho'}{\partial x_3}+\rho\frac{\partial T'}{\partial x_3}\right)\\
&\quad=\frac{1}{Re}\mu\left(\frac{\partial^2 u_3'}{\partial x_1^2}+\frac{\partial^2 u_3'}{\partial x_2^2}+\frac{4}{3}\frac{\partial^2 u_3'}{\partial x_3^2}+\frac{1}{3}\frac{\partial^2 u_1'}{\partial x_1\partial x_3}+\frac{1}{3}\frac{\partial^2 u_2'}{\partial x_2\partial x_3}\right)\\
&\quad\quad+\frac{1}{Re}\frac{\partial \mu}{\partial x_2}\left(\frac{\partial u_3'}{\partial x_2}+\frac{\partial u_2'}{\partial x_3}\right)
\end{aligned}\tag{B.1d}$$

$$\begin{aligned}
&\rho\frac{\partial T'}{\partial t}+\rho u_1\frac{\partial T}{\partial x_1}+\rho u_2\frac{\partial T}{\partial x_2}+(\gamma-1)\left(\rho T\frac{\partial u_1'}{\partial x_1}+\rho T\frac{\partial u_2'}{\partial x_2}+\rho T\frac{\partial u_3'}{\partial x_3}\right)\\
&\quad=\frac{\gamma}{Pr\,Re}\left(\mu\frac{\partial^2 T'}{\partial x_1^2}+\mu\frac{\partial^2 T'}{\partial x_2^2}+\mu\frac{\partial^2 T'}{\partial x_3^2}+\mu'\frac{\partial^2 T}{\partial x_2^2}+\frac{\partial \mu}{\partial x_2}\frac{\partial T'}{\partial x_2}+\frac{\partial \mu'}{\partial x_2}\frac{\partial T}{\partial x_2}\right)\\
&\quad\quad+\frac{\gamma(\gamma-1)Ma^2}{Re}\left(2\mu\frac{\partial \mu}{\partial x_2}\frac{\partial u_2'}{\partial x_1}+2\mu\frac{\partial u_1}{\partial x_2}\frac{\partial u_1}{\partial x_2}+\mu'\left(\frac{\partial u_1}{\partial x_2}\right)^2\right)
\end{aligned}\tag{B.1e}$$

As described in chapter 2, the fluctuating components of the above equations are replaced by the ansatz 2.11. The variables are then rearranged and transformed into matrix form, written in equation 2.12. The coefficient matrix $\mathcal{L}$ is then:

$$\mathcal{L}=\begin{pmatrix}
\alpha u_1 & \alpha\rho & -i(D\rho+\rho D) & \beta\rho & 0\\
\frac{\alpha T}{\rho\gamma Ma^2} & \Gamma_{22} & \Gamma_{23} & -\frac{i\mu\alpha\beta}{3\rho Re} & \Gamma_{25}\\
-\frac{i(DT+TD)}{\rho\gamma Ma^2} & \Gamma_{32} & \Gamma_{33} & \Gamma_{34} & \Gamma_{35}\\
\frac{\beta T}{\rho\gamma Ma^2} & -\frac{i\alpha\beta\mu}{3\rho Re} & \Gamma_{43} & \Gamma_{44} & \frac{\beta}{\gamma Ma^2}\\
0 & \Gamma_{52} & \Gamma_{53} & (\gamma-1)\beta T & \Gamma_{55}
\end{pmatrix},\tag{B.2}$$

where D corresponds to the discretized derivative in the cross-wake direction. The individual components of the above matrix are:

$$\Gamma_{22} = \alpha u_1 - \frac{i}{\rho Re}\left(\mu\left(\frac{4}{3}\alpha^2 - D^2 + \beta^2\right) - \frac{d\mu}{dT}DTD\right), \tag{B.3a}$$

$$\Gamma_{23} = iDu_1 - \frac{\alpha}{\rho Re}\left(\frac{1}{3}\mu D + \frac{d\mu}{dT}DT\right), \tag{B.3b}$$

$$\Gamma_{25} = \frac{\alpha}{\gamma Ma^2} + \frac{i}{\rho Re}\left(Du_1\frac{d^2\mu}{dT^2}DT + \frac{d\mu}{dT}D^2u_1 + Du_1\frac{d\mu}{dT}D - Du_1\frac{d\mu}{dT}DT\right), \tag{B.3c}$$

$$\Gamma_{32} = -\frac{\alpha}{\rho Re}\left(\frac{1}{3}\mu D - \frac{2}{3}\frac{d\mu}{dT}DT\right), \tag{B.3d}$$

$$\Gamma_{33} = \alpha u_1 - \frac{i}{\rho Re}\left(\mu\left(\alpha^2 - \frac{4}{3}D^2 + \beta^2\right) - \frac{4}{3}\frac{d\mu}{dT}DTD\right), \tag{B.3e}$$

$$\Gamma_{34} = -\frac{\beta}{\rho Re}\left(\frac{1}{3}\mu D - \frac{2}{3}\frac{d\mu}{dT}DT\right), \tag{B.4a}$$

$$\Gamma_{35} = -\frac{i\left(D\rho + \rho D\right)}{\rho\gamma Ma^2} - \frac{\alpha}{\rho Re}Du_1\frac{d\mu}{dT}, \tag{B.4b}$$

$$\Gamma_{43} = -\frac{\beta}{\rho Re}\left(\frac{1}{3}\mu D + \frac{d\mu}{dT}DT\right), \tag{B.4c}$$

$$\Gamma_{44} = \alpha u_1 - \frac{i}{\rho Re}\left(\mu\left(\alpha^2 - D^2 + \frac{4}{3}\beta^2\right) - \frac{d\mu}{dT}DTD\right), \tag{B.4d}$$

$$\Gamma_{52} = \alpha\left(\gamma - 1\right)T + \frac{2i\gamma\left(\gamma - 1\right)Ma^2\mu}{\rho Re}Du_1D, \tag{B.4e}$$

$$\Gamma_{53} = i\left(DT + \left(\gamma - 1\right)TD\right) - \frac{2\gamma\left(\gamma - 1\right)Ma^2\mu}{\rho Re}\alpha Du_1, \tag{B.4f}$$

$$\begin{aligned}\Gamma_{55} = {} & \alpha u_1 + \frac{i\gamma\left(\gamma - 1\right)Ma^2}{\rho Re}\frac{d\mu}{dT}\left(Du_1\right)^2 - \frac{i\gamma}{\rho RePr}\left(\mu\left(\alpha^2 - D^2 + \beta^2\right)\right) \\ & - \frac{i\gamma}{\rho RePr}\left(-\frac{d^2\mu}{dT^2}\left(DT\right)^2 - \frac{d\mu}{dT}\left(2DTD + D^2T\right)\right)\end{aligned} \tag{B.4g}$$

Appendix C

Numerical Properties of the MacCormack Scheme

C.1 Verification of the numerical method

An investigation is conducted in order to better comprehend the behaviour of the numerical schemes for resolving sharp gradients in high-speed flows. The investigation is conducted in two parts. Firstly, the Burgers' equation is solved as a surrogate for the Navier-Stokes equations, as it admits an analytical solution. Secondly, the full set of Euler equations are solved on canonical one-dimensional flows with shocks. The studied test cases are the NACA 1135 nozzle, the shock-tube problem and the Shu-Osher problem. These are presented as archival material for the development of the numerical code.

C.1.1 Burgers' equation

The Burgers' equation contains a diffusive part but, more importantly, it contains a nonlinear convective term which makes the equation very similar in form to the Navier-Stokes equations. Although the partial differential equation has a parabolic form in the linear case, the nonlinear equation shows many characteristics of a hyperbolic type of

equations. The nonlinear Burgers equation is written as:

$$\frac{\partial u}{\partial t} = -u\frac{\partial u}{\partial x} + \mu\frac{\partial^2 u}{\partial x^2}, \tag{C.1}$$

where, $\mu = 0.1$, approximates the coefficient of viscosity. In the present test case, the initial condition was given as a step function defined as: $u(x,0) = 1 - \tanh\left(\frac{x-x_c}{2\mu}\right)$. The spatial domain was defined on: $x \in [0, 20]$. Physically, this model equation represents a sharp discontinuity convecting to the right of the computational domain. The inflow boundary condition is: $u\,(0,t) = 2.0$ and the outflow condition is extrapolated from the information inside the computational domain. The equation (C.1) admits an analytical solution of the form:

$$u\,(x,t) = 1 - \tanh\left(\frac{x - x_c - t}{2\mu}\right). \tag{C.2}$$

All the schemes are evaluated at a time $t = 5000$ with a time-step of $\Delta t = 0.001$. In the present case, a comparison is done on a homogeneous grid with 100 grid points. The figure C.1(a) (left), is a close-up of the discontinuity. The MacCormack 22 scheme shows a large overshoot which results in a dispersive error for the shock resolution. The fourth-order MacCormack and Padé schemes are very similar in their ability to capture this discontinuity. But it should be noted that when reducing to even fewer points, the Padé scheme shows a great advantage. It can also be seen that the shock can be fully resolved with the MacCormack scheme without noticeable oscillations for about 250 points, which corresponds to about 10 points in the shock. The use of the analytical solution of the Burgers' equation allows for a numerical verification of the order of accuracy of the schemes. It can be seen in figure C.1(a) (right), that the theoretical order of accuracy of the schemes compares favourably with the numerical order of accuracy.

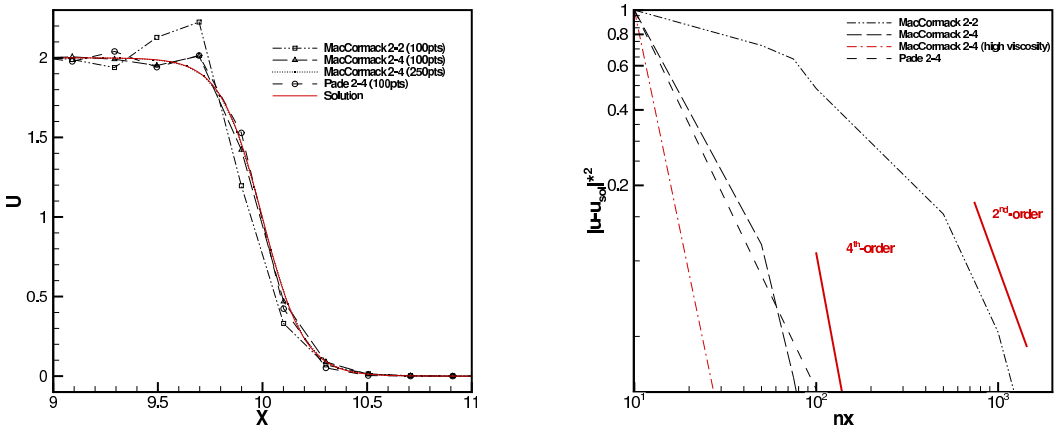

Figure C.1: Comparison of different numerical schemes for the resolution of a shock-wave like discontinuity in the Burgers' equation (left). The normalized error of various numerical scheme (right).

C.1.2 Euler equations

The second set of validations is conducted on simplified one-dimensional fluid dynamic problems. The purely hyperbolic Euler equations are solved axe they admit a perfectly discontinuous shock-type solution (step function). The Euler equations represent the limit case of the Navier-Stokes equation when the shock is infinitely thin. An evaluation of the quasi-one-dimensional NACA 1135 diverging nozzle, the shock-tube problem and the Shu-Osher problem is proposed.

C.1.2.1 Quasi-one-dimensional NACA 1135 problem

The NACA 1135 nozzle with supersonic inlet and subsonic outlet is solved. This particular nozzle has a varying area which corresponds to $S(x) = 1.398 + 0.347 \tanh(0.8x - 4)$.

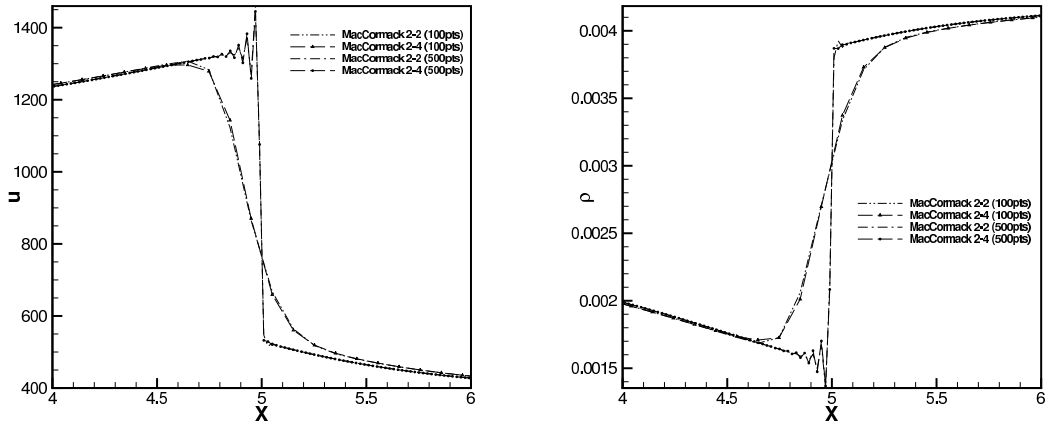

Figure C.2: The velocity (left) and density (right) variation for the NACA 1135 nozzle across the shock-wave. The simulation is conducted using the MacCormack schemes with a low grid resolution (100 pts) and a higher grid resolution (500 pts).

By multiplying the area by the conservation variables, we may solve a quasi-one dimensional problem for the Euler equations (Chung, 2002). The inlet conditions are supersonic and therefore, all variables must be defined on this plane. We have:

$$Ma = 1.5;\ p = 1000;\ \rho = 0.00237;\ \rho u = 2.7323;\ \rho E_t = 4075$$

Only one parameter needs to be specified at the exit plane as the flow is subsonic; we choose to define the velocity: $u = 390.75$.

The initial conditions were chosen in order to obtain a rapid convergence of the simulation to the steady-state. The inflow conditions are used as initial conditions on: $x = [0, 2.8]$. From $x = [2.8, 10]$, we define: $\rho = 0.00237$, $\rho u = 0.92608$ and $\rho \mathrm{E_t} = 2680.93$. The figure C.2(right) shows that for a lower resolution with 100 grid points, the discontinuity is diffused and the shock is artificially smooth. For higher resolution with 500 points, the

location of the discontinuity is correctly achieved but the oscillations are clearly visible on both sides of the discontinuity. The oscillations are not eliminated when the resolution is increased but their domain of influence is reduced. The oscillations are the strongest at the trailing edge of the shock which is clearly observed in figure C.2 (right). This is caused by the order in which the forward and backward finite differencing of the convective terms is accomplish in the predictor/corrector stages of the MacCormack scheme.

C.1.2.2 Shock-tube problem

The Sod problem is a shock-tube problem initially proposed by Sod (1978). Physically, this problem represents a tube with two stagnant regions with different pressures and density separated by a diaphragm. Initially, the setup is described by:

$$\rho_u = 1.0,\ u_u = 0.0,\ p_u = 1.0 \qquad \text{For } x = [0, 0.5] \tag{C.3a}$$

$$\rho_d = 0.25,\ u_d = 0.0,\ p_d = 0.1 \qquad \text{For } x = [0.5, 1.0] \tag{C.3b}$$

where the subscripts u and d are respectively the upstream and downstream position from the diaphragm. By writing the one-dimensional Euler equations in conservative form we can find the characteristics of the system. The three-characteristics obtained represent a shock-wave, a contact wave and an expansion wave; all three need to be resolved by the numerical schemes. The present simulation was conducted for 22,500 timesteps using the MacCormack schemes and compared against a finite-volume Roe solver. The Roe solver approximates a Riemann solution and is very well adapted to these types of problems. It is often used in many mainstream CFD applications for shock resolution because of its very high numerical stability. The MacCormack scheme clearly has the ability to capture all three compression and expansion structures in the flow and compares very favorably to the Roe solver for a similar resolution. Although it should be noted, that with a further

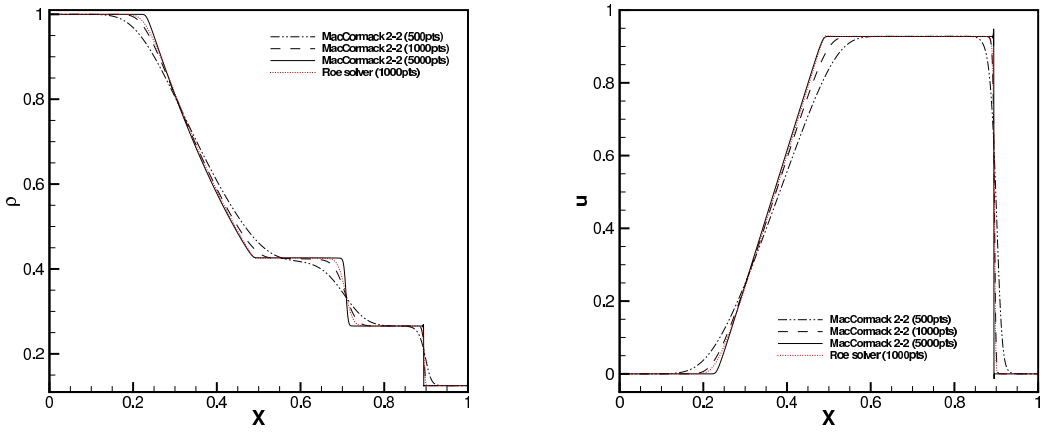

Figure C.3: The density (left) and velocity (right) profiles for the shock-tube problem with various resolution of the MacCormack scheme. A comparison with the solution using the Roe solver is also proposed.

reduction below 500 grid points, the MacCormack scheme is unable to resolve these flow properties, whereas the Roe solver does. Furthermore, the MacCormack scheme shows only very slight oscillations on the shock-wave where as the expansion wave is free of any oscillations.

C.1.2.3 Shu-Osher problem

The Shu-Osher test problem was first proposed by Shu & Osher (1989). It physically represents a moving shock at Mach 3 interacting with a sinuously varying density region. This test problem represents a formidable challenge for numerical schemes to reproduce. The initial conditions for this problem are:

$$\begin{aligned} \rho = 3.857143; \qquad u = 2.629369; \qquad p = 10.33333; \qquad \text{For } x \in [-\infty, -4]\,, \\ \rho = 1 + B\sin(5x)\,; \qquad u = 0; \qquad p = 1; \qquad \text{For } x \in [-4, \infty]\,; \end{aligned} \tag{C.4}$$

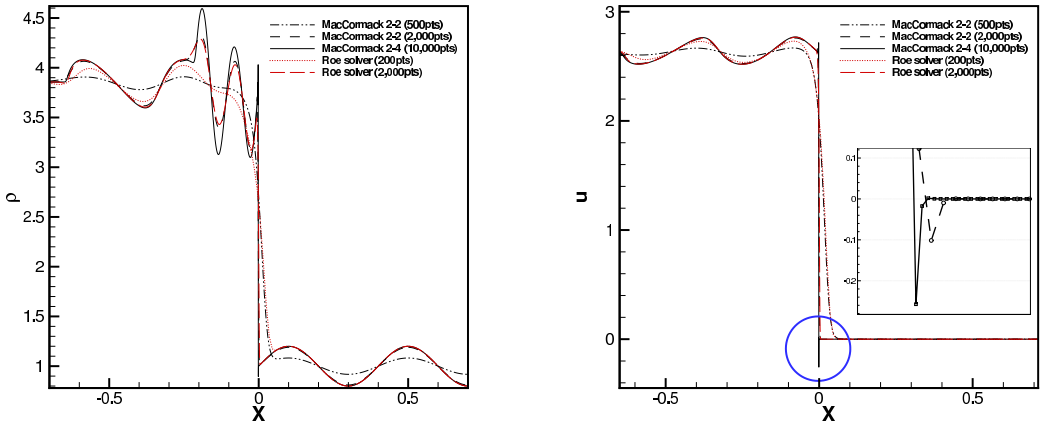

Figure C.4: Density (left) and velocity (right) profiles of the shock interacting with sinusoidal density variation in the Shu-Osher problem. Both MacCormack schemes are essentially identical, hence only the 2-2 scheme is presented and compared with the Roe solver which is an approximate Riemann solver.

where, $B = 0.2$ for the test case presented. The characteristics are propagating toward the right of the domain, hence the boundary conditions at the outlet must be extrapolated from the interior. The inlet boundary maintains the same conditions as the initial state.

The figure C.4 (left) shows that for the post-shock density variation, the MacCormack scheme is at par with the Roe solver for 2000 grid points but for the under-resolved cases, the Roe solver is clearly advantaged. By a five-fold increase in the resolution, the MacCormack scheme accurately captures the main features of the interaction and admits a nearly perfect discontinuity but still maintains a finite level of oscillations in the shock extremities. These oscillations become problematic when looking at figure C.4 (right) which permits a non-physical negative velocity.

Appendix D

Computation of the Non-Reflective Boundary Conditions

The non-dimensionalization used in the developed solver requires a slight modification to the definition of the non-reflecting boundary conditions (NRBC) in Thompson (1990). Therefore, the details of the computation of the NRBC are presented. From the Euler equation for compressible flow (recall equation (3.7)), the coefficients of the normal derivatives to the boundary yields:

$$\mathbf{A} = \begin{pmatrix} v & 0 & 0 & \rho & 0 \\ 0 & v & 0 & u & 0 \\ 0 & 0 & 0 & v & 0 \\ 0 & \frac{1}{\rho\gamma Ma^2} & 0 & v & 0 \\ 0 & 0 & 0 & 0 & v \end{pmatrix}. \tag{D.1}$$

The eigenvalues of the above matrix are:

$$\lambda_1 = -\frac{\sqrt{p\rho} - \rho v Ma}{\rho Ma}; \qquad \lambda_2 = v; \qquad \lambda_3 = v; \qquad \lambda_4 = v; \qquad \lambda_5 = \frac{\sqrt{p\rho} + \rho v Ma}{\rho Ma}. \tag{D.2}$$

By grouping the eigenvalues in a diagonal 5×5 matrix, we obtain:

$$\mathbf{\Lambda} = \begin{pmatrix} -\frac{\sqrt{p\rho}-\rho v Ma}{\rho Ma} & 0 & 0 & 0 & 0 \\ 0 & v & 0 & 0 & 0 \\ 0 & 0 & v & 0 & 0 \\ 0 & 0 & 0 & v & 0 \\ 0 & 0 & 0 & 0 & \frac{\sqrt{p\rho}+\rho v Ma}{\rho Ma} \end{pmatrix}. \tag{D.3}$$

The corresponding left ($\mathbf{S}$) and right ($\mathbf{S}^{-1}$) eigenvectors are mutually orthogonal and satisfy:

$$\mathbf{S}^{-1}\mathbf{A}\mathbf{S} = \mathbf{\Lambda} \tag{D.4}$$

Based on the above equations, the corresponding eigenvectors are:

$$\mathbf{S} = \begin{pmatrix} 1 & \frac{p\gamma}{\rho} & 0 & -\frac{\sqrt{p}}{Ma\rho^{3/2}} & 0 \\ 1 & 0 & 0 & 0 & 0 \\ 0 & 0 & 1 & 0 & 0 \\ 0 & 0 & 0 & 0 & 1 \\ 1 & \frac{p\gamma}{\rho} & 0 & \frac{\sqrt{p}}{Ma\rho^{3/2}} & 0 \end{pmatrix}. \tag{D.5}$$

and

$$\mathbf{S}^{-1} = \begin{pmatrix} 0 & 1 & 0 & 0 & 0 \\ \frac{\rho}{2p\gamma} & -\frac{\rho}{p\gamma} & 0 & 0 & \frac{\rho}{2p\gamma} \\ 0 & 0 & 1 & 0 & 0 \\ -\frac{Ma\rho^{3/2}}{2\sqrt{p}} & 0 & 0 & 0 & \frac{Ma\rho^{3/2}}{2\sqrt{p}} \\ 0 & 0 & 0 & 1 & 0 \end{pmatrix}. \tag{D.6}$$

These eigenvectors are used in the computation of the characteristics-based boundary conditions.

Appendix E

Theoretical Solution of the Viscous Shock

The theoretical solution of the viscous shock problem is detailed for completeness, the development of the solution is attributed to Howarth (1953). We start with the one-dimensional steady-state conservation equations for mass, momentum and energy. The energy equation presented here is analogous to the energy equation presented in equation(2.7c),except it is written as a function of the enthalpy, h, as opposed to E_t. The equations are:

$$\frac{\partial}{\partial x}(\rho u) = 0, \tag{E.1a}$$

$$\rho u \frac{\partial u}{\partial x} = -\frac{\partial p}{\partial x} + \frac{\partial}{\partial x}\left(4/3\mu \frac{\partial u}{\partial x}\right), \tag{E.1b}$$

$$\rho u \frac{\partial h}{\partial x} - u\frac{\partial p}{\partial x} = \frac{\partial}{\partial x}\left(\kappa \frac{\partial T}{\partial x}\right) + 4/3\mu \left(\frac{\partial u}{\partial x}\right)^2. \tag{E.1c}$$

The momentum equation is multiplied by the velocity and added to the energy equation. Defining the Prandtl number as, $Pr = \mu C_p/\kappa$, yields:

$$\rho u \frac{\partial}{\partial x}\left(h + 1/2u^2\right) = \frac{\partial}{\partial x}\left(\mu\left(\frac{1}{Pr}\frac{\partial h}{\partial x} + \frac{4}{3}u\frac{\partial u}{\partial x}\right)\right). \tag{E.2}$$

The integration of the continuity, momentum and the modified energy equations can be evaluated on either side of the shock wave. Quite naturally, the following quantities are

conserved across the shock:

$$\rho u = \rho_u u_u = \rho_d u_d = m, \tag{E.3a}$$

$$mu + p - \frac{4}{3}\mu\frac{\partial u}{\partial x} = mu_u p_u = mu_d p_d = mV, \tag{E.3b}$$

$$\begin{aligned} m\left(h + \frac{1}{2}u^2\right) - \mu\left(\frac{1}{Pr}\frac{\partial h}{\partial x} + \frac{4}{3}u\frac{\partial u}{\partial x}\right) = \\ m\left(h_u + \frac{1}{2}u_u^2\right) = m\left(h_d + \frac{1}{2}u_d^2\right) = mh_0. \end{aligned} \tag{E.3c}$$

Assuming a constant Prandtl number across the shock, the equation of state can be re-written as:

$$p = \rho RT = \rho\left(C_p - C_v\right)T = \frac{m}{u}\left(h - e\right), \tag{E.4}$$

Inserting the above equation into the equation for the conservation of momentum and energy, yields:

$$\frac{4}{3}\mu u\frac{\partial u}{\partial x} = m\left[h - e + u\left(u - V\right)\right], \tag{E.5a}$$

$$\frac{\mu}{Pr}\frac{\partial h}{\partial x} = m\left(e + uV - 1/2u^2 - h_0\right). \tag{E.5b}$$

By eliminating the temperature, T, from the above equations, we obtain a relationship:

$$\begin{aligned} \frac{\mu}{m}\left[\frac{4}{3}u + \frac{\gamma}{Pr}\left(2u - V\right)\right]\frac{\partial u}{\partial x} - \frac{4}{3}\frac{\gamma}{Pr}\frac{\mu^2}{m^2}\frac{\partial}{\partial x}\left(u\frac{\partial u}{\partial x}\right) = \\ \frac{\gamma+1}{2}u^2 - \gamma Vu + \left(\gamma - 1\right)h_0. \end{aligned} \tag{E.6}$$

The second term on the right hand side is shown to be negligible compared to the first term and, through a series of manipulations (Howarth, 1953), we obtain:

$$Dc_u\frac{\partial u}{\partial x} = -\left(u_u - u\right)\left(u - u_2\right), \tag{E.7}$$

where:

$$D = \frac{2}{\gamma+1}\left(\frac{4}{3} + \frac{\gamma - 1}{\mathrm{Pr}}\right)\frac{\nu_u}{c_u}. \tag{E.8}$$

The solution of this equation is a relation between the velocity and the position in the

shock. Given a velocity, the position can be calculated as:

$$x = \frac{D}{Ma_u\,(1 - u_d/u_u)} \ln \frac{u_u - u}{u - u_d} + cst. \tag{E.9}$$

Appendix F

Domain Size Independence

A computational domain size dependence study was conducted to verify that the results are not influenced by the selection of the domain size. The domain size independence is particularly important for LT and TT cases in chapter 4 because of the use of a spatially evolving initial condition. Here, the TT wake is computed on a regular domain size ($L_x \times L_y \times L_z$ =$75 \times 40 \times 20$) and compared to the computational domain used by Moser *et al.* (1998) ($L_x \times L_y \times L_z$ =$50 \times 40 \times 12.5$). In both these simulations, the grid spacing and computational parameters remain approximately constant. For the regular grid size, two side-by-side turbulent boundary layers are used on either side of the wake; for the smaller domain, only a single turbulent boundary layer is used. Figure F.1 compares the evolution of the spread rate, the velocity defect and the maximal streamwise and spanwise normal Reynolds stresses.

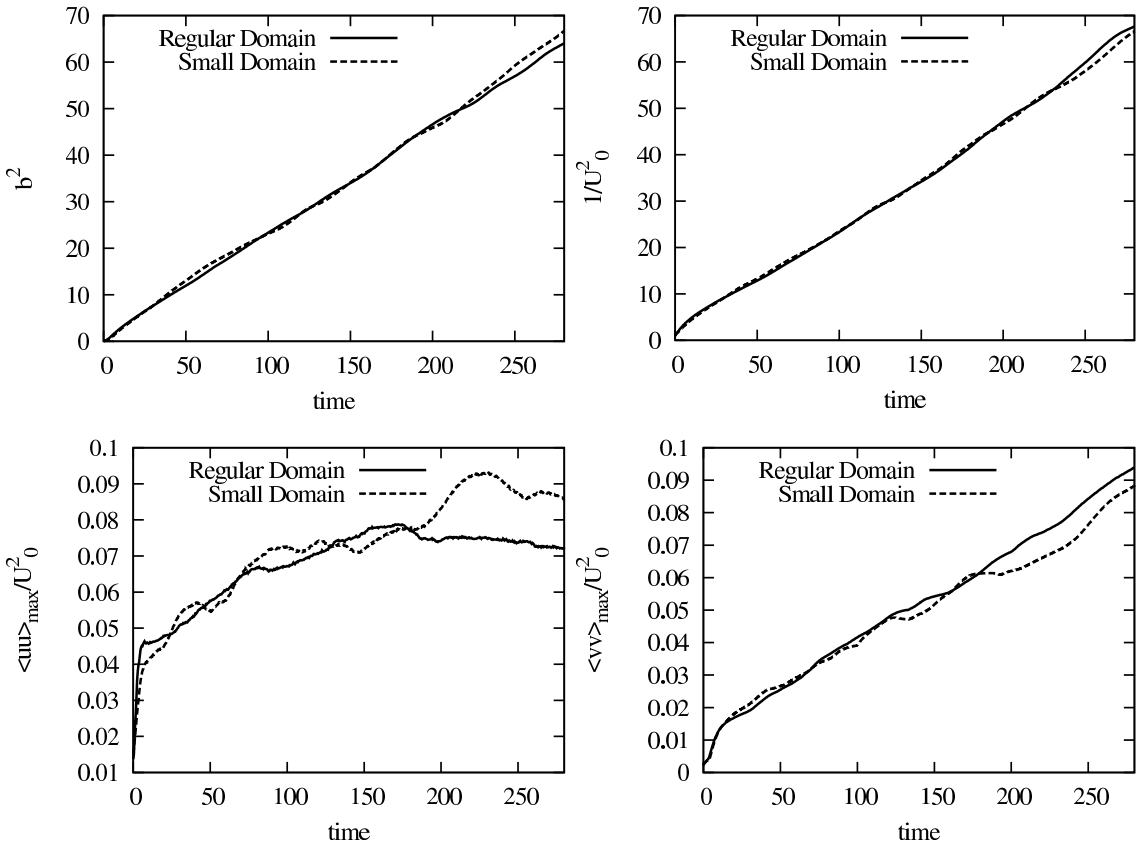

Figure F.1: Influence of the computational domain on the TT case, comparison between the baseline case and a reduced computational domain. Clockwise from top-left: squared spread-rate, inverse of the velocity defect squared, cross-wake and streamwise maximum normalized fluctuations. The larger discrepancies in the turbulence statistics at $t > 200$ are a result of the limited computational domain.

Appendix G

Grid Convergence and Resolution

Given the increased complexities of simulating compressible flows, care was taken to fully resolve all scales of turbulence during transition. Figure G.1 (top) shows the evolution of the minimal ratio of the Kolmogorov length scale to the grid spacing. For all simulations, the coarsest resolution is only slightly below unity after transition, therefore we can confidently state that all the scales of turbulence are adequately resolved by our simulations. Since the validation of temporal planar wake transition is tenuous with spatially evolving experiments, we carefully conducted grid converse tests. A grid convergence study was done by comparing the evolution of the maximal turbulent kinetic energy for three different grid resolutions (all other parameters remained unchanged, see table 5.1): 77×10^6 (1/2 grid in each direction), 413×10^6 ($1/\sqrt{2}$ grid in each direction) and 619×10^6. The grid convergence is shown in figure G.1 (bottom); other statistical parameters such as integrated production show a similarly good agreement (less than 1.6% variation in the peak production value). Needless to say that the agreement of the mean profiles is nearly perfectly captured among the different grid resolutions.

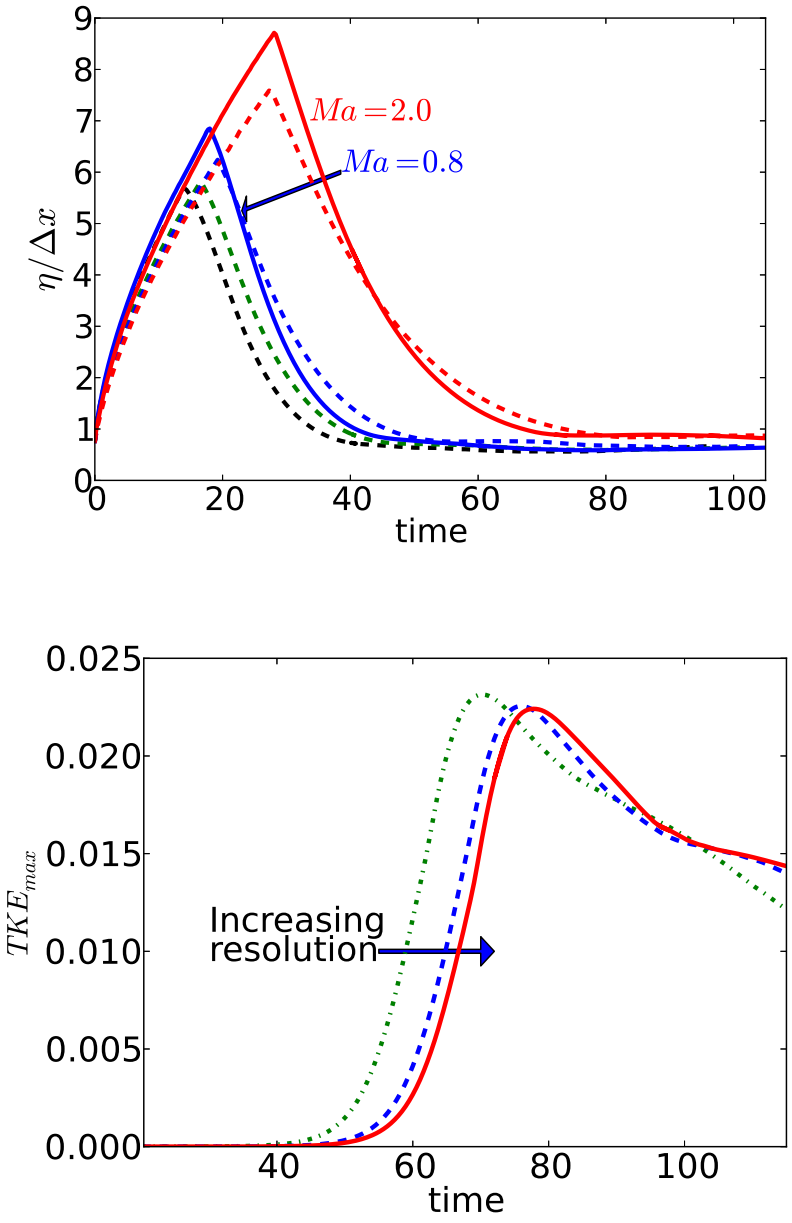

Figure G.1: Evolution of the minimal ratio of $\eta/\Delta x$ during transition (top); simulations at $Re = 1500$ (dashed lines) and $Re = 3000$ (full lines). Grid convergence test based on the evolution of the peak turbulent kinetic energy for the wake at $Ma = 2.0$ using three different grid densities: 77, 413 and 619 million nodes (bottom).

Appendix H

Developed numerical software

A significant effort was put forth in the development of new software over the course of this thesis. All the solvers and post-processing tools have been developed from scratch. For archival purposes, the python source codes for the linear stability and the ray tracing analysis (used in chapter 5) are presented:

H.1 Linear stability code

```
#=============================================================================================
#Name:           LinStab.py
#Description:  A linear stability code for high-speed inviscid and viscous free-shear flows
#Written by:  Jean-Pierre Hickey
#Date :       April 2011
#
#References:  Sandham, 1989; Chen et al. 1990; Watanabe & Maekawa 2004
#=============================================================================================

# Importing main libraries
import numpy as np
from  math import *
from mpmath import *
import matplotlib.pyplot as plt
from pylab import *
import h5py
```

```
z=complex(0,1)

#====================
# Defining Parameters
#====================
N      = 150          # Number of modes
Re     = 3000.        # Reynolds number of flow
Ma     = 2.0          # Mach number of the flow
Pr     = 1.0          # Prandtl number of flow
gamma  = 1.4          # Gamma of air or fluid
a      = 4.           # Stretching parameter (lim -> 0 center clustered, lim ->infty spread)
U0     = 0.692        # Initial centerline defect
c      = 0.69315      # Velocity profile constant
viscosity =1


gridx=arange(0.,alpha_size,dx_alpha)
gridy=arange(0.,beta_size,dx_beta)



#====================================
#
#    Initialization of all the variables was removed.
#       Must be added here!
#
#====================================


#====================
# Define mapping and grid.
#====================
dx=1.0/(N-1)
for i in xrange(N):
    compgrid[i]=i*dx
compgrid[0]  =compgrid[0]  +1E-9   # We add these terms to avoid singularities at infinity
compgrid[N-1]=compgrid[N-1]-1E-9

for i in xrange(N):
    realgrid[i]=-a*cot(pi*compgrid[i])
    # Be careful of coefficient Sandham = 2 (ML) while Watanabe =1 (WAKE)

#====================
# Use Cain(1984) mapping to find derivative matrices
#====================
for j in xrange(N):
    for i in xrange(N):
        if i==j:
            D0[i,j] = 1.0
            D1[i,j] = -(float(N)-1.0)/(a*float(N))*sin(2.0*pi*compgrid[j])
```

```
            D2[i,j] = - 1.0/(2.0*float(N)*a**2.0)*(cos(4.0*pi*compgrid[j])-
            4.0*cos(2.0*pi*compgrid[j])+3.0)*1.0/3.0*(float(N)/2.0-1.0)*float(N)/2.0*(float(N)-1.0)\
                -(float(N)-1.0)/(float(N)*a**2)*(cos(4.0*pi*compgrid[j])-    cos(2.0*pi*compgrid[j]))
        else:
            D0[i,j] = 0.0
            D1[i,j] =-1.0/(2.0*a)*(cos(2.0*pi*compgrid[j])-1.0)*
            (-1.0)**(float(i)-float(j))*cot((pi*(float(i)-float(j)))/float(N))\
                - 1.0/(float(N)*a) * sin(2.0*pi*compgrid[j]) *sin((1.0-1.0/float(N))*
                pi*(float(i)-float(j))) /sin(pi*(float(i)-float(j))/float(N))
            D2[i,j] = - (-1.0)**(float(i)-float(j))/(4.0*a**2.0)*(cos(4.0*pi*compgrid[j]) -
            4.0*cos(2.0*pi*compgrid[j]) + 3.0) *(1.0/((sin(pi*(float(i)-float(j))/float(N)))**2.0)
            -float(N)/2.0)\ - 3.0*(-1.0)**(float(i)-float(j))/(4.0*a**2.0)*
            (2.0*sin(2.0*pi*compgrid[j])- sin(4.0*pi*compgrid[j]))*
            cot(pi*(float(i)-float(j))/float(N)) \
                - 1.0/(float(N)*a**2.0)*(cos(4.0*pi*compgrid[j])-cos(2.0*pi*compgrid[j]))*
                sin((1.0-1.0/float(N))*pi*(float(i)-float(j)))/sin(pi*(float(i)-float(j))/float(N))


#====================
# Define flow conditions
#====================
for i in xrange(N):
    #Ucol[i] = 1.0-U0*exp(-c*realgrid[i]**2)    #Wake velocity profile
   # Ucol[i] = abs((realgrid[i]/5.0))**(1.0/7.0)       #Turbulent BL profile approximate (Prandtl)
    Ucol[i] = 1.0 - 1.0 * exp(-log(2.0)*(realgrid[i]/0.5)**2.0)
    print Ucol[i]
    if abs(realgrid[i]/5.0)>1.0:
        Ucol[i]=1.0
    Tcol[i] = 1+0.5*Ma**2*(gamma-1)*(1.0-(Ucol[i])**2)
    rhocol[i] = 1.0/Tcol[i]


for j in xrange(N):
    for i in xrange(N):
        if i==j:
            U[i,j]=Ucol[i]
            T[i,j]=Tcol[i]
            rho[i,j]=rhocol[i]
            invrho[i,j]=1/rhocol[i]

#====================
# Calculate derivatives of U, rho and T
#====================
rhocol= np.dot(D1,rhocol)
Ucol  = np.dot(D1,Ucol)
U2col = np.dot(D2,Ucol)
DTcol  = np.dot(D1,Tcol)
DT2col = np.dot(D2,Tcol)

for j in xrange(N):
```

```
    for i in xrange(N):
        if i==j:
            DU[i,j]     = Ucol[i]
            D2U[i,j]    = U2col[i]
            Drho[i,j]   = rhocol[i]
            DT[i,j]     = DTcol[i]
            D2T[i,j]    = DT2col[i]
            mu[i,j]     = Tcol[i]**(2./3.)               # Assume relation of mu = T **(2/3)
            dmudT[i,j]  =  2./3. * (Tcol[i])**(-1./3.)
            d2mudT2[i,j]= -2./9. * (Tcol[i])**(-4./3.)

#=====================================================
# Start covering the alpha and beta ranges.
#=====================================================
#Viscous component (if viscosity =0 then skip!)
if viscosity ==1:
    dmudT_DT = np.dot(dmudT,DT)         # dmu/dT * DT
    muD      = np.dot(mu,D1)            # mu * D1
    coef     = gamma*(gamma-1.)*Ma**2/Re
    V22      =  - z/Re     * ( np.dot(mu,(4./3.*D0*alpha**2 - D2 + D0*beta**2))-np.dot(dmudT_DT,D1))
    V23      =  - alpha/Re * (muD/3. + dmudT_DT)
    V24      =  - z * alpha*beta/(3.*Re) * mu
    V25      =  + z/Re     * (np.dot(np.dot(DU, d2mudT2),DT) + np.dot(dmudT,D2U) +
     np.dot(np.dot(DU,dmudT),D1) - np.dot(DU, dmudT_DT))
    V32      =  - alpha/Re * (muD/3. - 2./3.* dmudT_DT)
    V33      =  - z/Re     * (np.dot(mu, (D0*alpha**2 - 4./3.*D2 + D0*beta**2 ))
        - 4./3. * np.dot(dmudT_DT,D1))
    V34      =  - beta/Re  * (muD/3. - 2./3.*dmudT_DT)
    V35      =  - alpha/Re * (np.dot(DU,dmudT))
    V42      =  - z * alpha*beta/(3.*Re) * mu
    V43      =  - beta/Re  * (muD/3.+dmudT_DT)
    V44      =  - z/Re     * (np.dot(mu,(D0*alpha**2 - D2 + 4./3.*D0*beta**2)) - np.dot(dmudT_DT,D1))
    V52      =  + 2 * z *coef*( np.dot(DU,D1))
    V53      =  - 2 * alpha* coef * (DU)
    V55      =  +   z * coef*np.dot(dmudT,np.dot(DU,DU))\
                -   z * gamma/(Re*Pr)*(np.dot(mu,(D0*alpha**2- D2 + D0*beta**2))-
               np.dot(d2mudT2,np.dot(DT,DT)) \
                -   np.dot(dmudT, (2*np.dot(DT,D1)+D2T)))


#====================
# Add density term to viscous components
#====================
    V22= np.dot(invrho,V22)
    V23= np.dot(invrho,V23)
    V24= np.dot(invrho,V24)
    V25= np.dot(invrho,V25)
    V32= np.dot(invrho,V32)
    V33= np.dot(invrho,V33)
    V34= np.dot(invrho,V34)
```

```
    V35= np.dot(invrho,V35)
    V42= np.dot(invrho,V42)
    V43= np.dot(invrho,V43)
    V44= np.dot(invrho,V44)
    V52= np.dot(invrho,V52)
    V53= np.dot(invrho,V53)
    V55= np.dot(invrho,V55)


#====================
#Inviscid part
#====================
A11      = alpha   * U
A12      = alpha * rho
A13      = - z * (Drho + np.dot(rho,D1))
A14      = rho * beta
A15      = np.zeros([N,N])

A21      = alpha / (gamma * Ma**2) * np.dot(T,invrho)
A22      = alpha * U     + V22
A23      = - z * DU                + V23
A24      =                         + V24
A25      = alpha/(gamma*Ma**2) * D0 + V25

A31      = - z/( gamma * Ma**2) *np.dot(invrho,(DT + np.dot(T,D1)))
A32      =                           + V32
A33      =  alpha * U                + V33
A34      =                           + V34
A35      = - z/( gamma * Ma**2) *np.dot(invrho,(Drho + np.dot(rho,D1))) + V35

A41      = beta /( gamma * Ma**2)*np.dot(T,invrho)
A42      =                          + V42
A43      =                          + V43
A44      = alpha * U                + V44
A45      = beta /(gamma*Ma**2)*D0

A51      = np.zeros([N,N])
A52      = (gamma-1.)*alpha*invrho    + V52
A53      = - z *(DT + (gamma-1) *np.dot(T,D1)) + V53
A54      = T * beta*(gamma-1)
A55      = alpha * U              + V55


A=np.concatenate((A11,A12,A13,A14,A15),1)
B=np.concatenate((A21,A22,A23,A24,A25),1)
C=np.concatenate((A31,A32,A33,A34,A35),1)
D=np.concatenate((A41,A42,A43,A44,A45),1)
E=np.concatenate((A51,A52,A53,A54,A55),1)

A=np.concatenate((A,B,C,D,E),0)
```

```
AT=A.conj().T
AAT=np.dot(A,AT)
ATA=np.dot(AT,A)
res=ATA==ATA
if res.all() :
    print "We have a normal matrix"

 eig,eigvec=np.linalg.eig(A)

loceig=-999999.   # Find the maximum eigenvalue for specific (alpha,beta)

#====================
# Find maximum symmetric and anti-symmetric modes
#====================
max_u=-1.
max_v=-1.
symeig = -999.   # Anti-symmetric
asymeig = -999.   # symmetric
center= N/2   # center of wake (add modulus to find the center)



for i in xrange(5*N):
    #for j in xrange(N):
    tempu=np.sqrt(eigvec[1*N+center-5:1*N+center+5,i].real**2 +
     eigvec[1*N+center-5:1*N+center+5,i].imag**2)
    tempv=np.sqrt(eigvec[2*N+center-5:2*N+center+5,i].real**2 +
     eigvec[2*N+center-5:2*N+center+5,i].imag**2)
    tempu=(eigvec[1*N+center-5:1*N+center+5,i].real)
    tempv=(eigvec[2*N+center-5:2*N+center+5,i].real )
    tempx = realgrid[center-5:center+5]
    testu=np.poly1d(np.polyfit(tempx,tempu,4))
    testv=np.poly1d(np.polyfit(tempx,tempv,4))
    u1tilde=abs(testu(0.0)/np.max(testu))
    Du2tilde=np.abs((testv(0.1)-testv(-0.1))/np.max(tempv))
    print u1tilde,Du2tilde
   # u0   = np.sqrt(eigvec[1*N+center,i].real**2 + eigvec[1*N+center,i].imag**2)
    #v0   = np.sqrt(eigvec[2*N+center,i].real**2 + eigvec[2*N+center,i].imag**2)
    if  u1tilde < 0.1 and Du2tilde<0.1:     # SYMMETRIC MODE
        if eig[i].imag > symeig:
            symeig = eig[i].imag
            symeig_r=eig[i].real
            symnum=i
          #  print "we have in symmetric", u0,v0
    else:                                    # aSYMMETRIC MODE
        if eig[i].imag > asymeig:
            asymeig = eig[i].imag
            asymeig_r=eig[i].real
            asymnum=i
```

```
print "What are the modes?" ,symnum,asymnum
for i in xrange(N):
    rhop[i]=eigvec[0*N+i,asymnum].real
    up[i]=eigvec[1*N+i,asymnum].real
    vp[i]=eigvec[2*N+i,asymnum].real
    wp[i]=eigvec[3*N+i,asymnum].real
    Tp[i]=eigvec[4*N+i,asymnum].real
    rhoi[i]=eigvec[0*N+i,asymnum].imag
    ui[i]=eigvec[1*N+i,asymnum].imag
    vi[i]=eigvec[2*N+i,asymnum].imag
    wi[i]=eigvec[3*N+i,asymnum].imag
    Ti[i]=eigvec[4*N+i,asymnum].imag

    srhop[i]=eigvec[0*N+i,symnum].real
    sup[i]=eigvec[1*N+i,symnum].real
    svp[i]=eigvec[2*N+i,symnum].real
    swp[i]=eigvec[3*N+i,symnum].real
    sTp[i]=eigvec[4*N+i,symnum].real
    srhoi[i]=eigvec[0*N+i,symnum].imag
    sui[i]=eigvec[1*N+i,symnum].imag
    svi[i]=eigvec[2*N+i,symnum].imag
    swi[i]=eigvec[3*N+i,symnum].imag
    sTi[i]=eigvec[4*N+i,symnum].imag

for i in xrange(N):
    magu[i]=np.sqrt(up[i]**2+ui[i]**2)
    magv[i]=np.sqrt(vp[i]**2+vi[i]**2)
    magT[i]=np.sqrt(Tp[i]**2+Ti[i]**2)
    magrho[i]=np.sqrt(srhop[i]**2+srhoi[i]**2)
    smagu[i]=np.sqrt(sup[i]**2+sui[i]**2)
    smagv[i]=np.sqrt(svp[i]**2+svi[i]**2)
    smagT[i]=np.sqrt(sTp[i]**2+sTi[i]**2)
    smagrho[i]=np.sqrt(srhop[i]**2+srhoi[i]**2)



startend= 5

#====================
# Output
#====================
print "We have values of symmetric " ,eig.real[symnum],eig.imag[symnum]
print "We have values of anti-symmetric " ,eig.real[asymnum],eig.imag[asymnum]
k2=sqrt(alpha**2+beta**2)
print " convective speed of assymmetric mode " , eig.real[asymnum]/k2
print " convective speed of symmetric mode " , eig.real[symnum]/k2
matplotlib.pyplot.figure(0)
matplotlib.pyplot.scatter(eig.real,eig.imag)
matplotlib.pyplot.scatter(eig.real[symnum],eig.imag[symnum],c='r',s=116,marker='o')
```

```
#matplotlib.pyplot.scatter(eig.real[asymnum],eig.imag[asymnum],c='g',s=116,marker='s',label='as')
matplotlib.pyplot.xlim([-0.5,1.3])
matplotlib.pyplot.figure(1)
matplotlib.pyplot.subplot(221)
matplotlib.pyplot.plot(realgrid,up, label="Real part", linewidth=2)
matplotlib.pyplot.plot(realgrid,ui, "--",label="Iamg part", linewidth=2)
matplotlib.pyplot.plot(realgrid,magu,label="Magnitude", linewidth=2)
xlim([-startend,startend])
matplotlib.pyplot.title('u')
matplotlib.pyplot.subplot(222)
matplotlib.pyplot.plot(realgrid,vp, label="Real part", linewidth=2)
matplotlib.pyplot.plot(realgrid,vi, "--",label="Iamg part", linewidth=2)
matplotlib.pyplot.plot(realgrid,magv,label="Magnitude", linewidth=2)
xlim([-startend,startend])
matplotlib.pyplot.title('v')
matplotlib.pyplot.subplot(223)
matplotlib.pyplot.plot(realgrid,Tp,label="Real part", linewidth=2)
matplotlib.pyplot.plot(realgrid,Ti, "--",label="Iamg part", linewidth=2)
matplotlib.pyplot.plot(realgrid,magT,label="Magnitude", linewidth=2)
xlim([-startend,startend])
matplotlib.pyplot.title('T')
matplotlib.pyplot.subplot(224)
matplotlib.pyplot.plot(realgrid,rhop, label="Real part", linewidth=2)
matplotlib.pyplot.plot(realgrid,rhoi, "--",label="Iamg part", linewidth=2)
matplotlib.pyplot.plot(realgrid,magrho,label="Magnitude", linewidth=2)
matplotlib.pyplot.title('rho')

matplotlib.pyplot.figure(2)
matplotlib.pyplot.subplot(221)
matplotlib.pyplot.plot(realgrid,sup, label="Real part", linewidth=2)
matplotlib.pyplot.plot(realgrid,sui, "--",label="Iamg part", linewidth=2)
matplotlib.pyplot.plot(realgrid,smagu,label="Magnitude", linewidth=2)
xlim([-startend,startend])
matplotlib.pyplot.title('u')
matplotlib.pyplot.subplot(222)
matplotlib.pyplot.plot(realgrid,svp, label="Real part", linewidth=2)
matplotlib.pyplot.plot(realgrid,svi, "--",label="Iamg part", linewidth=2)
matplotlib.pyplot.plot(realgrid,smagv,label="Magnitude", linewidth=2)
xlim([-startend,startend])
matplotlib.pyplot.title('v')
matplotlib.pyplot.subplot(223)
matplotlib.pyplot.plot(realgrid,sTp,label="Real part", linewidth=2)
matplotlib.pyplot.plot(realgrid,sTi, "--",label="Iamg part", linewidth=2)
matplotlib.pyplot.plot(realgrid,smagT,label="Magnitude", linewidth=2)
xlim([-startend,startend])
matplotlib.pyplot.title('T')
matplotlib.pyplot.subplot(224)
matplotlib.pyplot.plot(realgrid,srhop, label="Real part", linewidth=2)
matplotlib.pyplot.plot(realgrid,srhoi, "--",label="Iamg part", linewidth=2)
matplotlib.pyplot.plot(realgrid,smagrho,label="Magnitude", linewidth=2)
```

```
matplotlib.pyplot.title('rho')

xlim([-startend,startend])
show()


namefile="EigVect_" + str(N)
if viscosity == 1 :
    namefile=namefile+'_Re_'+str(Re)+'_Ma_'+str(Ma)+'.h5'
    print namefile
elif viscosity == 0 :
    namefile=namefile+'_inviscid.h5'
f=h5py.File(namefile, 'w')

Overall=f.create_group("AntiSymmetric")
sg_1=Overall.create_dataset("u_real",data=up)
sg_1=Overall.create_dataset("u_imag",data=ui)
sg_1=Overall.create_dataset("magu",data=magu)
sg_1=Overall.create_dataset("v_real",data=vp)
sg_1=Overall.create_dataset("v_imag",data=vi)
sg_1=Overall.create_dataset("magv",data=magv)
sg_1=Overall.create_dataset("T_real",data=Tp)
sg_1=Overall.create_dataset("T_imag",data=Ti)
sg_1=Overall.create_dataset("magT",data=magT)
sg_1=Overall.create_dataset("rho_real",data=rhop)
sg_1=Overall.create_dataset("rho_imag",data=rhoi)
sg_1=Overall.create_dataset("magrho",data=magrho)

Overall1=f.create_group("Symmetric")
sg_1=Overall1.create_dataset("u_real",data=sup)
sg_1=Overall1.create_dataset("u_imag",data=sui)
sg_1=Overall1.create_dataset("magu",data=smagu)
sg_1=Overall1.create_dataset("v_real",data=svp)
sg_1=Overall1.create_dataset("v_imag",data=svi)
sg_1=Overall1.create_dataset("magv",data=smagv)
sg_1=Overall1.create_dataset("T_real",data=sTp)
sg_1=Overall1.create_dataset("T_imag",data=sTi)
sg_1=Overall1.create_dataset("magT",data=smagT)
sg_1=Overall1.create_dataset("rho_real",data=srhop)
sg_1=Overall1.create_dataset("rho_imag",data=srhoi)
sg_1=Overall1.create_dataset("magrho",data=smagrho)

Overall2=f.create_group("Grid")
sg_1=Overall2.create_dataset("realgrid",data=realgrid)
f.close()


##ans=np.linalg.eig(A)
```

H.2 Ray tracing code

```
#=============================================================================================
#Name:           RayTrace.py
#Description:  Geometric acoustics of high-speed free shear flow
#Written by:  Jean-Pierre Hickey
#Date :       January 2012 - June 2012
#
# References: Papamoschou, 1993; Papamoschou, 1994
#=============================================================================================
import numpy as np
import matplotlib.pyplot as plt

#===================
# Runge-Kutta (4th-order) time advancement
#===================
def RayTraceRK4(nmax,nbpoints,x_init,y_init,Ma_inf,typeflow,y_rec):
    x=np.zeros((nmax,nbpoints))
    y=np.zeros((nmax,nbpoints))
    ray=np.zeros((nbpoints,2))
    I=np.zeros((nbpoints,2))
    mytime=np.zeros((nmax,nbpoints))
    ic=np.linspace(-np.pi,np.pi,nbpoints)
    for i in xrange(len(ic)):
        theta_init=ic[i]
        x[0,i]=x_init
        y[0,i]=y_init
        switch="false"
        pretheta=0.0
        first=0
        for j in xrange(nmax-1):
            mytime[j+1,i]=dt*j
   #Euler Step
            Ma_loc=getMa(y[j,i],Ma_inf,typeflow)
            theta,sign,switch=getsnell(theta_init,Ma_loc,Ma_init,switch,pretheta)
            f_p=getf(y[j,i],a,theta,Ma_init)
            g_p=getg(a,theta,theta_init,sign)
                #print theta_init,theta, g_p,y[j,i],Ma_loc
            x_p=x[j,i]+dt/2.0*f_p
            y_p=y[j,i]+dt/2.0*g_p
            pretheta=theta

    #SECOND STEP
            Ma_loc=getMa(y_p,Ma_inf,typeflow)
            theta,sign,switch=getsnell(theta_init,Ma_loc,Ma_init,switch,pretheta)
            f_pp=getf(y_p,a,theta,Ma_init)
            g_pp=getg(a,theta,theta_init,sign)
            x_pp=x[j,i]+dt/2.0*f_pp
            y_pp=y[j,i]+dt/2.0*g_pp
```

```
            pretheta=theta

            #Third STEP
            Ma_loc=getMa(y_pp,Ma_inf,typeflow)
            theta,sign,switch=getsnell(theta_init,Ma_loc,Ma_init,switch,pretheta)
            f_ppp=getf(y_pp,a,theta,Ma_init)
            g_ppp=getg(a,theta,theta_init,sign)
            x_ppp=x[j,i]+dt*f_ppp
            y_ppp=y[j,i]+dt*g_ppp
            pretheta=theta

      #Last STEP
            Ma_loc=getMa(y_ppp,Ma_inf,typeflow)
            theta,sign,switch=getsnell(theta_init,Ma_loc,Ma_init,switch,pretheta)
            f_pppp=getf(y_ppp,a,theta,Ma_init)
            g_pppp=getg(a,theta,theta_init,sign)
            x[j+1,i]=x[j,i]+dt/6.0*(f_p+ 2.0*(f_pp+f_ppp)+f_pppp)
            y[j+1,i]=y[j,i]+dt/6.0*(g_p+ 2.0*(g_pp+g_ppp)+g_pppp)
            pretheta=theta
            # Calculate intensity along receptor line
            if y[j+1,i]<y_rec:
                if y[j,i]>y_rec:
                    if first==0:
                        sign=1.0
                        if x[j,i] < 0:
                            sign=-1.0
                        m=(y[j+1,i]-y[j,i])/(x[j+1,i]-x[j,i])
                        b=y[j,i]-m*x[j,i]
                        ray[i,0]= sign*(y_rec-b)/m
                        ray[i,1]= m
                        first=1

    dtheta=2.0*np.pi/(nbpoints-1.0)
    for j in xrange(nbpoints-1):
        if ray[j,1] != 0.0:
            m=0.5*(ray[j+1,1]+ray[j,1])
            dxdtheta=np.abs(ray[j+1,0]-ray[j,0])/dtheta
            theta_rec=np.arctan(1.0/m)
            I[j,0]=1.0/np.abs(np.cos(theta_rec)*dxdtheta)
            I[j,1]= 0.5*(ray[j+1,0]+ray[j,0])

    return (x,y,mytime,ray,I)

#====================
# Define characteristics
#====================
def getf(y,a,theta,M_init):
    #f=u(y)-a*sin(theta)
    u_loc=getMa(y,M_init,typeflow)
    f=u_loc-a*np.sin(theta)
```

```
    return (f)

def getg(a,theta,theta_init,sign):
    #g=-a cos(theta)
    g=sign*a*np.cos(theta)
    return (g)

#====================
# Compute local Mach number
#====================
def getMa(y,M_inf,typeflow):
    #Mixing layer
    if typeflow=="ML":
        Ma=Ma_inf*np.tanh(2*y)/np.tanh(2)
    elif typeflow=="wake":
        Ma= Ma_inf*(1.0 - np.exp(-np.log(2.0)*(y/0.5)**2.0))
    elif typeflow=="MLpapa":
        M_top=1.5*M_inf
        M_bot=0.5*M_inf
        A= 0.5*(M_top-M_bot)
        B= 0.5*(M_top-M_bot)
        beta = -1.0/np.tanh(A/B)
        alpha= 1.0/np.tanh((M_top-A)/B)-beta
        Ma= A+B*np.tanh(alpha*y+beta)
    elif typeflow=="MLpapa94":
        Ma=Ma_inf*np.tanh(2*y)
    return (Ma)

 #====================
# Compute Snell law
#====================
def getsnell(theta_init,M_loc,M_init,switch,pretheta):
    sign=-1.0
    if np.abs(theta_init)>np.pi/2:
        sign=1.0
    denom=(1.0+(M_loc-M_init)*np.sin(theta_init))
    div=np.sin(theta_init)/denom

    if abs(div) > 1.0:
         theta=pretheta
         switch="true"
    else:
         theta=np.arcsin(div)

    if switch=="true":
         sign=sign*(-1.0)
   # print theta,np.sin(theta_init)/denom
    return (theta,sign,switch)

def forceAspect(ax,aspect=1):
```

```
    im = ax.get_images()
    extent =  im[0].get_extent()
    ax.set_aspect(abs((extent[1]-extent[0])/(extent[3]-extent[2]))/aspect)


# =======================
#  Define Flow characteristics
# =======================
Ma_inf=1.500
nmax=50
nbpoints=50
typeflow="wake"   # or 'wake' or "MLpapa"or "MLpapa94""
x_init=0.0
y_init=0.50
dt=0.1
a=1.0
y_rec=0.0
printfile=0 # if 0 no write

trace='true'
front="false"

font = { 'size'   : 25}

plt.rc('font', **font)



# =======================
# Compute Ray trace
# =======================
Ma_init= getMa(y_init,Ma_inf,typeflow)
x,y,mytime,ray,I=RayTraceRK4(nmax,nbpoints,x_init,y_init,Ma_inf,typeflow,y_rec)


myy=np.linspace(-3,3,400)
sel=np.arange(0,nbpoints-nbpoints/30,nbpoints/30)
if trace=='true':
    plt.plot(x[:,sel],y[:,sel],'k-',lw=0.3)

    plt.xlim(-2,5)
    plt.ylim(-2,2)
       # plt.text(1.75,1.2,'Mean profile')
    if y_init==0.0:
        print" OK in here"
        plt.text(-1.7+x_init,2+y_init,"Ma="+str(Ma_inf),fontsize=27,bbox=dict(facecolor='white'))

       # plt.text(-0.7,1.6,'Ma='+ str(Ma_inf))
    plt.xlabel('$x/b$',fontsize=31)
    plt.ylabel('$y/b$',fontsize=31)
```

```
    plt.ylim(-2,2)
    if Ma_inf == 0.1:
        plt.text(-0.15+x_init,0.1+y_init,'source',fontsize=20)
    if typeflow=="wake":
        plt.axhline(y=0.5,lw=0.5)
        plt.axhline(y=-0.5,lw=0.5)
    else:
        plt.axhline(y=1)
        plt.axhline(y=-1)
    levels=np.arange(0.0,60,0.6)
    plt.contour(x, y, mytime, levels,lw=4)
    plt.scatter(x_init, y_init, s=50, c='r', marker='o')
    plt.axes().set_aspect('equal', 'datalim')
    plt.xlim(-2,5)
    if Ma_inf == 0.1:
       # ax2 = plt.twiny()
        #plt.xlim(-Ma_inf*2.0,Ma_inf)
        #plt.xlabel('Mach')
        #plt.xticks(np.linspace(0,Ma_inf,3))

        plt.plot(4+(getMa(myy,Ma_inf,typeflow)*7),myy,'r-',lw=3)
    dec=str(Ma_inf)

plt.figure()
plt.plot(ray[:,0],I[:,0])
plt.show()
```

Appendix I

Additional Scientific Contributions

In addition to the study of the wake, additional contributions have been made during the present doctoral thesis. These works have resulted in two journal publications, an ongoing technical report and conference presentations. A summary of the contributions and the abstracts of the paper/report are listed for archival purposes:

I.1 Bypass Boundary Layer Transition

A study of bypass boundary layer transition under periodically passing wakes was conducted. The investigation was presented at the International Symposium on Turbulence and Shear Flow Phenomena in Seoul, South Korea in June 2009 (Hickey *et al.*, 2009). The work was selected as one of the top twenty contributions and invited for publication in the International Journal of Heat and Fluid Flow (Hickey *et al.*, 2010).

Abstract:

We present a numerical study of a flat-plate boundary layer with free-stream periodically passing planar wakes without external pressure gradients from

$Re_\theta = 80$ to fully turbulent. Two direct numerical simulations were performed on the same flow with slightly different simulations parameters. In the con- strained simulation design, the wakes are restricted to six boundary layer thicknesses above the wall at the inlet, while in the other design the wakes are un-constrained. Boundary layer statistics before, during and after transition are thoroughly evaluated through comparison with theoretical and experimental data of the zero-pressure gradient flat-plate boundary layer. Three-dimensional flow visualizations reveal the instant and location of breakdown events. Negative streaks are not of the shape of a rectangular box, rather, their wedged shape narrows towards the downstream passing wake and their strength diminishes towards the wall and towards the upstream direction. Matured turbulent spots have arrowheads directed upstream. Despite the intermittency of the passing wake disturbances, statistics in the early transitional region exhibit characteristics in agreement with previous studies on boundary layer. Statistics in the turbulent boundary layers differ from the canonical case only mildly near the outer edge.

I.2 Turbulence Interaction in Turbine Passages

The distortion of a continuous stream of isotropic turbulence within a turbine passage was studied using a direct numerical simulation. The work was presented at the annual meeting of the Canadian Aeronautics and Space Institute (CASI) in Montréal in 2011. The corresponding paper titled, *Visualization of Continuous Stream of Grid Turbulence Past the Langston Turbine Cascade*, was published in the The American Institute of Aeronautics and Astronautics Journal in 2012 (Wu & Hickey, 2012). This paper contains a validation

of the developed numerical solver using decaying isotropic turbulence in the incompressible limit.

Abstract:

This paper describes a direct numerical simulation visualization study on the migration and distortion of a continuous stream of grid turbulence passing through a representative turbine cascade with and without being segregated by the blade leading edge. For the non-impinging case, as the turbulent stream starts to enter the turbine cascade, there is a coarsening and reorientation of the small-scale and random grid-turbulence structures into short vortex tubes; inside the cascade, these short vortex tubes are further stretched into relatively long quasi-streamwise vortices. For the impinging case, very long streamwise vortices on the pressure surface are observed that correspond nicely to the colored-fingers phenomenon reported in previous turbine heat transfer experiments. The spanwise locations of the observed vortices vary with time. The origin of such turbine pressure-side streamwise vortices is revealed using a relatively complete sequence of images documenting their life cycle. For the impinging case, the short vortex tubes formed at the stagnation are gradually distorted into the shape of a hockey stick. The long stick is nearly parallel to the blade pressure surface, whereas the short end is bent toward the freestream. This process can be well explained by invoking results from previous fundamental studies on simple stagnation flows and on the stretching and rotation of material lines by the mean strain-rate field under the assumption of rapid distortion. Taken together with earlier investigations on turbine distortion of migrating planar wake and migrating isolated turbulent block, it is

quite likely that Taylor-Goertler centrifugal instability may not be an important player in the formation of pressure-side elongated streamwise vortices in turbomachinery applications.

I.3 Modelling Shock/Boundary Layer and Shock/Shock Interactions

As part of The Technical Cooperation Program (TTCP) through Defence Research and Development Canada (DRDC) in Valcartier, a three-year study was undertaken starting in May 2011 to evaluate the modelling capabilities of modern computational fluid dynamic software. Monthly progress reports were given to the funding agency (DRDC) and yearly presentations were given to the TTCP international partners at the annual meeting in Australia in March 2012. A technical report is currently being redacted for DRDC.

Abstract:

The present work describes the Canadian contribution to the Key Task Area (KTA)2-31-11 as part of the Technical Cooperation Programme (TTCP). The objective of the KTA is to assess the capabilities of modern Computational Fluid Dynamic (CFD) solvers for the prediction of fundamental flow physics for high-speed missiles. The Canadian contribution rests on the evaluation and comparison of the commercial CFD package *Fluent*® (ANSYS) and the open-source alternative *OpenFOAM* ® . Three canonical test cases of shock/boundary layer (SBLI) and shock/shock (SSI) interaction are investigated: UFAST (e.g. Piponniau *et al.*, 2009), Kussoy & Horstman (1992) and Brosh & Kussoy (1983). The simulated canonical flows are compared against the available experimental data. The prediction of the complex flows rests primarily on the use of Reynolds-Averaged closure models (RANS) and coarse Large-Eddy

Simulation (LES). Various turbulence closure models and grid resolutions are investigated; the sensitivity of the boundary conditions are also assessed. The main flow features of both SBLI and SSI are captured with *Fluent*® and *OpenFOAM*®, although the selection of the turbulence models play an important role in the SBLI. Despite some deficiencies for high-speed flows, *OpenFOAM*® shows much promise for the use in predictive CFD simulations, especially since the highly-scalable code is hardware limited and not license limited. A best-practice guide was established for the use of *OpenFOAM*®.

Part II

Curriculum Vitae

Curriculum Vitae

Name	Jean-Pierre Hickey
Date and place of birth	April 19, 1980 Hull, Québec, Canada
Education	**Ph.D.** Mechanical Engineering, 2008–2012 Royal Military College of Canada, Canada Advisor: Prof. Xiaohua Wu **M.Sc.** Computational and Mechanical Engineering, 2005–2007 Technische Universität Darmstadt, Germany Advisor: Prof. Dr.-Ing. Martin Oberlack **B.Ing.** Mechanical Engineering, 2000–2004 École Polytechnique de Montréal, Canada Exchange: Czech Technical University (2002–2003)
Teaching	MEC315 - Fluid Mechanics (2009) GCF319 - Civil Engineering Analysis II (2010, 2011, 2012) TAships: Fluid Mechanics (MEC311, MEC411) and Heat Transfer (MEC421)
Experience	Engineering Intern, 2005 (6 months) Energi E2, Copenhagen, Denmark Engineering Intern, 2004 (12 months) General Electric - Hydro Division, Montréal, Canada
Awards	Natural Sciences and Engineering Research Council (NSERC) Post-Graduate Scholarship, 2010-2012 Best Student Paper Award (2^{nd} place), Computational Fluid Dynamics Society of Canada, Montréal, Canada, 2011 Department of Mechanical and Aerospace Engineering Post-Graduate Scholarship, 2010 Bourse de mobilité du Québec, 2002-2003